

https://dspace.org/

Synthesis, characterization and application of 2d semiconducting layered inorganic nanostructures of In2S3 and WS2 in gas sensing

Gqoba, Siziwe Sylvia

2018

https://hdl.handle.net/10539/27401

Gqoba, Siziwe (2018) Synthesis, characterization and application of 2D layered inorganic nanostructures of In2S3 and WS2 in gas sensing, University of the Witwatersrand, Johannesburg, https://hdl.handle.net/10539/27401

Downloaded from a DSpace repository. https://dspace.org/

SYNTHESIS, CHARACTERIZATION AND APPLICATION OF 2D SEMICONDUCTING LAYERED INORGANIC NANOSTRUCTURES OF In_2S_3 AND WS_2 IN GAS SENSING

BY

Siziwe Sylvia Gqoba

(298480)

A thesis submitted to the Faculty of Science at the University of the Witwatersrand, Johannesburg in fulfilment of the requirements for the degree of Doctor of Philosophy in Chemistry

Advisor: Prof. Nosipho Moloto

Johannesburg, 2018

DECLARATION

I declare that this thesis is my own, unaided work under the supervision of Professor Nosipho Moloto. It is being submitted for the degree of Doctor of Philosophy in Science at the University of the Witwatersrand, Johannesburg. It has not been submitted before for any degree or examination in any other University.

Siziwe Sylvia Gqoba

_____day of _____

ABSTRACT

2D semiconductor nanostructure based chemical sensors hold the promise of portable, fast, low power, simple and low cost technologies for the detection of volatile organic compounds (VOCs) and gases. Detection, monitoring and quantification of these analytes are important for the improvement of the quality of human life, safety and the surrounding environment. Their electrical conductance is extremely sensitive to changes in the local chemical environment and can be chemically modified to increase selectivity. Nanostructures have tunable band gaps and exhibit new and improved properties at the quantum confinement limit. The band gap is affected by the size, shape, dimensionality and chemical composition of the nanostructures. So, precise control of these factors is achieved by manipulating reaction parameters like time, temperature, choice of precursors and choice of capping agent as well as concentration. In this study, we unravel the effect of reaction parameters on the structural, optical and morphological properties of In_2S_3 and WS_2 nanostructures during colloidal synthesis. The reaction parameters under investigation were time, concentration, solvent or capping agent and precursor.

For instance, different shapes of ß-In_2S_3 were obtained for mono- and bi-ligand systems, reaction time, concentration of the precursor and solvent. Capping agents influence the growth kinetics and the shape of nanostructures. Well defined hexagonal ß-In_2S_3 nanostructures of the tetragonal phase were obtained as a function of time with elemental S and indium chloride reacted at 1:1 mole ratio in oleylamine (OLA) medium. OLA, an alkylamine played the triple role of the reducing agent, solvent and capping agent. An increased amount of S to In^{3+} proved to be an unfavourable condition for the formation of the hexagonal shape as seen with the 1:2 mole ratio. Hexadecylamaine (HDA) and octadecylamine (ODA), alkylamines like OLA were also used in separate experiments. The hexagonal shape like with OLA evolved with time for ODA while it never materialized for HDA. Dodecanethiol (1-DDT), a thiol ligand produced microspheres as a function of time. These alkylamines were then each used in bi-ligand systems with a controlled amount of 1-DDT at a 1:1 mole ratio of In^{3+} and S. For OLA/1-DDT, the hexagonal morphology was favoured and retained regardless of the duration of the reaction time. However, the hexagonal shape transformed into nanorods with prolonged reaction time for the ODA/1-DDT combination. The morphology was rather elusive for HDA/1-DDT system even at extended reaction time. HDA and ODA yielded the cubic phase of ß-In_2S_3 in both the mono- and

biligand systems. An increased amount of 1-DDT to OLA resulted in mixed morphologies regardless of the reaction time, once again proving the importance of concentration. It is interesting to note that hexagonal nanostructures were retained when 1-DDT was used as a source of S (1:1) with OLA serving a triple role. In the case of WS_2, only OLA was used as a capping agent and the variation of reaction of time yielded nanoflowers, nanoflake-like and nanorod-like structures.

The nanostructures of these semiconductors were used as components in chemi-resistive sensors for the detection and identification of NH_3 gas and selected VOCs. Unlike their oxide counterparts, their gas sensing potential has been largely overlooked despite their capability of operating at room temperature. Preliminary studies on ß-In_2S_3 sensors based on the 330 min nanostructures showed gas sensing potential towards formaldehyde vapour. In the case of WS_2 nanostructures, all the sensors regardless of the reaction time exhibited gas sensing potential. However, the percentage of that response was based on the morphology which was associated with the reaction time. For instance, the microflower morphology obtained at 15 and 45 min displayed the best response compared to 60, 180 and 240 min. However, 45 min had a higher response than 15 min because the 'petals'which make up the microflowers had opened up. This meant that the reaction not only took place on the surface of the microflower but also in between the 'petals'. It is well known that humidity is an interferant and can either reduce or improve a sensor's performance. The sensor's performances towards NH_3 varied depending on the relative humidity they were operating under. Annealing of the sensors showed improved performance at lower temperatures while higher temperatures led to reduced performance. OLA, a long chain ligand renders the semiconductor an insulator thereby reducing its performance. Effect of replacement of OLA with shorter chain ligands on the gas response was also investigated. Mercaptoethanol (ME) and ethanedithiol (1, 2-EDT) were used as the short chain ligands and showed improved response towards a lower concentration of NH_3. Application of the OLA/WS_2 sensors in a tristimulus analysis proved that they can be used in chemical sensor arrays despite the fact that they are made of the same chemical composition. The various morphologies obtained at different time intervals provided the distinguishing factor between the nanostructures.

ACKNOWLEDGEMENT

I would like to convey my sincere gratitude to Prof. Nosipho Moloto for her unwavering support and guidance. Thank you for introducing me to research student supervision. Your wisdom, knowledge of the subject matter and love for science are enviable. You deserve all the accolades you have been receiving. Your selfless nature is admirable.

This thesis would not have come to fruition had it not been for the support of the following people and organizations:

- My family and friends for the support and always listening to my frustrations even though you did not know what I was on about. Everyone needs a cheerleader in their corner
- Professors Neil Coville and Joseph Michael for the support and guidance
- Professor Dean Brady for the support
- Mr Yoosuf Hassim for your words of encouragement and your belief in me
- Mrs Nandi Msimang and Collen Masiye for believing in my dreams as though they were your own. You are not just colleagues, I could rely on you at any time and you held the fort when I needed to go away for conferences and research visits.I wish you the very best in your own studies
- Mrs Gail Brankin and Dr Sadhna Mathura for standing in for me when I was on sabbatical leave
- The undergraduate laboratories staff especially Ignatia Khumalo, Joyce Gama Andries Makwela and the entire School of Chemistry for the support
- CATMAT group. Thank you for all those grilling sessions and exchange of knowledge during presentations. You guys were lit!
- Moloto group, especially Dr Mildred Airo, Dr Pierre Kalenga from whom I learnt so much. Dr Stefan Govindraju, Rudo Kadzuto, Lerato Machogo, Grace Ngubane, Siyabonga Nkabinde and Prince Shumbula-thank you for all the support, exchange of ideas and all the fun during group meetings. You guys are the real MVPs! To the newest members of the group, make sure you learn as much as you can from the old guard
- The research students I have co-supervised throughout the years: Miss Sharon Mphahlele (MSc), Mr Zakhele Ndala (PhD), Kedibone Jojo Kgaphola (Hons), Tshegofatso Mabilane (Hons), Nkosikhona Nzimande (Hons) and Titus Mkhize

(Research Assistant). Thank you for your immense and invaluable contribution to this work

- University of the Witwatersrand, Thuthuka through NRF and the Department of Higher Education and Training for the funding
- XRD and MMU facilities for the analyses of results
- Professor Ivo A. Hümmelgen and the UFPR for allowing me to use your facilities during my research visit. Your guidance throughout the application part of this work has been amazing. To the GOOD research group, you welcomed me and shared your space with me. You did not complain when I hogged the equipment, you understood because I had a limited time to do the work in your lab. For that I am forever grateful. Rafael Rodrigues (soon to be Dr), you are such a good teacher! Thank you for all the knowledge you passed on to me and for being a good friend. I wish you all the best in your future endeavours. My Portuguese is still bad though! Dr Isidro Cruz Cruz, Dr Anderson Hoff, Dr Ali Nawaz, Elton Alves de Moura, Anna Carolina, Anna Cristina thank you for everything
- Schirley Esaki and Dragan Petrović for giving me a place to stay in Brazil and treating me like family
- Last but not least, I would like to thank God Almighty for seeing me through the trials and tribulations during this journey. I have lost count of the number of times I felt like giving up but my confidence and strength were always restored after having conversations with Him.

DEDICATION

To the loving memory of my late dad

LIST OF PUBLICATIONS

[1] Mildred A.Airo, Siziwe Gqoba, Mubiayi P.Kalenga, Stefan Govindraju, Makwena J.Moloto, Nosipho Moloto. Synthesis and characterization of indium monoselenide nanosheets: A proposed pseudo top-down mechanism. (2014). J. of Crystal Growth 6.

[2] Siziwe Gqoba , Mildred Airo, Nthabiseng Ntholeng, Lerato Machogo , Rudo Sithole , Makwena J. Moloto , Juanita van Wyk , Nosipho Moloto. Evolution of In_2S_3 nanoplates with time. (2015). Materials Today: Proceedings 2. 7th International Symposium on Macro- and Supramolecular Architectures.

[3] Mildred A. Airo, Siziwe Gqoba, Francis Otieno, Makwena J. Moloto and Nosipho Moloto. Structural modification and band-gap crossover in indium selenide nanosheets. (2016). RSC Adv. 6.

[4] Mildred A. Airo, Rafael Rodrigues, Siziwe Gqoba, N. Ntholeng, Francis Otieno, Makwena J. Moloto, Márcia W. C. C. Greenshields, Ivo A. Hümmelgen, Nosipho Moloto. Colloidal InSe nanostructures: Effect of morphology on their chemical sensitivity to methanol and formaldehyde fumes. (2016). Sensors and Actuators B 236.

[5] Nthabiseng Nthole, Benny, Mojela, Siziwe Gqoba, Mildred Auwor Airo, Stefan Govindraju, M. J. Moloto, Juanita van Wyk, Nosipho Moloto. Colloidal synthesis of pure CuInTe2 crystallites based on the HSAB theory. (2016). New Journal of Chemistry 40 (12).

[6] Rudo K. Sithole, Lerato F. E. Machogo, Mildred A. Airo, Siziwe S. Gqoba, Makwena J. Moloto, Poslet Shumbula, Juanita Van Wyk, Nosipho Moloto. Synthesis and characterization of Cu_3N nanoparticles using pyrrole-2-carbaldpropyliminato Cu(II) complex and $Cu(NO_3)_2$ as single-source precursors: the search for an ideal precursor. (2018). New J. Chem. 42.

[7] Lerato Machogo, Phumlani Tetyana, Rudo Sithole, Siziwe Gqoba, Neo Phao, Mildred Airo, Poslet M. Shumbula, Makwena J. Moloto, Nosipho Moloto. Unravelling the structural properties of mixed-valence α- and β-AuSe nanostructures using XRD, TEM and XPS. (2018). Applied Surface Science 456.

MANUSCRIPTS TO BE SUBMITTED

[8] Siziwe Gqoba, Tshegofatso Mabilane, Mildred Airo, Lerato Machogo , Rudo Sithole , Makwena J. Moloto, Nosipho Moloto. Defining the role of 1-DDT in OLA/1-DDT biligand system during the colloidal synthesis of In_2S_3 hexagonal nanoplates.

[9] Siziwe Gqoba, Sharon Mphahlele, Zakhele Ndala, Mildred Airo, Lerato Machogo , Rudo Sithole , Makwena J. Moloto, Nosipho Moloto. Limiting the oxidation of WS_2 nanostructures by passivating the surface using an organic capping agent for room temperature NH_3 sensing.

[10] Siziwe Gqoba, Rafael Rodrigues, Mildred Airo, Lerato Machogo, Rudo Sithole, Makwena J. Moloto, Ivo. A Hümmelgen, Nosipho Moloto. Application of a set of sensors based on different geometrical characteristics of WS_2 nanostructures to detect volatile compounds.

[11] Siziwe Gqoba, Rafael Rodrigues, Mildred Airo, Lerato Machogo, Rudo Sithole, Makwena J. Moloto, Ivo. A Hümmelgen, Nosipho Moloto Selectivity of OLA/WS_2 sensors towards different VOCs and their sensitivity to NH_3 under relatively humid conditions.

[12] Siziwe Gqoba, Rafael Rodrigues, Mildred Airo, Lerato Machogo, Rudo Sithole, Makwena J. Moloto, Ivo. A Hümmelgen, Nosipho Moloto. Effect of ligand exchange and annealing on the sensitivity of OLA/WS_2 sensors towards NH_3.

[13] Rafael Rodrigues, Mildred Airo, Messai Mamo, Siziwe Gqoba, Marcia Greenshields, Nosipho Moloto, Neil coville, Ivo A. Hümmelgen. Chemical sensor arrays analysis for concentration determination in a binary mixture of analytes.

CONFERENCES

[1] Effect of reaction time on growth of β-indium sulphide nanosheets. Poster presentation at the 5th International Conference on Nanoscience and Nanotechnology, NanoAfrica 2014, 30 March - 2 April 2014 Vanderbijlpark, South Africa.

[2] Effects of concentration and reaction time on the growth of β-indium sulphide nanoparticles 7th International Symposium on Macro- and Supramolecular Architecture and Materials MAM-14 Emperors Palace, South Africa 23 - 27 November 2014.

[3] Low temperature synthesis of molybdenum sulphide nanomaterials in an organic medium. Poster presentation at the 17th South African Chemical Institute Inorganic Chemistry Conference 28 June - 2 July 2015, Grahamstown, South Africa.

[4] The role of 1-dodecanethiol in the growth of β-indium sulphide thin nanoplates. Poster [presentation at the 6th international conference on Nanoscience and Nanotechnology, NanoAfrica2016, 03 - 06 April 2016, University of South Africa (UNISA), Roodepoort, South Africa.

[5] The role of 1-DDT on growth of β-InS3 nanoplates: effect on morphology, phase and optical properties. Oral presentation at the International Conference on Pure and Applied Chemistry (ICPAC 2016), July 18-22, 2016, Flic En Flac, Mauritius.

[6] Synthesis, Characterization and Application of WS_2 nanostructures in Gas Sensing. Presented a poster at the 18th edition of Trends in Nanotechnology International Conference (TNT2017), June 05-09, TU Dresden Auditorium Center, Dresden, Germany.

[7] Application of a set of sensors based on different geometrical characteristics of WS_2 nanostructures to detect volatile compounds. Poster to be presented at the 7^{th} EuCheMS Chemistry Congress 2018, Liverpool 25 -31 August 2018.

RESEARCH VISITS

[1] Universidade Federal do Paraná, Departemente Física, Curitiba, Brazil, 31 August - 29 November 2016.

[2] Universidade Federal do Paraná, Departemente Física, Curitiba, Brazil, 14 July-17 October 2017.

[3] Course on Materials for Energy and Sustainability VII of the International School of Materials for Sustainable Development and Energy University, Italy, Erice, 5- 12 July 2018.

TABLE OF CONTENTS

DECLARATION ii
ABSTRACT iii
ACKNOWLEDGEMENT v
DEDICATION vii
LIST OF PUBLICATIONS viii
MANUSCRIPTS TO BE SUBMITTED viii
CONFERENCES ix
RESEARCH VISITS x
LIST OF FIGURES xv
LIST OF TABLES xxiii
LIST OF ABBREVIATIONS xxiv
Chapter 1 : Introduction 1
1.1 Organization of the thesis 1
1.2 Problem statements 1
1.3 Background and motivation 2
1.4 Aims and objectives of the study 4
1.5 References 5
Chapter 2 : Literature review 8
2.1 Introduction to colloidal inorganic semiconductor nanocrystals 8
2.1.1 Electronic structure of a semiconductor NC 9
2.1.2 Effects of quantum confinement 9
2.1.3 Colloidal nanostructures of layered 2D semiconducting metal sulphides 16
2.2 Synthesis of metal sulphide semiconductor NCs 16
2.2.1 Thermal decomposition routes 17
2.2.2 Solvothermal or hydrolysis methods 18
2.2.3 Other synthetic routes 18
2.3 Growth, size and shape control of semiconductor nanostructures 18
2.3.1 Nucleation 18
2.3.2 Growth of NCs 22
2.4 Reaction parameters affecting growth of nanostructures 23
2.4.1 Solvents 23
2.4.2 Time 24

2.4.3 Heating temperature 24
2.4.4 Reactivity of precursors 24
2.5 Application of semiconductor NCs in chemical sensing 25
2.5.1 Types of gas sensors 25
2.5.2 Chemiresistor sensors based on 2D layered metal sulphide semiconductor NCs 25
2.5.3 Working principle and gas sensing mechanism of chemical sensors 27
2.6 Factors controlling sensitivity 30
2.6.1 Receptor function 30
2.6.2 Transducer function 31
2.6.3 Utility 31
2.7 Properties of a gas sensor 31
2.7.1 Sensitivity 32
2.7.2 Response and recovery time 32
2.7.3 Selectivity 32
2.7.4 Stability 33
2.8 Improvement of gas sensing performance 33
2.8.1 Sensitivity 33
2.8.2 Selectivity 35
2.8.3 Response and recovery 36
2.9 Operation conditions and gas detection 36
2.9.1 Operating temperature 36
2.9.2 Humidity 36
2.10 Fabrication and design of gas sensing devices 36
2.10.1 Wet chemical methods 37
2.10.2 Dry methods 37
2.11 References 37
Chapter 3 : Synthesis, characterization and application of OLA/WS_2 nanostructures in chemical sensors for detection of solvent vapours 46
3.1 Passivation of the Surface of WS_2 Nanostructures with an Organic Capping Agent for Room Temperature NH_3 Sensing 46
3.1.1 Introduction 46
3.1.2 Experimental procedure 49
3.1.3 Results and discussion 55
3.1.4 Conclusion 81

3.1.5 References 81

3.2 Application of tristimulus analysis to a set of geometrically different OLA/WS_2 nanostructures for the detection of toxic VOCs 88

3.2.1 Introduction 88

3.2.2. Experimental set-up 90

3.2.3. Results and discussion 93

3.2.4 Conclusion 112

3.2.5 References 112

3.3 Selectivity of OLA/WS_2 sensors towards different VOCs and their sensitivity to NH_3 under relatively humid conditions 116

3.3.1 Introduction 116

3.3.2. Experimental set-up 117

3.3.3. Results and discussion 119

3.3.6 Conclusion 138

3.3.7 References 138

3.4 Effect of ligand exchange and annealing on the sensitivity of OLA/WS_2 sensors towards NH_3 142

3.4.1 Introduction 142

3.4.2. Experimental set-up 143

3.4.3. Results and discussion 145

3.4.5 Conclusion 152

3.4.6 References 152

Chapter 4 : Synthesis, characterization and application of indium sulphide nanostructures in gas sensing 154

4.1 Investigation of the influence of reaction time and concentration of sulphur on the morphology of β-In_2S_3 nanostructures. 154

4.1.1 Introduction 154

4.1.2 Experimental procedure 156

4.1.3 Characterization techniques 158

4.1.4 Results and discussion 159

4.1.6 Gas sensing performance ..... **Error! Bookmark not defined.**

4.1.7 Conclusions 172

4.1.8 References 172

4.2 Amine and thiol ligand tag team for β-In_2S_3 hexagonal nanoplates 177

4.2.1 Introduction 177
4.2.2 Experimental procedure 179
4.2.3 Characterization techniques 180
4.2.4 Results and discussion 180
4.2.7 Conclusions 194
4.2.8 References 195
4.3 Tuning the optical properties of β-In_2S_3 nanostructures with alkylamine ligands and the influence of 1-dodecanethiol on their shape 199
4.3.1 Introduction 199
4.3.2 Experimental procedure 200
4.3.3 Results and discussion 201
4.3.4 Conclusions 209
4.3.5 References 209
Chapter 5: General conclusions and recommendations 213
5.1 Conclusions 213
5.1.1 Synthesis and characterization of capped WS_2 and ß-In_2S_3 nanostructures 213
5.1.2 Application of OLA/WS_2 and OLA/ ß-In_2S_3 nanostructures in gas detection 214
5.2 Recommendations 214

LIST OF FIGURES

Figure 2.1: A depiction of the electronic energy states of: (a) bulk inorganic semiconductors, (b) inorganic semiconductor NCs, and (c) molecular semiconductors [3]. 8

Figure 2.2: Schematic representation of (a) direct and (b) indirect electronic transitions [14]. 9

Figure 2.3: Illustration of the quantum confinement effects on: (a) the band gap and (b) fluorescence of dispersions of CdSe QDs with different sizes under excitation with a UV-lamp in the dark [12].....10

Figure 2.4: Schematic representation of shape evolution of crystals as defined by (a) DOS versus E showing a continuous curve for 3D crystals and changes into a discrete line for 0D NCs, and b) confinement of 3D crystals along one- (z), two- (xy), three (xyz) directions resulting in 2D, 1D, and 0D NCs, respectively [20].....11

Figure 2.5: (a) Absorption spectra of colloidal suspensions of CdTe NCs of different sizes and (b) colloidal suspensions of CdTe NCs of different sizes under UV excitation [12]. 12

Figure 2.6: Possible exciton recombination pathways in semiconductors. (1) Radiative recombination, (2) defect assisted radiative recombination, and (3) non-radiative recombination [12].....13

Figure 2.7: Schematic representation of resonant exciton energy transfer from the donor QD (left) to the acceptor QD [12].....15

Figure 2.8: Schematic representation of the LaMer diagram [78].....19

Figure 2.9: A maximum free energy ΔG at a critical cluster size, r_c, which defines the first stable particles – the nuclei [78, 81]. 21

Figure 2.10: A Schematic for mass flow between the solution and the surface of a particle during the crystallization reaction [79].....23

Figure 2.11: A schematic representation of a simplified model of band bending in a wide bandgap semiconductor after chemisorption of charged species (*e.g.* ionosorption of oxygen) on surface sites. E_C, E_V, and E_F represent the energy of the conduction band, valence band, and the Fermi level, respectively, while Λ_{air} denotes the thickness of the space-charge layer, and $eV_{surface}$ the potential barrier. The conducting electrons are represented by e^- and + represents the donor sites [94]. 29

Figure 2.12: Receptor and transducer function of a semiconductor gas sensor: a) surface, providing the receptor function, b) microstructure of the sensing layer, providing the

transducer function, and c) element, enabling the detection of the change in output resistance of the sensing layer, here deposited on an interdigital microelectrode [94]. 31
Figure 3.1: Brillouin zone for WS_2 monolayer [8]. 47
Figure 3.2: (a) top and (b) cross-section view of the WS_2 atomic structure [8]. 47
Figure 3.3: Diagrams showing different colour changes during growth of OLA/WS_2 nanostructures. 51
Figure 3.4: Optical image of the IDE is represented by (a) while (b) shows soldering of contacts onto IDEs. 52
Figure 3.5: IDEs before (a) and after (b) deposition of OLA/WS_2 nanostructure film respectively. 52
Figure 3.6: Schematic representation of gas chambers used in the gas sensing measurements: (a) the rubber stoppered filtering flask and (b) glass bottle with a sweep cover. 53
Figure 3.7: Passivation of WS2 nanostructures by OLA. 56
Figure 3.8: SEM images of OLA/WS_2 synthesized at different times. 57
Figure 3.9: TEM micrographs of OLA/WS_2 nanostructures synthesized at different times. .59
Figure 3.10: EDS of OLA/WS_2 nanostructures synthesized at 180 min. 60
Figure 3.11: XRD patterns of OLA/WS_2 nanostructures synthesized at different reaction times. Insert shows the labelled peaks of the diffraction pattern of the 45 min sample. 61
Figure 3.12: Raman spectra of OLA/WS_2 nanostructures from the different reaction times. Inset shows the first and second order peaks of the spectrum from the 45 min sample. 62
Figure 3.13: Lorentzian multi-peak fit of the Raman spectra of OLA/WS_2 nanostructures at 45 min. The black line represents the experimental data; the red, magenta, blue, cyan and green lines represent the combined peak fitting, the individual contributions of the most intense phonon modes. 63
Figure 3.14: XPS survey spectrum of OLA/WS_2 nanostructures synthesized in 45 min. 65
Figure 3.15: High resolution core level spectra of OLA/WS_2 with focus on C 1s, O 1s, W 4f and S 2p.....66
Figure 3.16: UV-vis spectra of OLA/WS_2 nanostructures from the different reaction times. Insert shows the spectrum of the 45 min sample different peaks A, B and C. 68
Figure 3.17: Electronic band structure (left) and total density of states (right) for (a) WS_2 bulk and (b) monolayer [8]. 70
Figure 3.18: PL spectra of WS_2 nanostructures from the different reaction times. 71

Figure 3.19: PL intensities for mono-, bi- and three-layered WS_2 nanostructures at 488 nm excitation wavelength with the positions for the excitons A and B as well as the indirect band gap (I) [8]. 72
Figure 3.20: FTIR spectra of pure OLA and OLA/ WS_2 nanostructures synthesized at different reaction times. 73
Figure 3.21: (a)-(e) Gas response of the OLA/WS_2 based sensors (15, 45, 60, 180 and 240 min) to NH_3 vapour at different concentrations. 75
Figure 3.22: Sensitivities of the different reaction times towards NH_3 from (i) to (v). 76
Figure 3.23: Response for 45 min OLA/WS_2 based sensor exposed to 1024 ppm of ammonia. 78
Figure 3.24: Response for OLA/WS_2 based sensors exposed to 240 ppm of ammonia. 80
Figure 3.25: Schematic representation of the gas chamber used in sensor measurements. 91
Figure 3.26: Geometrical representation of the tristimulus vector crossing a unitary spherical shell, projecting the crossing point to the xy plane, and the two angles (θ and ϕ) that characterize the direction of the vector [25]. 93
Figure 3.27: SEM micrographs of OLA/WS_2 nanostructures at 15, 45, 60, 180 and 240 min. 94
Figure 3.28 (a-k) Relative conductance of OLA/WS_2 sensors (15 min) vs time for NH_3 and several VOCs. Corresponding relative conductance *vs* concentration for each analyte (i-xi) [inset]. 97
Figure 3.29: (a-k) Relative conductance of OLA/WS_2 sensors (45 min) vs time for NH_3 and several VOCs. Corresponding relative conductance *vs* concentration for each analyte (i-xi) [inset]. 100
Figure 3.30: (a-k) Relative conductance of OLA/WS_2 sensors (60 min) vs time for NH_3 and several VOCs. Corresponding relative conductance *vs* concentration for each analyte (i-xi) [inset]. 102
Figure 3.31: (a-k) Relative conductance of OLA/WS_2 sensors (180 min) vs time for NH_3 and several VOCs. Corresponding relative conductance *vs* concentration for each analyte (i-xi) [inset]. 104
Figure 3.32: (a-k) Relative conductance of OLA/WS_2 sensors (240 min) vs time for NH_3 and several VOCs. Corresponding relative conductance *vs* concentration for each analyte (i-xi) [inset]. 106

Figure 3.33: Bidimensional plot showing the separation between NH_3 and the various VOCs using an array of three OLA/WS_2 chemiresistive sensors (15, 45 and 60 min) at different concentrations. 108
Figure 3.34: TA results differentiating NH_3 from polar and non-polar VOCs at different concentrations. 109
Figure 3.35: Discrimination between (a) non-polar solvents; (b) polar aprotic. 110
Figure 3.36: Discrimination between ammonia and other polar protic solvents. 110
Figure 3.37: Discrimination between polar protic solvents (alcohols). 111
Figure 3.38: Schematic representation of the gas chambers used in sensor measurements. 118
Figure 3.39: Schematic representation of the gas chamber with a sweep cover used under humid conditions.....119
Figure 3.40: SEM micrographs of OLA/WS_2 nanostructures at 15, 45, 60, 180 and 240 min. 120
Figure 3.41: XPS survey spectrum of OLA/WS_2 nanostructures (45 min). 121
Figure 3.42: High resolution XPS spectrum of OLA/WS_2 nanostructures (45 min).....122
Figure 3.43: Response curves of OLA/WS_2 nanostructures (15 min). 124
Figure 3.44: Response curves of OLA/WS_2 nanostructures (45 min). 125
Figure 3.45: Response curves of OLA/WS_2 nanostructures (60 min). 126
Figure 3.46: Response curves of OLA/WS_2 nanostructures (180 min). 127
Figure 3.47: Response curves of OLA/WS_2 nanostructures (240 min). 128
Figure 3.48: Selectivity tests of the OLA/WS_2 sensor (15 min) at 1.5, 3.0, 4.5 and 6.0 µL of NH_3 and various VOCs. 130
Figure 3.49: Selectivity tests of the OLA/WS_2 sensor (45 min) at 1.5, 3.0, 4.5 and 6.0 µL of NH_3 and various VOCs. 131
Figure 3.50: Selectivity tests of the OLA/WS_2 sensor (60 min) at 1.5, 3.0, 4.5 and 6.0 µL of NH_3 and various VOCs. 132
Figure 3.51: Selectivity tests of the OLA/WS_2 sensor (180 min) at 1.5, 3.0, 4.5 and 6.0 µL of NH_3 and various VOCs. 132
Figure 3.52: Selectivity tests of the OLA/WS_2 sensor (240 min) at 1.5, 3.0, 4.5 and 6.0 µL of NH_3 and various VOCs. 133
Figure 3.53: Histograms representing the response of OLA/WS_2 sensor (15 min) towards (a) 240 ppm, (b) 479 ppm, (c) 719 ppm and (d) 958 ppm of NH_3 under various humid conditions. 134

Figure 3.54: Histograms representing the response of OLA/WS_2 sensor (45 min) towards (a) 240 ppm, (b) 479 ppm, (c) 719 ppm and (d) 958 ppm of NH_3 under various humid conditions. 135
Figure 3.55: Response curves of OLA/WS_2 sensors (15, 45, 60, 180 and 240 min) towards at 240 ppm of NH_3 for five hours.....138
Figure 3.56: Schematic representation of the gas chambers used in sensor measurements. 144
Figure 3.57: XRD patterns of WS_2 nanostructures synthesized at 15 and 45 min: (a) OLA/WS_2 before annealing; (b) OLA/WS_2 after annealing and (c) EDT/WS_2 after annealing. The annealing was performed for 3 h at 200 ℃.....145
Figure 3.58: Histograms representing the response of OLA/WS_2, EDT/WS_2 and ME/WS_2 sensors from the (a) 15 min and (b) 45 min towards 240, 479, 719 and 958 ppm of NH_3 under limited light and low humidity.....146
Figure 3.59: Histograms representing the response of OLA/WS_2, EDT/WS_2 and ME/WS_2 sensors from the 15 min reaction time towards 240, 479, 719 and 958 ppm of NH_3 under limited light and low humidity.....148
Figure 3.60: Histograms representing the response of OLA/WS_2, EDT/WS_2 and ME/WS_2 sensors from the 45 min reaction time towards 240, 479, 719 and 958 ppm of NH_3 under limited light and low humidity.....150
Figure 4.1: Structure model of β-In_2S_3 unit cell. The indium vacancies are marked as grey spheres. In the tetragonal β-In_2S_3 configuration, the vacancies are ordered on a 41 screw axis parallel to the c-axis of the crystal. In the α-In_2S_3 configuration, the vacancies are randomly distributed over all tetrahedral indium sites. The edges of the unit cell of the tetragonal β-In_2S_3 structure (cubic α-In_2S_3) structure are indicated by black (blue) lines [43]. 155
Figure 4.2: Schematic representation of the gas chamber (with a sweep cover).....157
Figure 4.3: The TEM images of OLA/β-In_2S_3 nanostructures in the 1:1 (In:S) reaction system at: (a) 60 min, (b) 90 min, (c) 120 min, (d) 150 min, (e) 210 min, (f) 300 min, (g) 330 min; (h) and (i) represent size distribution for 60 and 90 min nanostructures respectively...160
Figure 4.4: XRD patterns of OLA/β-In_2S_3 nanostructures at different reaction times in the 1:1 (In:S) reaction system. 161
Figure 4.5: UV-vis spectra of OLA/β-In_2S_3 nanostructures at (a) 60 min, (b) 90 min, (c) 120 min, (d) 150 min, (e) 210 min, (f) 300 min, and (g) 330 min in the 1:1 (In:S) reaction system. 162
Figure 4.6: PL spectra of OLA/β-In_2S_3 nanostructures at (a) 60 min, (b) 90 min, (c) 120 min, (d) 150 min, (e) 210 min, (f) 300 min, and (g) 330 min in the 1:1 (In:S) reaction system....163

Figure 4.7: The TEM images of OLA/β-In_2S_3 nanostructures for (a) 60 min, (b) 120 min, and (c) 150 min in 1:1.5 (In:S) reaction system. 165
Figure 4.8: XRD patterns of OLA/ β-In_2S_3 nanostructures synthesized for (a) 60 min, (b) 120 min, and (c) 150 min in the 1:1.5 (In:S) reaction system. 165
Figure 4.9: UV-vis spectra of OLA/β-In_2S_3 nanostructures synthesized for (a) 60 min, (b) 120 min, and (c) 150 min in the 1:1.5 (In:S) reaction system. 166
Figure 4.10: PL spectra of OLA/ β-In_2S_3 nanostructures synthesized for (a) 60 min, (b) 120 min, and (c) 150 min in the 1:1.5 (In:S) reaction system. 167
Figure 4.11: TEM images of OLA/ β-In_2S_3 nanostructures synthesized for (a) 60 min, (b) 120 min, and (c) 150 min in the 1:2 (In:S) reaction system. 168
Figure 4.12: XRD patterns of OLA/β-In_2S_3 nanostructures synthesized for (a) 60 min, (b) 120 min, and (c) 150 min in the 1:2 (In:S) reaction system. 168
Figure 4.13: UV-vis spectra of OLA/β-In_2S_3 nanostructures synthesized for (a) 60 min, (b) 120 min, and (c) 150 min in the 1:2 (In:S) reaction system. 169
Figure 4.14: PL spectra of OLA/β-In_2S_3 nanostructures synthesized for (a) 60 min, (b) 120 min, and (c) 150 min in the 1:2 (In:S) reaction system. 170
Figure 4.15: Response of β-In_2S_3 sensor to successive introductions of formaldehyde vapour over time. 171
Figure 4.16: The TEM images of OLA/β-In_2S_3 nanostructures in the 1:1 (In:S) reaction system: (a) 60 min, (b) 90 min, (c) 120 min and (d) 150 min. 181
Figure 4.17: The TEM images of β-In_2S_3 nanostructures in: OLA_0.2 mL of 1-DDT at (a) 60 min, (b) 90 min, and (c) 150 min; OLA_0.4 mL of 1-DDT at (d) 60 min, (e) 90 min, and (f) 150 min in the 1:1 (In:S) reaction system. 182
Figure 4.18: A schematic illustration of the growth mechanism of β-In_2S_3 nanostructures in: OLA_0.2 mL of 1-DDT at (a) 60 min, (b) 90 min, and (c) 150 min in the 1:1 (In:S) reaction system. 183
Figure 4.19: TEM images of 1-DDT/β-In_2S_3 nanostructures synthesized for (a) 60 min, (b) 90 min, and (c) 150 min in the 1:1 (In:S) reaction system. 184
Figure 4.20: TEM images of OLA/β-In_2S_3 nanostructures synthesized for (a) 120 min, (b) 150 min, and (c) 180 min in OLA with 1-DDT as source of sulphur. 185
Figure 4.21: XRD patterns of OLA/β-In_2S_3 nanostructures at (a) 60 min, (b) 90 min, and (c) 150 min; (i) OLA /0.2 mL of 1-DDT and (ii) OLA /0.4 mL 1-DDT. 186

Figure 4.22: XRD patterns of (i) 1-DDT/β-In_2S_3 nanostructures at (a) 60 min, (b) 90 min, and (c) 150 min; (ii) OLA/β-In_2S_3 nanostructures at (a) 120 min, (b) 150 min, and (c) 180 min. 187
Figure 4.23: Solution ^{1}HNMR spectra obtained on $CDCl_3$ dispersions of pure OLA.....188
Figure 4.24: Solution ^{1}HNMR spectra obtained on $CDCl_3$ dispersions of pure 1-DDT. 188
Figure 4.25: Solution ^{1}HNMR spectra obtained on $CDCl_3$ dispersions of the free capping agents and capped β-In_2S_3 nanostructures.....189
Figure 4.26: UV-vis spectra of (i) OLA/0.2 mL_1-DDT/β-In_2S_3 nanostructures and (ii) OLA/0.4 mL_1-DDT/β-In_2S_3 nanostructures at (a) 60 min, (b) 90 min, and (c) 150 min. ...190
Figure 4.27: PL spectra of (i) OLA/0.2 mL_1-DDT/β-In_2S_3 nanostructures and (ii) OLA/0.4 mL_1-DDT/β-In_2S_3 nanostructures at (a) 60 min, (b) 90 min, and (c) 150 min. 191
Figure 4.28: (i) UV-vis spectra of OLA/β-In_2S_3 at (a) 120 min, (b) 150 min, and (c) 180 min with 1-DDT as sulphur source; (ii) 1-DDT/β-In_2S_3 at (a) 60 min, (b) 90 min, and (c) 150 min. 192
Figure 4.29: (i) PL spectra of OLA/β-In_2S_3 at (a) 120 min, (b) 150 min, and (c) 180 min with 1-DDT as sulphur source; (ii) 1-DDT/β-In_2S_3 at (a) 60 min, (b) 90 min, and (c) 150 min. ..193
Figure 4.30: TEM images of HDA/β-In_2S_3 at (a) 60 min, (b) 90 min, and (c) 150 min; HDA/1-DDT_β-In_2S_3 at (d) 60 min, 90 min and (f) 150 min.....202
Figure 4.31: TEM images of ODA/β-In_2S_3 at (a) 60 min, (b) 90 min, and (c) 150 min; ODA/1-DDT_β-In_2S_3 (d) 60 min, (b) 90 min and (f) 150 min.....203
Figure 4.32: XRD patterns of (i) HDA/β-In_2S_3 at (a) 60 min, (b) 90 min, and (c) 150 min; (ii) HDA/1-DDT_β-In_2S_3 at (a) 60 min, (b) 90 min and (c) 150 min. The reflections marked with # represent InS. 203
Figure 4.33: XRD patterns of (i) ODA/β-In_2S_3 at (a) 60 min, (b) 90 min, and (c) 150 min; (ii) ODA/1-DDT_β-In_2S_3 at (a) 60 min, (b) 90 min and (c) 150 min. The reflections marked with # represent ODA. 204
Figure 4.34: UV-vis spectra of (i) HDA/β-In_2S_3 at (a) 60 min, (b) 90 min, and (c) 150 min; (ii) HDA/1-DDT_β-In_2S_3 at (a) 60 min, (b) 90 min and (c) 150 min.....205
Figure 4.35: PL spectra of (i) HDA/β-In_2S_3 at (a) 60 min, (b) 90 min, and (c) 150 min; (ii) HDA/1-DDT_β-In_2S_3 at (a) 60 min, (b) 90 min, and (c) 150 min.....206
Figure 4.36: UV-vis spectra of (i) ODA/β-In_2S_3 at (a) 60 min, (b) 90 min, and (c) 150 min; (ii) ODA/1-DDT_β-In_2S_3 at (a) 60 min, (b) 90 min, and (c) 150 min.....207

Figure 4.37: PL spectra of (i) ODA/β-In_2S_3 at (a) 60 min, (b) 90 min, and (c) 150 min; (ii) ODA/1-DDT_β-In_2S_3 at (a) 60 min, (b) 90 min, and (c) 150 min.....208

LIST OF TABLES

Table 2.1: A summary of the responses by n- and p-type semiconductors [129]. 27

Table 3.1: Volume and concentration of NH_4OH. 54

Table 3.2: Raman intensity ratios and frequencies for the main phonon modes. 64

Table 3.3: Summary of the atomic composition stoichiometric assignments obtained from the fitting of the XPS spectra reported in Figure 3.15. 67

Table 3.4: A summary of the absorption edges and gaps of the OLA/WS_2 nanostructures at different reaction times. 69

Table 3.5: Emission maxima for the different nanostructures. 71

Table 3.6: A summary of conductance changes ($\Delta G/G$) and standard deviation for each sensor element exposed to eleven solvents (at 1.5 µL increments). 107

Table 3.7 A summary of the responses of the 15 min sensors towards 249 ppm NH_3. 149

Table 3.8: A summary of the responses of the 45 min sensors towards 249 ppm NH_3. 151

Table 4.1: Optical parameters at different reaction times for 1:1 (In:S) mole ratio in OLA. 164

Table 4.2: Optical parameters at different reaction times for 1:1.5 (In:S) mole ratio in OLA. 167

Table 4.3: Optical parameters at different reaction times for 1:2 (In:S) mole ratio in OLA. 170

Table 4.4: Optical parameters at different reaction times. 192

Table 4.5: Optical parameters for the OLA/β-In_2S_3 (1-DDT as S source) and 1-DDT/β-In_2S_3 nanostructures. 194

Table 4.6: Optical parameters at different reaction times. 206

Table 4.7: Optical parameters at different reaction times. 208

LIST OF ABBREVIATIONS

VOCs: Volatile Organic compounds

TMDCs: Transition metal chalocogenides

S: sulphur

NH_3: Ammonia

MOXs: Metal oxides

OLA: Oleylamine

HDA: Hexadecylamine

ODA: Octadecylamine

1-DDT: 1-Dodecanethiol

ME: Mercaptoethanol

1, 2- EDT: 1, 2- Ethanedithiol

PXRD: Powder X-Ray diffraction

UV-vis: Ultraviolet-visible

PL: Photoluminescence

NMR: Nuclear Magentic Resonance

FT-IR: FourierTransform-Infrared

HRTEM: High resolution transmission electron microscopy

SEM: Scanning electron microscopy

EDS: Energy Dispersive Energy

XPS: X-ray photoelectron spectroscopy

NCs: Nanocrystals

DMF: Dimethylformamide

Chapter 1 : Introduction

1.1 Organization of the thesis

Chapter 1 provides a framework of the order that the topics of the thesis will follow. The problem statement, motivation, aim and objectives of the study are narrated in this chapter.

Chapter 2 entails the background on semiconductor nanocrystals of metal chalcogenides, their methods of preparation, factors affecting their properties, chemical sensors and gas sensing mechanism. A literature review on studies of metal chalcogenides is presented.

Chapter 3 discusses synthesis, characterization of OLA/WS_2 and its application in gas sensing of VOCs and NH_3 under limited light and humidity; and relative humidities. Use of the sensors in tristimulus analysis, effects of ligand exchange and annealing of sensors on gas sensing performance towards NH_3 are also investigated.

Chapter 4 discusses the synthesis of capped ß-In_2S_3:

(i) Through a mono-ligand system in OLA, HDA, ODA (alkylamines) and 1-DDT (thiol).

(ii) Bi-ligand system with the amine ligands and 1-DDT

(iii) Effect of concentration of 1-DDT in the bi-ligand system (OLA/1-DDT)

(iv) Effect of a sulphur source

(v) Effect of reaction time

Chapter 5 discusses general conclusions and recommendations for future work.

1.2 Problem statements

Today's detection, identification and measuring of pollutants in the environment require online real-time analysis using cheap, simple devices. This is something that cannot be achieved through conventional analytical instruments like gas chromatography-mass spectrometry (GC-MS) as the analysis is time-consuming; sample preparation is sometimes required making online, real-time analysis difficult, expensive, complex and bulky. In light of these observations the development of miniature gas detection devices has to be realized, a concept which got the science community looking to nanostructures as the new materials to provide sensitive, stable, simple and efficient designs for gas detection technology. Nanostructures of layered semiconducting metal oxides (SMOs) on the other hand, are one of the most studied 2D materials; and are the most readily available chemiresistive gas sensors on the market for the detection of a wide range of air pollutants, VOCs, organophosphates, *etc*. However, they are plagued by high operating temperatures (200-500 ℃) which not only pose power consumption problems but also thermal safety problems. Nanostructures of metal

chalcogenides are now being investigated for gas sensing properties as they hold the promise of being operated at room temperature.

1.3 Background and motivation

The superior optical, electrical, thermal, physical, chemical and mechanical properties of graphene, a 2D layered material have led to its extensive study since its isolation in 2004 [1-8]. Graphene has shown great potential as a material for use in several applications such as electronics and photonics, energy conversion and storage, medicine, chemical and biological and gas sensing. However, the absence of a band gap has limited its use in semiconductor electronics like FETs and optoelectronic applications [1, 4, 5, 7, 9-12] which require switch-off [7, 12]. This predicament has paved the way into finding post graphene 2D materials with sizable and tunable band gaps. The quest to find such materials has seen an outburst of renewed interest and extensive research into other 2D layered materials and their suitability as nanoelectronic components [1-4, 6, 7, 13-17]. The accessibility of 2D materials in different chemical compositions and structural forms makes for interesting electronic and optical properties derived from metals, semimetals, insulators, semiconductors and superconductors with direct and indirect band gap covering a wide range of the solar spectrum [3, 10, 12, 18, 19]. The catalogue of 2D materials includes but not limited to nitrides (hexagonal boron nitride [h-BN]), III-VI compounds, transition metal dichalcogenides [TMDCs]) and layered metal oxides [12, 18, 20]. In bulk, 2D materials exist as strongly bonded layers [4]. An atomically thin 2D material has its free charges confined in one spatial dimension but free in the other two [10]. Generally, alternative 2D materials present extraordinary and compelling properties that almost match those of graphene [4, 10] including gas sensing owing to their high surface-to-volume ratio, low noise, long-range of lattice periodicity that provides a better channel for carrier transportation, enhancing the efficiency of the devices, improved diffusion processes upon the intercalation of guest molecules, high carrier mobility, low power consumption and high compatibility for the integration with modern electronic technologies and sensitivity of electronic properties to the changes in the surroundings [2, 4, 21-23].

However, realization of the possibilities offered by these materials requires thinning them down to one or few layers in order to unlock the exquisite electronic and optical properties including a band gap cross over [10, 12]. Properties of these materials are often shape or size-dependent. Precise control and monitoring of shape, size distribution and anisotropy are very

important in determining the ultimate application of these materials. A lot of growth techniques, physical and chemical have been dedicated to fabricate these materials with different shapes. To date chemical methods have emerged as more powerful and versatile than physical methods by affording the synthesis of uniform-sized nanostructures and their size control. In the last few years, exotic shapes of nanostructures have been fabricated through solvothermal or hydrothermal synthesis of the In_2S_3 [21, 24] and WS_2 [25, 26] with and without capping agents at relatively low temperatures. Capping agents also play an important role in the morphology of the resultant nanostructure.

Chemical vapour sensing is very important in environmental pollution, industrial emission monitoring and process control, medical and pharmaceutical industries, public security and military, food quality control, cosmetics, agriculture and indoor air quality control [4, 27-29]. Semiconducting metal oxides (SMOs) are one of the most studied [30] and readily available type of chemiresistive gas sensors on the market for the detection of a wide range of air pollutants, VOCs, organophosphates, *etc*. [4, 30, 31]. The gas sensing mechanism is based on the change in the electrical resistance of the oxide film when gases interact with its surface [32]. SMOs are plagued by high operating temperatures (200 °C to 500 °C) [4], and this has forced researchers to look for alternatives like their sulphide counterparts with molybdenum (MoS_2) as the most prominent example. The study on MoS_2 has paved the way for WS_2; both belong to the same TMDC family and have similar properties [33]. The number of reports on the gas sensing potential of WS_2 of chemical vapours of ammonia, ethanol [5], humidity [34, 35] is still low despite WS_2 reportedly displaying higher thermal stability, wider operation temperature range, favourable band structure [4, 5] and broader emission linewidth than MoS_2 [33]. According to recently published calculations, WS_2 has the potential to outperform other 2D materials in field effect transistors (FETs) applications [5]. In_2S_3 has been studied mainly for its potential for use as a buffer layer for CIS-based ($CuInS_2$, Se_2) thin film solar cells [36, 37] and photocatalyst [38, 39] but rarely as a material for the next generation gas sensing systems. All in all, research into 2D materials is still in its infancy and metal sulphides in general have been poorly studied as sensing materials [40]. Therefore a lot still needs to be discovered about the sensing properties of metal sulphides in order to answer the many questions that have been posed. In addition, with solvothermal or hydrothermal synthesis, the sky is the limit in terms of morphology, composition and size control. This study, aims to explore the various properties afforded by the different morphologies of In_2S_3

and WS_2 obtained through colloidal synthesis in the gas sensing of specific VOCs and other air pollutants.

1.4 Aims and objectives of the study

1. Synthesis and characterization of WS_2 nanostructures via a simple colloidal route. The effect of reaction time on morphology and inherent optical properties will be investigated.
2. Application of WS_2 nanostructures in gas sensing as:
   (a) OLA-capped nanostructures for the detection of VOCs, NH_3 and humidity
   (b) EDT or ME capped nanostructures for the detection of VOCs and NH_3 after ligand exchange
   (c) Application of OLA/WS_2 nanostructures in tristimulus analysis.
3. Synthesis and characterization of In_2S_3 nanostructures via a simple colloidal route. The following will be investigated:
   (a) Effect of different amine ligands on morphology and inherent optical properties
   (b) Effect of thiol ligand on morphology and inherent opticalproperties
   (c) Effect of using bi-ligand (amine/thiol) system on morphology and optical properties
   (d) Effect of ratio of amine/thiol in bi-ligand system on morphology and inherent optical properties
   (e) Effect of reaction time on morphology and inherent optical properties
   (f) Effect of sulphur precursor on morphology and inherent optical properties
   (g) Gas sensing potential of the In_2S_3 nanostructures towards formaldehyde.

1.5 References

[1] Kidd, D. W., Zhang, D. K. and Varga, K. (2016). Physical Review B, 93, 125423, 1-10.

[2] Liu, L., Kumar, S. B., Ouyang, Y. and Guo, J. Guo (2011). IEEE Transactions on Electron Devices 58(9), 3042-3047.

[3] Bhimanapati, G. R., Lin, Z., Meunier, V., Jung Y., Cha, J., Das, S., Xiao, D., Son, Y., Strano, X. M. S., Cooper, X. V. R., Liang, O. L., Louie, S. G., Ringe, E., Zhou W., Kim, O. S. S., Naik, R. R., Sumpter, B. G., Terrones, O. H., Xia F., Wang, Y., Zhu, J., Akinwande, D., Alem, N., Schuller, J. A., Schaak, R. E., Terrones, M. and Robinson, J. A. (2015). ACS Nano 9 (12), 11509-11539.

[4] Varghese, S. S., Varghese, S. H., Swaminathan, S., Singh, K. K. and Mittal, V. (2015). Electronics 4, 651-687.

[5] Huo, N., Yang, S., Wei, Z., Li, S-S., Xia, J-B. and Li, J. (2014). Sci. Rep. 4, 5209; DOI:10.1038/srep05209.

[6] Jariwala, D., Marks, T. J. and Hersam, M. C. (2016). Nature Materials, DOI: 10.1038/NMAT4703.

[7] Schwierz, F. (2016). Electronics 5 (30), 1-4.

[8] Some, S., Xu, Y., Kim, Y., Yoon, Y., Qin, H., Kulkarni, A., Kim, T. and Lee, H. (2013). Sci. Rep. 3, 1868; DOI:10.1038/srep01868.

[9] Choi, J., Zhang, H. and Choi, J. H. (2016). ACS Nano 10, 1671-1680.

[10] Das, S., Kim, M., Lee, J. and Choi, W. (2014). Critical Reviews in Solid State and Materials Sciences 9:231-252.

[11] O'Brien, M., Lee, K., Morrish, R., Berner, N. C., McEvoy, N., Wolden, C. A. and Duesberg, G. S. (2014). Chemical Physics Letters 615, 6-10.

[12] Lee, J. Y., Shin, J-H., Lee, G-H. and Lee, C-H. (2016). Nanomaterials 6 (193), 1-18.

[13] Ryder, C. R., Wood, J. D., Wells, S. A. and Hersam, M. C. (2016). ACS Nano 10, 3900-3917.

[14] Son, Y., Li, M-Y., Cheng, C-C., Wei, K-H., Liu, P., Wang, Q. H., Li, L-J. and Strano, M. S. (2016). Nano Lett.16, 3571−3577.

[15] Fiori, G., Bonaccorso, F., Iannaccone, G., Palacios, T., Neumaier, D., Seabaugh, A., Banerjee, S. K. and Colombo, L. (2014). Nature Nanotechnology 9, 768-779.

[16] Yazyev, O. V. and Chen, Y. P. (2014). Nature Nanotechnology 9, 755-767.

[17] Rao, C. N. R., Gopalakrishnan, K. and Maitra, U. (2015). ACS Appl. Mater. Interfaces 7, 7809-7832.

[18] Miró, P., Audiffred, M and Heine, T. Chem. Soc. Rev. DOI:10.1039/c4cs00102h.

[19] Heine, T. (2015). Acc. Chem. Res. 48, 65-72.

[20] Mudd, G. W., Svatek, S. A., Ren, T., Patanè , A., Makarovsky, O., Eaves, L., Beton, P.H., Kovalyuk , Z. D., Lashkarev, G. V., Kudrynskyi, Z. R. and Dmitriev, A. I. (2013). Adv. Mater. 25, 5714-5718.

[21] Acharya, S., Dutta, M., Sarkar, S., Basak, D., Chakraborty, S. and Pradhan, N. (2012). Chem. Mater. 24, 1779-1785.

[22] Wu, Z., Fang, B., Bonakdarpour, A., Sun, A., Wilkinson, D. P. and Wang, D. (2012). Applied Catalysis B: Environmental, 2012, 125, 59-66.

[23] Kulkarni, G. S., Reddy, K., Zhong, Z. and Fan, X. (2014). Nat. Commun. 5:4376 doi: 10.1038/ncomms5376.

[24] Zhang, L. X., Zhang, Y. C. and Zhang, M. (2009). Materials Chemistry and Physics, 2009, 118, 223-228.

[25] Feng, C., Huang, L., Guo, Z., Liu, H. (2007). Electrochemistry Communications, 2007, 9, 119-122.

[26] Cao, S., Zhao, C and Peng, L. (2016). Materials Letters 164, 452- 455.

[27] Zhang, T., Mubeen, S., Myung, N. V. and Deshusses, M. A. (2008). Nanotechnology 19, 332001, 1-14.

[28] Zohora, S. E., Srivastava, A. K. and Dey, N. (2016). 3rd International Conference on Electrical, Electronics, Engineering Trends, Communication, Optimization and Sciences (EEECOS), 178-183.

[29] Wilson, A. D. and Baietto, M. (2009). Sensors 9, 5099-5148.

[30] Kanan, S. M., El-Kadri, O. M., Abu-Yousef, I. A. and Kanan, M. C. (2009). Sensors 9, 8158-8196.

[31] Waghe, A., Kanan, S. M., Abu-Yousef, I., Jensen, B. and Tripp, C. P. (2006). Res. Chem. Intermed. 32 (7), 613-623.

[32] Ionescu, R., Llobet, E., Brezmes, J., Vilanova, X. and Correig, X. (2003). Sensors and Actuators B 95, 177-182.

[33] Scrace, T., Tsai, Y., Barman, B., Schweidenback, L., Petrou, A., Kioseoglou, G., Ozfidan, I., Korkusinski, M. and Hawrylak, P. (2015). Nature Nanotechnology 10, 603-607.

[34] Pawbake, A. S., Waykar, R. G., Late, D. J. and Jadkar, S. R. ACS Appl. Mater. Interfaces, DOI: 10.1021/acsami.5b11325.

[35] Jha, R. K. and Guha, P. K. (2016). Nanotechnology 27, 475503, 1-11.

[36] Timoumi, A., Bouzouita, H., Kanzari, M. and Rezig, B. (2005). Thin Solid Films 480-481, 124-128.

[37] Gao, W., Liua, W., Leng, Y., Wang, X., Wang, X., Hu, B., Yu, D., Sang, Y. and Liu, H. (2015). Applied Catalysis B: Environmental 176, 83-90.

[38] Ge, S., Cai, L., Li, D., Fa, W., Zhang, Y., Zheng, Z. (2015). J Nanopart Res 17:488, 1-11.

[39] Gaiardo, A., Fabbri, B., Guidi, V., Bellutti, P., Giberti, A., Gherardi, S., Vanzetti, L., Malagù, C. and Zonta, G. (2016). Sensors 16, 296, 1-19.

Chapter 2 : Literature review

2.1 Introduction to colloidal inorganic semiconductor nanocrystals

Semiconductor nanocrystals (NCs), as the most investigated nanoscale materials boast unique electrical, optical, catalytic and magnetic properties which are central to the advancement of a vast range technological applications and modern science. These NCs have at least one dimension in the range of 1–100 nm [1-4] with new properties that are different from bulk or even from the individual units that make up the semiconductor [5]. Their unique characteristics are closely linked to phenomena such as the quantum confinement of charge carriers, surface effects, and geometrical confinement [6]. Quantized levels are a consequence of strong quantum confinement. They are very different from the continuous band of the bulk semiconductor but resemble discrete molecular semiconductors as shown in Figure 2.1 [2, 7, 8]. Quantum confinement manifests when one dimension of a semiconductor is smaller than its Bohr exciton radius. The result is the modification of the band structure which subsequently blue shifts to higher energy [3, 8-11]. It is at this size regime that the size-dependence of the band structure is revealed. The possibility to tune the band structure of the semiconductor NCs by merely manipulating their sizes to attain desired optical and electrical properties becomes a reality [3].

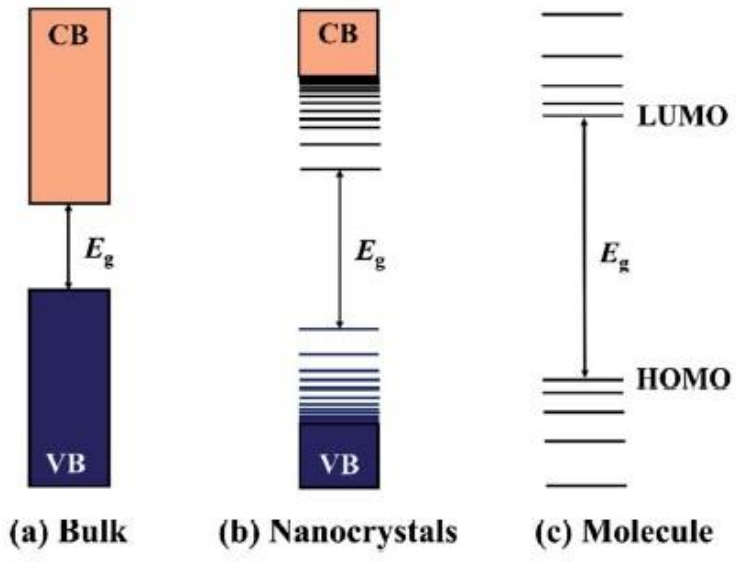


Figure 2.1: A depiction of the electronic energy states of: (a) bulk inorganic semiconductors, (b) inorganic semiconductor NCs, and (c) molecular semiconductors [3].

2.1.1 Electronic structure of a semiconductor NC

The electronic structure of a semiconductor NC comprises of a valence (VB) and conduction bands (CB) which is the highest occupied energy band; and the lowest unoccupied energy band respectively [12, 13]. Band gap energy, *E*g is the minimum energy required to excite an electron from the VB to the CB [5, 12]. Semiconductors are characterized by *E*g of between 0 < *E*g < 4 eV and a band structure which can be direct or indirect [2, 3, 12]. The top of the VB with respect to the bottom of the CB can be found at the same k-value for a direct band gap semiconductor. Meanwhile, the location is at different k-values in the case of an indirect band gap semiconductor as depicted in Figure 2.2 [12].

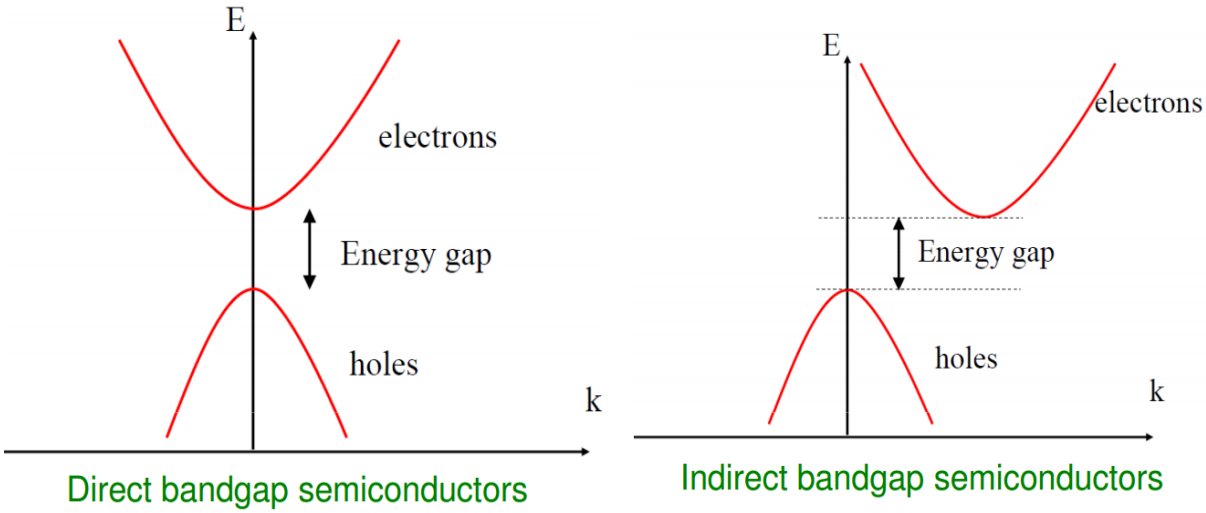


Figure 2.2: Schematic representation of (a) direct and (b) indirect electronic transitions [14].

2.1.2 Effects of quantum confinement

As mentioned previously, size affects the band gap as a result of quantum confinement. A smaller NC size translates to a larger band gap with the emergence of discrete energy levels at the band-edges of both the CB and VB as shown in Figure 2.3 (a). A large shift of energy levels accompanies a strong confinement when the NC radius is smaller than its exciton Bohr radius (a_0) [12]. This shift is however smaller with weak confinement and is normally negligible for sizes larger than 2-3 times the a_0. Quantum confinement also manifests itself in the fluorescence of semiconductor NCs. A common example is the different colours exhibited by different sizes of CdSe dispersions as depicted in Figure 2.3 (b) [12]. The $1S_h$ to $1S_e$-levels (h denotes the hole and e the electron) represent the lowest energy optical transition; while the transition to the $1P_h$ to $1P_e$ level represents the second level [12].

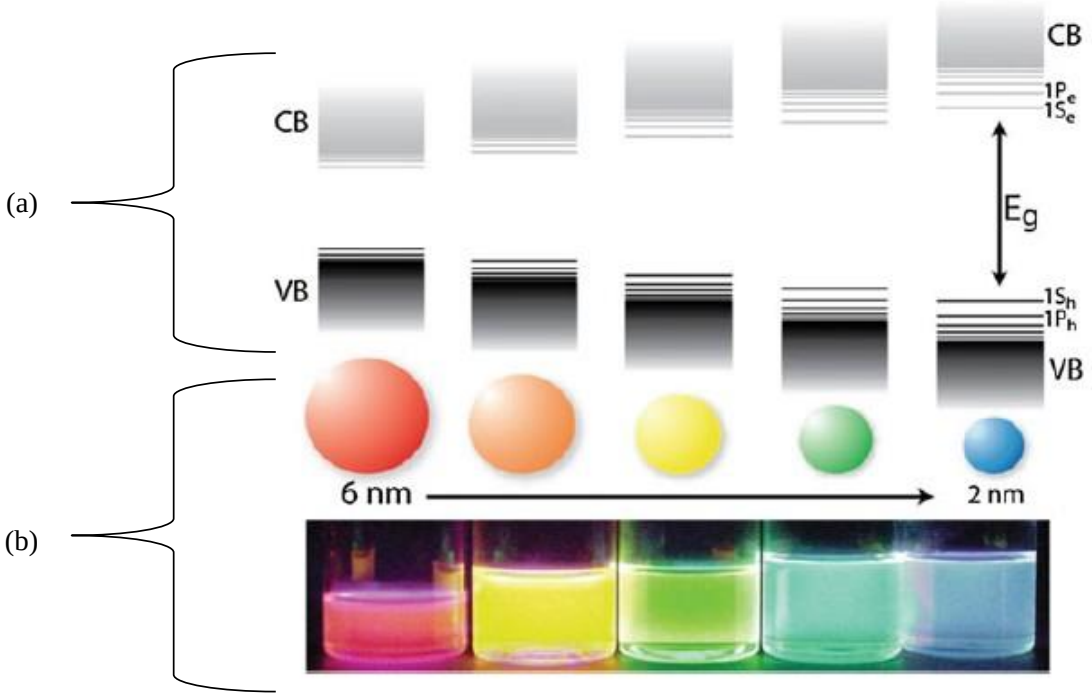


Figure 2.3: Illustration of the quantum confinement effects on: (a) the band gap and (b) fluorescence of dispersions of CdSe QDs with different sizes under excitation with a UV-lamp in the dark [12].

Band gap crossover is another consequence of quantum size-effects exhibited by 2D layered metal chalcogenide semiconductors of the group III-VI compounds and transition metal chalcogenides when bulk is reduced to few or monolayer regime. A direct to indirect band gap transition has been exhibited by InSe, GaAs and InP (group III-VI); while MoS_2, $MoSe_2$, $MoTe_2$ and WS_2 displayed an indirect to direct band gap transition (transition metal chalcogenides) [15-19]. The band gap transition is often accompanied by new or improved characteristics.

Shape is another important geometric parameter which plays a significant role in the determination of the properties of NCs as mentioned previously. It can be classified by the dimensionality of the NC and degree of confinement of the exciton in the NC. These two factors determine the precise energy to which the band gap can be tuned [2, 12]. The exciton can be confined in three dimensions (0D, e.g. quantum dots, isotropic spheres, cubes and polyhedrons), two dimensions (1D, e.g. quantum wires and rods), or one dimension (2D, e.g.

quantum wells, disks, prisms and plates) as presented in Figure 2.4 (b) [2, 12, 20]. Non-spherical semiconductor NCs can be fabricated on condition that all dimensions are small enough with respect to a_0. This means that the electronic structure of the QD will still be characterized by a series of discrete energy levels as in Figure 2.4 (a). Variations in the degree of quantum confinement are a common occurrence due to the shape of the nanostructure [12]. The effects of quantum confinement become more distinguished with the transformation of density of energy states (DOS), ρE. In this instance, the dimensionality decreases from continuous levels in bulk (3D) into discrete states (0D) as shown in Figure 2.4 (a) [h]. The ρE is defined by $\rho E \sim \rho E^{D/2-1}$, where D is dimensionality.

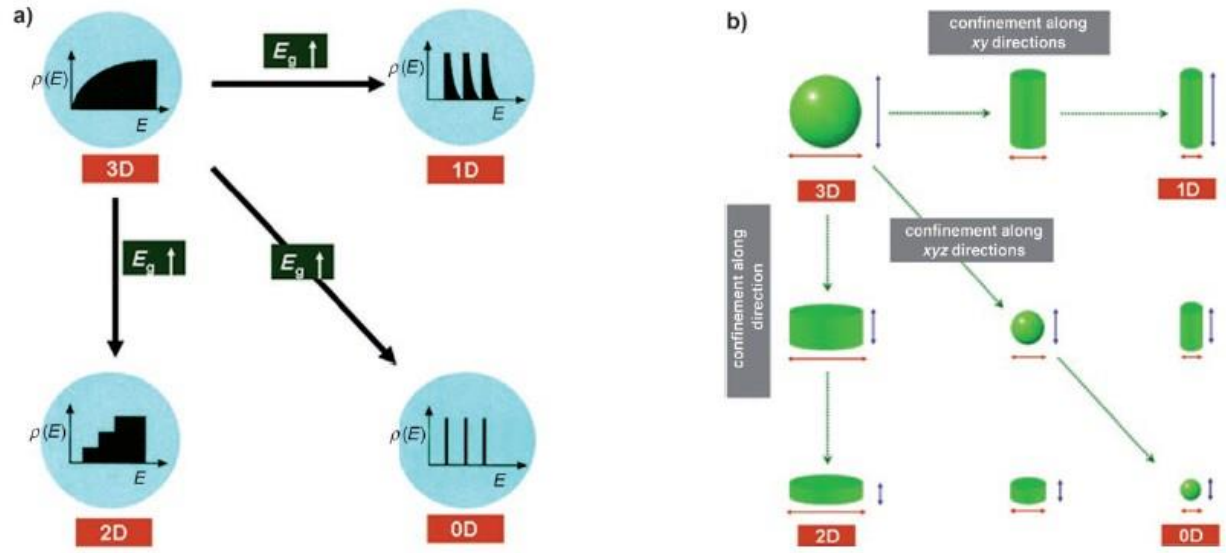
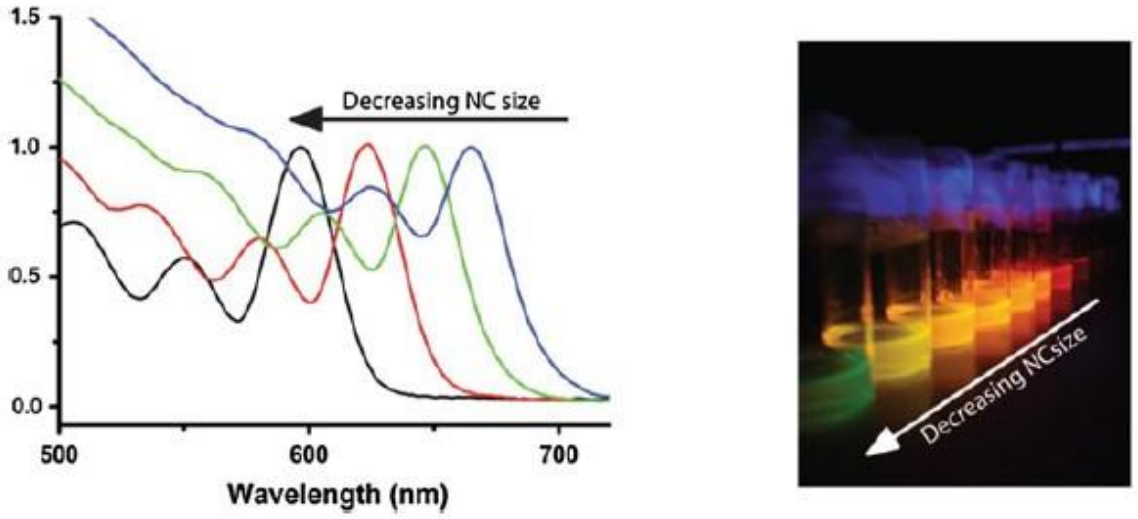


Figure 2.4: Schematic representation of shape evolution of crystals as defined by (a) DOS versus E showing a continuous curve for 3D crystals and changes into a discrete line for 0D NCs, and b) confinement of 3D crystals along one- (z), two- (xy), three (xyz) directions resulting in 2D, 1D, and 0D NCs, respectively [20].

A reduction in the size of NCs results in an increased number of surface atoms due to the large surface area-to-volume ratio. The contribution of the surface becomes more significant and eventually dominant [2, 5] leading to possible changes to some properties (e.g. solubility) and generation of completely new effects (e.g. surface plasmon resonance) [5, 21]. Existence of incomplete bonding of the surface atoms interfers with the crystalline periodicity leaving one or more "dangling orbital" on each atom pointed outward from the crystal [10]. These dangling orbitals may form a band structure to trap charge carriers at the surface [5, 10]. The

chances of non-radiative decay events are highly increased by the presence of trapped charge carriers. Capping of semiconductor NCs with organic ligands such as trioctylphosphine oxide (TOPO) or hexadecylamine (HDA) passivates the dangling bonds on the exposed facets by bonding with atoms or molecules [5]. The sensitivity of optical absorption spectrum of semiconductor NCs to quantum confinement renders itself a useful to evaluate its effect [8]. Absorption of a photon leads to the excitation of an electron from the (VB) to the (CB) and is associated with Eg; hν ≥ Eg to produce an electron in the CB and a hole in the VB [k]. The result is an exciton which is formed by the positive hole left in the valence band and the separated electron [2, 5]. The exciton may yield a current in the presence of an electric field [2]. Smaller dimensions of the NC lead to higher energy transitions as depicted in Figure 2.5 (a).



(a) (b)

Figure 2.5: (a) Absorption spectra of colloidal suspensions of CdTe NCs of different sizes and (b) colloidal suspensions of CdTe NCs of different sizes under UV excitation [12].

The exact size of exciton within the crystal depends on the material and is defined by the a_0 which can vary from 1 nm to more than 100 nm [2, 5]. Excitations above the CB edge result when the absorption of photons is characterized by energy much greater than Eg. The excess energy can be lost radiation-less processes [k]. The equation below, Eq. (2.1.1) can be used to define the absorption (A) of light by a semiconductor NC:

$$A = \alpha l \qquad (2.1.1)$$

where, l = thickness and α = absorption coefficient.

The absorption spectrum of a semiconductor NC can be used to estimate its *E*g and by using the equation below:

$$\alpha(h\nu) \propto (E_g - h\nu)^{1/2} \qquad (2.1.2)$$

An exciton travels through the semiconductor bulk crystal until it is trapped or destroyed if it collides with another exciton [2, 5]. The electron-hole pair dissipates excess energy in the form of heat as it relaxes to its ground states ($1S_e$-$1S_h$ exciton). This happens through a number of intra-band non-radiative relaxation steps [12]. The relaxation steps can occur very quickly either by coupling with phonons (i.e., lattice or ligand vibrations) of suitable energy, or by Auger scattering processes [12]. Further relaxation occurs on the ground where the exciton energy is released either radiatively or non-radiatively (Figure 2.6) [12].

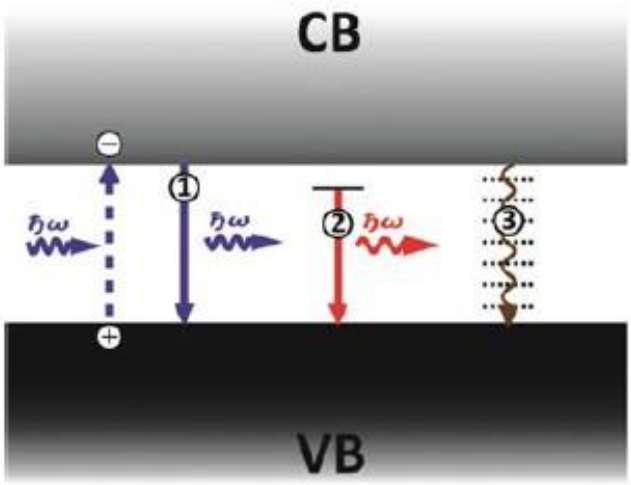


Figure 2.6: Possible exciton recombination pathways in semiconductors. (1) Radiative recombination, (2) defect assisted radiative recombination, and (3) non-radiative recombination [12].

The emission of a photon results from radiative exciton recombination represented by a well-defined peak; its energy is close to the lowest energy absorption transition. It is the reverse of the lowest energy absorption transition; its peak positions are also dictated by the size of the

NC. The peak widths are determined by the averaged size and shape distribution of the ensemble of NCs (inhomogeneous line broadening). Emission of a photon is necessary to prevent an indefinite excited state of the electron. This is realized by external stimulation of the mixing of both the excited and the ground state orbitals. It is used in lasers and is given by Eq. (2.1.3).

$$\Gamma_{rad}(\omega) = \frac{\omega^3 n |\mu i,f|^2}{3\pi\varepsilon_0 \hbar c^3} \qquad (2.1.3)$$

Where, Γ_{rad} = radiative decay rate for spontaneous emission
ω = frequency of light
n = refractive index
ε_0 = permittivity of free space
$\mu_{i,f}$ = transition dipole moment between initial and final states

Non-radiative exciton recombination usually occurs through defects or impurities. The dissipation of the exciton energy by coupling to phonons is very unlikely due to the requirement of simultaneous creation of a large number of phonons (>50 for CdSe QDs) [12]. Trapping of one of the charge carriers at a defect or surface state can effectively compete with radiative recombination because it is faster. It leads to quenching of the exciton emission, strong carrier localization and reduces the overlap between the electron and hole wave functions. The possibility of a radiative recombination is thus less likely. A broad emission band at lower energies than the band gap (trap or defect related luminescence) is produced if radiative recombination occurs due to trapping of the exciton in a defect or surface state [12]. The trap states predominantly occur on the surface of NCs. As discussed earlier, surface atoms have fewer neighbours than their interior counterparts, and therefore possess unsatisfied chemical bonds (dangling bonds). These unshared atomic orbitals give rise to energy levels within the HOMO-LUMO gap of the semiconductor NC (surface states) [12]. Surface defects (e.g., vacancies) give rise to even more strongly localized energy states, which can very effectively trap the electron or hole. Control of the surface quality of semiconductor NCs is paramount to eliminate dangling bonds through passivation. This can be achieved either by overgrowing a shell of a wider band gap semiconductor or by coating the surface with suitable organic ligands [12].

Dipole-dipole interaction is another possible pathway of non-radiative recombination. The exciton energy is transferred between QDs in close proximity. A physical displacement of the exciton from the donor QD to the neighbouring acceptor QD occurs without external stimulation (Figure 2.7) [12].

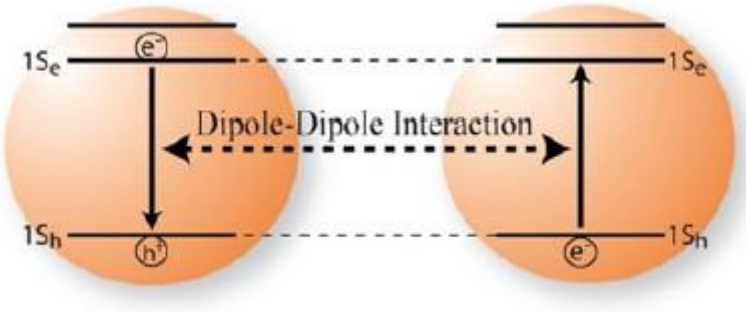


Figure 2.7: Schematic representation of resonant exciton energy transfer from the donor QD (left) to the acceptor QD [12].

$$\Gamma_{ET} = \frac{2\pi}{\hbar}\frac{\mu^2 D^{\mu^2} A^{\kappa^2 \Theta}}{R^6 n^4} \qquad (2.1.4)$$

The lifetime of an exciton in a QD can be determined from the photoluminescence (PL) decay times τ, and can be described as:

$$\tau = {}^{1}/_{W_{TOT}} = {}^{1}/_{W_{Rad}} + {}^{1}/_{W_{NRad}} + {}^{1}/_{W_{ET}} \qquad (2.1.5)$$

Where, W_{TOT} = total decay rate

W_{Rad} = radiative decay rate

W_{NRad} = non-radiative decay rate

W_{ET} = energy transfer rate

A single exponential pattern is followed if the excitons decay only radiatively:

$$N(t) = N_o e^{-t/\tau} \qquad (2.1.6)$$

Where, t = elapsed time after excitation

τ = exciton radiative lifetime

N_0 = population of the emission state at t = 0 which determines the PL intensity at t = 0.

The properties of semiconductor NCs are also highly dependent on the composition, shape, structure, and surface chemistry during quantum confinement [3, 5]. In light of this, NCs with uniform size distribution and well-defined shapes must be synthesized in order to take advantage of their unique properties.

2.1.3 Colloidal nanostructures of layered 2D semiconducting metal sulphides

Given their ease of fabrication and versatility to which they can be manipulated; colloidal semiconductor nanostructures are promising candidates as active components in a number of different fields. Wet chemical synthetic routes are preferred as they provide an almost perfect environment for tuning of the size and shape of nanostructures. This tuning is realized by careful control of the reaction conditions [22]. These nanostructures possess physical and chemical properties of molecules while their optoelectronic properties resemble those of semiconductors [23]. The nanostructures are found in single, bi- or multi-layers with a thickness of a few nanometers and lateral dimensions of up to many centimeters. They can be crystalline and referred to as nanocrystals (NCs) or amorphous. 2D layered materials are highly anisotropic [24] with direction and dimension determining the resulting properties thereby adding another interesting angle to the design of new devices [25-28]. An atomically thin 2D material has its free charges confined in one spatial dimension. The study into these materials is currently one of the fastest growing active research areas in gas sensing. Understandably so, for graphene's lack of a band gap has limited its use in semiconductor electronics like FETs and optoelectronic applications [29-37] which require switch-off [32, 36].

2.2 Synthesis of metal sulphide semiconductor NCs

Precise control and monitoring of shape, size distribution, structure, composition and anisotropy are very important in determining the ultimate application of these materials. This is due to the strong correlation between these parameters and the properties of nanostructures [38, 39]. 2D layered materials exhibit a strong dependence of the band gap on the layer thickness [40]; therefore thinning them down to one or few layers unlocks the extraordinary optical properties. Significant advances in solution phase methods have seen the successful

fabrication of mono, bi- and multilayers of 2D layered materials. These methods not only are low cost and scalable; but occur at relatively lower temperatures and have emerged as more powerful and versatile by affording control over size, shape, edge morphologies and degree of crystallization of colloidal semiconductor nanostructures [41, 42, 43, 44, 45, 46]. The ability of these methods to allow for control of growth kinetics, temperature, time, choice of precursors, reducing agents and capping agents have ensured these successes. Nanostructures produced by these methods have proven to be easily dispersible in either aqueous or non-hydrolytic media [47]. However, optimum stoichiometry still remains a challenge in solution phase methods, hence the on-going research to optimize these methods [34]. Several methods have been developed to fabricate β-In_2S_3 and WS_2 with a variety of morphologies from carefully selected precursors.

2.2.1 Thermal decomposition routes

Non-hydrolytic routes have been very effective thus far in the synthesis of both β-In_2S_3 [48-51] and WS_2 [52-54] nanostructures with well-controlled size and good size dispersion [52]. A high boiling point solvent is used and the crystal surface is fully passivated by organic stabilizing ligands [47, 54]. The hot-injection route requires the rapid injection of a cold solution (room temperature) of precursor molecules into a hot solution (180-350 ℃) [47, 44, 45, 55-59]. The rapid injection increases the precursor concentration (supersaturation) above the nucleation threshold followed by a nucleation burst [45, 59] while the drop in temperature after injection limits nucleation [58], thereby creating the required separation between the two steps.

The heating-up method on the other hand involves the initial mixing of all the reactants at room temperature. Subsequent controlled heating initiates chemical reactions to produce monomers for nucleation and subsequent growth of nanostructures [45, 55, 57]. The choice of precursor and ligand chemistry is even more important in this route to define how the monomers and nanostructures evolve over time [45, 57]; as continuous production of monomers results in inability to separate the nucleation and growth stages of the reaction. This method was followed in this project to synthesize nanostructures of In_2S_3 and WS_2 due to its simplicity.

2.2.2 Solvothermal or hydrolysis methods

These methods encompass all the strategies based on chemical processes performed in a sealed vessel (autoclave) above ambient temperature (above boiling point of solvent used) and pressure [56, 60-62]. The term hydrothermal synthesis is used when water is used as the solvent. High quality nanostructures of WS_2 [63-67] and β-In_2S_3 [68-72] have been obtained via these alternative routes.

2.2.3 Other synthetic routes

Several other methods like the microwave (MW)-assisted synthesis [73], chemical precipitation [74], solution dispersion route [75]; mechanical and chemical exfoliation [76] have also been followed to synthesize these nanostructures.

2.3 Growth, size and shape control of semiconductor nanostructures

It is widely accepted that the formation processes of monodispersed NCs mainly experiences two stages, nucleation and growth. Nucleation and growth are often referred to as the appearance of a new phase out of an old phase [77]. Both stages require careful control.

2.3.1 Nucleation

Nucleation is defined as the process whereby nuclei (seeds) act as templates for crystal growth [78]. It represents the initial stages during crystallization [79]. The nucleation and growth of the nanostructures in solution is governed by the LaMer theory [42, 47, 56, 80]. The induction of a single nucleation event known as burst nucleation [80], and prevention of additional nucleation during the subsequent growth process is important for the preparation of monodispersed NCs [81, 82]. Control of size distribution becomes very difficult with continuous nucleation, leading to polydispersity. Therefore, separation of the nucleation and subsequent growth steps is a requirement to monodispersed nanostructures [58]. According to LaMer's diagram, monodispersity can be achieved through:

(i) a high rate of nucleation leading to a burst of nuclei formation in a short period;

(ii) an initial fast rate of growth of these nuclei for the rapid reduction of the concentration below the nucleation concentration and;

(iii) finally, a slow rate of growth for a longer growth period compared to the nucleation period [83].

Homogeneous and heterogeneous nucleation processes can both be utilized to synthesize monodispersed NCs by separating nucleation and growth [81]. Homogeneous nucleation is a result of uniform formation of nuclei throughout the parent phase. Meanwhile, heterogeneous nucleation occurs at preferential sites like container surfaces, impurities, phase boundaries and dislocations [78, 79, 81]. The effective surface energy is lower at these preferential sites and decreases the activation energy leading to high possibility of nucleation. It is for this reason that heterogeneous nucleation occurs more often than homogeneous nucleation [81]. The stable nucleating surface provided by the liquid phase is conducive for heterogeneous nucleation [78]. LaMer and *et al.* detailed the use of homogeneous nucleation to separate nucleation and growth where nuclei appear in a homogeneous solution without any seed for heterogeneous nucleation [12, 78]. The change from homogeneous to heterogeneous phase is spontaneous due to the existence of a high energy barrier to nucleation.

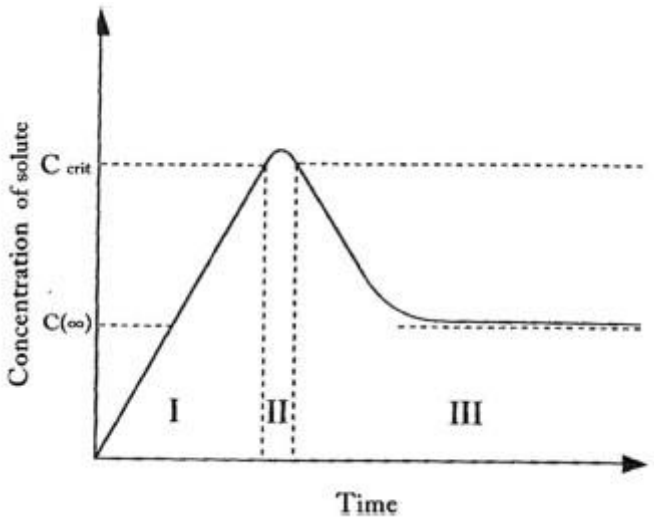


Figure 2.8: Schematic representation of the LaMer diagram [78].

The relationship between burst nucleation and energy barrier is represented in four stages using the LaMer plot in Figure 2.8. In stage I, a constant increase in monomer concentration occurs but does not result in precipitation even under supersaturation ($S > 1$) due to the extremely high energy barrier required for spontaneous homogeneous nucleation [81]. However, the degree of supersaturation in stage II is high enough to overcome the energy barrier leading to the formation and accumulation of stable nuclei [80]. The monomer concentration decreases to a point where the net nucleation rate (the number of nuclei formed per unit time) is zero; the rate of monomer consumption exceeds the rate of monomer supply.

Stage III is then experienced below this level wherein nucleation is effectively stopped and the particles keep growing as long as the solution is supersaturated [81]. Significant depletion of monomers gives way to the growth process by Ostwald ripening which is stage IV. It is at this stage that smaller (higher-surface-energy) particles are sacrificed. Growth of larger particles follows, leading to fewer particles in the system.

A thermodynamic interpretation of the energy barrier to the homogeneous nucleation can also be used. The Gibbs free energy of formation ΔG, of spherical crystals with radius r, surface energy per unit area γ and the free energy, ΔG_v is given in Eq. (2.1.7) [78].

$$\Delta G = 4\pi^2\gamma + \frac{4}{3}\pi r^3 \Delta G_v \qquad (2.1.7)$$

The free energy depends on temperature T, Boltzmann's constant k_B, the supersaturation of the solution S, and its molar volume,V as defined in Eq. (2.1.8) [78].

$$\Delta G_v = -k_B T ln \frac{S}{V} \qquad (2.1.8)$$

γ is always positive, and ΔG_v is negative as long as the solution is supersaturated. ΔG_v is dependent on temperature T. The value of radius at which ΔG is maximum is called the critical radius r_c. It is the minimum radius of a nucleus that can grow spontaneously in the supersaturated solution. Setting dΔG/dr = 0 allows determination of r_c as in Eq. (2.1.9).

$$\Delta G_{crit} = \frac{4}{3}\pi\gamma r_{crit}^2 \qquad (2.1.9)$$

In homogeneous nucleation, S should be sufficiently high for r_c to be smaller than the size of the crystal embryos that form the nuclei for the homogeneous nucleation. A critical free energy is required to obtain stable particles within solution as shown in Figure 2.9 [78]. An Arrhenius type equation, Eq. (2.1.10) can be used to describe the rate of nucleation of N particles during time t, where A is a pre-exponential factor.

$$\frac{dN}{dt} = Ae^{\frac{[-\Delta G_{crit}]}{\kappa_B T}} \qquad (2.1.10)$$

$$\frac{dN}{dt} = Ae^{\frac{[16\pi\gamma^3V^2]}{[3k_B^3T^3(In\,S)^2]}} \qquad (2.1.11)$$

Supersaturation, temperature, and the surface free energy can be varied using Eq. (2.1.11).

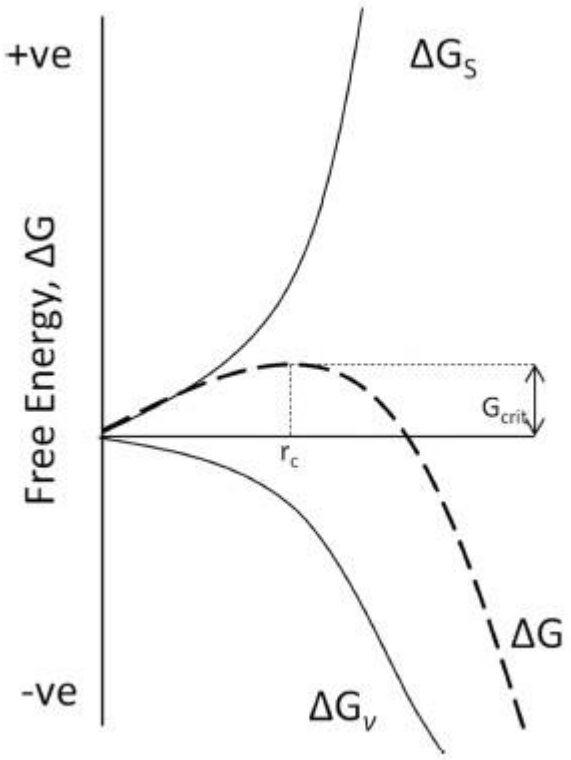


Figure 2.9: A maximum free energy ΔG at a critical cluster size, r_c, which defines the first stable particles – the nuclei [78, 81].

Unlike the relatively simple LaMer plot, it is not easy to thermodynamically define the exact critical supersaturation level. This is due to energy fluctuation in the solution. The particles formed in an unsaturated solution could re-dissolve unless they are stable enough to resist the free energy fluctuation of their surroundings [78]. A high nucleation rate is required to equal or surpass the redissolution rate of the particles to start the accumulation and the growth of the nuclei; another condition associated with the degree of supersaturation. S_c is the point where the nucleation rate is so high that the number of nuclei increases despite the dissolution of smaller nuclei [12]. γ and ΔGv are strongly influenced by size. It is well known that the particle size decreases with a significant increase in the ratio of surface atoms to the bulk atoms. Consequently, a strong driving force, especially for nanocrystals with a size of few nanometers develops to minimize the surface free energy by reconstructing the surface

structure or changing the crystal structure (e.g., through phase transitions or lattice contraction [12]. Nucleation can also be physically separated from growth by using preformed nanocrystals as seed nuclei, a method known as seed-mediated growth. In this method, heterogeneous nucleation is used to suppress the formation of additional nuclei by homogeneous nucleation [12]. Homogeneous nucleation is suppressed by keeping a low monomer concentration during growth. Hot-injection and heating-up methods which were mentioned earlier in this document utilize homogeneous nucleation to synthesize monodisperse nanocrystals in the organic.

2.3.2 Growth of NCs

Growth without additional nucleation is very important for the achievement of a narrow size distribution of particles. Nucleation continues over a period of time with constant monomer concentration until a surface growth of clusters takes place which leads to depletion the monomer supply [83]. It ends when the monomer concentration falls below the critical level for nucleation (critical supersaturation level). The growth rate of colloidal particles depends on parameters including their size [79]. Growth of nanoparticles is through the surface reaction and the monomer's diffusion to the surface as shown in Figure 2.10 [78, 79]. Initially, the monomers are transported from the bulk solution onto the crystal surface as governed by Fick's law of diffusion in Eq. (2.1.12) [79]:

$$j = -D\frac{d[M]}{dx} \qquad (2.1.12)$$

where *j* and *D* are the monomer flux and the diffusion constant, respectively. This is followed by the reaction of the monomers on the surface whose rate k is defined by Eq. (2.1.13) and is assumed to be independent of the particle size [79].

$$j = 4\pi r^2 k(C_i - C_r) \qquad (2.1.13)$$

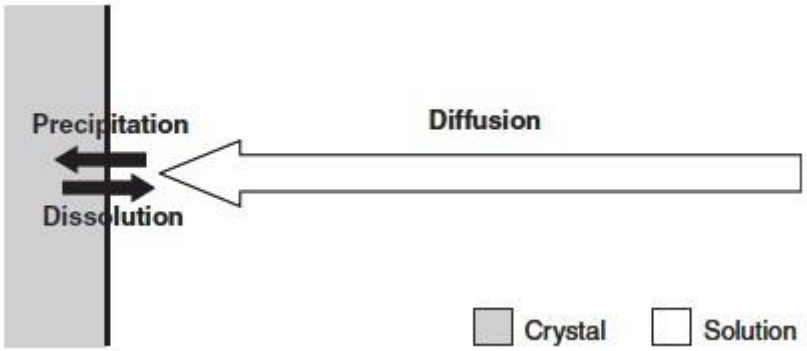


Figure 2.10: A Schematic for mass flow between the solution and the surface of a particle during the crystallization reaction [79].

Slow growth and sphere-like nanostructures with relatively large size distributions are a result of thermodynamic control. This happens at low monomer concentration to minimize the surface area and energy difference between different facets [42, 55-57]. Monodispersed sphere-like nanostructures are achieved when the monomer concentration increases [57, 58]. Growth of highly anisotropic shapes is observed with continued increase in monomer concentration under kinetic control [42, 56, 57]. Facets arise due to a lower surface energy and/or lower growth rate of certain facets than others leading to a larger surface area [59].

2.4 Reaction parameters affecting growth of nanostructures

A narrow size distribution, good crystallinity, shape, structure, composition and optical properties can be obtained by careful manipulation of experimental variables such as the nature of solvents, concentration of metal precursors, reaction temperature and time.

2.4.1 Solvents

Use of organic reagents offers the opportunity to tune the reaction temperature over a wide range; in this environment the precursors are exhaustively explored [84]. Colloidal nanostructures tend to aggregate rapidly, hence the need for ligands. Various coordinating solvents (*e.g.* ethers), alkyl thiols, amines, carboxylic and phosphonic acids, phosphines, phosphine oxides, phosphates, phosphonates, are commonly used as ligands [59]. They provide steric stabilization and passivation of the electronic surface states which are crucial in obtaining luminescent nanocrystals [58, 59, 85-87]. Ligands also play a key role in the

control of nucleation and growth kinetics slowing down the growth rate, allowing the nanocrystal cores to anneal for improved crystallinity [58, 59]. They sometimes act as solvents, precursors and reducing agents [60, 86]. The reducing action of ligands plays a key role in tuning the reactivity of the monomers, and in regulating the temporal evolution of the nanostructure size over time [59]. Certain ligands are used to tune the surface energy due to their ability to influence the anisotropic growth of colloidal nanostructures by selectively adsorbing to specific facets [88, 89]. During growth process, ligands continuously adsorb and desorb from the surface of the nanostructures through their polar head groups [59]. Strongly adsorbed (tightly bound) ligands retard growth, while weakly bound ligands kinetic growth [89, 90]. Effect of ligands on the shape [66, 91, 92] is well documented.

2.4.2 Time

Heating time is directly proportional to the size of the nanostructures. It is well-known that longer heating time results in larger nanostructures that emit at longer wavelengths. Furthermore, investigation of the morphology at different reaction times provides information on the growth mechanism of nanostructures [48, 49, 72] and the number of layers have been shown to form as a function time in the case of WS_2 [52].

2.4.3 Heating temperature

Temperature has been shown to strongly influence the growth of nanostructures in different ways. It can also have an effect on the phase and morphology of the nanostructures. Zhang, *et al.* demonstrated the effect of temperature on the evolution of the hierarchical morphology via a solvothermal method from cubes, dendritic hierarchical, octagonal hierarchical flowerlike and vertebration shapes of PbS between 80 and 180 ℃ [93]. Nanosheets of β-In_2S_3 with different thicknesses were obtained as a function of temperature by Acharya and co-workers [50].

2.4.4 Reactivity of precursors

The reactivity of the precursors has been increasingly explored as a means of controlling the final size of nanostructures, composition, and morphology [87]. The decomposition of the precursor species induces a short burst of nucleation that is subsequently followed by growth of the monomers [59].

2.5 Application of semiconductor NCs in chemical sensing

The quest for cheaper, faster, more sensitive, selective and stable sensors is the driving force behind new developments in the gas sensing field towards ‘‘nanosensors’’ [94]. Chemical sensors or gas sensors have been extensively used to detect and monitor a huge variety of gases and vapours, including toxic or explosive gases, humidity, and odors. Chemical sensing is required in applications such as automotive, aerospace, industrial, health care, domestic sector, food industries and security sector [94]. The semiconductor provides electrical conductivity while the morphology of the NCs provides selective binding site for the adsorption of analyte, large gas absorptive capacity, increased sensitivity, etc. This is highly exciting because sensor properties can be controlled by design which can be made possible by careful control of reaction parameters during synthesis of NCs.

2.5.1 Types of gas sensors

Several types of chemical sensors that are in existence have been developed for the detection of chemical species in the gaseous phase. These sensors are based on thermoelectric effects, thermal conductivity, catalytic combustion (combustible gas sensors), surface plasmon resonance, and both aqueous and solid-state electrochemistry; surface acoustic wave, optical and fiber optical effects, and magnetic effects, chemoresistive/semiconductive [95, 96]. Among these, chemoresistive/semiconductive sensors are the most applied.

2.5.2 Chemi-resistor sensors based on 2D layered metal sulphide semiconductor NCs

Solid state gas sensors based on 2D semiconducting nanostructures of metal oxides (MOXs) like In_2O_3, WO_3, *etc.*, are the most studied and widely used in the development of commercial gas sensors [94-101]. Among their many advantages are small size, low power consumption, simple construction, low weight, and low cost [100, 101]. Their resistance depends on the composition of gaseous atmosphere; the individual constituents of the gaseous atmosphere participating in chemical reactions take place on the surface of grains of the gas-sensitive material [102]. Despite all the good benefits provided by MOX based sensors, their application is marred by great challenges associated with the high operating temperatures (e.g. from 300 ℃) *e.g.* high power consumption; risk of ignition during detection of flammable or explosive analytes; decrease of sensor stability and lifespan due to a thermally induced growth of metal oxide grains (*e.g.* from 300 ℃) [105, 103-105].

For this reason, nanostructures of 2D layered metal chalcogenides have taken centre stage as potential materials for efficient gas detection. Metal chalcogenide semiconductors have lower band gaps than their MOX counterparts [106]. This translates to low working temperatures for the activation of intrinsic surface reactions. A different catalytic mechanism on the surface reaction exists due to the absence of oxygen in the crystal lattice of metal sulphides. Furthermore, the constant drift of the signal suffered by MOXs maybe solved by the absence of oxygen. The drift is associated with the in/out diffusion of oxygen vacancies, which alters the doping level [106]. 2D layered metal chalcogenides possess large reactive sites, high surface area-to-volume ratio due to their nanometre-scale thickness; and unique photocatalytic and optical activities [30, 106-108]. They are potentially faster, and have greater modulation of electrical properties (e.g. capacitance, resistance) upon exposure to analytes due to a greater interaction zone over the cross-sectional area. Their high electrical conductivities and low noise allow for the detection of even the smallest change in charge carrier concentration as a result of exposure to a gaseous species [30]. Enhanced gas sensing is also made possible by the long-range of lattice periodicity which provides a better channel for charge carrier transportation; improved diffusion processes upon the intercalation of gas molecules and high charge carrier mobility [30, 107, 109-112].

MoS_2 has been the prominent example of potential alternatives to MOXs which can be operated at relatively low temperatures. The study on MoS_2 has paved the way for WS_2 as a potential gas sensing material; both belong to the same transition metal dichalcogenide (TMDC) family of semiconductors. In addition to the many similarities WS_2 shares with MoS_2, it reportedly displays higher thermal and oxidative stability, a wider operation temperature range, favourable band structure [30, 31, 113] and broader emission linewidth than MoS_2 [1114]. In addition, WS_2 has a larger spin-orbit coupling, suggesting WS_2 may exhibit larger band edge spin splittings and stronger magnetic field effects for optoelectronic and spintronic functionalities [114]. According to recently published calculations, WS_2 has the potential to outperform other 2D materials in field effect transistors (FETs) applications [31]. It is for this reason that the number of published reports on the gas sensing potential of WS_2 of chemical vapours such as ammonia, ethanol [31], humidity [115, 116], *etc.* is steadily growing. While studies into the gas sensing potential of WS_2 are gaining momentum, In_2S_3, (a member of the group III-VI compounds) has been largely overlooked. To our best knowledge, the study into potential gas sensing properties of In_2S_3 is still in its infancy judging by the absence of published data.

2.5.3 Working principle and gas sensing mechanism of chemical sensors

The working principle of chemiresistors is based on the change in electrical conductivity upon their interaction with gas molecules due to the induced charge transfer by the gas molecules present in their immediate environment [27, 111, 117-125]. The accumulation of analyte gas molecules in the sensitive layer of the device is reversible. The change in resistance or conductance is due to a relatively stronger charge transfer interaction (chemisorption) as opposed to weaker dipole or van der Waals (physisorption) [126-129]. The conductance of a semiconductor is determined by the carrier concentration and carrier mobility [129, 130]. For gas sensing to take place, one or both parameters should be affected by gas adsorption. Semiconductors are divided into n-type (*e.g* In_2O_3, WO_x, and MoO_3) and p-type (*e.g* CuO, NiO and TeO_2) based on the charge carriers [131]. Analyte gases are classified into oxidizing gas or electron acceptors such as O_2, NO_2 and reducing gas or electron donor such as HCHO and ethanol [131]. N-type semiconductors have electrons as the majority charge carriers, and an increase in conductivity occurs in the presence of a reducing gas. Meanwhile, interaction with an oxidizing gas decreases the conductivity due to a depletion of electrons. Positive holes are the majority charge carriers in p-type semiconductors; where the conductivity increases upon interaction with an oxidising gas. Introduction of negative charges by a reducing gas reduces the positive (hole) charge carrier concentration resulting in a decrease in conductivity, Table 2.1 [94, 117, 121, 122, 124, 129, 131-133].

Table 2.1: A summary of the responses by n- and p-type semiconductors [129].

Classification	Oxidizing gases	Reducing gases
n-type	resistance increase	resistance decrease
p-type	resistance decrease	resistance increase

The gas sensing mechanism however is said to be very complex and not fully understood yet. Surface interactions of the gas/semiconductor that occur at the grain boundaries of the metal chalcogenide/oxide film underlie the gas sensing mechanism of chemiresistive gas sensors [128]. Such surface interactions may differ based on the gas sensing material and detected

gas [134]. The reactions of chemical sensors with the adsorbed gaseous species generally include reduction/oxidation processes of the semiconductor; adsorption of the chemical species directly on the semiconductor and/or adsorption by reaction with surface states associated with pre-adsorbed ambient oxygen (in the case of oxides); electronic transfer of delocalized conduction-band electrons to localized surface states and vice versa; catalytic effects and in general complex surface chemical reactions between the different adsorbed chemical species [135].

2.5.3.1 Adsorption

Gaseous species can be attracted and retained on the surface of a gas sensor in two well-accepted types of adsorption: physisorption and chemisorption [95, 128, 132]. During chemisorption a charge exchange between adsorbed species and metal oxide occurs [128, 132]. It is an endothermic process whose activation energy (heat of chemical adsorption, ΔH_{CHEM}) can be supplied by thermal or non-equilibrium ones such as illumination [132]. It involves pre-adsorption of oxygen on semi-conducting material surface, adsorption of target gas, reaction between oxygen and adsorbed gas and desorption of reacted gas on surface [136-138]. The conductivity of the semiconductor gas sensor increases when the adsorbed oxygen molecules play the role of acceptor during a reaction of adsorbed oxygen molecules with the gaseous species. On the other hand, the conductivity decreases when the adsorbed oxygen molecules play the role of donor [136, 137]. These surface interactions result in a reversible and significant change in electrical conductivity by exposing the sensor to air (or an inert environment). Meanwhile, physisorption is associated to a neutral state [128] and is the first step of the interaction of the gas species with the sensor surface [132]. It is exothermic and is the predominant process in low temperature range [95, 132]. However, desorption of molecules requires an activation energy of (heat of physisorption, ΔH_{PHY}). In practical terms, adsorption occurs through physisorption followed by chemisorption for which the much smaller energy of activation, ΔE_A is needed [95].

SnO_2, a wide-bandgap, n-type semiconductor will be used to explain gas sensing mechanism of a MOX under no humidity conditions and in the presence of oxygen (e.g., in synthetic air). Its working principle is based on a shift of the state of equilibrium of the surface oxygen reaction due to the presence of the target analyte (receptor function). The resulting change in

chemisorbed oxygen is recorded as a change in resistance of the sensor material (transducer function) [94].

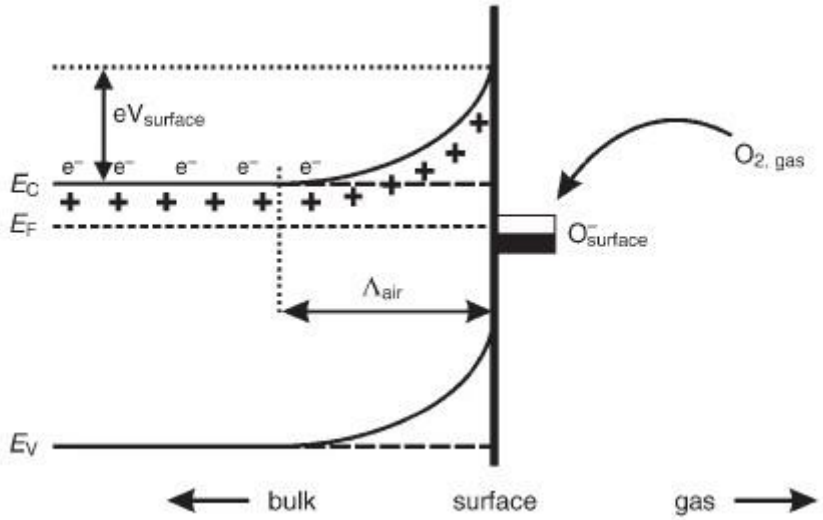


Figure 2.11: A schematic representation of a simplified model of band bending in a wide bandgap semiconductor after chemisorption of charged species (*e.g.* ionosorption of oxygen) on surface sites. E_C, E_V, and E_F represent the energy of the conduction band, valence band, and the Fermi level, respectively, while Λ_{air} denotes the thickness of the space-charge layer, and $eV_{surface}$ the potential barrier. The conducting electrons are represented by e^- and + represents the donor sites [94].

The adsorbed oxygen captures electrons due to their relative energetic position with respect to the Fermi level E_F (Figure 2.11) [94]. The stoichiometry of the adsorbed oxygen ion is dependent on the operating temperature. For instance, it is mostly adsorbed as: O_2^- below 420 K; O^- ions between 420 - 670 K (operating temperature) and O^{2-} above 670 K [94, 138]. Intrinsic oxygen vacancies (donor sites) provide electrons for this process from the conduction band E_C. The electrons are trapped at the surface resulting in an electron-depleted surface region also known as the so-called space-charge layer Λ_{air} [94].

The variations in conductivity are said to be related to the formation of a space charge layer at the semiconductor surface after gas adsorption. Hence, the ratio of the thickness of the space charge layer to the conductive channel dimension determines the sensitivity of the sensor. A higher surface area-volume ratio results in a higher dimension ratio of the space charge region to the conductive channel [139]. The equilibrium between the Fermi level and the energy of surface-adsorbed sites is dictated by the Weisz limitation which is a maximum

surface coverage of about 10^{-3} to 10^{-2} cm^{-1} ions is dictated [94]. The surface charge is determined by the amount and type of adsorbed oxygen which in turn governs the height ($eV_{surface}$) and depth (Λ_{air}) of the band bending depend [94]. Λ_{air} also depends on the Debye length L_D, a characteristic of the semiconductor material for a particular donor concentration [94].

2.5.3.2 Reduction/oxidation

The gas sensing mechanism can also be explained through redox reactions. Exposure of the MOX sensor to a reducing or oxidizing gas may affect the density of charge carriers in the near-surface region of nanostructure [138, 140]. For instance, a reducing gas will extract surface-bound oxygen atoms acting as donors for the n-type MOX; while an oxidizing gas will immobilize further conduction-band electrons from the near-surface region by creating additional surface-acceptor [138]. These oxidation-reduction reactions change the thickness of the depletion layer changed [138, 140]. Thus, a reducing gas increases the conductivity of the material, while an oxidizing gas reduces it. Consequently, the height of the Schottky barrier is reduced leading to an increase of the conductance of the whole sensing layer [94, 138].

2.6 Factors controlling sensitivity

Three independent factors control sensitivity of the active sensing element, *viz.* receptor function, transducer function (Figure 2.12) and utility or peculiarities of sensor construction.

2.6.1 Receptor function

It is associated with the ability of the surface of the sensor to interact with the target gas: its rate, selectivity and reversibility [94, 128, 136, 141, 142]. It is determined by the chemical properties of the surface material. The gas/semiconductor surface interactions (e.g. adsorption) on which the gas-sensing mechanism of chemiresistive gas sensors is based occur at the grain boundaries of the film [128, 134]. Gas adsorption occurs due to the high reactivity of sensor surface. Gaseous species can be attracted and retained on the surface of a gas sensor in two well-accepted types of adsorption: physisorption and chemisorption [95, 128, 132]. These surface interactions result in a reversible and significant change in electrical conductivity [128] by exposing the sensor to air (or an inert environment).

2.6.2 Transducer function

It is related to the ability of the sensor to convert the signal caused by chemical interaction on the sensor surface (work function change) into an electrical signal [94, 128, 141, 142]. Each boundary between the grains performs this function to which a double-Schottky barrier model can be applied. Resistance depends on the barrier height and concentration of the target gas [141].

2.6.3 Utility

It refers to the accessibility of inner grains of the active material to the target gas. The target gas reacts with the surface while diffusing into the bulk of the device. A balance has to be struck between the rate of reaction on the surface and diffusion. A large rate of reaction to diffusion results in the loss of sensor response due to inaccessibility of the grains located at inner sites, leaving them un-utilized for gas sensing [63].

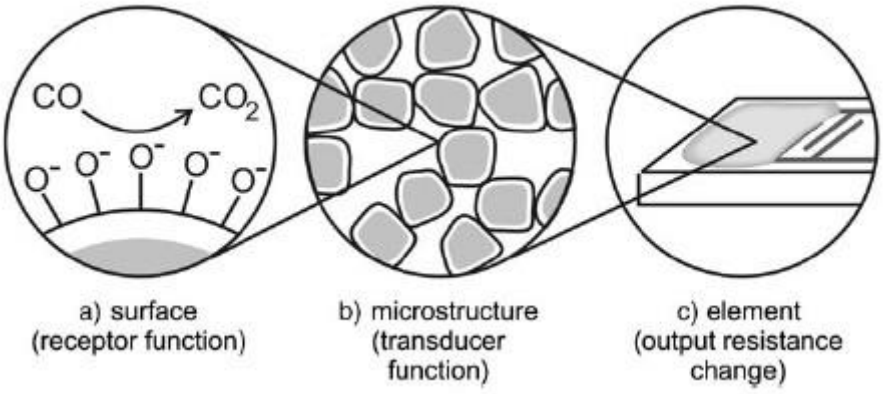


Figure 2.12: Receptor and transducer function of a semiconductor gas sensor: a) surface, providing the receptor function, b) microstructure of the sensing layer, providing the transducer function, and c) element, enabling the detection of the change in output resistance of the sensing layer, here deposited on an interdigital microelectrode [94].

2.7 Properties of a gas sensor

The performances of these chemiresistive sensors are characterized by various parameters. For realization of practical and optimal gas detection, a gas sensor must meet key performance and reliability related requirements: sensitivity, selectivity, speed (response and recovery time) and stability. Other parameters are linear range, stability (aging, low drift,

interfering gases), low noise, low power consumption, low detection limits (LOD) of an analyte and low sensitivity to humidity in the atmosphere [96, 119, 128, 132, 134, 136, 143-147]. The said properties of a sensor depend on the structural features, the presence and state of catalytically active surface dopants, and the working temperature [94].

$$Q(\%) = 100\ X\ \frac{{}^{dy}/_{dx'}}{{}^{dy}/_{dx}} \qquad (2.1.15)$$

2.7.1 Sensitivity

The ability of the sensor to detect a given concentration of a gaseous molecule (analyte) is known as the sensor response S (%) and is defined as the ratio between the change in the resistance value of the sensor in the presence and absence of gas molecules with respect to the initial resistance of the sensor:

$$S(\%) = \frac{[R_g - R_{air}]}{R_{air}}\ X\ 100 \qquad (2.1.16)$$

where R_{air} is the resistance of the sensor in air and R_g is the resistance of the sensor in the presence of target gas [94, 95, 104, 117, 119, 132]. Sensitivity (S) can also be defined as the change of measured signals per analyte concentration unit. Normally, this value can be extracted from the slope of a calibration plot, i.e. a plot of concentration vs. sensor response [106, 119].

2.7.2 Response and recovery time

These are key parameters used to determine the rate of sensor response [117, 119]. The response time is the time taken to reach 90 % of the full response after incremental exposure to the analyte while the recovery time is the time taken to return to 90% after the analyte is removed [94, 117, 119, 132]. Long recovery times can be due to strong analyte sorption or a chemical reaction between the analyte and the receptor [127]. The sensor can however be regenerated under modified operation conditions, *e.g.* UV irradiation.

2.7.3 Selectivity

Selectivity (*Q*) is the ability of a sensor to discriminate a measure of the response to a specific group of analytes or even to a single analyte among a mixture of analytes [94, 119]. High

selectivity is required because the adsorption and the catalytic reaction of species other than the target gas leads to cross-sensitivity [95]. It is defined by the cross sensitivity to all other analytes which occur with the concentration x'.

2.7.4 Stability

It is an important measurand which characterises the quality of a signal over time [119]. Gas sensors should display high chemical stability upon interaction with gases and solutions to avoid corrosion, high thermo-dynamic stability (a necessity for gas sensing materials operating at high temperature), low drift and should produce a stable and reproducible signal for the period of at least 2-3 years [128].

2.8 Improvement of gas sensing performance

The requirements to be met by a chemi-risistive gas sensor are all related to the sensing material [119]. Therefore, the selection and processing of the sensing material have a significant role in the research and development of gas sensors [122, 124]. The nature of the surface of the sensor is one of the parameters that heavily influence its interaction with gaseous species because the change in the concentration of conduction electrons is due to surface chemical reactions [134, 141]. Both experimental and theoretical studies have demonstrated that during gas sensing; processes like combustion, electrical response, interaction with water vapour and adsorbed species occurred at different surface sites. This leads to differences in the interaction of various gases with these surface sites [134]. Therefore, modification of the surface can improve gas sensing parameters by acting as adsorption sites for analytes, surface catalysts, or as elements that improve the thermal stability of the nanostructures, or stabilizes a specific valence state and increases the electron exchange rate or stabilizes the catalyst against reduction [122, 124, 134, 148].

2.8.1 Sensitivity

2.8.1.1 Functionalization

A gas sensing matrix with elements of different physical–chemical properties gives additional factors influencing the important parameters of a given sensor [104]. For an example, these additives can change parameters such as concentration of charge carriers; chemical and physical properties of the metal oxide matrix; electronic and physical-chemical properties of the surface (energetic spectra of surface states, energy of adsorption and desorption, sticking coefficients, etc.); surface potential and inter-crystallite barriers; phase composition; sizes of

crystallites, etc. [134]. Nanoparticles of noble metals have been deposited on the surface of the gas sensing material to assume the role of surface sites for adsorbates, promoters for surface catalysis, or as elements promoting the improvement in thermal stability of film nanostructure by acting as inhibitors or activators of the surface reactions [134, 141, 149].

2.8.1.2 Surface properties

Density of surface states, defined as the localized electronic energy level at the surface [133] is an important surface parameter for solid-state gas sensors. Low concentrations of density of surface states provide thermal and temporal stability of parameters required for effective operation of solid-state gas sensors [128]. For adsorption type gas sensors, smaller activation energy of chemisorption and higher activation energy of desorption lead to a bigger gas-sensing effect [128].

2.8.1.3 Structure

Nano- and polycrystalline materials have been the most used in gas sensor applications due to large surface area, cheap design technology, and stability of both structural and electro-physical properties. A combination of a large surface area to volume ratio and a grain size (D) comparable to the Debye length of electrons, LD (or thickness of surface space charge layer, LS) are an important benefit in the development of highly sensitive gas sensors [95, 128].

2.8.1.4 Grain size and film thickness

Reduction of grain size to the nanometer level leads to the dramatic increase of density of surface sites available for gas adsorption in nanocrystalline materials, leading to enhanced gas sensing properties [104, 132, 150]. When the grain size is smaller than the critical value (Dc), sensitivity increases sharply [141, 150]. Dc can be changed to increase the sensitivity of a sensor through the thickness of surface space charge layer of active material which is a function of the concentration of electron donors [151]. Thin films with smaller grain size are desirable as the increased surface to volume ratio, carrier concentration and enhanced catalytic activity, facilitate its interaction with a larger number of gas molecules.

2.8.1.5 Ligand exchange

The length of surface ligand is known to play an important role in charge transfer and transport [152]. Henceforth, the often bulky and electrically insulating as-synthesized ligands

need to be replaced with a shorter functional group to improve the conductivity [85, 152-154] as they hinder the mobility of charge carriers [155]. Ligand exchange has been extensively applied in solution with pyridine, aliphatic amines, thiols, thiophenes; or in the solid state with crosslinking agents like dithiols or diamines has been extensively applied [85].

2.8.2 Selectivity

The gas detection community is faced with one of the most difficult challenges in finding specific materials that have both high sensitivity and good selectivity to target analyte [156]. Semiconducting metal chalcogenides have good sensitivity, but like all the other chemical sensors tend to respond to a group of reducing or oxidizing gases in a similar manner [157]. Concerted efforts have been put into improving selectivity of chemical sensors as this problem cannot be eliminated completely.

2.8.2.1 Chemical sensor arrays

Use of chemical sensor arrays is one of the approaches that have been widely studied and developed to improve selectivity to different odors, chemical components and vapors [158]. Unlike the 'lock-and-key' design where a sensor responds in a highly selective manner to a specific target compound or class of target compounds; sensor arrays make use of less specific elements that respond to a broad range of gaseous molecules. The collective response of the different elements provides a fingerprint for an analyte of interest [96, 146, 156, 159, 160]. The resulting signal is processed in order to classify and identify the stimulus from the array output data either statistically using standard chemometric methods or through hardware and/or software implementations of neural networks [156].

2.8.2.2 Tristimulus analysis

This is another tool used to overcome the absence of specificity of the sensors. It is basically a mathematical treatment that allows the calculation of the coordinates (in a tristimulus space) that univocally represent a set of responses in a bi-dimensional graph [161-163]. The approach relies on the different sensitivities of the sensors to the same analyte. In this project it was used to quantify a collective response proportional to analyte concentration from a set of three sensors.

2.8.3 Response and recovery

While thermal or optical energy have successfully improved gas sensor recovery, the response has been compromised due to the increased desorption rate [149]. Noble metal functionalization can change the energy of adsorption and desorption *e.g.* Ag nanowire functionalization of WS_2. Both response and recovery were significantly improved upon exposure to NO_2, while an incomplete recovery was exhibited with pristine WS_2 [149]. The catalytic effect of the metal improves both response and recovery by acting as a surface catalyst thereby reducing the energy required for reacting with gas molecules [122, 128, 134, 141, 148, 149].

2.9 Operation conditions and gas detection

The surrounding atmosphere and application determine the selection of gas sensing material.

2.9.1 Operating temperature

It impacts on the receptor function of a sensor by affecting the chemical dynamics at the gas-solid interface. This in turn influences important sensing parameters such as response, selectivity, stability, and recovery times [164].

2.9.2 Humidity

The level of humidity in the atmosphere largely influences the sensor response because the water vapour absorbed on the surface affects the electronic and ionic conducting properties of the gas sensing material. Therefore, the response of a chemiresistive gas sensor surface highly depends on the composition of atmosphere; especially water (wet atmosphere) and oxygen (dry atmosphere) which defines the baseline for the sensor response and calibration [164].

2.10 Fabrication and design of gas sensing devices

The constituent materials are deposited onto a substrate previously coated with a pair of gold electrodes by wet or dry methods to produce thin and thick films [129, 130]. The substrate can be conventional silicon wafer, ceramic, polymer, cellulose-based paper, sapphire, aluminium or h-BN, etc. [95, 124, 165].

2.10.1 Wet chemical methods

The processing of nanostructures and films are separated. This allows for synthesis of tailored and stabilized nanostructures prior to their assembly in films. The nanostructures are dispersed in a solvent, typically via ultrasonication and deposited onto electrodes by deposition techniques like screen printing, drop-, dip-, and spin-coating and doctor blading to produce highly sensitive and reasonably stable films [123, 124, 136, 166]. Thick films with particulate morphology are obtained, while porous films are also possible through calcination/sintering at elevated temperatures [124]. However, processing of the sensing films by these methods generally presents poor reproducibility due to crack formation during evaporation of solvents and additives, and limited control over the film thickness and porosity thereby impeding sensor response optimization [124].

2.10.2 Dry methods

These methods involve direct assembly of nanostructured films from the gas phase thereby offering rapid and scalable synthesis of semiconductor sensing films. They allow control over both film structural parameters (pore size, film morphology, surface accessibility) and the material properties (crystal size, agglomeration, sinter necks) Control over thickness and porosity of the films is superior to wet methods. Dry deposition of the films is either by chemical or vapor deposition methods e.g. classical chemical vapor deposition (CVD) or sputtering and aerosol technologies [124]. However, one of the main challenges lies in the stabilization of the mostly physically bounded, porous films as their mechanical stability is generally poor [124].

2.11 References

[1] Xia, Y., Xiong, Y., Lim, B. and Skrabalak, S. E. (2009). Angew. Chem. Int. Ed. 48, 60 – 103.

[2] Smith, A. M. and Nie, S. (2010). Acc. Chem. Res. 43 (2), 190-200.

[3] Chang, J. and Waclawik, E. R. (2014). RSC Adv. 4, 23505–23527.

[4] Zhang, J., Huang, F. and Lin, Z. (2010). Nanoscale 2, 18-34.

[5] El-Sayed, M. A. (2004). Acc. Chem. Res. 37, 326-333.

[6] de Mello Donegá, C., Hickey, S. G., Wuister, S. F., Vanmaekelbergh, D. and Meijerink, A. (2003). J. Phys. Chem. B 107, 489-496.

[7] Alivisatos, A. P. (1996). J. Phys. Chem. 100, 13226-13239.

[8] Trindade, T., O'Brien, P. and Pickett, N. L. (2001). Chem. Mater. 13, 3843-3858.
[9] Zhang, J. Z. (2000). J. Phys. Chem. B 104, 7239-7253.
[10] Hines, D. A. and Kamat, P. V. (2014). ACS Appl. Mater. Interfaces 6, 3041-3057.
[11] Klimov, V. I. (2007). Annu. Rev. Phys. Chem. 58, 635-673.
[12] Koole, R., Groeneveld, E., Vanmaekelbergh, D., Meijerink, A. and de Mello Donegá, C. (2014). Nanoparticles, Springer, 13-51.
[13] Vanmaekelbergh, D. and Liljeroth, P. (2005). Chem. Soc. Rev. 34, 299-312.
[14] Wells, B. (2015). Bandgap measurements of nonspecular materials using a bifurcated fiber optic method of diffuse reflectance. Oregon State University, Department of Physics.
[15] Airo, M. A., Gqoba, S., Otieno, F., Moloto, M. J. and Nosipho Moloto. (2016). RSC Adv. 6, 40777-40784.
[16] Sun, Y., Wang, D. and Shuai, Z. (2016). J. Phys. Chem. C 120, 21866-21870.
[17] Díaz, J. G. and Bryant, G. W. (2007). Physical Review B 75, 245433, 1-13.
[18] Tongay, S., Zhou, J., Ataca, C., Lo, K., Matthews, T. S., Li, J., Grossman, C. and Wu, J. (2012). Nano Lett. 12, 5576-5580.
[19] Lezama, I. G., Arora, A., Ubaldini, A., Barreteau, C., Giannini, E., Potemski, M. and Morpurgo, A. F. (2015). Nano Lett. 15, 2336-2342.
[20] Jun, Y-W., Choi, J-S. and Cheon, J. (2006). Angew. Chem. Int. Ed. 45, 3414-3439.
[21] Cheong, S., Watt, J. D. and Tilley, R. D. (2010). Nanoscale 2, 2045-2053.
[22] Kwon, S. G. and Hyeon, T. (2008). Acc. Chem. Res. 41 (12), 1696-1709.
[23] Shim, M. and Guyot-Sionnest, P. (2000). Nature 407 (26), 981-983.
[24] Tonti, D., Varsano, F., Decker, F., Ballif, C., Regula, M. and Remškar, M. (1997). J. Phys. Chem. B 101, 2485-2490.
[25] Sajanlal, P. R., Sreeprasad, T. S., Samal, A. K. and Pradeep, T. (2011). Nano Reviews 2: 5883-DOI: 10.3402/nano.v2i0.5883.
[26] Marzán, L. M. L. (2006). J. Mater. Chem. 16, 3891-3892.
[27] Xia, Y., Xia, X. and Peng, H-C. (2015). J. Am. Chem. Soc. 137, 7947-7966.
[28] Min, Y., Akbulut, M., Kristiansen, K., Golan, Y. and Israelachvili, J. (2008). Nature Materials 7, 527-538.
[29] Kidd, D. W., Zhang, D. K. and Varga, K. (2016). Physical Review B 93, 125423, 1-10.
[30] Varghese, S. S., Varghese, S. H., Swaminathan, S., Singh, K. K. and Mittal, V. (2015) Electronics 4, 651-687.
[31] Huo, N., Yang, S., Wei, Z., Li, S-S., Xia, J-B. and Li, J. (2014). Sci. Rep. 4, 5209; DOI:10.1038/srep05209.

[32] Schwierz, F. (2016). Electronics 5 (30), 1-4.

[33] Choi, J., Zhang, H. and Choi, J. H. (2016). ACS Nano 10, 1671-1680.

[34] Das, S., Kim, M., Lee, J. and Choi, W. (2014). Critical Reviews in Solid State and Materials Sciences 9, 231-252.

[35] O'Brien, M., Lee, K., Morrish, R., Berner, N. C., McEvoy, N., Wolden, C. A. and Duesberg, G. S. (2014). Chemical Physics Letters 615, 6-10.

[36] Lee, J. Y., Shin, J-H., Lee, G-H. and Lee, C-H. (2016). Nanomaterials 6 (193), 1-18.

[37] Withers, F., Del Pozo-Zamudio, O., Mishchenko, A., Rooney, A. P., Gholinia, A., Watanabe, K., Taniguchi, T., Haigh, S. J., Geim, A. K., Tartakovskii, A. I. and Novoselov, K. S. (2015). Nature Materials 14, 301-306.

[38] Xue, B., Xu, F., Wang, B. and Dong, A. (2016). CrystEngComm 18, 250-256.

[39] Batabyal, S. K., Lu, S. E. and Vittal, J. J. (2016). Cryst. Growth Des. 16, 2231-2238.

[40] Balakrishnan, N., Staddon, C. R., Smith, E. F., Stec, J., Gay, D., Mudd, G. W., Makarovsky, O., Kudrynskyi, Z. R., Kovalyuk, Z. D., Eaves, L., Patanè, A. and Beton, P. H. (2016), 2D Mater. 3 (025030), 1-8.

[41] Dhanabalan, S. C., Ponraj, J. S., Zhang, H., Bao, Q. (2016). Nanoscale 8, 6410-6434.

[42] Chikan, V. and McLaurin, E. J. (2016). Nanomaterials 85, 1-9.

[43] de Mello Donegá, C. (2011). Chem. Soc. Rev. 40, 1512–1546.

[44] Rempel, J. Y., Bawendi, M. G. and Jensen, K. F. (2009). J. Am. Chem. Soc. 131, 4479-4489.

[45] van Embden, J., Chesman, A. S. R. and Jasieniak, J. J. (2015). Chem. Mater. 27, 2246-2285.

[46] Sebastian, V., Smith, C. D. and Jensen, K. F. (2016. Nanoscale 8, 7534-7543.

[47] Jun, Y-W. Choi, J-S. and Cheon, J. (2006). Angew. Chem. Int. Ed. 45, 3414-3439.

[48] Xing, Y., Zhang, H., Song, S., Feng, J., Lei, Y., Zhao, L. and Li. M. (2008). Chem. Commun., 1476-1478.

[49] Kim, Y. H., Lee, J. H., Shin, D-W., Park, S. M., Moon, J. S., Nam, J. G. and Yoo, J-B. (2010). Chem. Commun. 46, 2292-2294.

[50] Acharya, S., Sarkar, S. and Pradhan, N. (2012). J. Phys. Chem. Lett. 3, 3812-3817.

[51] Chen, X., Zhang, Z., Zhang, X., Liu, J. and Qian, Y. (2005). Chemical Physics Letters 407, 482-486.

[52] Altavilla, C., Sarno, M. and Ciambelli, P. (2011). Chem. Mater. 23, 3879-3885.

[53] Jiang, Z., Zhang, Y., Yang, G., Yang, K., Zhang, S., Yu, L. and Zhang, P. (2016). Tribol Lett 61(24), 1-14.

[54] Fu, H. and Tsang. Nanoscale. (2012) 4, 2187-2201.
[55] Han, J. H., Lee, S. and Cheon, J. (2013). Chem. Soc. Rev. 42, 2581-2591.
[56] Kumar, S. and Nann. T. (2006). Small 2(3), 316-329.
[57] Hu, M. Z. and Zhu, T. (2015). Nanoscale Research Letters 10 (469), 1-15.
[58] Vanmaekelbergh, D. and Liljeroth, P. (2005). Chem. Soc. Rev. 34, 299-312.
[59] Cozzoli, P. D., Pellegrino, T. and Manna, L. (2006). Chem. Soc. Rev. 35, 1195-1208.
[60] Cara, C., Musinu, A., Mameli, V., Ardu, A., Niznansky, D., Bursik, J., Scorciapino, M. A., Manzo, G. and Cannas, C. (2015). Cryst. Growth Des. 15, 2364-2372.
[61] Demazeau, G. (1999). J. Mater. Chem., 1999, 9, 15-18.
[62] Zhu, Y., Mei, T., Wanga, Y. and Qian, Y. (2011). J. Mater. Chem. 21, 11457-11463.
[63] Cao, S., Zhao, C., Peng, L. (2016). Materials Letters 164, 452-455.
[64] Therese, H. A., Li, J., Kolb, U. and Tremel, W. (2005). Solid State Sciences 7, 67-72.
[65] Ratha, S. and Rout, C. S. (2013). ACS Appl. Mater. Interfaces 5, 11427-11433.
[66] Cao, S., Liu, T., Hussain, S., Zeng, W., Peng, X. and Pan, F. (2014). Materials Letters 129, 205-208.
[67] Wu, J. and Fu, X. (2007). Materials Letters 61, 4332-4335.
[68] Chen, W., Bovin, J-O., Joly, A. G., Wang, S., Su, F. and Li, G. (2004). J. Phys. Chem. B 108, 11927-11934.
[69] Chen, L-Y., Zhang, Z-D. and Wang, W-Z. (2008). J. Phys. Chem. C 112, 4117-4123.
[70] Du, W., Zhu, J., Li, S. and Qian, X. (2008). Cryst. Growth Des. 8 (7), 2130-2136.
[71] Zhu, H., Wang, X., Yang, W., Yang, F. and Yang, X. (2009). Materials Research Bulletin 44, 2033-2039.
[72] Rengaraj, S., Venkataraj, S., Tai, C-W., Kim, Y., Repo, E. and Sillanpää, M. (2011). Langmuir 27, 5534-5541.
[73] Gawande, M. B., Shelke, S. N., Zboril, R. and Varma, R. S. (2014). Acc. Chem. Res. 47, 1338-1348.
[74] Avivi (Levi), S., Palchik, O., Palchik, V., Slifkin, M. A., Weiss, A. M. and Gedanken, A. (2001). Chem. Mater. 13, 2195-2200.
[75] Cao, G., Zhao, Y. and Wu, Z. (2009). Journal of Alloys and Compounds 472, 325-327.
[76] Chou, S. S., Huang, Y-K., Kim, J., Kaehr, B., Foley, B. M., Lu, P., Dykstra, C., Hopkins, P. E., Brinker, C. J., Huang, J. and Dravid, V. P. (2015). J. Am. Chem. Soc. 137, 1742-1745.
[77] Finney, E. E. and Finke, R. G. (2008). Journal of Colloid and Interface Science 317, 351-374.

[78] Thanh, N. T. K., Maclean, N. and Mahiddine. S. (2014). Chem. Rev. 114, 7610-7630.

[79] Kwon, S. G. and Hyeon, T. (2011). Small 7 (19), 2685-2702.

[80] Polte, J. (2015). CrystEngComm 17, 6809-6830.

[81] Park, J., Lee, E., Hwang, N-M., Kang, M., Kim, S. C., Hwang, Y., Park, J-G., Noh, H-J., Kim, J-Y., Park, J-H. and Hyeon, T. (2005). Angew. Chem. Int. Ed. 44, 2872-2877.

[82] Viswanatha, R. and Sarma, D. D. Growth of Nanocrystals in Solution. 139-170.

[83] Yu, H., Gibbons, P. C., Kelton, K. F. and Buhro, W. E. (2001). J. Am. Chem. Soc. 123, 9198-9199.

[84] Baginskiy, I., Lai, T-C., Cheng, L-C., Chan, Y-C., Yang, K-Y., Liu, R-S., Hsiao, M., Chen, C-H., Hu, S-F., Her, L-J., and Tsai, D. P. (2013). J. Phys. Chem. C 117, 2396−2410.

[85] Lefrançois, A., Pouget, S., Vaure, L., Lopez-Haro, M., and Reiss, P. (2016). ChemPhysChem 3, 17 (5), 654-659.

[86] Sowers, K. L., Swartz, B. and Krauss, T. D. (2013). Chem. Mater. 25, 1351-1362.

[87] You, H., Yang, S., Dinga, B. and Yang, H. (2013). Chem. Soc. Rev. 42, 2880-2904.

[88] Nair, P. S., Fritz, K. P. and Scholes, G. D. (2007). Small 3 (3), 481-487.

[89] Chen, H. M. and Liu, R-S. (2011). J. Phys. Chem. C 115, 3513-3527.

[90] Wu, J. and Fu, X. (2007). Materials Letters 61, 4332-4335.

[91] Xiong, Y., Xie, Y., Du, G. and Tian, X. (2002). J. Mater. Chem. 12, 98-102.

[92] Zhang, B., Guo, F., Yang, L. and Wang, J. (2014). Journal of Crystal Growth 405,142-149.

[93] Gurlo, A. (2011). Nanoscale 3, 154-165.

[94] Franke, M. E., Koplin, T. J. and Simon, U. (2006). Small 2 (1), 36-50.

[95] Park, C. O. and Akbar, S. A. (2003). Journal of Materials Science 38**,** 4611-4637.

[96] Capone, S., Forleo, A., Francioso, L., Rella, R., Siciliano, P., Spadavecchia, J., Presicce, D. S. and Taurino, A. M. (2003). Journal of Optoelectronics and Advanced Materials 5 (5), 1335-1348.

[97] Kanan, S. M., El-Kadri, O. M., Abu-Yousef, I. A. and Kanan, M. C. (2009). Sensors 9, 8158-8196.

[98] Calvi, A., Ferrari, A., Sbuelz, L., Goldoni, A. and Modesti, S. (2016). Sensors 16 (731), 1-9.

[99] Vuong, N. M., Chinh, N. D., Huy, B. T. and Lee, Y-I. (2016). Sci. Rep. 6, 26736; doi: 10.1038/srep26736.

[100] Sun, Y-F., Liu, S-B., Meng, F-L., Liu, J-Y., Jin, Z., Kong, L-T. and Liu, J-H. (2012). Sensors 12, 2610-2631.

[101] Suchorska-Woźniak, P., Rac, O., Fiedot, M. and Teterycz, H. (2014). Sensors 14, 20480-20499.
[102] Li, B., Sauve´, G., Iovu, M. C., Jeffries-EL, M., Zhang, R., Cooper, J., Santhanam, S., Schultz, L., Revelli, J. C., Kusne, A. G., Kowalewski, T., Snyder, J. L., Weiss, L. E., Fedder, G. K., McCullough, R. D. and Lambeth, D. N. (2006). Nano Letters 6 (8), 1598-1602.
[103] Chiu, S-W. and Tang, K-T. (2013). Sensors 13, 14214-14247.
[104] Zhang, J., Liu, X., Neri, G. and Pinna, N. (2016). Adv. Mater. 28, 795-831.
[105] Gaiardo, A., Fabbri, B., Guidi, V., Bellutti, P., Giberti, A., Gherardi, S., Vanzetti, L., Malagù, C. and Zonta, G. (2016). Sensors 16, 296, 1-19.
[106] Huang, C., Wang, Z., Ni, Y., Wu, H. and Chen, S. (2017). RSC Adv. 7, 23486-23493.
[107] Neri, G. (2017). Chemosensors 5, (21), 1-20.
[108] Liu, L., Kumar, S. B., Ouyang, Y. and Guo, J. (2011). IEEE Transactions on Electron Devices 58 (9), 3042-3047.
[109] Acharya, S., Dutta, M., Sarkar, S., Basak, D., Chakraborty, S. and Pradhan, N. (2012). Chem. Mater. 24, 1779-1785.
[110] Wu, Z., Fang, B., Bonakdarpour, A., Sun, A., Wilkinson, D. P. and Wang, D. (2012). Applied Catalysis B: Environmental 125, 59-66.
[111] Kulkarni, G. S., Reddy, K., Zhong, Z. and Fan, X. (2014). Nat. Commun. 5:4376 doi: 10.1038/ncomms5376.
[112] Zhao, X., Xia, C., Wang, T. and Dai, X. (2016). Journal of Alloys and Compounds 654, 574-579.
[113] Scrace, T., Tsai, Y., Barman, B., Schweidenback, L., Petrou, A., Kioseoglou, G., Ozfidan, I., Korkusinski, M. and Hawrylak, P. (2015). Nature Nanotechnology 10, 603-607.
[114] Zhou, Y., Deng, B., Zhou, Y., Ren, X., Yin, J., Jin, C., Liu, Z. Peng, H. (2016). Nano Lett. 16, 2103-2107.
[115] Pawbake, A. S., Waykar, R. G., Late, D. J. and Jadkar, S. R. (2016). ACS Appl. Mater. Interfaces 8 (5), 3359-3365.
[116] Jha, R. K. and Guha, P. K. (2016). Nanotechnology 27, 475503, 1-11.
[117] Korotcenkov, G. (2008). Materials Science and Engineering R 61, 1-39.
[118] Thamri, A., Baccar, H., Struzzi, C., Bittencourt, C., Abdelghani, A. and Llobet, E. (2016). Sci. Rep. 6, 35130; doi: 10.1038/srep35130.
[119] Kannan, P. K., Late, D. J., Morgan, H. and Rout, C. S. (2015). Nanoscale, 7, 13293-13312.

[120] Shaik, M., Rao, V. K., Gupta, M., Murthy, K. S. R. C. and Jain, R. (2016). RSC Adv. 6, 1527-1534.

[121] Neri, G. (2015). Chemosensors 3, 1-20.

[122] Shankar, P., Rayappan, J. B. B. (2015). Science Jet 4 (126), 1-18 and references therein.

[123] Yang, W., Gan, L.; Li, H. and Zhai, T. (2016). Inorg. Chem. Front. 3, 433-451.

[124] Tricoli, A., Righettoni, M. and Teleki, A. (2010). Angew. Chem. Int. Ed. 49, 7632-7659.

[125] Reungchaiwat, A., Wongchanapiboon, T., Liawruangrath, S. and Phanichphant, S. (2007). Sensors 7, 202-213.

[126] Wang, L-C., Tang, K-T., Teng, I-J., Kuo, C-T., Ho, C-L., Kuo, H-W., Su, T-H., Yang, S-R., Shi, G-N. and Chang, C-P. (2011). Sensors 11, 7763-7772.

[127] Marr, I., Groß, A. and Moos, R. (2014). J. Sens. Sens. Syst. 3, 29-46.

[128] Korotcenkov, G. (2007). Materials Science and Engineering B 139, 1–23.

[129] Fine, G. F., Cavanagh, L. M., Afonja, A. and Binions, R. (2010). Sensors 10, 5469-5502.

[130] Wang, Z., Zhao, K., Li, H., Liu, Z., Shi, Z., Lu, J., Suenaga, K., Joung, S-K., Okazaki, T., Jin, Z., Gu, Z., Gao, Z., Iijima, S. (2011). J. Mater. Chem. 21, 171-180.

[131] Arafat, M. M., Dinan, B., Akbar, S. A. and Haseeb, A. S.M. A. (2012). Sensors 12, 7207-7258.

[132] Huang, J. and Wan, Q. (2009). Sensors 9, 9903-9924.

[133] Berna, A. (2010). Sensors 10, 3882-3910.

[134] Korotcenkov, G. (2005). Sensors and Actuators B 107, 209-232.

[135] Mirica, K. A., Azzarelli, J. M., Weis, J. G., Schnorr, J. M. and Swager, T. M. (2013). PNAS, E3265-E3270.

[136] Lee, D-D. and Lee, D-S. (2001). IEEE SENSORS Journal 1 (3), 214-224.

[137] Batzill, M. (2006). Sensors 6, 1345-1366.

[138] Ponzoni, A., Baratto, C., Cattabiani, N., Falasconi, M., Galstyan, V., Nunez-Carmona, E., Rigoni, F., Sberveglieri, V., Zambotti, G. and Zappa, D. (2017). Sensors 17, 714, 1-27.

[139] Zhao, X., Cai, B., Tang, Q., Tong, Y. and Liu, Y. (2014). Sensors 14, 13999-14020.

[140] Gu , H., Wang, Z. and Hu, Y. (2012). Sensors 12, 5517-5550.

[141] Yamazoe, N. (2005). Sensors and Actuators B 108, 2-14.

[142] Strelcov, E., Lilach, Y. and Kolmakov, A. (2009). Nanoletters, 9 (6), 2322-2326.

[143] Moseley, P. T. (1997). Sci. Technol. 8, 223-237.

[144] Llobet, E. (2013). Sensors and Actuators B 179, 32-45.
[145] Yue, Q., Shao, Z., Chang, S. and Li, J. (2013). Nanoscale Research Letters 8 (425), 1-7.
[146] Some, S., Xu, Y., Kim, Y., Yoon, Y., Qin, H., Kulkarni, A. Kim, T. and Lee, H. (2013). Sci. Rep. 3, 1868, DOI:10.1038/srep01868.
[147] Chou, S. M., Teoh, L. G., Lai, W. H., Su, Y. H. and Hon, M. H. (2006). Sensors 6, 1420-1427.
[148] Jiménez-Cadena, G., Riu, J. and Rius. F. X. (2007). Analyst 132, 1083-1099.
[149] Ko, K. Y., Song, J-G., Kim, Y., Choi, T., Shin, S., Lee, C. W., Lee, K., Koo, J., Lee, H., Kim, J., Lee, T., Park, J. and Kim, H. (2016). ACS Nano 10, 9287-9296.
[150] Rella, R., Spadavecchia, J., Manera, M. G., Capone, S., Taurino, A., Martino, M., Caricato, A. P., and Tunno, T. (2007). Sensors and Actuators B 127 (2007) 426-431.
[151] Korotcenkov, G. and Cho, B. K. (2009). Sensors and Actuators B 142, 321-330.
[152] Kim, W. J., Kim, S. J., Lee, K-S., Samoc, M., Cartwright, A. N. Prasad, P. N. (2008). Nano Letters 8 (10), 3262-3265.
[153] Dasgupta, N. P., Sun, J., Liu, C., Brittman, S., Andrews, S. C., Lim, J., Gao, H., Yan, R. and Yang, P. (2014). Adv. Mater. 26, 2137-2184.
[154] Murray, C. B., Kagan, C. R. and Bawendi, M. G. (2000). Annu. Rev. Mater. Sci. 30, 545-610.
[155] Kumar, B. G. and Muralidharan, K. (2011). J. Mater. Chem. 21, 11271-11275.
[156] Doleman, B. J., Lonergan, M. C., Severin, E. J., Vaid, T. P. and Lewis, N. S., (1998). Anal. Chem. 70, 4177-4190.
[157] Sohn, J. C., Kim, S. E., Kim, Z. W. and Yu, Y. S. (2009). Transactions on electrical and Electronic Materials 10 (4), 135-139.
[158] Jeong, G-M., Nghia, N. T. and Choi, S.-I. (2015). Sensors 15, 656-671.
[159] Wilson, A. D. and Baietto, M. (2009). Sensors 9, 5099-5148.
[160] Khalaf, W., Pace, C. and Gaudioso, M. (2009). Sensors 9, 1678-1691.
[161] Rodrigues, R., and Hümmelgen, I. A. (2016). J Solid State Electrochem 20, 1295-1301.
[162] Greenshields, M. W. C. C., Mamo, M. A., Coville, N. J., Pimentel, I. C., Destro, J. G., Porsani, M. V., Bozza, A. and Hümmelgen, I. A. (2013). Sensors and Actuators B 188, 378-384.
[163] Cesarino, I. and Hümmelgen, I. A. (2015). J Solid State Electrochem 19, 3045-3050.
[164] Zhu, Y., Wang, X., Zhang, M., Cai, C. and Xie, L. (2016). Nano Research 9 (10), 2931-2937.

[165] Zhang, B., Guo, F., Yang, L. and Wang, J. (2014). Journal of Crystal Growth 405,142-149.
[166] Yan, H., Song, P., Zhang, S., Yang, Z. and Wang, Q. (2016). Journal of Alloys and Compounds 662, 118-125.

Chapter 3 : Synthesis, characterization and application of OLA/WS_2 nanostructures in chemical sensors for detection of solvent vapours

3.1 Passivation of the Surface of WS_2 Nanostructures with an Organic Capping Agent for Room Temperature NH_3 Sensing

3.1.1 Introduction

Several materials such as polymeric materials, nanoparticles and metal oxides have been employed as active layers in chemical sensors. Metal oxides remain the most widely used owing to their low cost of synthesis, small dimensions, high sensitivity and stability. However, these materials have drawbacks, as their high potential energy in the interface between grains increases the working temperature of the devices [1]. Two dimension (2D) layered semiconducting materials such as graphene and more recently transition metal dichalcogenides (TMDCs) have received interest in gas sensing application due to their morphology dependent properties [2]. TMDCs can be chemically represented as MX_2 where M is the metal of group IV (Mo, W) and X is the chalcogen such as S, Se or Te.

MoS_2 is by far the most studied TMDC; however, WS_2 exhibits a notably high ON/OFF current ratio, high thermal stability [3-5], absence of dangling bonds, electrostatic integrity [4] and wider operation temperature range as lubricants [3], a more favorable band structure, higher phonon-limited electron mobility making it an ideal candidate for room temperature gas sensing [5]. Bulk WS_2 has an exciton Bohr radius of 4 nm and exists as an indirect narrow band gap semiconductor of 1.4 eV [3, 4, 6- 9]. Meanwhile, its monolayer counterpart presents a wide direct band gap of 2.1 eV [3, 4, 6, 8, 9]. This band gap cross over is accompanied by new properties as a result of quantum confinement and edge effects [10]. A direct gap is said to exist at the K points of the Brillouin zone between the spin orbit split valence band and the doubly degenerate conduction band [8, 11] as predicted in Figure 3.1. Meanwhile, an indirect gap forms between a local conduction band minimum at a midpoint between Γ and K and the valence band maximum at the Γ point [11].

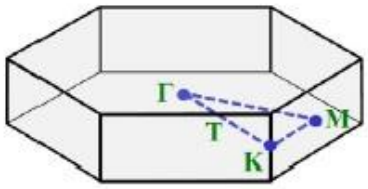


Figure 3.1: Brillouin zone for WS_2 monolayer [8].

The band gap of WS_2 is determined by crystallinity, size and shape [7]. An atomic layer of covalently bonded in-plane S-W-S atoms form the WS_2 crystal [4, 12] as presented in Figure 3.2 (a) and (b). These atoms are composed two sheets of S and one sheet of W atoms that are hexagonally packed [4, 13, 14]. Weak van der Waals forces bind together adjacent layers in WS_2 crystals [4, 11, 12, 15]. W is a group 6 metal with a trigonal-prismatic coordination which is directly related to the semiconducting properties of WS_2 [14].

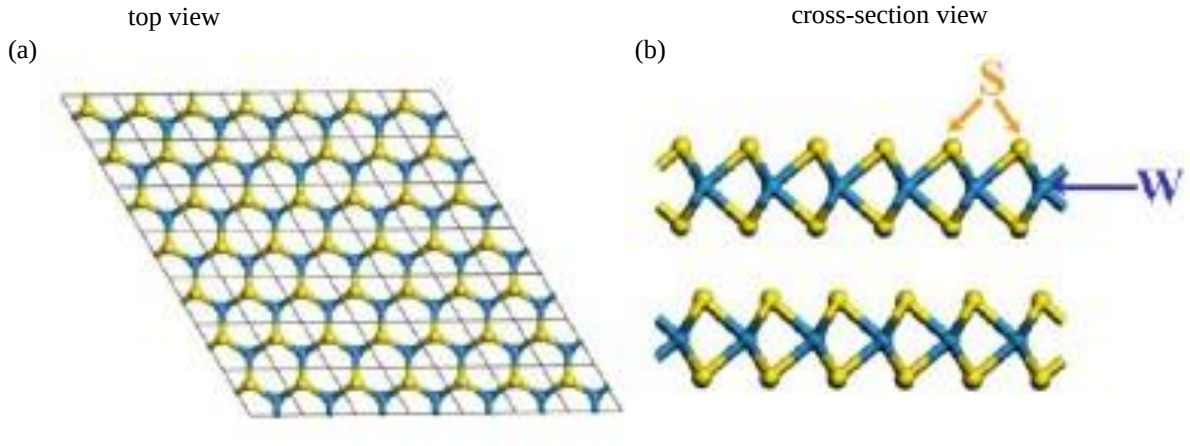


Figure 3.2: (a) top and (b) cross-section view of the WS_2 atomic structure [8].

Nanostructures of WS_2 have found application in lithium ion batteries [10, 11, 16], lubricants [6, 10, 11, 16], field emission [6], tips of scanning probes [10, 11], low power FETs [4, 6], optoelectronic devices [3, 4, 10, 11, 15], memory devices, chemical sensors [3, 4, 6, 15], photonic devices [3, 15], water splitting [6], shock absorbers [11], catalysis [11, 16] and hydrogen storage media [16]. The absence of interlayer coupling and the lack of inversion symmetry in the case of supported films in individual layer form of WS_2 results in optical and electronic properties that differ significantly from those of the bulk [7, 13]. WS_2 exhibits a

notably high ON/OFF current ratio, high thermal stability, absence of dangling bonds, electrostatic integrity and wider operation temperature range as lubricants [3, 4].

WS_2 nanomaterials from mono to multilayers have been grown using different methods of synthesis for application in gas sensing. It has been previously shown that 2D WS_2 has a fast response to ammonia gas with excellent selectivity and fast recovery coupled with a low limit of detection down to 0.8 ppm at room temperature [15, 17]. For the sake of practicality, the conductance of a sensor is expected to revert back to its original value during all response/recovery cycles which is an indicating that the sensing process is reversible for the sensor. The response time (T_{res}) and recovery time (T_{rec}) are defined as the time taken by the sensor to achieve 90% of its saturation after applying or switching off the gas [18, 19]. Huo, *et al.* demonstrated room temperature response by a field effect transistor (FET) based on mechanically exfoliated multilayer WS_2 nanoflakes to not only NH_3 (reducing gas) [3]. The room temperature gas sensing capability of WS_2 was also demonstrated by O'Brien and her co-workers when plasma assisted synthesized thin films were exposed to NH_3 gas [15]. A photodetector based on chemical vapour deposition (CVD) grown monolayer WS_2 displayed enhanced photoresponsivity during exposure to NH_3 gas which holds promise of room temperature sensing of this gas [17]. However, mono and few layered WS_2 nanosheets are quite unstable and highly prone to surface oxidation which induces degradation and the large amounts of WO_3 formed hamper sensitivity towards room temperature NH_3 sensing [20, 21]. This was evident with Jha, *et al*. who investigated the sensitivity of WO_3/WS_2 (70:30 wt.%) over a temperature range of 25 – 400 °C and concentration range of 250 –2000 ppm [22]. The sensor showed optimized performance to NH_3 when operated at 250 °C. To avoid high operating temperatures while maintaining high sensitivity to NH_3, limiting the amount of WO_3 is the best strategy as demonstrated by Perozzi, *et al.* [23].

A number of studies have shown that by forming a WS_2/metal oxide composite; the rate of the formation of the crystalline phase of WO_3 can be reduced thus not greatly affecting the sensing ability of WS_2 at room temperature [23-26]. Qin, *et al.* decorated mono or few layered WS_2 nanosheets with different amounts of TiO_2 quantum dots (QDs) for room-temperature NH_3 sensing [24]. The composites not only showed enhanced sensitivity of nearly 17 times higher than that of pristine WS_2 but also exhibited relatively significant long-term stability. Herein, an alternative strategy is pursued where colloidal WS_2 nanostructures are capped with organic molecules in solution using a non-aqueous solvent as the reaction medium. The soft organic shell that caps the particles provides protection from oxidation of

WS_2 (hard inorganic core). This strategy of using capping agents to protect the core NP from oxidation has been previously reported in several studies where the formation of large organic shells provided protection from oxidation of Cu NPs to CuO [27-37].

In addition to the prevention of oxidation, capping agents can:

(a) stabilize the high energy surface of the nanostructures,

(b) inhibit nanoparticle overgrowth, dissolution aggregation and control the structural characteristics of the resulted nanostructures,

(c) prevent degradation and thereby preserve the properties of the nanostructures,

(d) act as ligands to form complexes with original metal precursors and thereby affect their reduction kinetics,

(e) selective adsorption on particular crystallographic planes that induces the anisotropic growth of nanostructures,

(f) increase the compatibility with another phase,

(g) introduce additional functionalities or

(h) alter the surface the chemistry of NPs for specific applications [38-42].

Different morphologies with varying stabilities compared to few layer exfoliated nanosheets can be formed. The morphology, hence properties in the colloidal synthesis can be tweaked by varying reaction conditions such as the choice of precursors, concentration, capping agents, time and temperature made possible by the colloidal synthesis route [40, 43-45].

3.1.2 Experimental procedure

3.1.2.1 Chemicals and materials

Tungstic acid (H_2WO_4), thiourea ($CS(NH_2)_2$), oleylamine (OLA), ammonium hydroxide (NH_4OH), ethanol (CH_3CH_2OH), hexane (C_6H_{14}), chloroform ($CHCl_3$), toluene ($C_6H_5CH_3$), acetone ($(CH_3)_2CO$) and isopropyl alcohol (C_3H_8O) were all of analytical grade and were used as received. Interdigitated electrodes (IDE) of electroless nickel immersion gold (ENIG) patterned onto FR4 substrate were of the following specifications:

a) 18 pairs of 7.9 mm long ENIG interdigitated electrodes with 0.1 mm between electrode paths.

b) 9 pairs of 7.5 mm long ENIG interdigitated electrodes with 0. 3 mm between electrode paths.

3.1.2.2 Synthesis of OLA/WS_2 nanostructures from W: S (1:4)

For the synthesis of WS_2 nanostructures, a 1:4 ratio of H_2WO_4 to $CS(NH_2)_2$ was used. Light yellow OLA (20 mL) was heated and stirred continuously under N_2 gas flow for 15 min in a three-neck round bottom flask at room temperature [Figure 3.3 (a)]. White crystals of $CS(NH_2)_2$ (1.6016 g) were then added to the mixture [Figure 3.3 (b)] followed by the yellow crystals of H_2WO_4 (1.2492 g) and heated rapidly to 320 °C to allow for the decomposition of both precursors [Figure 3.3 (c)]. The reaction was characterized by several colour changes at different reaction temperatures indicating the formation of intermediates [Figure 3.3 (k)]. The mixture started boiling and turned milky yellow at about 150 °C [Figure 3.3 (d): $CS(NH_2)_2$ decomposes between 100 - 120 °C]. As the reaction progressed colour changed to grey, green, brown and ultimately thick black [150 - 320 °C, Figure 3.3 (e - j)] pointing out the formation of WS_2 nanostructures. The colour changes were punctuated by bubbling and foaming followed by smoking and squirting. The oil in the gas bubbler turned yellow [Figure 3.3 (l)] during the reaction and a white deposit was observed on the joints of the 3-neck round bottom flask [Figure 3.3 (j)]. The reaction was held at 320 °C for 15 min to allow for growth of nanostructures. Subsequent aliquots of the black product were taken at 20, 30, 45, 60, 90, 120, 150, 180 and 240 min. After cooling the samples for 5 min, ethanol was added to separate the colloids from the growth solution. The nanostructures were collected by centrifugation and excess OLA was washed off several times with a 1:1 ratio of ethanol to hexane. The black powders were dried at room temperature and re-dispersed in chloroform for further characterization.

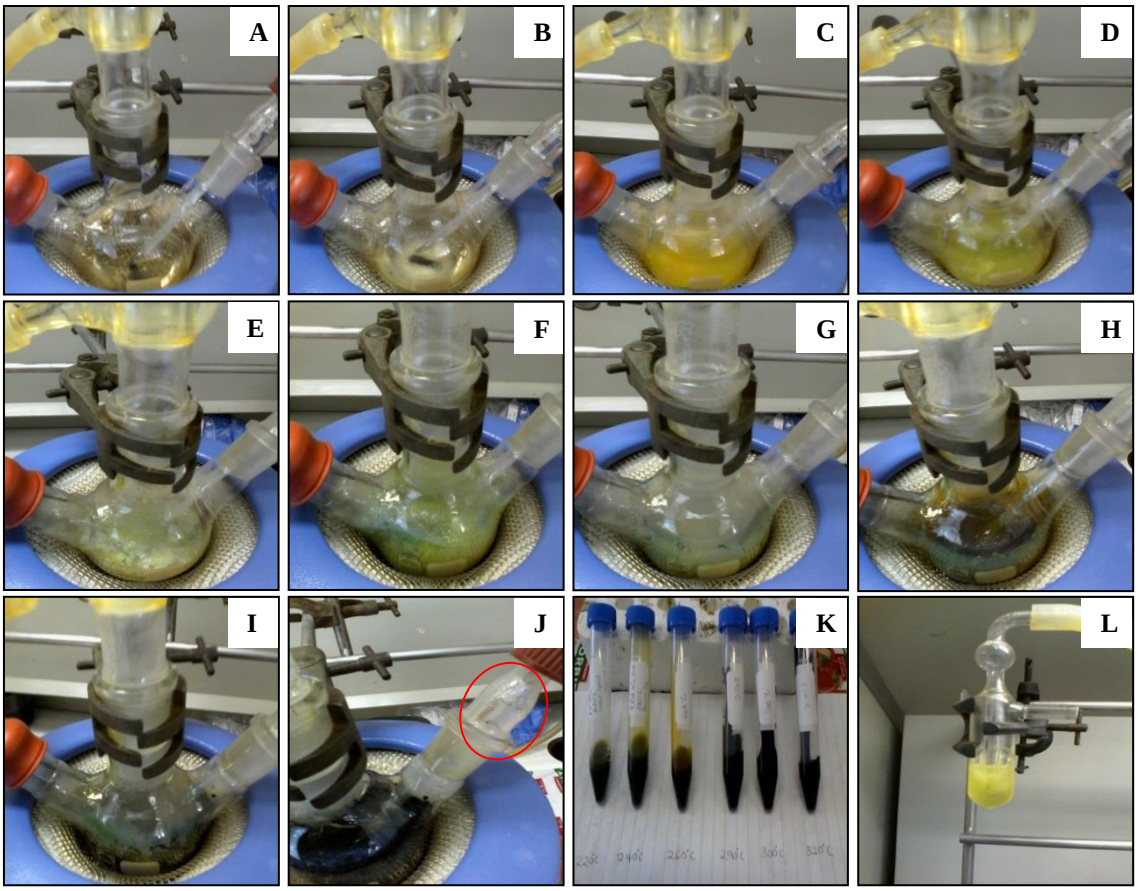


Figure 3.3: Diagrams showing different colour changes during growth of OLA/WS_2 nanostructures.

3.1.2.3. Preparation of nanostructure dispersions

OLA/WS_2 dispersions of each reaction time (15, 45, 60, 180 and 240 min) were prepared by placing 2.5 mg of the finely ground powder in 500 µL of toluene. The dispersions were sonicated at room temperature for 30 min.

3.1.2.4 Fabrication of OLA/WS_2 gas sensors

(i) Preparation of devices

Metal contacts were soldered onto IDEs [Figure 3.4 (b)] and cleaned by sonicating in acetone, water and isopropanol sequentially in a 135 W ultrasonic bath for 20 min each. The IDEs were air dried and finally placed in a UV ozone cleaner (Novascan; intense 185 nm and 254 nm ultraviolet light) for 30 min to remove organic residues.

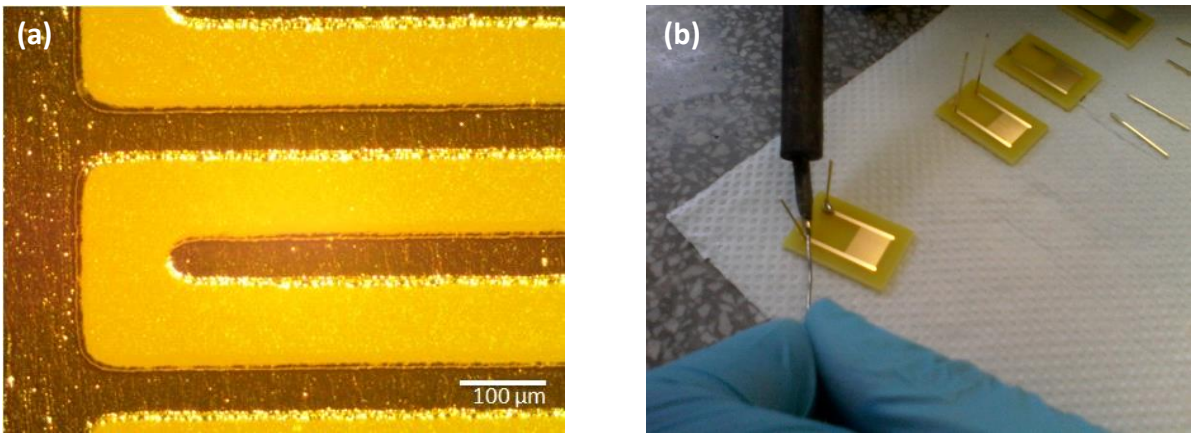


Figure 3.4: Optical image of the IDE is represented by (a) while (b) shows soldering of contacts onto IDEs.

(ii) Preparation of thick films

Films of OLA/WS_2 from each reaction time were deposited by drop casting 20 µL of the nanostructure dispersions onto the IDEs [Figure 3.5 (b)]. The IDEs were later dried in the oven at 100 ℃ under vacuum for 30 min.

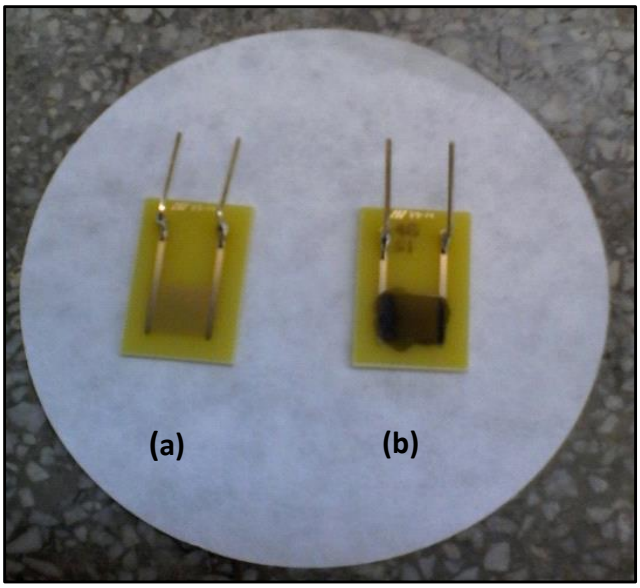


Figure 3.5: IDEs before (a) and after (b) deposition of OLA/WS_2 nanostructure film respectively.

3.1.2.5 Gas sensing measurements

All electrical measurements were performed in the dark at room temperature; and under dry N_2 environment unless otherwise stated. An LCR meter (Agilent 4284A 20 Hz – 1 MHz Precision LCR meter) attached to a computer interfaced with a GPIB was used for data acquisition. An operational voltage and frequency of 1000 mV and 10 kHz were selected respectively due to their higher signal-to-noise ratio. The systems were allowed to stand for 1h before measurements were performed. The change in conductance was monitored for 50 s, providing a stable baseline before the 1.5 µL of the analyte was introduced. The opening was sealed off immediately to prevent moisture from getting into the chamber. The devices were allowed to reach saturation point (around 300 s) before the next increment.

(i) Preparation of gas chambers

Clean and dry 1 L filtering Erlenmeyer flasks and 2.4 L glass bottles (Figure 3.6) were used as gas chambers. The chambers were covered with aluminium foil and black tape to create a dark environment. The aluminium foil was earthed to reduce its noise contribution.

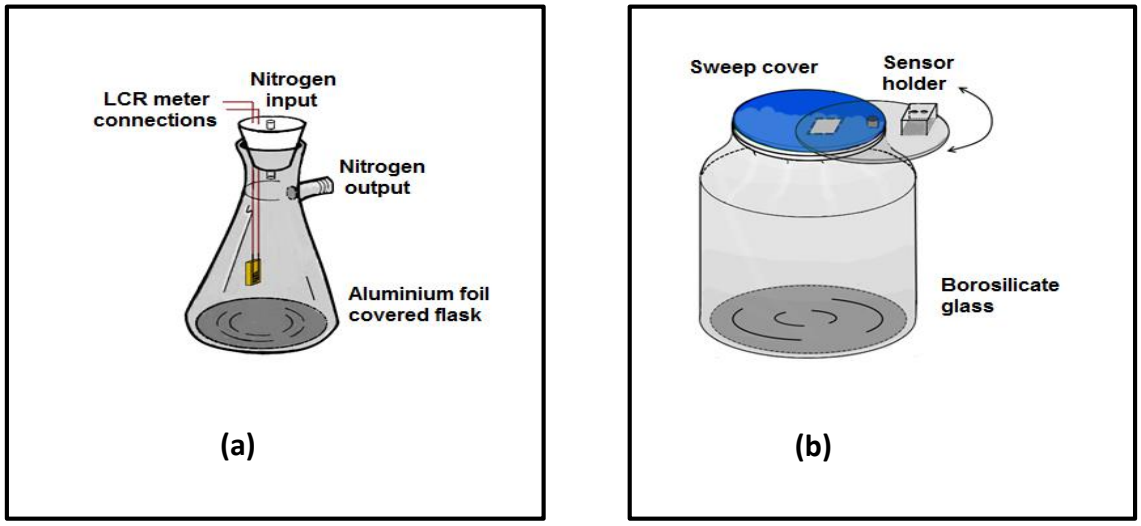


Figure 3.6: Schematic representation of gas chambers used in the gas sensing measurements: (a) the rubber stoppered filtering flask and (b) glass bottle with a sweep cover.

(ii) Sensitivity of OLA/WS_2 nanostructures to NH_3 vapour under dry N_2

The device was placed in a 1 L rubber stoppered filtering Erlenmeyer flask as represented in Figure 3.6 (a). The system was purged with dry N_2 for 30 min to reduce the relative humidity inside the system to less than 20%. NH_4OH volumes ranging from 1.5 to 6.0 µL were quickly

dropped into the sealed chamber at every 200 s using a micropipette. The time interval was enough to evaporate NH_4OH. The corresponding concentrations are summarized in Table 3.1.

Table 3.1: Volume and concentration of NH_4OH.

Volume (µL)	Concentration (ppm)
1.5	240
3	479
4.5	719
6	958

(iii) Response and recovery measurements of OLA/WS_2 nanostructures to NH_3 vapours under dry N_2

The change in conductance was monitored in a glove box under a constant flow of dry N_2 by switching the sensor response between the inside of the chamber (NH_3 vapour) and the outside of the chamber (dry N_2) using a rotating cap as represented in Figure 3.5 (b).

3.1.2.6 Characterization techniques

(i) Optical properties of the nanostructures

A toluene dispersion of OLA/WS_2 nanostructures was placed in a quartz cuvette with a 1 cm path length for the determination of its optical properties. A Specord 50 AnalytikJena UV-Vis spectrophotometer was used to carry out the absorption measurements while an Agilent Cary Eclipse fluorescence spectrometer was used to measure the photoluminescence of the nanostructures at room temperature in air with a wavelength of 300 nm excitation. The presence of the capping agent on the surface of the nanostructures was confirmed with a Bruker Tensor 27 FT-IR. The number of layers was estimated using spectra obtained through Raman from Bruker Senterra at 532 nm laser excitation wavelength. Infinity 1 software for the optics with a 50 × optical objective was used for viewing the samples at 0.2 mV laser power and integration power of 15 s.

(ii) Structural properties of the nanostructures

The stoichiometry and phase of the finely ground black powder of WS_2 were determined by a Bruker MeasSrv (D2-205530)/D2-205530 diffractometer using secondary graphite monochromated CuKα radiation (λ 1.54060 Å) at 30 kV/30 mA. The evolution of the

morphology was monitored by electron microscopy techniques: transmission electron microscope (TEM) by Technai G2 TEM Spirit operated at 200 kV; a high resolution electron microscope (HRTEM) by JEOL JEM-2100 operated at 200 kv and a scanning electron microscope (SEM) by FEI Nova NanoLab FIB/SEM. TEM samples were prepared by drop casting the sonicated chloroform dispersion onto the carbon-coated copper grids and allowed to dry at room temperature. Meanwhile, the finely ground black powder was spread out evenly on the sample holder. Energy dispersive X-ray (EDX) spectroscopy was used to analyze the elements on the surface of the nanostructures. X-ray photoelectron spectroscopy (XPS) was also used to determine the surface properties through a Physical Electronics Quantum 2000 operating with a 200 μm, 50 W Monochromatic Al kα (1486.7eV) X-ray beam.

(iii) Device properties

The final film thickness of the devices was measured with a Bruker Dektak XT surface profilometer.

3.1.3 Results and discussion

3.1.3.1 Colloidal synthesis of OLA/WS_2 nanostructures

The reaction was characterized by several colour changes at different reaction temperatures indicating the formation of intermediates [Fig.3.3 (k)]. Tungstic acid loses the water molecule between 100 and 120 ℃ and further heating results in tungsten trioxide (WO_3). Thiourea is known to decompose thermally between 182 and 240 ℃ into carbon disulphide (CS_2), NH_3 and cyanamide (H_2NCN) [46, 47]. It is the WO_3 that reacts with CS_2 to form WS_2 nanostructures. Based on similarities with published results of WS_2 nanostructures obtained through various synthetic routes [48-53], the ultimate formation of WS_2 happens through a series of reactions as summarized below. The sulfurization of WS_2 nanostructures involves a change of oxidation state from 6^+ in WO_3 to 4^+ in WS_2 [54].

$$H_2WO_4\,(s) + CS\,(NH_2)_2\,(s) \xrightarrow[N_2,\ 320\ ℃]{OLA} WS_2\,(s) \qquad (3.1.1)$$

$$H_2WO_4\,(s) \xrightarrow[N_2,\ 320\ ℃]{OLA} WO_3\,(s) + H_2O\,(g) \qquad (3.1.2)$$

$$2CS\,(NH_2)_2\,(s) \xrightarrow[N_2,\ 320\ ℃]{OLA} CS_2\,(g) + H_2NCN\,(g) + 2NH_3\,(g) \qquad (3.1.3)$$

$$2WO_3\,(s) + 3CS_2\,(g) \xrightarrow[N_2,\ 320\ ^\circ C]{OLA} 2WS_2\,(s) + 3CO_2\,(g) + 2S\,(s) \quad (3.1.4)$$

The polar head of OLA adsorbs to the surface of the nanostructure while the apolar tail is soluble [55]. Below is the proposed mechanism for the passivation of the nanostructures by OLA.

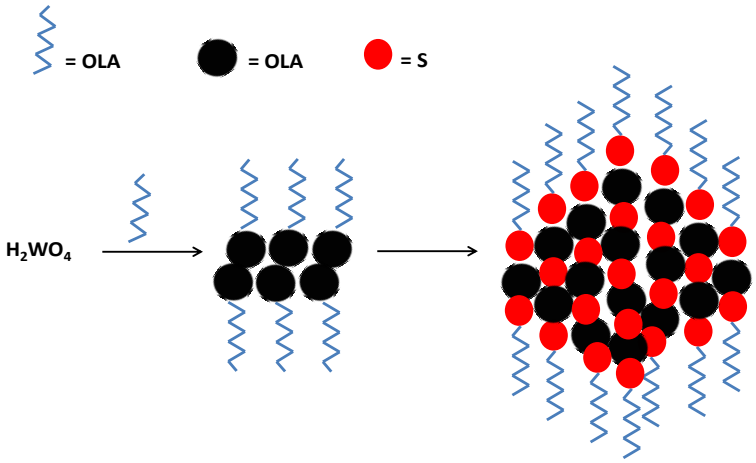


Figure 3.7: Passivation of WS_2 nanostructures by OLA.

3.1.3.2 Characterization of OLA/WS_2 nanostructures

The morphologies of the resulting OLA/WS_2 nanostructures were monitored by subjecting the samples from different reaction times to SEM analysis as shown in Figure 3.8. Hierarchical nanostructures with a flower-like morphology formed within 15 min of the reaction time. The 3D nanoflowers of OLA/WS_2 were characterized by tightly closed petals of ≈ 375 nm. These hierarchical nanostructures provide a high surface-to-volume ratio, one of the features taken into consideration when selecting a gas sensing material. A large surface area is important for the facilitation of gas diffusion and mass transport in sensor material to improve the sensitivity and response time of the gas sensor [56-58]. The petals began to open with a slight increase in the diameter of the nanoflowers to ≈ 400 nm when the reaction time was extended to 45 min. The nanoflower morphology was completely dismantled after 60 min and 2D flake-like structures were formed instead. These flake-like structures appear to be a result of the the nanoflowers completely opening. The flakes were in fact connected to a central core as was seen with SnSe [56] and Fe_2O_3 nanoparticles [59]. There is also evidence of the flakes curling up. The flakes curled up to rod-like structures after prolonging the time

to 180 min. Rod-like structures with ≈ 450 nm widths were ultimately formed after 240 min. The curling, curving or rolling of flakes is considered an important step for the formation of the tubular morphology in layered structures. This phenomenon was also witnessed by other groups [60, 61]. Feng and co-workers in particular observed that the curling up of WS_2 nanosheets was followed by seaming of the layers to form nanotubes [60].

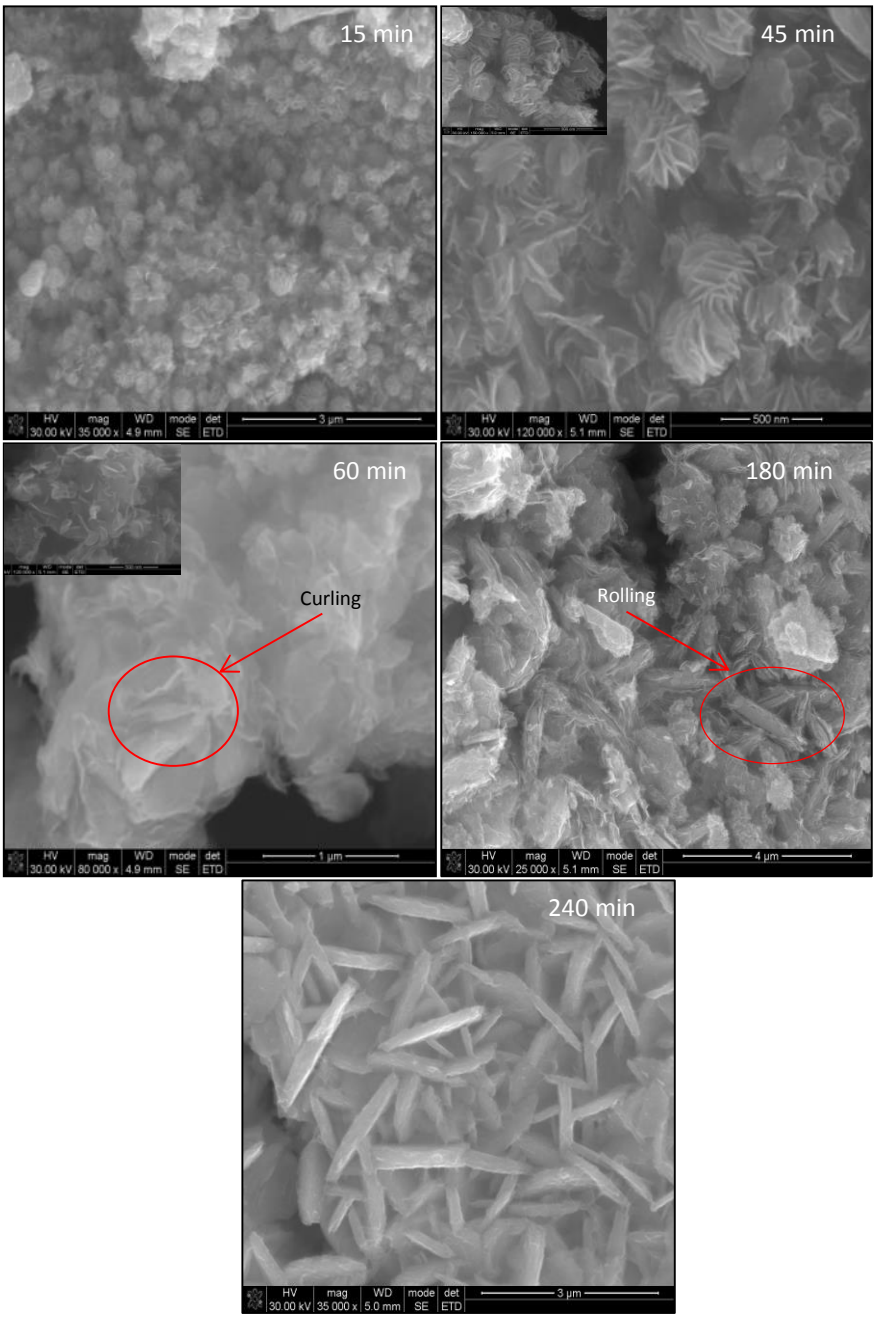


Figure 3.8: SEM images of OLA/WS_2 synthesized at different reaction times.

It is argued that the presence of unsaturated dangling bonds of atom W or S at the edges of the exposed nanosheets make them highly unstable and active. The transformation of the nanoflakes to nanorods can be explained using the well-known fact that the sphere is the most stable shape. The exposed nanoflakes are thin and have a tendency to interact with each other to eliminate the dangling bonds and therefore reduce the energy level to the lowest. The sequence in the transformation of one morphology to the next informed the conclusion that the nanorods evolved from the nanoflakes which had interconnected at the core to form nanoflowers. The corresponding TEM images are shown in Figure 3.9. The particles synthesized in 15 min show densely packed fluffy-like spherical particles which correspond to the tightly closed flower petals seen in SEM. At 60 min, the more open nanoflowers are observed as shown on the inset. The flower petals are made up of fine hair-like strands. As the time is prolonged to 180 min, crumpled-up sheets are formed and these are also composed of fine strands as shown on the inset. The 180 and 240 min samples, confirm the idea that the nanostructures have similar structures as the strand-like morphologies are yet again observed.

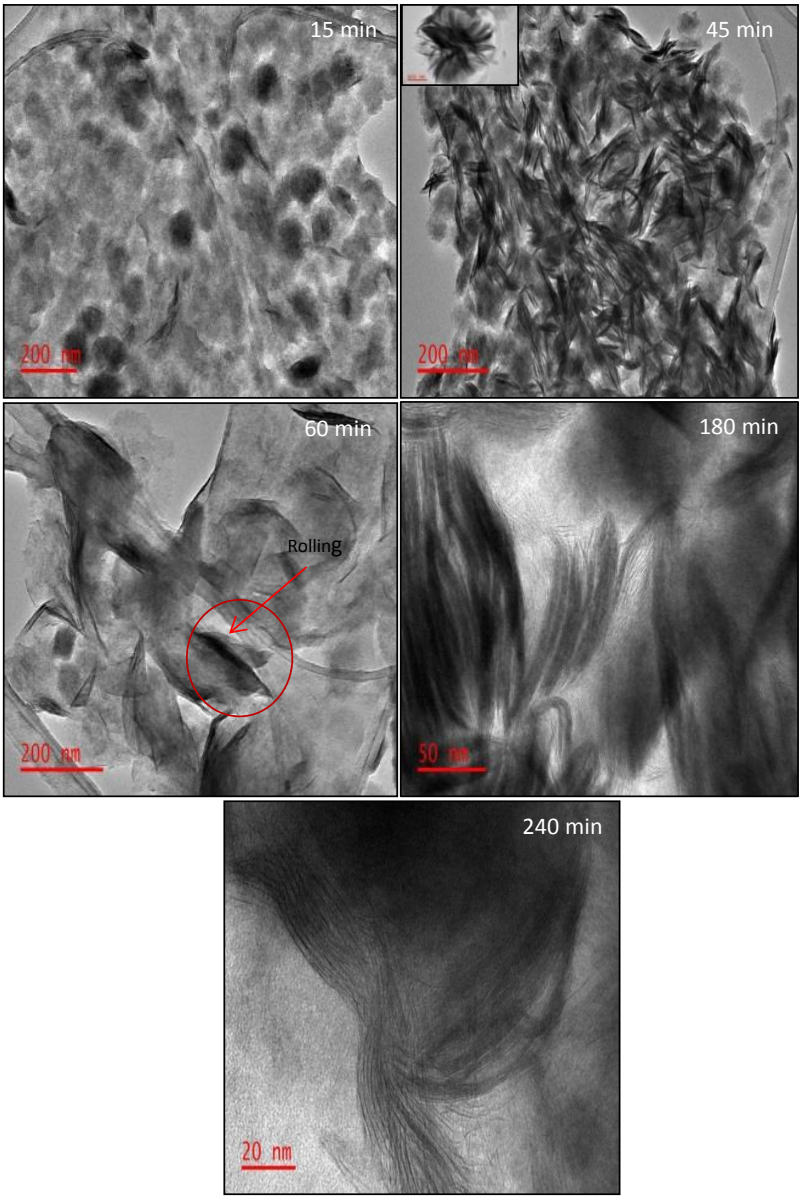


Figure 3.9: TEM micrographs of OLA/WS_2 nanostructures synthesized at different reaction times.

It therefore appears that all the nanostructures arise from the initial structure similar to metamorphosis. It is evident then that by varying the time, one can easily vary the morphology of the particles. This is only achievable through the colloidal synthesis. The EDS spectrum presented in Figure 3.10 shows the presence of W and S which confirmed the formation of WS_2. The O, Cu and C elements are from the carbon coated copper grid used as a substrate for the OLA/WS_2 samples. All the EDS graphs for the rest of nanostructures have the same composition of atoms; hence only 180 min is showed.

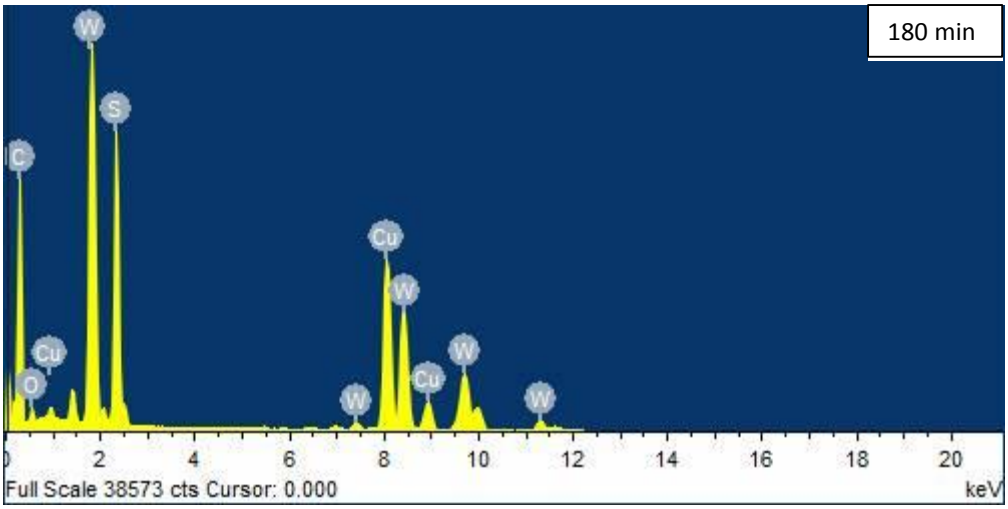


Figure 3.10: EDS of OLA/WS_2 nanostructures synthesized at 180 min reaction time.

The as synthesized nanostructures were then characterized with X-ray diffraction to confirm the crystal phase and purity of OLA/WS_2. XRD patterns of the nanostructures synthesized at different times are shown in Figure 3.11. All the nanostructures from different reaction times showed primary peaks at 16.26 (002), 27.59 (004), 32.35 (101), 38.71 (103), 45.42 (006), 56.44 (106), 68.95 (008) degrees indicating that they are practically similar, regardless of the reaction time. All the diffraction patterns are indexed to the 2H-WS_2 polytype (PDF No: 00-002-0131\JCP2.2CA). The samples showed good crystallinity. The broadness and relative intensity of the (002) plane in all the samples suggests reduced size of the nanostructures as well as layer stacking along the c direction respectively [12, 62-64]. The (002) plane shifted to higher angles compared to the bulk (2° = 14.32°) [52]. WS_2 can be easily oxidized back to WO_3. There is a small peak at 29.5° for both 15 min and 45 min samples which could be associated with:

(a) the presence of WO_3 on the surface of OLA/WS_2 nanostructures. The peak however disappears as the time is prolonged indicating a reduced quantity of WO_3 making the bulk of the sample or

(b) could be indexed to (100) which is known as the edge plane of the basal plane.

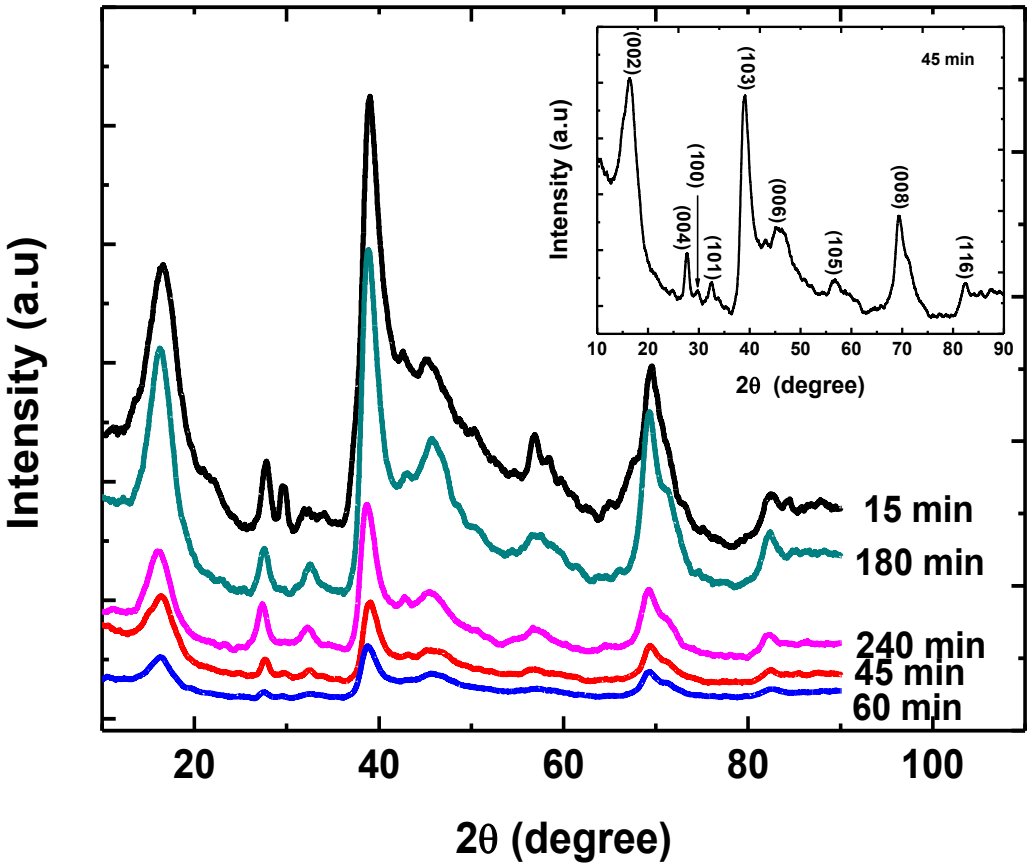


Figure 3.11: XRD patterns of OLA/WS_2 nanostructures synthesized at different reaction times. Insert shows the labelled peaks of the diffraction pattern of the 45 min sample.

It is vertical to the (002) plane in the hexagonal crystal system [65]. Intensities of (100) and (101) are relatively weak indicating the presence of a well-stacked layered nanostructure [62]. The complete disappearance of the (100) plane at prolonged times suggests a significant decrease in the number of stacked layers [65]. The peaks arising from the symmetry of the vertical crystal planes (004), (006), and (008)) confirm that the nanostructures are growing along the (002) axis [65, 66]. The (004), (103), (006) and (105) planes are governed by the long periodic layers of the crystal and their broad nature indicate a poor long distance order within the nanotubes [67].

Raman spectroscopy can also be used to characterize the structure of 2D layered materials. The shifts and peak positions determine stacking sequence, number of layers [5, 68-75], quality of layers (presence of defects) [71-75], effect of doping [73-75], strain effects [74, 75], electronic band structure and other electronic properties [68, 75]. The well-studied first

and second order phonon modes of bulk WS_2 were detected using a laser wavelength of 514 nm at approximately 356, 421 and 176 cm^{-1}; the in-plane $E^1_{2g}(\Gamma)$ representing metal and chalcogen atoms, out-of-plane $A_{1g}(\Gamma)$ for the chalcogen atoms and the longitudinal acoustic mode at point M, LA(M) respectively [5, 8, 65, 70, 76, 77]. A 532 nm laser wavelength was used for the OLA/WS_2 nanostructures synthesized in this project. Two prominent peaks, the second order longitudinal acoustic 2LA(M) and out-of-plane A1g(Γ) at approximately 350 cm^{-1} and 415 cm^{-1} respectively were observed for all the samples as shown in Figure 3.12.

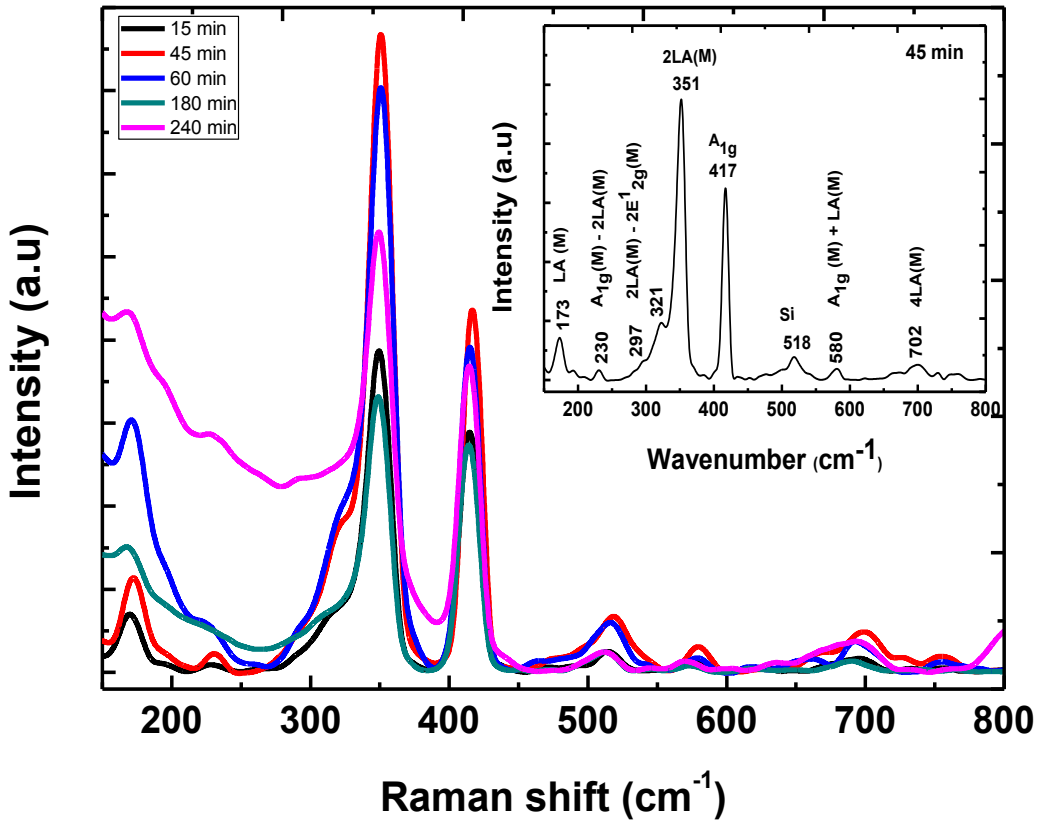


Figure 3.12: Raman spectra of OLA/WS_2 nanostructures from the different reaction times. Inset shows the first and second order peaks of the spectrum from the 45 min sample.

These peak positions are in agreement with other studies [74, 78]. The red shift by $A_{1g}(\Gamma)$ to lower frequencies (approximately 416 cm^{-1}) from bulk (421 cm^{-1}) is observed. It is accompanied by the stiffening of the lattice by the van der Waals interactions between the layers in bulk TMDCs which is consistent with the softening of the A1g(Γ) mode in monolayer [8, 74]. This is consistent with results obtained by Varghese *et al.* [79] and Tan *et*

al. for bi-layers [8, 80]. The labelled peaks of the nanostructures from 45 min are shown in the inset in Figure 3.12. The peak positions and intensities of the individual phonon modes were obtained by performing multi-peak Lorentzian fittings on each spectrum as shown in Figure 3.13. The peak positions, frequency differences ($\Delta\omega$) between $A_{1g}(\Gamma)$ and 2LA(M); and intensity ratio ($I_{2LA(M)}$ / I_{A1g}) for the nanostructures from different reaction times are summarized in Table 3.2. The intensities of the 2LA(M) are significantly higher than those of $A_{1g}(\Gamma)$ for all the samples in agreement with results obtained by Iqbal, *et al.* [4]; and the ratios are depicted in Table 3.2. According to Elías, *et al.*, the intensity for the 2LA(M) is twice that of the $A_{1g}(\Gamma)$ mode for a monolayer [5]. Herein, the intensity of 2LA(M) is not double that of $A_{1g}(\Gamma)$, but still higher, thus suggesting more than one layer of the as synthesized OLA/WS_2 nanostructures.

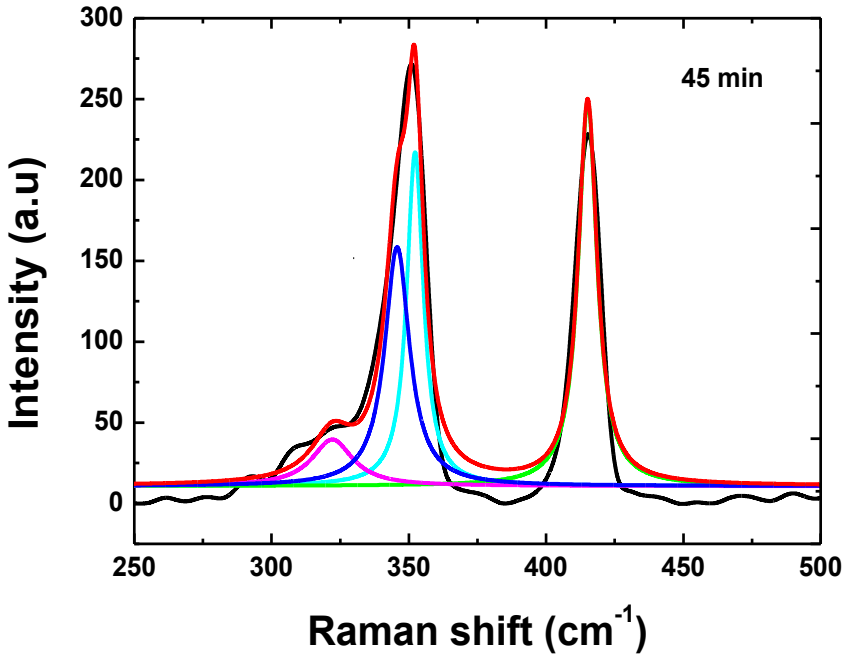


Figure 3.13: Lorentzian multi-peak fit of the Raman spectra of OLA/WS_2 nanostructures at 45 min. The black line represents the experimental data; the red, magenta, blue, cyan and green lines represent the combined peak fitting, the individual contributions of the most intense phonon modes.

Table 3.2: Raman intensity ratios and frequencies for the main phonon modes.

Sample	I_{A1g}	$I_{2LA(M)}$	$I_{2LA(M)}/I_{A1g}$	A_{1g} (cm^{-1})	2LA(M) (cm^{-1})	$\Delta\omega = A_{1g}$ -2LA(M)
15 min	1.2	1.6	1.3	415	350	65
45 min	3.3	5.8	1.8	417	351	66
60 min	3	5.3	1.8	416	351	65
180 min	1.8	2.3	1.3	414	349	65
240 min	3	4.3	1.4	414	349	65

The intensity ratio, $I_{2LA}(M)/A_{1g}$ decreases with an increase in the number of layers from 2.2 for monolayers [4, 65] to 0.43 for bulk [65, 73]. When compared to Raman analysis (λ = 514.5 nm) by Berkdemir, *et al.* of CVD grown WS_2, the OLA/WS_2 nanostructures seem to correspond to mono- and bi-layers. The frequency difference between $A_{1g}(\Gamma)$ and 2LA(M) can also be used as an indication of the number of layers [4]. For a monolayer of CVD grown WS_2, Iqbal, *et al.* reported a value of 65.3 cm^{-1} [4] while Khalil, *et al.* obtained 70.3 cm^{-1} [65]. The values for the OLA/WS_2 nanostructures are depicted in Table 3.2 and they too suggest the formation of mono- and bi- layers [81]. It is worthy to note that accurate determination of the number of layers based on published data is not possible as the peak positions are affected by the laser wavelength as well as the method of synthesis. However, it is clear that the OLA/WS_2 nanostructures have more than one layer but have not reached bulk range [13]. The formation of more than one layer is plausible based on the morphologies observed in Figure 3.8 as well as the prominence of (002) peak in Figure 3.11. Previous studies on the synthesis of WS_2 and other 2D layered TMDCs like MoS_2 detail the formation of multi-layered nanosheets by OLA [82, 83]. OLA stabilizes the TMDC nanostructures by selectively binding strongly to the reactive edge facets thereby restricting lateral growth [84]. Conversely, this facilitates vertical growth which results in smaller multi-layered nanosheets. Jung and co-workers conducted a study to elucidate the multilayer promoting character of OLA on WSe_2 by comparing it to oleic acid and oleyl alcohol [84]. Multilayers of WSe_2 nanosheets with reduced lateral growth were formed with OLA while oleyl alcohol produced 2 to 3 layers of significantly large lateral size. Oleic acid resulted in single layered nanosheets characterized by even larger lateral size. The group discovered the influence of functional groups to the binding energy of the particular capping agent being strongly related to its

electron-donating ability to the metal centre. This was supported by DFT calculations on the binding energies of methylamine, methyl alcohol and formic acid in that order [84].

XPS studies were conducted on OLA/WS_2 to determine the extent of oxidation which was suggested by a small peak detected by XRD. Shown in Figure 3.14 is the survey spectrum of the particles synthesized in 45 min. All the other samples showed identical results hence their spectra will not be shown. The strong C 1s peak presented by the spectrum confirms the presence of carbon due to the capping agent, OLA on the surface of the nanostructures. The attribution of the carbon peak to the capping agent is consistent with other reported work on capped nanoparticles and XPS has in fact been used to trace ligand exchange on the surface of the nanocrystals [85, 86].

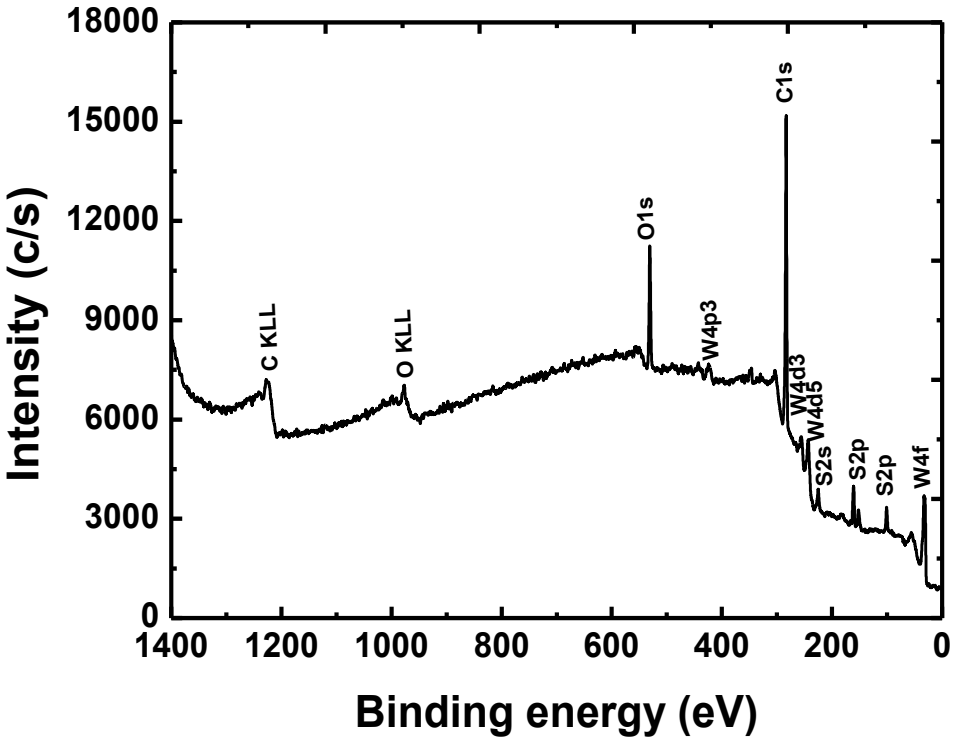


Figure 3.14: XPS survey spectrum of OLA/WS_2 nanostructures synthesized in 45 min.

The oxygen is attributed to the oxidation of tungsten to tungsten trioxide and the oxidation of the capping agent. Tungsten and sulphur peaks as a result of WS_2 and WO_3 are also observed. The high resolution XPS spectra with the focus on C 1s, O 1s, W 4f and S 2p were done to evaluate the surface in more details as shown in Fig. 3.15. The C 1s core level spectrum

shows the deconvoluted C-C peak attributed to OLA, the C-O and O-C=O due to the oxidation of OLA. The O 1s peak also shows the oxidation of OLA. Core level W 4f spectrum is characterized by the strong W $4f_{7/2}$ (30.9 eV) and W $4f_{5/2}$ (33.2 eV) doublet as well as a weaker W $5p_{3/2}$ (34.4 eV). This profile is similar to that obtained for OLA/WS_2 by Altavilla, *et al.*, hydrothermally processed WS_2-reduced graphene oxide (WS_2-rGO) hybrid by Zhang, *et al.* [83, 87] as well as WS_2 from other synthetic routes [6, 12, 24, 88-92]. The additional peak at a higher binding energy corresponding to the W^{6+} states signifies the presence of WO_3 (36.3 eV) [24, 89] due to partial oxidation of W.

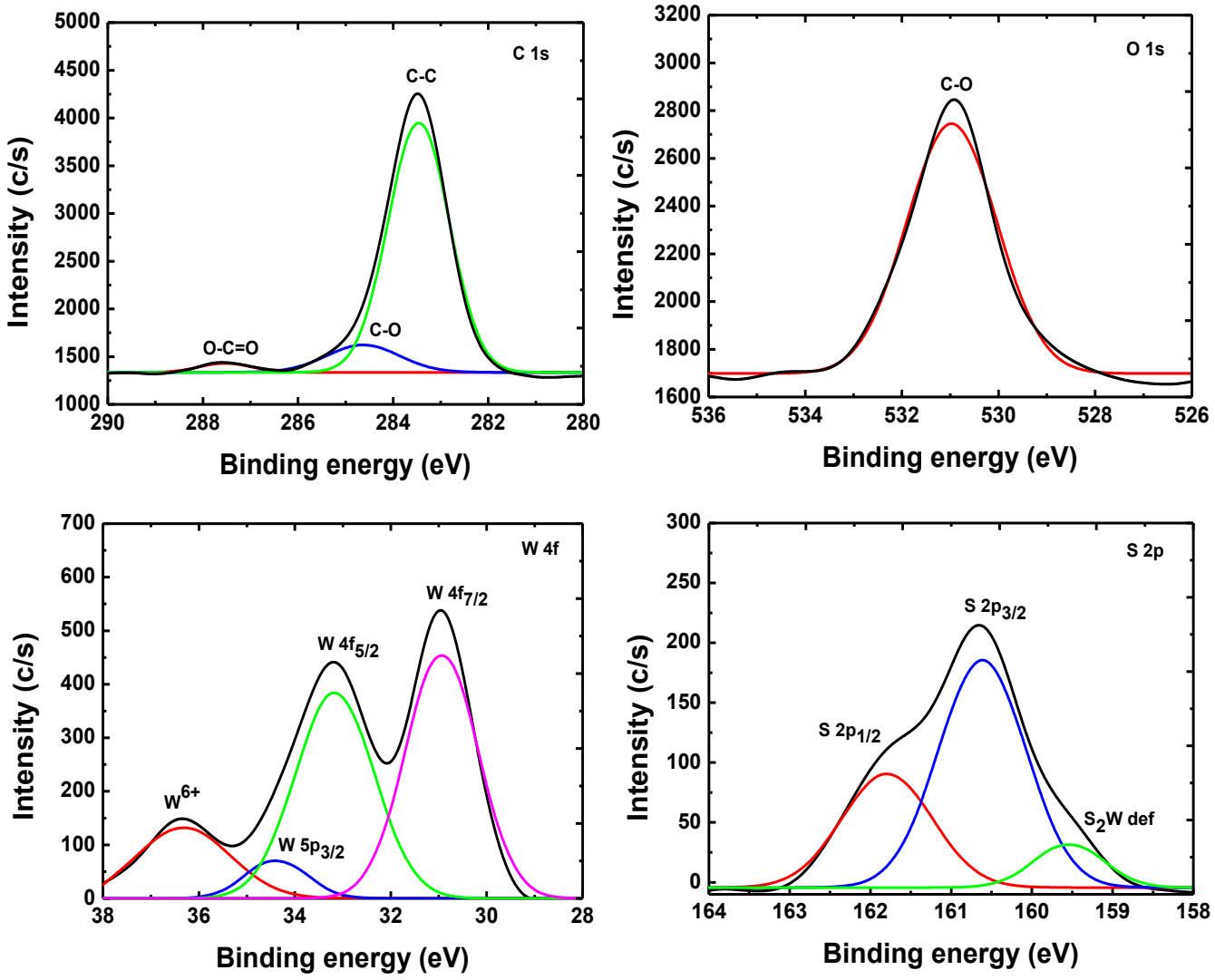


Figure 3.15: High resolution core level spectra of OLA/WS_2 with focus on C 1s, O 1s, W 4f and S 2p.

The W $4f_{7/2}$ and W $4f_{5/2}$ are ascribed to the 2H-WS_2 polytype with their binding energies corresponding to the W^{4+} states while W $5p_{3/2}$ is referred to as the common W valence [24, 88, 90, 93, 94]. The S 2p core level spectrum shows three peaks all attributed to the 2H-WS_2 polytype. Two peaks are assigned to the S $2p_{3/2}$ absorption peaks (159. 5 and 160.6 eV), while the third is the S $2p_{1/2}$ absorption peak (161. 8 eV) [24, 90, 91, 93, 95, 96]. Shown in Table 3.3 is the atomic % composition and peak area %. The sample is largely made up of carbon, 77.4 % attributed to the capping agent that forms a large organic shell around each particle. The W 4f component shows 21 % total abundance of WO_3 and 79 % abundance of WS_2.

These results are similar to other reported work and it has been shown that the presence of a small amount of WO_3 actually improves the sensing of NH_3 [23]. In addition, the presence of the defects (W^{6+} and defect S_2W) play a major role in gas sensing as additional active sites are therefore present for the adsorption of gas molecules thereby enhancing the sensing [23].

Table 3.3: Summary of the atomic composition stoichiometric assignments obtained from the fitting of the XPS spectra reported in Figure 3.15.

Element	Atomic %	Peak binding energy (eV)	Assignments	Peak area %
C	77.4	284.8	C-C	91
		286.3	C-O	6
		288.9	O-C=O	3
O	10.8	532.2	C-O	100
W	3.7	30.9	WS_2	41
		33.2	WS_2	38
		34.4	WS_2	6
		36.3	WO_3	15
S	6.2	159.5	S_2W def.	9
		160.6	S_2W	60
		161.8	S_2W	31

The optical properties of the synthesized OLA/WS_2 nanostructures were determined using UV-vis absorption and photoluminescence spectroscopy. The UV-Vis absorption spectra

presented in Figure 3.16 displayed three absorption peaks similar to results obtained by Cao *et al.* [7]. The results for all samples are summarized in Table 3.4. The blue shifted 625 - 630 nm and 505 -515 nm peaks correspond with excitons A and B (636 and 525 nm for bulk WS_2 respectively) [51]. Bulk WS_2 has an indirect band gap of 1.3 -1.4 eV and when thinned to monolayer a crossover to the direct band gap of 1.9 - 2.05 eV is obtained [11, 94]. The band gaps for all samples corresponding to the exciton A are between 1.96 - 198 eV thus confirming a direct band gap crossover. UV-vis spectra of the synthesized OLA/WS_2 nanostructures displayed a wide absorption in the visible and near infrared regions (390 -715 nm) as presented in Figure 3.16.

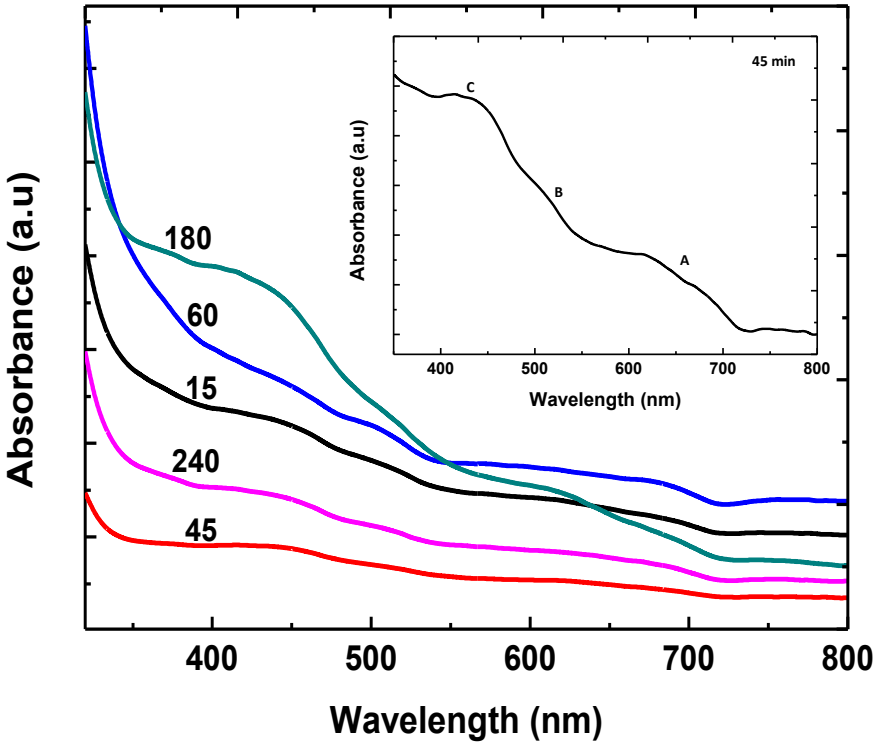


Figure 3.16: UV-vis spectra of OLA/WS_2 nanostructures from the different reaction times. Insert shows the spectrum of the 45 min sample different peaks A, B and C.

The inset in Figure 3.16 shows the spectrum for 45 min with a broad absorption edge centred at ~659 nm corresponding to exciton A; indicating a significant blue shift from bulk absorption edge (920 nm, [8, 52]). A weak absorption peak at ~513 nm which was found to correspond to exciton B and an additional peak C were observed (inset Figure 3.16). Excitonic peaks A and B arise from direct optical transitions at the K point of the Brillouin

zone due to spin-orbital splitting of the lowest energy level, the valence band [6, 11, 76, 98-101] while C arises from optical transitions between the density of states peaks in the valence and conduction bands (11, 65). Peak C is regarded as transition from indirect to direct bandgap [65] confirming assertion that the general band structure of WS_2 like WSe_2 and MoS_2 bears the coexistence of an indirect and direct band gap regardless of thickness [11]. The rest of the nanostructures from different reaction times are also blue shifted from the bulk with a band gap of ~1.90 eV as shown in Table 3.4 below. The band gaps were calculated from the absorption edges of the UV-Vis spectra using Eq. (3.1.5)

$$E_g = hc/\lambda \qquad (3.1.5)$$

Where, E_g = energy gap; h = Planck's constant; c = wavelength of light

This increase in the size of the band gap from ~1.3 eV (bulk) [3, 8, 11, 9, 68] form confirms the reduced size (nanostructures) of the synthesized OLA/WS_2. The band gap is in agreement with published values for WS_2 nanostructures obtained via various synthetic routes [8, 11, 98]. Because all the nanostructures have approximately the same band gap, it can be concluded that the reaction time did not affect their absorption properties.

Table 3.4: A summary of the absorption edges and gaps of the OLA/WS_2 nanostructures at different reaction times.

Reaction time (min)	Wavelength (nm) Peak A	Band gap (eV) Peak A	Wavelength (nm) Peak B	Wavelength (nm) Peak C
15	654	1.89	513	447
45	659	1.88	513	442
60	653	1.9	507	444
180	658	1.88	507	441
240	660	1.88	508	442

Meanwhile, it is at the monolayer regime that a crossover from indirect to direct band gap of ~2.1 eV is realized [3, 8, 11, 68, 70]. Our results suggest that the synthesized nanostructures are few-layered and have an indirect band gap. According to Figure 3.17 (a), an indirect band gap is formed between a local conduction band minimum at a midpoint between Γ and

κ, and the valence band maximum at the Γ point [8, 11]. The splitting is absent in a monolayer as shown in Figure 3.17 (b), suggesting that the synthesized OLA/WS_2 nanostructures in this project are few-layered. In contrast, a direct gap is found at the K points of the Brillouin zone between the spin-orbit split valence band and the doubly degenerate conduction band as presented in Figure 3.17 (b) [8, 11].

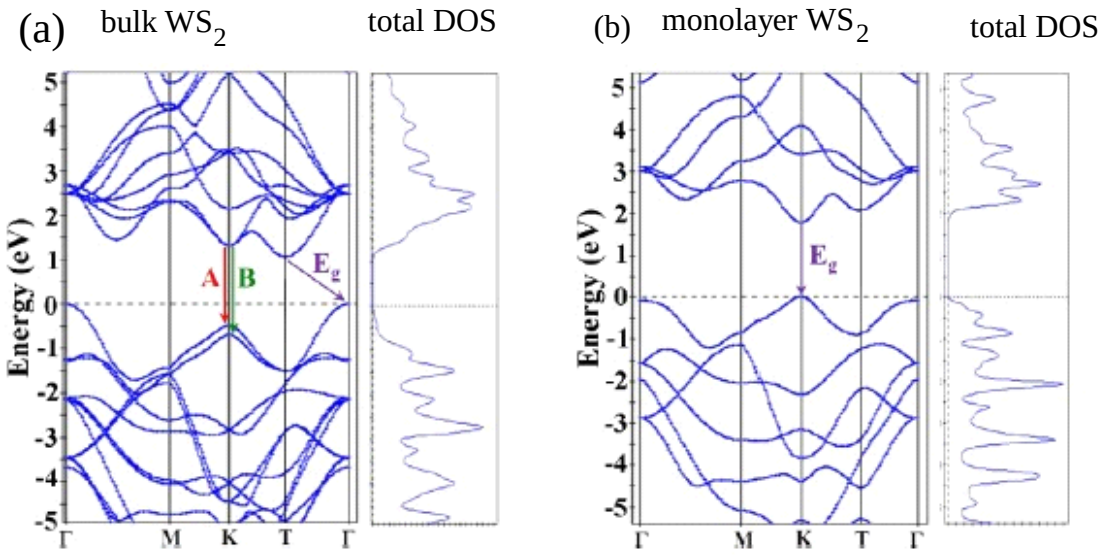


Figure 3.17: Electronic band structure (left) and total density of states (right) for (a) WS_2 bulk and (b) monolayer [8].

Monolayer WS_2 exhibit a direct band gap and have been reported to present a single sharp emission peak with intensity that is stronger than for multilayers [11, 68, 102]. All the synthesized OLA/WS_2 nanostructures in this project displayed a relatively weak broad emission peak (Figure 3.18). The emission maxima are summarized in Table 3.5 below. The emission corresponds to the excitonic "A" absorption in Figure 3.15. According to published data, a reduced emission is consistent with bi- to few layers of WS_2 nanostructures which suggest an incomplete evolution to the bulk configuration [68, 102]. Bulk WS_2 is known for the absence of emission [72] or the emergence of a less intense emission peak at longer wavelength, labelled as 'I' (Figure 3.19) [8, 11]. This peak is absent from the PL of our WS_2 nanostructures, also suggesting that the nanostructures are few layered. The PL results corroborate our UV-vis results.

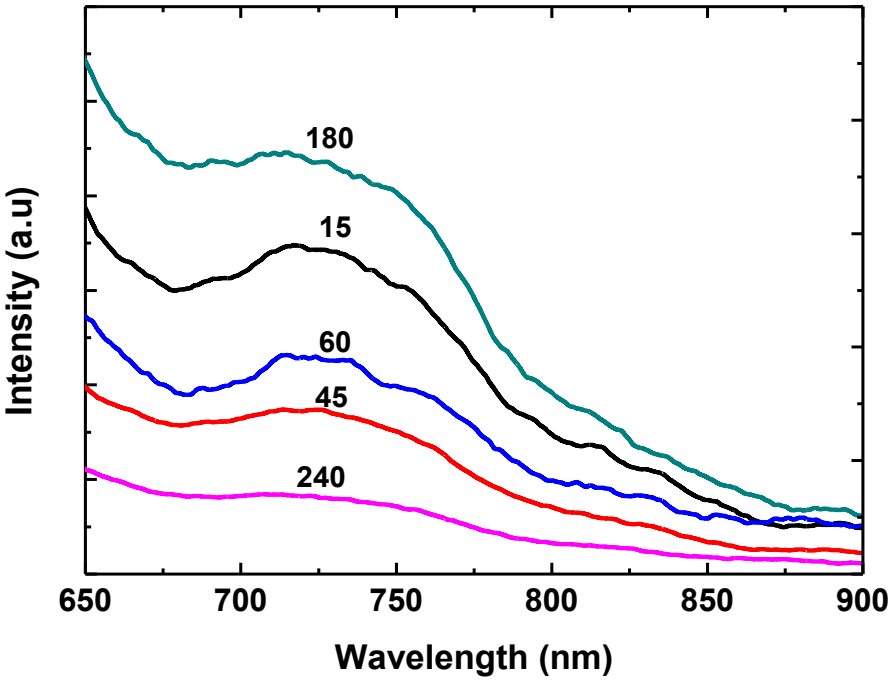


Figure 3.18: PL spectra of WS_2 nanostructures from the different reaction times.

Table 3.5: Emission maxima for the different nanostructures.

Reaction time (min)	Wavelength (nm)
15	718
45	725
60	714
180	714
240	708

The broad emission peak (680 to 790 nm) is due to the large size of the hierarchical morphology (microflowers) and polydispersity of the nanostructures. The red shifted PL emission suggests an indirect band gap [103].

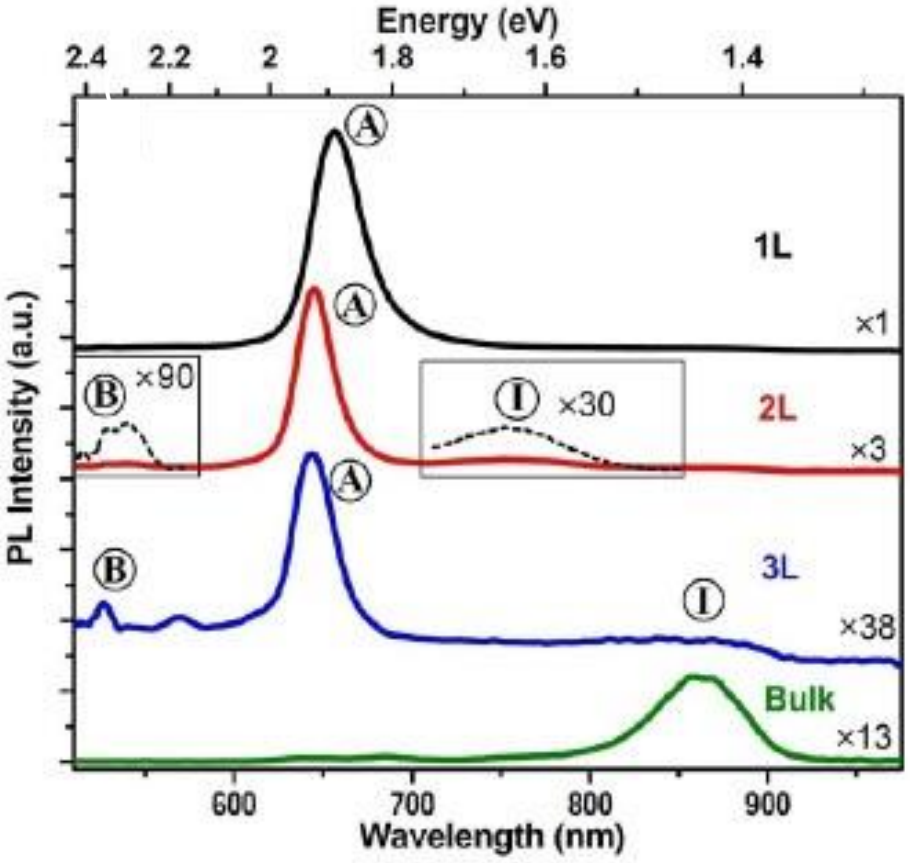


Figure 3.19: PL intensities for mono-, bi- and three-layered WS_2 nanostructures at 488 nm excitation wavelength with the positions for the excitons A and B as well as the indirect band gap (I) [8].

On comparing our results with the published data, it can be concluded that the nanostructures from all the reaction times fall within the few layer limit, in agreement with the UV-Vis band gap values and weakened PL emission. It is important to note that the shifts in peak positions and intensity ratios display layer dependence which varies slightly with laser excitation [74, 104]. In addition, the sensitivity of the modes to strain, doping and the substrate may lead to incorrect determination of number of layers [75]. This ambiguity, together with interferences brought about by adjacent second-order bands mean that Raman spectroscopy should be used in conjunction with other characterisation methods [74].

FT-IR was also used to confirm the presence of the capping agent as shown in Figure 3.20. The spectrum of OLA/WS_2 nanostructures resembles that of pure OLA with small shifts in wavenumbers observed. Compared with the spectrum of pure OLA, the stretching υ(NH) and

rocking modes δ(NH) of the amino group at 3320 and 1571 cm^{-1} respectively are absent for both pure OLA and OLA/WS_2 nanostructures.

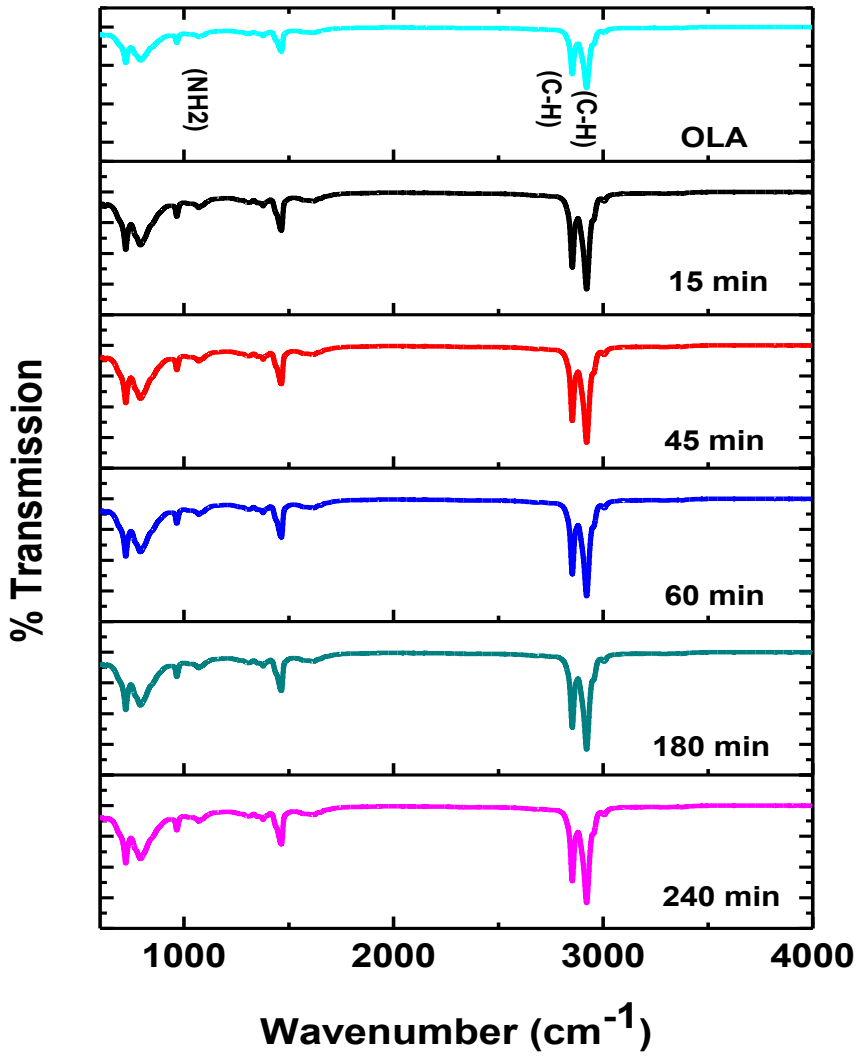


Figure 3.20: FTIR spectra of pure OLA and OLA/ WS_2 nanostructures synthesized at different reaction times.

On the other hand, the $\upsilon_{as}(-CH_2)$ and $\upsilon_s(-CH_2)$ modes of the methylene group for pure OLA are observed at 2916 and 2855 cm^{-1} respectively and corresponded to the OLA/WS_2 peaks found at 2906 and 2839 cm^{-1} respectively. The $\delta_{as}(-CH_3)$ and $\delta_s(-CH_3)$ modes of the terminal methyl group are observed at 1472 and 1371 cm^{-1} for pure OLA respectively and at 1447 and 1363 cm^{-1} for the nanostructures. The bending ($-NH_2$) mode is found at 967 cm^{-1} for pure OLA and at 959 cm^{-1} for the nanostructures. The results therefore confirm the capping of the nanostructures by OLA. The capping is necessary in the colloidal synthesis of the

nanostructures as it controls the nucleation and growth of the nanostructures and also passivates the surface thus avoiding agglomeration and rapid oxidation. The final thickness of the sensors was determined with a surface profiler (Dektak XT; Bruker) and was found to be about 600 nm for all samples.

3.1.2.7 Gas sensing performance

(i) Sensitivity and response to NH_3 vapour

There is a strong correlation between synthetic time of OLA/WS_2 and the resultant morphology of the nanostructures. The properties as shown can therefore be influenced by the morphology. This can alter the sensing characteristics and therefore impact their applicability in sensor technology. The electrical conductance measurements of sensors of WS_2 synthesized at different reaction times were performed as a function of ammonia concentration at room temperature (~ 23 °C) and humidity < 20%. The sensitivity of the different sensors to NH_3 as an analyte was calculated as:

$$S = \Delta G/G_0 \times 100 \qquad (3.1.6)$$

Where, S is the sensitivity in ppm^{-1},

$\Delta G/G_0 = (G_{dry\ nitrogen} - G_{gas})/ G_{dry\ nitrogen}$, the relative variation of the conductance

$G_{dry\ nitrogen}$ = conductance of sensor in dry nitrogen

G_{gas} = conductance of sensor in the particular gas atmosphere.

A change in the conductance of the OLA/WS_2 based sensors is displayed upon exposure to NH_3 vapour as shown in Figure 3.21 (a)-(e). The conductance increased from the baseline conductance. The sensitivity was measured over a range of concentrations for each sensor. It is noteworthy to mention that the response of the sensors based on shorter reaction times is in the opposite direction thereby giving negative values while positive values were obtained for the longer reaction times. NH_3, a reducing gas induced both reduction and oxidation characters on OLA/WS_2. OLA/WS_2 sensors from shorter reaction times (15, 45 and 60 min) exhibited p-type behaviour while the n-type character was observed for those from longer reaction times (180 min and 240 min). This suggests a transition of the electrical properties from p- to n-type as governed by the different morphologies. The reaction times 15, 45 and 60 min produced closed ‘petals’ microflowers, open ‘petals’ microflowers and nanosheets respectively; while rod-like nanostructures were obtained at 180 and 240 min (Figure 3.8). A

similar transition was observed as a function of temperature by Cantalini, *et al.* during the sensing of 1 ppm NO_2 by MoS_2 nanoflakes in dry air [79]. NO_2, an oxidizing gas induced p-type behaviour on the nanoflakes below 250 ℃ and n-type behaviour above 250 ℃.

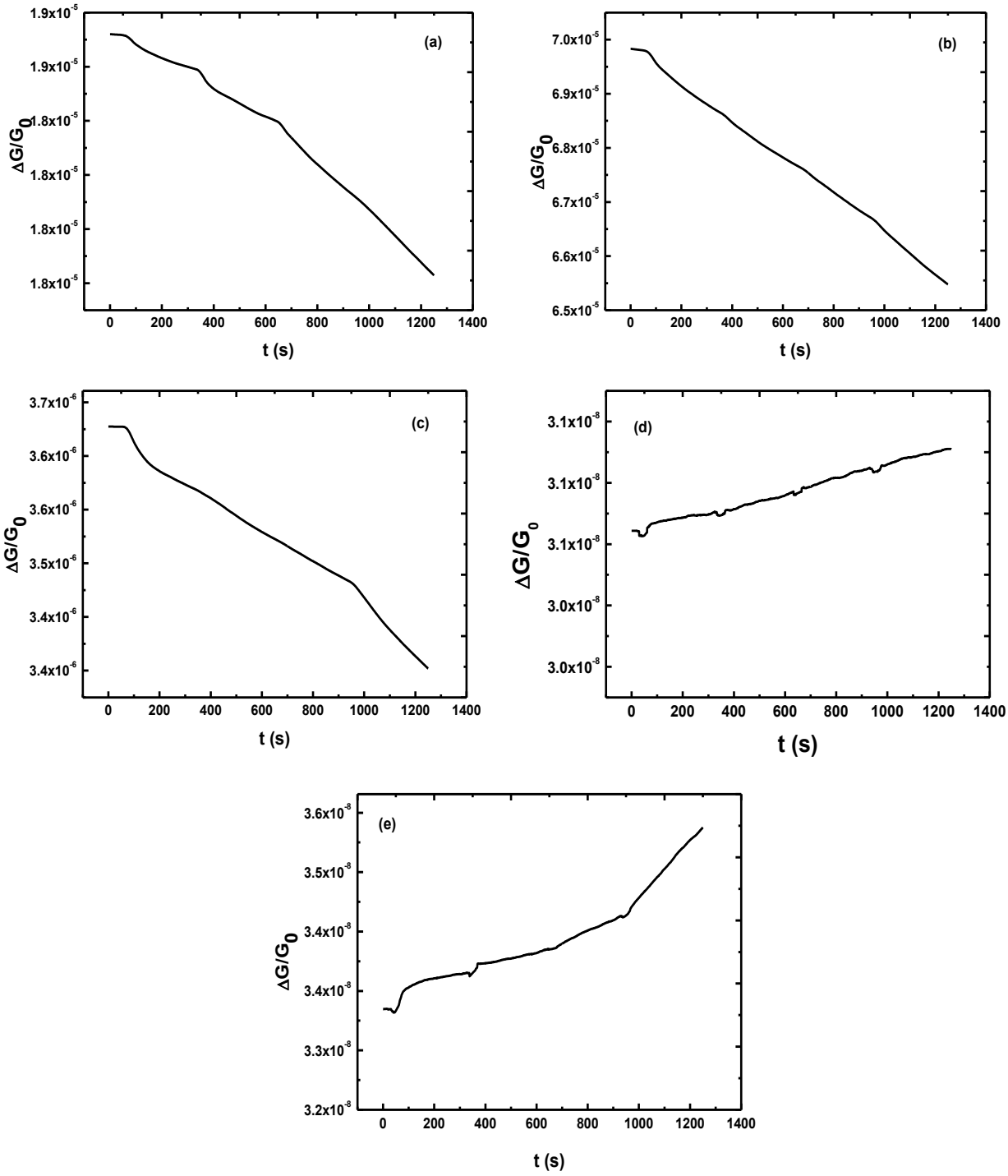


Figure 3.21: (a)-(e) Gas response of the OLA/WS_2 based sensors (15, 45, 60, 180 and 240 min) to NH_3 vapour at different concentrations.

The relationship between the sensor response and concentration of analyte is shown in Figure 3.22 (i)-(v). The calibration curves were derived from the corresponding gas responses in Figure 3.21 (a)-(e). The sensitivities show a linear dependence with analyte concentration in the studied range (from 256 ppm to 1024 ppm), as shown in Figure 3.22 (i)-(v), providing a constant sensitivity for all devices. The results presented were obtained using the chamber in Figure 3.6 (a).

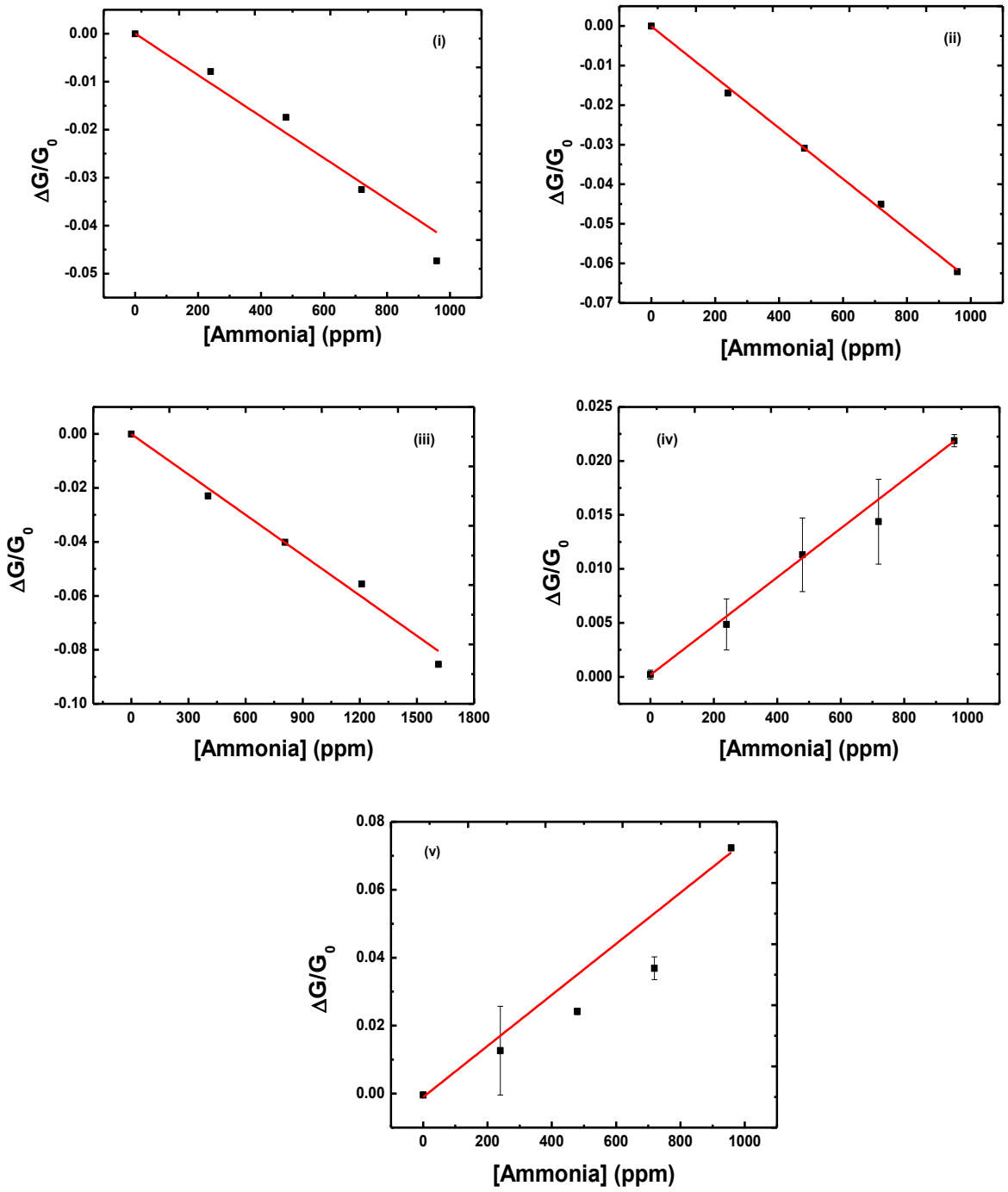


Figure 3.22: Sensitivities of the different reaction times towards NH_3 from (i) to (v).

The sensitivities show a linear dependence with analyte concentration in the studied range (from 256 ppm to 1024 ppm), as shown in Figure 3.22 (i)-(v), providing a constant sensitivity for all devices. The results presented were obtained using the chamber in Figure 3.5 (a). Comparing all the sensitivities, the mechanism displayed by the nanostructures is morphology dependent, with the sensors fabricated using OLA/WS_2 nanostructures synthesized in 45 min showing higher values. As shown in the SEM images (Figure 3.8), at this reaction time the nanoflowers are still present and have a higher surface area due to their "blossoming petals". This probably provides both sides for interaction with the ammonia, maximizing the active surface area. The gas sensing of hierarchical structures of metal oxide based sensors is well documented with fast and increased gas response due to the high surface area and well-defined pore framework which are ideal properties for gas sensing [105]. The surface area enhances the relative response to the analyte while the response and recovery times are impacted on by the pores which favour the diffusion of the gas in and out of the sensor [106]. The morphology dependent gas sensing behaviour was also observed by Li *et al.* where cone-shaped hierarchical structures of SnO_2 annealed at 500 °C exhibited the highest relative response compared to other morphologies tested [106]. The sensitivities values are however a little low; this can be attributed to the presence of the capping agent on the surface of the nanostructures as shown in the XPS (Figure 3.14) and FT-IR results (Figure 3.20).

(ii) Working principle and gas sensing mechanism of a chemiresistive gas sensor

As mentioned previously, the principle behind chemi-resistor is based on the reversible accumulation of analyte gas molecules in the sensitive layer of the device. Reducing gases like NH_3 and the other polar solvents act as electron donors owing to the existence of a lone pair electron, to provide electrons to weakly physisorption on the surface of OLA/WS_2 and easy desorption on account of the low adsorption energy, about −216 meV as reported previously [107]. This charge donation to the sensor leads to an increase of the conductivity (n-doping) while oxidizing vapours like O_3 result in a decrease in conductivity (p-doping). When the OLA/WS_2 sensors were exposed to electron-withdrawing vapors *e.g.* NH_3 the conductivity increased (180 and 240 min) or decreased (15, 45 and 60 min). This is consistent with an increase or decrease in the number of charge carriers (Figure 3.21, NH_3 response calibration curves). Surface interactions of the gas/semiconductor that occur at the grain boundaries of the metal chalcogenide film underlie the gas sensing mechanism of chemi-resistive gas sensors.

(iii) Response and recovery

For practical reasons, the conductance of a sensor is expected to revert back to its original value during all response/recovery cycles, indicating that the sensing process is reversible for the sensor. The typical response/recovery curve of OLA/WS_2 sensor 45 min after exposure to 1024 ppm of NH_3 with dry N_2 as the reference gas is shown in Figure 3.23. The measurements were performed under dry N_2 conditions using the chamber presented in Figure 3.6 (a). The conductance of the sensor decreased when the test gas was switched on giving a negative sensitivity. The curve clearly shows the slow recovery performance at room temperature by our OLA/WS_2 when the NH_3 vapour is removed. This is a common problem with NH_3 sensors based on TMDC thin films at low working temperatures [15, 107]. This slow recovery was also observed in graphene-based sensors and in previous MoS_2 sensor reports [108]. Complete recovery of the sensors was achieved by annealing at 100 ℃ before the next set of gas sensing measurements was performed. UV irradiation is also suggested as a means to desorb the analyte from the surface of the sensor [15].

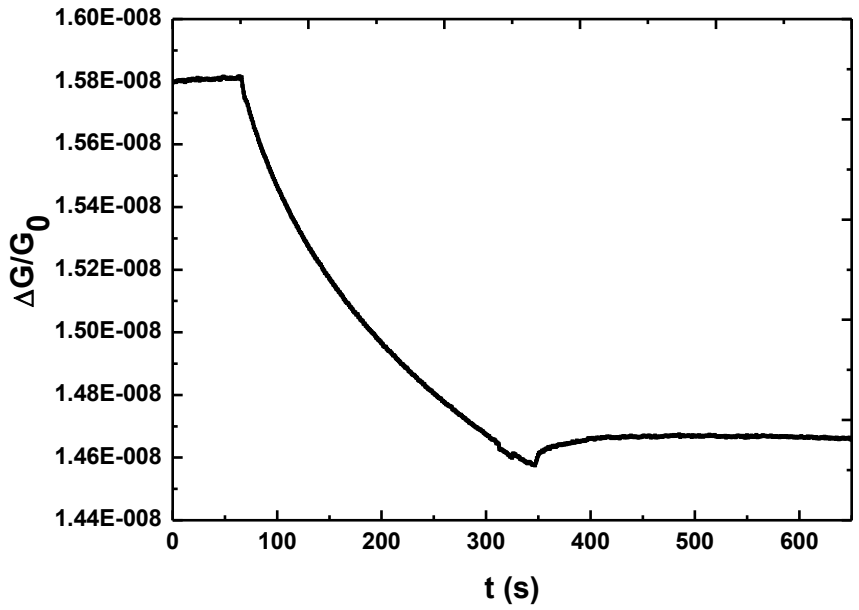


Figure 3.23: Response for 45 min OLA/WS_2 based sensor exposed to 1024 ppm of ammonia.

The analyte accumulation could be due to strong analyte adsorption or a chemical reaction between the analyte and the receptor which ultimately leads to strong chemisorption of NH_3 vapour on the surface of OLA/WS_2 [109, 110]. The case of strong chemisorption was observed previously for few-layered and bulk WS_2. The NH_3 molecule is said to insert into

the inner layers and interact with two adjacent layers, a sensing mechanism similar to the interaction process of NH_3 with layered TiS_2 and TaS_2 [111, 112]. The NH_3 molecules are easily adsorbed to the edge sites of few-layered and bulk WS_2 due to the strong electronegativity of the elemental sulfur layer of WS_2 layers. The transferred electrons to the WS_2 layers are then converted to NH_4^+ [111, 112]. The NH_4^+ ions are said to open the edges of two adjacent elemental sulfur layers and expand the interlayer space. This lets in more NH_3 molecules deeper inside and further expands the inner space until the entire interlayer is filled with NH_3. The NH_3 molecules are later converted to NH_4^+; resulting in the formation of intercalation compounds as $(NH_4^+)_X(NH_3)_Y(WS_2)^{X-}$ [111, 112]. The intercalated NH_3 molecules are much more difficult to desorb than the ones on the surface of WS_2 nanosheets. This is similar to the interaction process of NH_3 with TaS_2, which required the application of heat (over 147 ℃) to remove the ammonia molecules from the interlayer [111]. Therefore, it can be speculated that the different adsorption intensity between the surface and interlayer of WS_2 and ammonia maybe the reason for the slow recovery performance of few-layered WS_2 based NH_3 gas sensor at room temperature. The researchers went further and did the first-principles calculation to simulate the different interfacial interaction process between the surface and interlayer of WS_2 and ammonia to verify the above argument [111]. The same argument for the slow recovery process will be applied in this study since SEM, TEM, Raman and UV-vis results suggest that our OLA/WS_2 the nanostructures are few-layered. However, the signal recovered completely and the desorption of NH_3 was accelerated when the sensor was exposed to UV irradiation for 60 min or annealed in an oven for 30 min at 100 ℃.

Response/recovery measurements were also performed under ambient conditions using the chamber shown in Figure 3.6 (b). The typical response/recovery curves of OLA/WS_2 sensors (15, 45, 60, 180 and 240 min) when exposed to 240 ppm of NH_3 is shown in Fig. 3.24. The conductance of all the sensors increased sharply when the test gas was switched on and recovered when exposed to ambient. It took the OLA/WS_2 about 28 s to show 90 % change in the original conductance value. After a standing time of 300 s, the sensors were again exposed to ambient and the recovery time was measured to be about 42 s. The recovery times were relatively faster compared to the one performed under dry N_2 conditions (Figure 3.23).

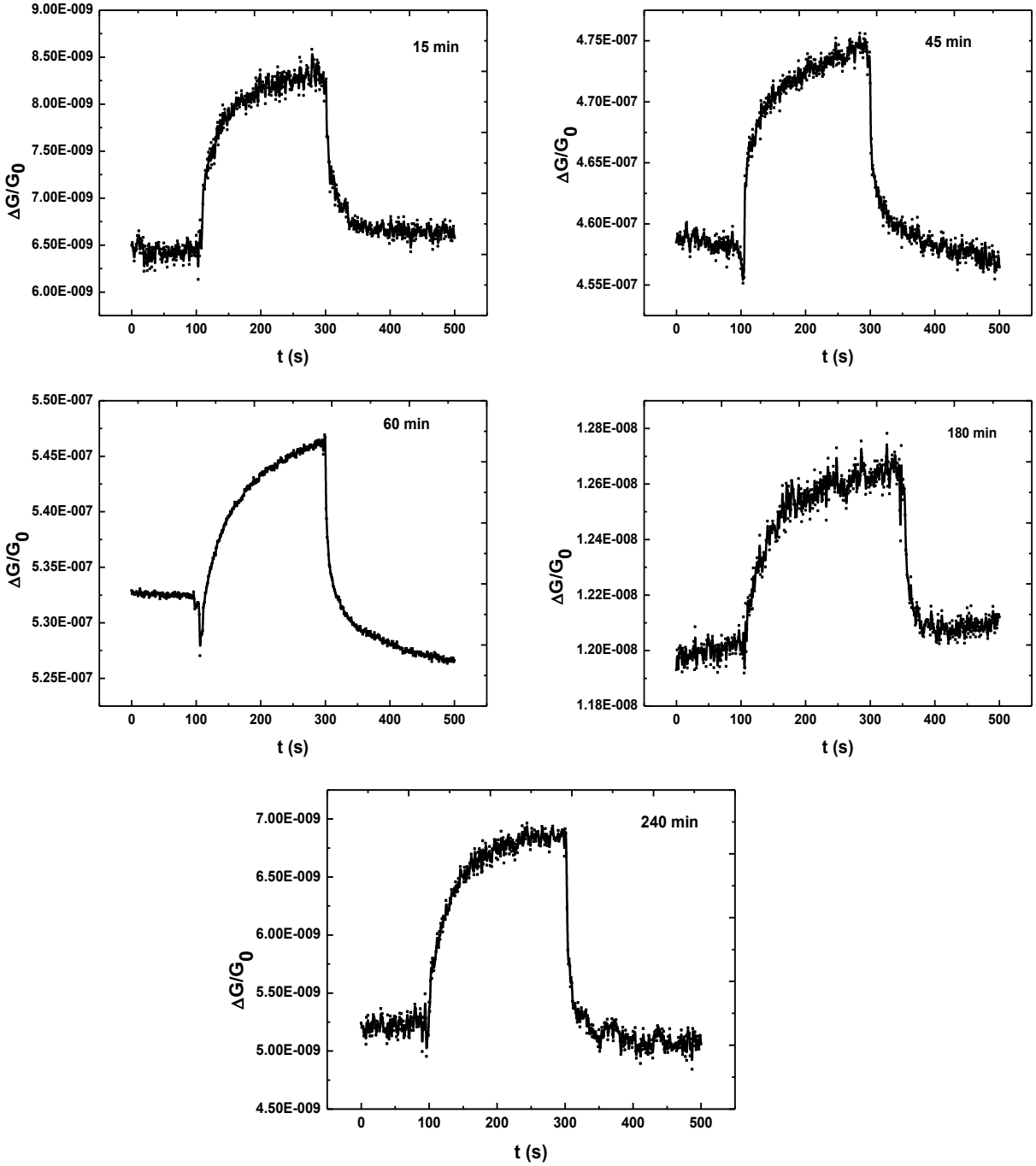


Figure 3.24: Response for OLA/WS_2 based sensors exposed to 240 ppm of ammonia.

3.1.4 Conclusion

In summary, few-layered OLA/WS_2 nanostructures were successfully synthesized from as short a reaction time as 15 min via a relatively low temperature colloidal route. The number of layers was estimated by Raman spectroscopy to being more than one and most likely two and this was corroborated by the band gap values, low photoluminescence intensities and the prominence of the (002) plane. The XPS showed that there was oxidation of the nanostructures however, the bulk of the oxidation occurred on the protective organic shell. It was further shown that these materials are promising for use as active layers in resistive chemical sensors operating at room temperature and the sensing was not compromised by the presence of WO_3 which only operates at higher temperatures. Between the analysed devices, the sensor based on OLA/WS_2 synthesized for 45 min gave the highest response to ammonia gas. This was attributed to the hierarchical nature of the nanoflowers, with their "blossoming petals" increasing the surface area for interaction with the target analyte. Furthermore, the well-defined porous frameworks enhance the diffusion of the analyte in and out of the compartments resulting in fast response time to ammonia. A slow recovery time was observed due to the strong interaction of ammonia with the OLA/WS_2 surface molecules under dry N_2 conditions. On the other hand, relatively faster recovery times were obtained under ambient conditions.

3.1.5 References

[1] Schonauer, D., Wiesner, K., Fleischer, M. and Moos, R. (2009). Sensors and Actuators B, 140, 585-590.

[2] Yang, W., Gan, L., Li, H. and Zhai, T. (2016). Inorg. Chem. Front. 3, 433-451.

[3] Huo, N., Yang, S., Wei, Z., Li, S-S., Xia, J-B. and Li, J. (2014). Sci. Rep. 4, 5209; DOI:10.1038/srep05209.

[4] Iqbal, M. W., Iqbal, M. Z., Khan, M. F., Shehzad, M. A., Seo, Y., Park, J. H., Hwang, C. and Eom, J. (2015). Sci. Rep. 5, 10699; doi: 10.1038/srep10699 and references therein.

[5] Elıas, A. L., Perea-Lopez, N., Castro-Beltran, C., Berkdemir, A., Lv, R., Feng, S., Long, A. D., Hayashi, T., Kim, Y. A., Endo, M., Gutierrez, H. R., Pradhan, N. R., Balicas, L., Mallouk, T. E., Lopez-Urıas, F., Terrones, H. and Terrones, M. (2013). ACS Nano 7 (6), 5235-5242.

[6] Pawbake, A.S., Waykar, R. G., Late, D. J., and Jadkar, S. R (2016). ACS Appl. Mater. Interfaces 8, 3359-3365.

[7] Cao, S., Zhao, C. and Peng, L. (2016). Materials Letters 164, 452-455.

[8] Gutiérrez, H. R., Perea-López, N., Elías, A. N., Berkdemir, A., Wang, B., Lv, R., López-Urías, F., Crespi, V. H., Terrones, H. and Terrones, M. (2013). Nano Lett. 13, 3447-3454.

[9] Zhao, X., Xia, C., Wang, T. and Dai, X. (2016). Journal of Alloys and Compounds 654, 574-579.

[10] Wang, Z., Zhao, K., Li, H., Liu, Z., Shi, Z., Lu, J., Suenaga, K., Joung, S-K., Okazaki, T., Jin, Z., Gu, Z., Gao, Z. and Iijima, S. (2011). J. Mater. Chem. 21, 171-180 and references therein.

[11] Zhao, W., Ghorannevis, Z., Chu, L., Toh, M., Kloc, C., Tan, P-H. and Eda, G. (2013). ACS Nano 7 (1), 791-797.

[12] Ratha, S. and Rout, C. S. (2013). ACS Appl. Mater. Interfaces 5, 11427−11433.

[13] Berkdemir, A., Gutiérrez, H. R., Botello-Me´ndez, A. R., Perea-López, N., Elías, A. L., Chia, C-I., Wang, B., Crespi, V. H., Lo´pez-Urías, F., Charlier, J-C., Terrones, H. and Terrones, M. (2013). Sci. Rep. 3, 1755; DOI:10.1038/srep01755.

[14] Zink, N., Pansiot, J., Kieffer, J., Therese, H. A., Panthöfer, M., Rocker, F., Kolb, U. and Tremel, W. (2007). Chem. Mater. 19, 6391–6400.

[15] O'Brien, M., Lee, K., Morrish, R., Berner, N. C., McEvoy, N., Wolden, C. A. and Duesberg, G. S. (2014). Chemical Physics Letters 615, 6-10.

[16] Cao, S., Liu, T., Hussain, S., Zeng, W., Peng, X. and Pan, F. (2014). Materials Letters 129, 205–208.

[17] Lan, C., Li, C., Yin, Y. and Lin, Y. (2015). Nanoscale 7, 5974-5980.

[18] Wang, F., Li, H., Yuan, Z., Sun, Y., Chang, F., Deng, H., Xie, L. and Li, H. (2016). RSC Adv. 6, 79343-79349.

[19] Zhang, H., Wu, R., Chen, Z., Liu, G., Zhang, Z. and Jiao, Z. (2012). CrystEngComm 14, 1775-1782.

[20] Cao, Q., Dai, Y. W., Xu, J., Chen, L., Zhu, H. Sun, Q. Q. and Zhang, D. W. (2017). ACS Appl. Mater. Interfaces 9, 18215-18221.

[21] He, Z., Wang, X., Xu, W., Zhou, Y., Sheng, Y., Rong, Y., Smith, J. M. and Warner, J. H. (2016). ACS Nano 10, 5847-5855

[22] Jha, R. K., Wan, M., Jacob, C. and Guha, P. K. (2018). IEEE Sensors Journal 18 (9), 3494-3501.

[23] Perrozzi, F., Emamjomeh, S. M., Paolucci, V., Taglier, G., Ottaviani, L. and Cantalini, C. (2017). Sensors and Actuators B 243, 812-822.

[24] Qin, Z., Ouyang, C., Zang, J., Wan, L., Wang, S., Xie, C. and Zeng, D. (2017). Sensors and Actuators B 253, 1034-1042.

[25] Donarelli, M., Prezioso, S., Perrozi, F., Bitsi, F., Nardone, M., Giancanterini, L., Cantalini, C. and Ottaviano, L. (2015). Sensors and Actuators B 207, 602-613.

[26] Rong, Y., He, K., Pacios, M., Robertson, A. W., Bhaskran, H. and Warner, J. H. (2015). ACS Nano 9 (4), 3695-3703.

[27] Magdassi, S., Grouchko, M. and Kamyshny, A. (2010). Materials 3(9), 4626-4638.

[28] Ang, T. P., Wee, T. S. A. and Chin, W. S. (2004). J. Phys. Chem. B 108 (30), 11001-11010.

[29] Dang, T. M. D., Le, T. T. T., Fribourg-Blanc, E. and Dang, M. C. (2011). Adv. Nat. Sci.: Nanosci. Nanotechnol. 2, 025004, 1-7.

[30] Deng, D., Jin, Y., Cheng, Y., Qi, T. and Xiao, F. (2013). ACS Appl. Mater. Interfaces 5, 3839-3846.

[31] Park, B. K., Jeong, S., Kim, D., Moon, J., Lim, S. and Kim, J. S. (2007). Journal of Colloid and Interface Science 311, 417-424.

[32] Kanninen, P., Johans, C., Merta, J. and Kontturi, K. (2008). Journal of Colloid and Interface Science 318, 88-95.

[33] Jeong, S., Lee, S. H., Jo, Y., Lee, S. S., Seo, Y-H., Ahn, B. W., Kim, G., Jang, G-E., Park, J-U., Ryu, B-H. and Choi, Y. (2013). J. Mater. Chem. C 1, 2704-2710.

[34] Dinesha, G., Dabera, M. R., Walker, M., Sanchez, A. M., Pereira, H. J., Beanland, R. and Hatton, R. A. (2017). Nature Communications 8 (1894), 1-10.

[35] Jeong, S., Woo, K., Kim, D., Lim, S., Kim, J. S., Shin, H., Xia, Y. and Moon, J. (2008). Adv. Funct. Mater. 18, 679-686.

[36] Engels, V., Benaskar, F., Jefferson, D. A., Johnson, B. F. G. and Wheatley, A. E. H. (2010). Dalton Trans. 39, 6496-6502.

[37] Granata, G., Yamaoka, T. and Pagnanelli, F. and Fuwa, A. (2016). J Nanopart Res 18,133, 1-12.

[38] Arulmozhi, K. T. and Mythili, N. (2013). AIP Advances 3, 122122, 1-9.

[39] Campisi, S., Schiavoni, M., Chan-Thaw, C. E. and Villa, A. (2016). Catalysts 6, 185, 1-21.

[40] Niu, Z. and Li, Y. (2014). Chem. Mater. 26, 72-83.

[41] Yang, G-b., Chai, S-t., Xiong, X-j., Zhang, S-m., Yu, L-g. and Zhang., P-y. (2012). Trans. Nonferrous Met. Soc. China 22, 366-372.

[42] Stankus, D. P., Lohse, S. E., Hutchison, J. E. and Nason, J. A. (2011). Environ. Sci. Technol. 45, 3238-3244.

[43] Airo, M. A., Rodrigues, R., Gqoba, S., Ntholeng, N., Otieno, F., Moloto, M. J., Greenshields, M. W. C. C., Hummelgen, I. A. and Moloto, N. (2016). Sensors and Actuators B 236, 116-125.

[44] Xaba, T., Moloto, M. J. and Moloto, N. (2015). Mater. Lett. 146, 91-95.

[45] Moloto, N., Moloto, M. J., Coville, N. J., Ray, S. S. (2011). Journal of Crystal Growth 324 (1), 41-52.

[46] Wang, S., Gao, Q. and Wang, J. (2005). J. Phys. Chem. B 109, 17281-17289.

[47] Wang, Z. D., Yoshida, M. and George, B. (2013). Computational and Theoretical Chemistry 1017, 91-98.

[48] Zhang, X., Xu, H., Wang, J., Ye, X., Lei, W., Xue, M., Tang, H. and Li, C. (2016). Nanoscale Research Letters 11:442, 1-9.

[49] Cao, S., Liu, T., Hussain, S., Zeng, W., Peng, X. and Pan, F. (2014). Materials Letters 129, 205–208.

[50] Feng, C., Huang, L., Guo, Z. and Liu, H. (2007). Electrochemistry Communications 9, 119-122.

[51] Panigrahi, P. K. and Pathak, A. (2008). Sci. Technol. Adv. Mater. 9, 045008, 1-6 and references therein.

[52] Cao, S., Zhao, C., Peng, L. (2016). Materials Letters 164, 452-455 and references therein.

[53] Yang, J., Voiry, D., Ahn, S. J., Kang, D., Kim, A. Y., Chhowalla, M. and Shin, H. S. (2013). Angew. Chem. Int. Ed. 52, 1-5.

[54] Remskar, M., Virsek, M. and Jesih, A. (2008). Nano Lett. 8 (1), 76-80.

[55] Klokkenburg, M., Hilhorst, J. and Erné, B. H. (2207). Vibrational Spectroscopy 43, 243–248.

[56] Ramasamy, P., Manivasakan, P. and Kim, J. CrystEngComm. (2015) 015, 17, 807-813.

[57] Xu, X., Zhao, P., Wang, D., Sun, P., You, L., Sun, Y., Liang, X., Liu, F., Chen, H. and Lu, G. (2013). Sensors and Actuators B 176, 405-412.

[58] Xu, X., Wang, D., Wang, W., Sun, P., Ma, J., Liang, X., Sun, Y., Ma, Y., Lu, G. (2012). Sensors and Actuators B 171-172, 1066-1072.

[59] Huang, L. and Fan, H. (2012). Sensors and Actuators B 171-172, 1257-1263.

[60] Feng, C., Huang, L., Guo, Z. and Liu, H. (2007). Electrochemistry Communications 9, 119-122 and references therein.

[61] Ye, C., Meng, G., Jiang, Z., Wang, Y., Wang, G. and Zhang, L. (2002). J. Am. Chem. Soc. 124, 15180-15181.

[62] Sun, S., Li, Z. and Chang, X. (2011). Materials Letters 65, 3164-3166.

[63] Wu, J. and Fu, X. (2007). Materials Letters 61, 4332-4335.

[64] Rout, C. S., Joshi, P. D., Kashid, R. V., Joag, D. S., More, M. A., Simbeck, A. J.,Washington, M., Nayak, S. K. and Late, D. J. (2013). Sci. Rep. 3, 3282; DOI:10.1038/srep03282.

[65] Jha, R. K. and Guha, P. K. (2016). Nanotechnology 27, 475503, 1- 11.

[66] Zeng, L., Tao, L., Tang, C., Zhou, B., Long, H., Chai, Lau, S. P. and Tsang, Y. H. (2016). Sci. Rep. 6, 20343; doi: 10.1038/srep20343.

[67] Sun, S., Zou, Z., Min, G. (2009). Materials Chemistry and Physics 114, 884-888.

[68] McCreary, K. M., Hanbicki, A. T., Singh, S., Kawakami, R. K., Jernigan, G. G., Ishigami, M., Ng, A., Brintlinger, T. H., Stroud, R. M. and Jonker, B. T. (2016). Sci. Rep. 6, 35154; doi:10.1038/srep35154.

[69] Cong, C., Shang, J., Wu, X., Cao, B., Peimyoo, N., Qiu, C., Sun, L. and Yu, T. (2014). Adv. Optical Mater. 2, 131–136.

[70] del Corro, E., Botello-Méndez, A., Gillet, Y., Elias, A. L., Terrones, H., Feng, S., Fantini, C., Rhodes, D., Pradhan, N., Balicas, L., Gonze, X., Charlier, J-C., Terrones, M. and Pimenta, M. A. (2016). Nano Lett. 16, 2363-2368.

[71] Tan, H., Fan, Y., Zhou, Y., Chen, Q., Xu, W., and Warner, J. H. (2016). ACS Nano 10, 7866-7873.

[72] Notley, S. M. (2013). Journal of Colloid and Interface Science 396, 160-164.

[73] Khalil, H. M., Khan, M. F., Eom, J. and Noh, H. (2015). ACS Appl. Mater. Interfaces 7, 23589-23596.

[74] Wang, F., Kinloch, I., Wolverson, D., Tenne, R., Zak, A., O'Connell, E., Bangert, U. and Young, R. J. (2016). 2D Mater. 4, 015007, 1-15.

[75] Lee, J-U., Kim, M. and Cheong, H. (2015). Appl Microsc 45 (3), 126-130.

[76] Zeng, L., Tao, L., Tang, C., Zhou, B., Long, H., Chai, Y., Lau, S. P., and Tsang, Y. H. (2016). Sci. Rep. 6, 20343; doi: 10.1038/srep20343.

[77] Georgiou, T., Yang, H., Jalil, R., Chapman, J., Novoselov, K. S. and Mishchenko, A. (2014). Dalton Trans 43, 10388- 10391.

[78] Kuru, C., Choi, D., Kargar, A., Liu, C. H., Yavuz, S., Choi, C., Jin, S. and Bandaru, P. R. (2016). Nanotechnology 27, 195501, 1-7.

[79] Varghese, S. S., Varghese, S. H., Swaminathan, S., Singh, K. K. and Mittal, V. (2015). Electronics 4, 651-687.

[80] Tan, H., Fan, Y., Zhou, Y., Chen, Q., Xu, W. and Warner, J. H. (2016). ACS Nano 10, 7866-7873.

[81] Chiu, S-W. and Tang, K-T. (2013). 13, 14214-14247.

[82] Jiang, Z., Zhang, Y., Yang, G., Yang, K., Zhang, S., Yu, L. and Zhang, P. (2016). Tribol Lett 61:24.

[83] Altavilla, C., Sarno, M. and Ciambelli, P. (2011). Chem. Mater. 23, 3879-3885.

[84] Jung, W., Lee, S., Yoo, D., Jeong, S., Miró, P., Kuc, A., Heine, T. and Cheon, J. (2015). J. Am. Chem. Soc., 137, 7266−7269.

[85] Atewologun, A., Ge, W. and Stiff-Roberts, A. D. (2013). Journal of Electronic Materials 42, 809-814.

[86] Liu, I-S., Lo, H-H., Chien, C-T., Lin, Y-Y., Chen, C-W., Chan, Y-F., Sue, W-F. and Liou, S-C. J. Mater. Chem. 18, 675-682.

[87] Zhang, J., Wang, Q., Wang, L., Li, X. and Huang, W. (2015). Nanoscale 7, 10391-10397.

[88] Li, X., Li, X., Li, Z., Wang, J. and Zhang, J. (2017). Sensors and Actuators B 240, 273-277.

[89] McCreary, K. M., Hanbicki, A. T., Jernigan, G. G., Culbertson, J. C. and Jonker, B. T. (2016). Sci. Rep. 6, 19159; doi: 10.1038/srep19159, 1-7.

[90] Pagona, G., Bittencourt, C., Arenal, R. and Tagmatarchis, N. (2015). Chem. Commun. 51, 12950-12953.

[91] Liu, S., Shen, B., Niu, Y. and Xu, M. (2017). Journal of Colloid and Interface Science 488, 20-25.

[92] Lukowski, M. A., Daniel, A. S., English, C. R., Meng, F., Forticaux, A., Hamers, R.J. and Jin, S. (2014). Energy Environ. Sci., 7, 2608-2613.

[93] Huo, N., Li, Y., Kang, J., Li, R., Xia, Q. and Li, J. (2014). Applied Physics Letters 104, 202406, 1-4.

[94] Lin, L., Xu, Y., Zhang, S., Ross, I. M., Ong, A. C. M. and Allwood, D. A. (2013). ACS Nano 7 (9), 8214-8223.

[95] Koçak, Y., Akaltun, Y. and Gür, E. (2016). Journal of Physics: Conference Series 707**,** 012028, 1-7.

[96] Zhou, L., Yan, S., Pan, L., Wang, X., Wang, Y. and Shi, Y. (2016). Nano Res. 9 (3), 857-865.

[97] Wang, Q. H., Kalantar-Zadeh, K., Kis, K., Coleman, J. N. and Strano, M. S. (2012). Nature Nanotechnology 7, 699-712.

[98] Tonti, D., Varsano, F., Decker, F., Ballif, C., Regula, M., Remš kar, M. (1997). J. Phys. Chem. B 101, 2485-2490 and references therein.

[99] Yan, Y., Zhang, C., Gu, W., Ding, C., Li, X and Xian, Y. (2016). J. Phys. Chem. C 120, 12170-12177.

[100] Zhu, B., Chen, X. and Cui, X. (2015). Sci. Rep. 5, 9218; DOI:10.1038/srep09218.

[101] Frey, G. L., Elani, S., Homyonfer, M., Feldman, Y., Tenne, R. (1998). Physical Review B 57 (11), 6666-6671.

[102] Kang, K. N., Godin, K. and Yang, E-H. (2015). Sci. Rep. 5, 13205; doi: 10.1038/srep13205.

[103] Song, X-X., Zhang, Z-Z., You, J., Liu, D., Li, H-O., Cao, G., Xiao, M. and Guo, G-P. (2015). Sci. Rep. 5, 16113; doi: 10.1038/srep16113.

[104] Schenato, Ricardo, C. L. A., Scardi, P., Edla, R., Miotello, A., Orlandi, M., Morrish, R. (2016). Applied Catalysis A: General 510, 156-160.

[105] Lee, J-H. (2009). Sensors and Actuators B 140, 319-336.

[106] Li, Y-X., Guo, Z., Su, Y., Jin, X-B., Tang, X-H., Huang, J-R., Huang, X-J., Li, M-Q. and Liu, J-H. (2017). ACS Sens. 2, 102-110.

[107] Qin, Z., Zeng, D., Zhang, J., Wu, C., Wen, Y., Shan, B., Xie, C. (2017). Applied Surface Science 414, 244–250.

[108] Late, D. J., Huang, Y-K. Liu, B., Acharya, J., Shirodkar, S. N., Luo, J., Yan, A., Charles, D., Waghmare, U. V., Dravid, V. P. and Rao, C. N. R. (2013). ACS Nano 7 (6), 4879-4891.

[109] Marr, I., Groß, A. and Moos, R. (2014). J. Sens. Sens. Syst. 3, 29-46.

[110] Li, H., Yin, Z., He, Q., Li, H., Huang, X., Lu, G., Fam, D. W. H., Tok, A. I. Y., Zhang, Q. and Zhang, H. (2012). Small 8 (1), 63-67.

[111] Qin, Z., Zeng, D., Zhang, J., Wu, C., Wen, Y., Shan, B. and Xie, C. (2017). Applied Surface Science 414, 244-250.

[112] Cantalini, C., Valentini, L., Armentano, I., Lozzi, L., Kenny, J. M. and Santucci, S. (2003). Sensors and Actuators B 95, 195-202.

3.2 Application of tristimulus analysis to a set of geometrically different OLA/WS_2 nanostructures for the detection of toxic VOCs

3.2.1 Introduction

The importance of gas sensing cannot be overemphasized as it impacts all aspects of everyday life. It has therefore become imperative to develop intelligent devices for the swift detection and determination of the presence of toxic and volatile gases in the surrounding environment at lowest of levels. Many volatile organic compounds are toxic and have a very fast evaporation rate which poses problems in the health of humans at high concentration levels in air and have been suspected as the cause of many allergies and diseases of the lungs and skin [1]. For practical reasons, sensors should be capable of operating at relatively low temperatures and have short calibration time. They must also have fast recovery time between runs and easy maintenance procedures to maintain low operating costs, short recording and analysis times, particularly when used as on-line systems, and also should have high sensor array stability [2].

The conventional lock-and-key design of chemical sensors is the most common option where the device responds only to one specific analyte. Even though chemical sensors are highly sensitive, their lack of specificity to analytes has restricted their wide application in gas sensing. The alternative design, referred to as chemical sensor arrays seeks to embrace this problem instead of overcoming it. Chemical sensor arrays involve the use of a large number of different types of broadly responsive elements which respond to a wide range of vapours or classes of vapours [1-5, 7-10]. Data measured by the different sensors is processed and classified via a pattern recognition method based on the characteristic pattern produced by each element of the array [8, 11-14] in response to a gas stimulus to create electronic fingerprints [7, 15]. These patterns are then used to construct a database, and train a pattern recognition technique for identification and classification of odorants in the vapour phase [7, 14, 15]. The identification and classification is possible even in real mixtures like cheeses and beers without breaking the mixture down into its individual components prior to analysis [2, 16]. A pattern recognition technique is employed based on the problems to be solved [15]. Methods like Linear Discriminant Analysis (LDA) and Principal Component Analysis (PCA) have been used to discriminate subtle differences in chemicals and to classify the gases [8, 15, 17-20]. The electronic signal is transformed into numerical data in vector form (2-D image) [15, 21]. Tristimulus analysis (TA) is a less numerical intensive method unlike PCA [22, 23]. It reduces the collective response information of the sensor set system into a

bidimensional plot [24]. Unlike the other methods, TA involves the use of three sensors as the magnitude of three orthogonal sensor response vectors in the tristimulus space [25, 26]. Chemical diversity is an important requirement of the elements for use in chemical sensor arrays to ensure a response over a wide cross section of analytes [16, 18] even those for which the array was not originally designed [16]. The design for the arrays is relatively simple, rapid and non-invasive compared to their classical counterparts.

Tuning the morphology of nanostructures during synthesis and composition of the sensor material is one of the approaches undertaken to improve gas sensing properties. 3D hierarchical structure-based morphologies boast combined features of micrometer and nanometer scaled building blocks in one crystal [27]. They are the higher dimensional structures that are assembled from low dimensional nano-sized building blocks such as 0D nanoparticles, 1D nanowires, nanorods, and nanotubes; and 2D nanosheets [26, 26, 29]. For example, 3D flower-like hierarchical structure is assembled from many 2D nanosheets while the urchin-like nanostructures consist of 1D nanowires or nanorods [30]. This morphology displays well-aligned porous structures which are associated with a large surface area, a high surface-to-volume ratio, low density and surface permeability [26, 29-31]. The large surface area enhances relative response while the pores ensure fast gas diffusion in/out of the sensing film to improve response and recovery time [32].

The most widely used class of gas sensors are the metal-oxide gas sensors [2]. Zhang *et al.* demonstrated the identification and pattern recognition of Chinese liquors based on their different flavours using nanoparticles of ZnO gas sensor array [33]. The elements are chemically different in the sense that the ZnO was doped by MnO_2, TiO_2 and Co_2O_3. Lonergan and co-workers used 17 elements of carbon black in a sensor array, each with a different organic polymer to identify and classify VOCs [34]. The arrays successfully resolved ethanol from methanol, toluene from benzene. A wide range of sensor arrays have been used by different researchers to identify and classify compounds in different matrices e.g. proteins [13, 35], heavy metal ions [17], aromatic amines [36]. Kanan *et al*. demonstrated how they were able to selectively detect methanol from dimethyl methylphosphonate (DMMP) by using a dual sensor based on porous and nonporous WO_3 powders [37]. In this study, we successfully demonstrate that selectivity towards various gaseous species by nanostructures derived from the same material but with different size and morphology has merits in gas sensing. These nanostructures were used to detect and identify vapours of

acetone, acetonitrile, ammonia, butanol, chloroform, dimethylformamide, ethanol, formic acid, isopropanol, methanol and toluene. The generalized tristimulus analysis was used to classify the responses to the different analytes to obtain analyte-specific patterns. To the best of our knowledge, a study into exploring the possibility of using materials of the same chemical composition from the same growth medium has not been investigated. The response of a gas sensor is also highly dependent on its operating temperature [29, 38, 39]. Oxide-based gas sensors are known for requiring use of an external heater which is associated with major disadvantages like high operating temperatures and thermal stability problems [40, 41]. It is therefore desirable to develop a gas sensor that can be operated at room temperature. In this study, sulfur based gas sensors were synthesized and applied for their potential in gas sensing at room temperature. WS_2, with its tunable band gap which is size-dependant is inherently desirable for chemoresistive gas sensing applications [41]. The OLA/WS_2 nanostructures used in this study were synthesized by a simple colloidal method.

3.2.2. Experimental set-up

3.2.2.1 Chemicals and materials

As-prepared OLA/WS_2 nanostructures (15, 45, 60, 180 and 240 min) were used as obtained. The solvents were all of analytical grade and were used as received. Interdigitated electrodes consisting of ENIG (Electroless Nickel Immersion Gold) electrodes in 18 pairs of 7.9 mm long with a gap of 0.1 mm between them and patterned onto FR4 substrate were purchased from Micropress SA.

3.2.2.2 Characterization of OLA/WS_2 nanostructures

The evolution of the morphology was monitored by a scanning electron microscope (SEM) by FEI Nova NanoLab FIB/SEM.

3.2.2.3 Gas sensing measurements

All electrical measurements were performed in the dark at room temperature; and under dry N_2 environment unless otherwise stated. An LCR meter (Agilent 4284A 20 Hz – 1 MHz Precision LCR meter) attached to a computer interfaced with a GPIB was used for data acquisition. An operational voltage and frequency of 1000 mV and 10 kHz were selected respectively due to their higher signal-to-noise ratio. The systems were allowed to stand for 1h before measurements were performed. The change in conductance was monitored for 50 s, providing a stable baseline before the 1.5 µL of the analyte was introduced. The opening was

sealed off immediately to prevent moisture from getting into the chamber. The devices were allowed to reach saturation point (around 300 s) before the next increment.

(i) Preparation of gas chambers

Clean and dry 1 L filtering Erlenmeyer flasks (Figure 3.25) was used as gas chamber. The chamber was covered with aluminium foil and black tape to create a dark environment. The aluminium foil was earthed to reduce its noise contribution. The chamber was flushed with dry nitrogen to ensure low humidity conditions.

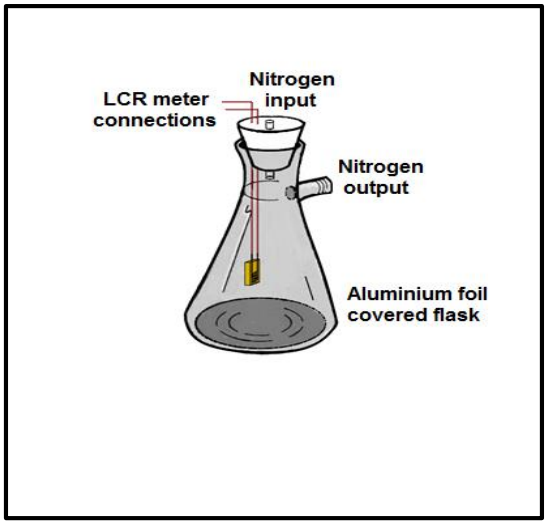


Figure 3.25: Schematic representation of the gas chamber used in sensor measurements.

(ii) Chemical vapour measurements under limited light and low humidity environment

The devices were placed in a 1 L glass jar with a rubber stopper covered with an aluminium foil as shown in Figure 3.25. After fitting the contacts of the device in the cover, the chamber was purged with dry nitrogen for 30 min thereby decreasing the humidity inside the chamber to less than 20 % RH.

(iii) Tristimulus analysis

The tristimulus analysis used in this study is a mathematical tool similar to that reported previously [25]. This approach basically takes the intensity of the responses of an array of three different unspecific sensors (R_1, R_2 and R_3) and assumes that the sensors present a response when there is an analyte in the system; and has an absence of response when the

analyte is absent. Following these requirements, the intensity of each response can be written as:

$$R_1 = \alpha^A[\mathrm{A}],\ R_2 = \beta^A[\mathrm{A}] \text{ and } R_3 = \gamma^A[\mathrm{A}] \qquad (3.1)$$

where α^A, β^A and γ^A are the sensitivities of each respective sensor to analyte A and [A] is the concentration of the target analyte A. Taking the intensities of response, a tridimensional vector can be constructed:

$$\vec{r} = \alpha^A[\mathrm{A}]\hat{x} + \beta^A[\mathrm{A}]\hat{y} + \gamma^A[\mathrm{A}]\hat{z} \qquad (3.2)$$

This tristimulus vector has some specificities that can be used to determine an analyte independently of the concentration of the analyte. As the sensitivities are constant (linear response), if the concentration of the target VOC change only the [A] term will change equally for all the sensors, and the tristimulus vector will keep the same direction and sense, change only their magnitude. In order to analyse and establish a fingerprint for the target analyte, we calculate the coordinates of the point where the vector intercepts a unitary plan given by:

$$x + y + z = 1 \qquad (3.3)$$

The coordinates of the point are, mathematically described as:

$$\begin{cases} x = \frac{R_1}{R_1+R_2+R_3} = \frac{\alpha^A}{\alpha^A+\beta^A+\gamma^A} \\ y = \frac{R_2}{R_1+R_2+R_3} = \frac{\beta^A}{\alpha^A+\beta^A+\gamma^A} \\ z = \frac{R_3}{R_1+R_2+R_3} = \frac{\gamma^A}{\alpha^A+\beta^A+\gamma^A} \end{cases} \qquad (3.4)$$

Graphically, the interception point can be described as in Figure 3.26. This point will be the fingerprint for the analyte A. In order to measure a system that can have a different analyte B or C, different vector will be constructed and will intercept the plane in a different spatial region (only if the sensitivity of set is different for each analyte).

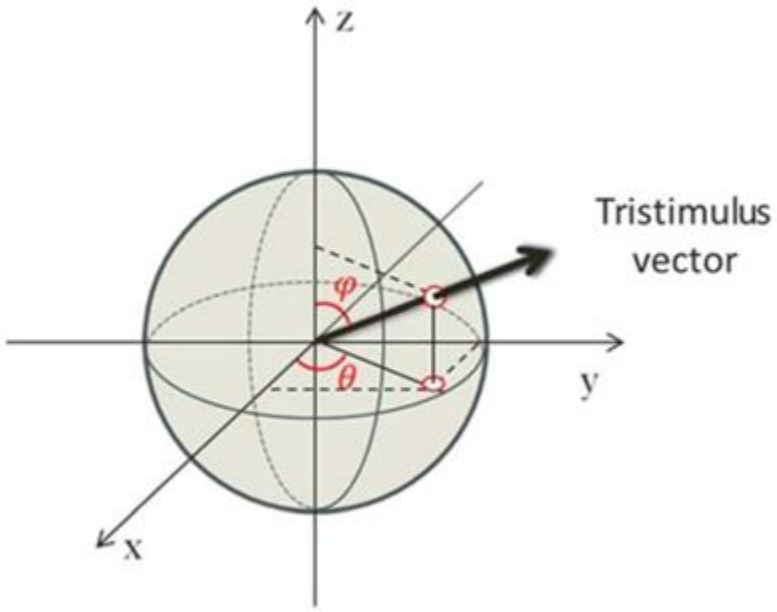


Figure 3.26: Geometrical representation of the tristimulus vector crossing a unitary spherical shell, projecting the crossing point to the xy plane, and the two angles (θ and ϕ) that characterize the direction of the vector [25].

3.2.3. Results and discussion

3.2.3.1 Characterization of the OLA/WS_2 nanostructures

Nanostructure sizes and morphology of the powders were studied using a scanning electron microscope (SEM) by FEI Nova NanoLab FIB/SEM. Figure 3.27 shows the OLA/WS_2 nanostructures as presented by the SEM micrographs. The presence of both the 3D hierarchical structures (also known as microflowers) and nanosheets at all reaction times but at varied quantities with respect to reaction time hinted at one morphology transforming into another. It was therefore important to understand the growth mechanism of these nanostructures. Therefore, the aliquots of the nanostructures were taken at different reaction times and subjected to SEM analysis for monitoring of the development of the morphologies. Generally, it was found that the microflowers were the dominating morphology at both 15 and 45 min because they were found in most areas of the copper grid while the nanosheets were fewer. The microflowers are made up of 'petals' which are seen as still closed at 15 min.

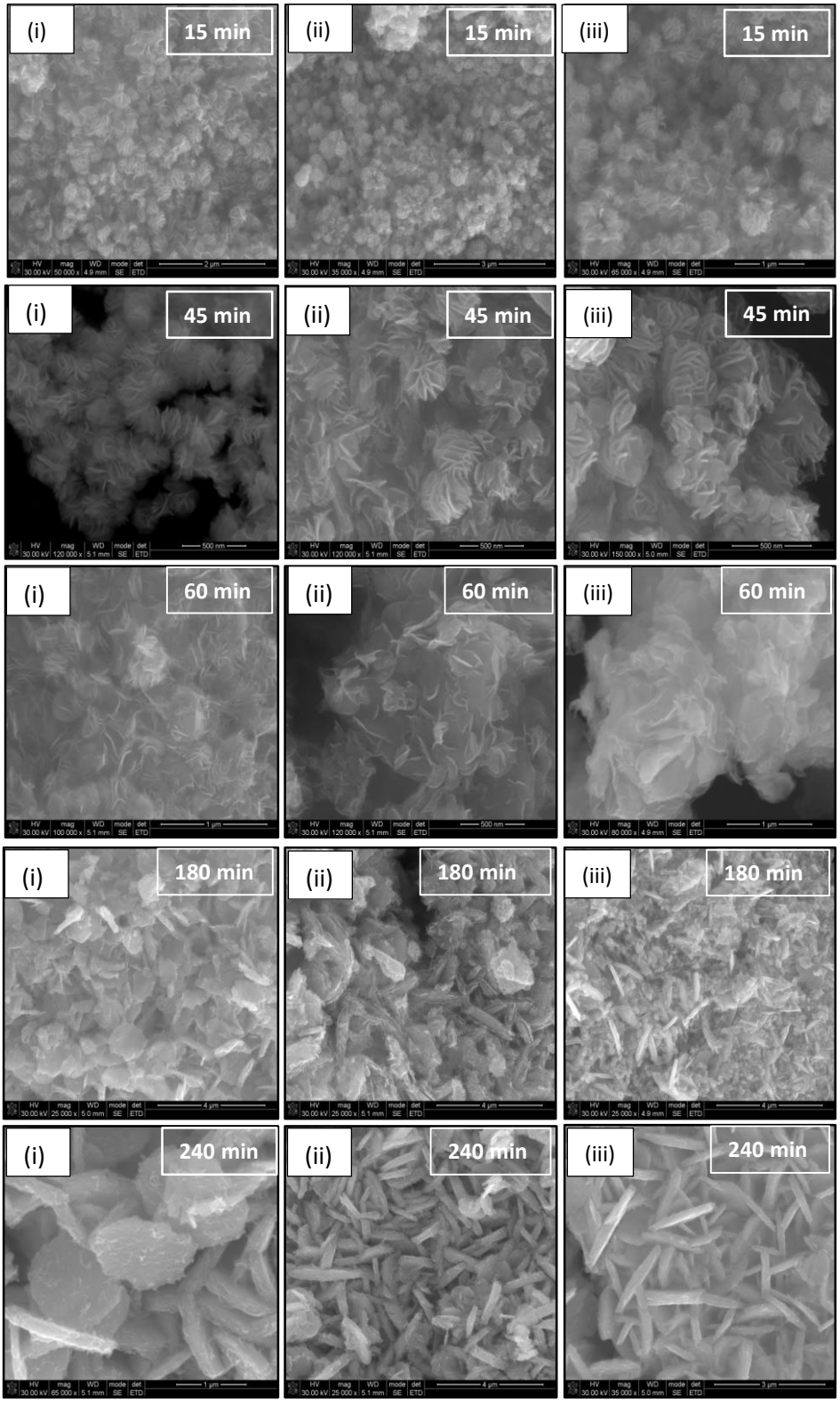


Figure 3.27: SEM micrographs of OLA/WS_2 nanostructures at 15, 45, 60, 180 and 240 min.

However, the ‘petals’ start opening up at 45 min revealing 2D nanosheets that make up the microflower. Heating the reaction mixture to 60 min saw the microflower morphology disintergrating completely into 2D nanosheets which started to curl up and were found to be the dominating morphology. Further heating of the reaction mixture to 180 min resulted in the nanosheets rolling up and were later transformed into 1D rod-like nanostructures. Micrographs at 240 min showed that the rod-like nanostructures were the dominant morphology.

3.2.3.2 Gas sensing performance

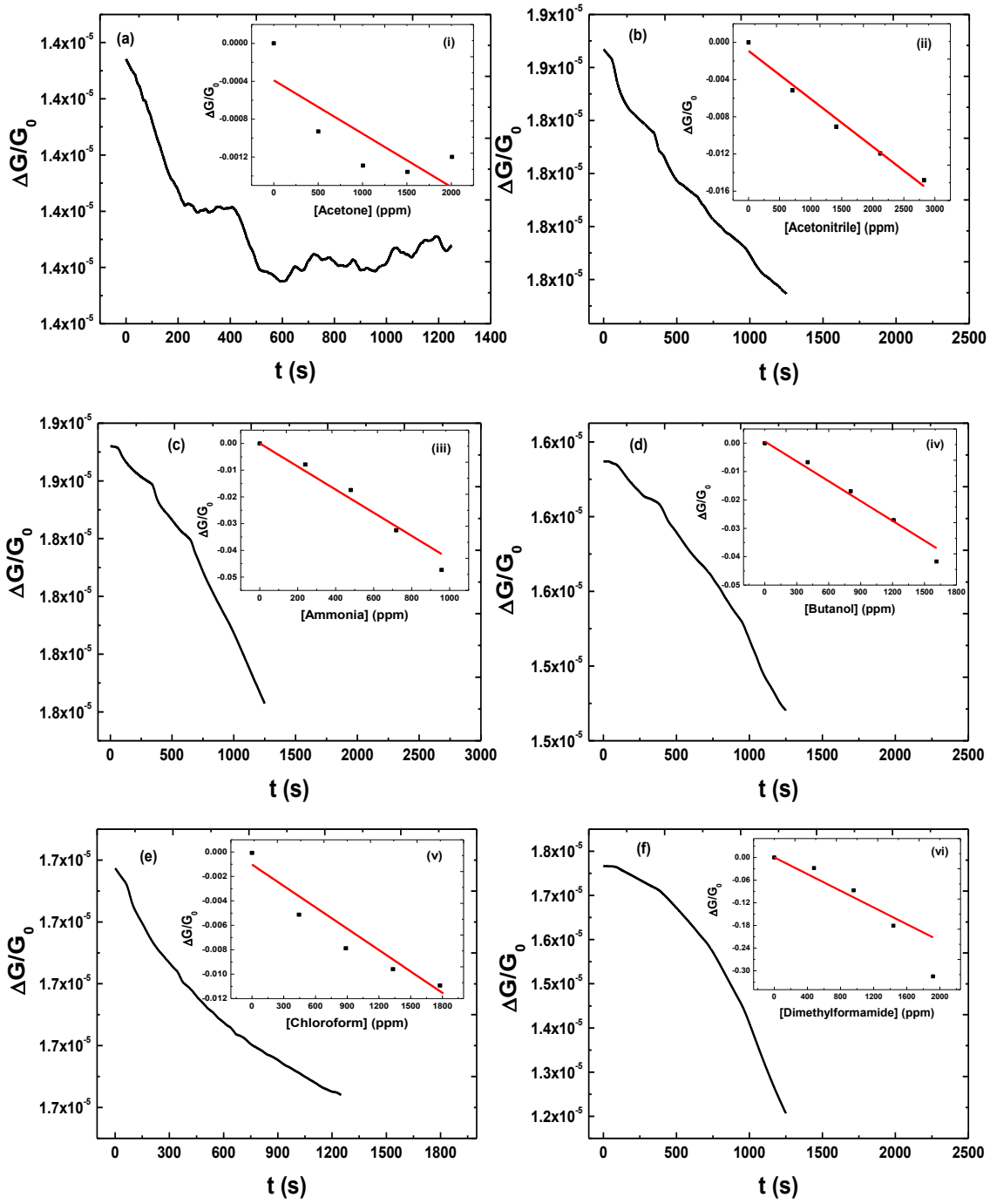
(i) Sensitivity and response to different analytes

Generally, TMDCs are considered as one of the most promising candidates for the next generation room temperature gas sensors [45]. Room temperature gas sensing properties of the five different OLA/WS_2 nanostructure based devices were evaluated by measuring their electrical conductance during repeated exposure to different solvent vapours. Figures 3.28-3.32 (a-k) show the change in conductance vs time within a wide concentration range of different VOCs. Insets (i) – (xi) of Figures 3.28-3.32 show calibration curves of 15, 45, 60, 180 and 240 min responses *vs.* concentration of each analyte. The sensor response is correlated with the change in conductance before and after interaction with the target analyte using the following equation:

$$R = \frac{(G_{gas} - G_{nitrogen})}{(G_{nitrogen})} \times 100 \qquad (3.5)$$

where G_{gas} is the value of conductance after exposure of the sensor to the target analyte, and $G_{nitrogen}$ is the conductance in N_2. The slope of this curve represents sensitivity of the target analyte. The devices generally displayed significant sensitivity to detect NH_3 and VOCs within a wide range of concentration as shown in the insets (i) – (xi). The conductance of OLA/WS_2 sensors derived from 15, 45 and 60 min nanostructures decreased with the adsorption of all eleven analytes giving a negative sensitivity. This kind of gas sensing behaviour was displayed by MoS_2 gas sensors upon exposure to NH_3 vapours [46]. The sensitivity shows a dependence on the concentration of the target analyte. The sensors displayed sensitivity to all target analytes with the polar ones (reducing agents) eliciting stronger response than the non-polar ones (chloroform and toluene).

(a) Sensitivity and response of 15 min to different analytes



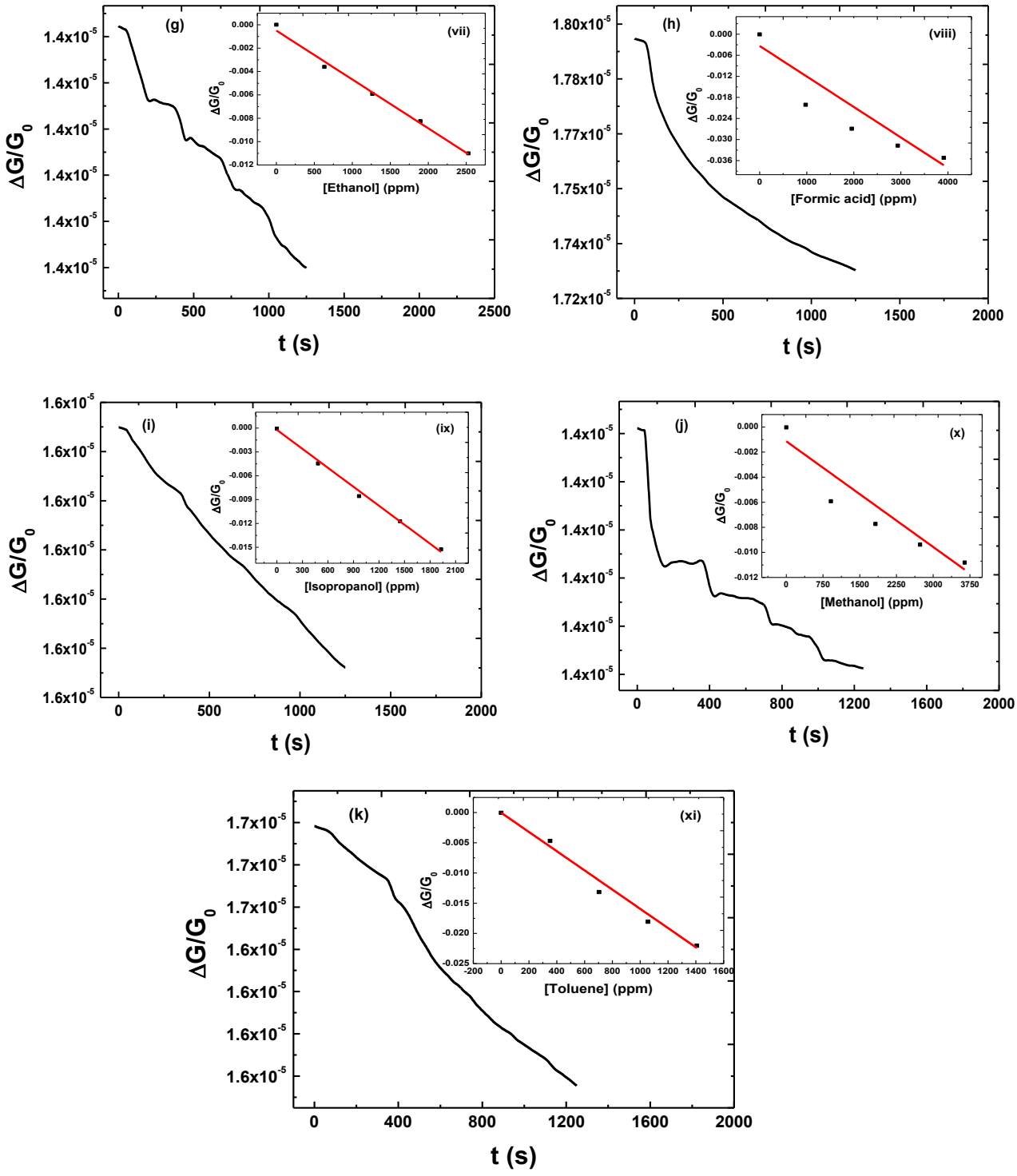
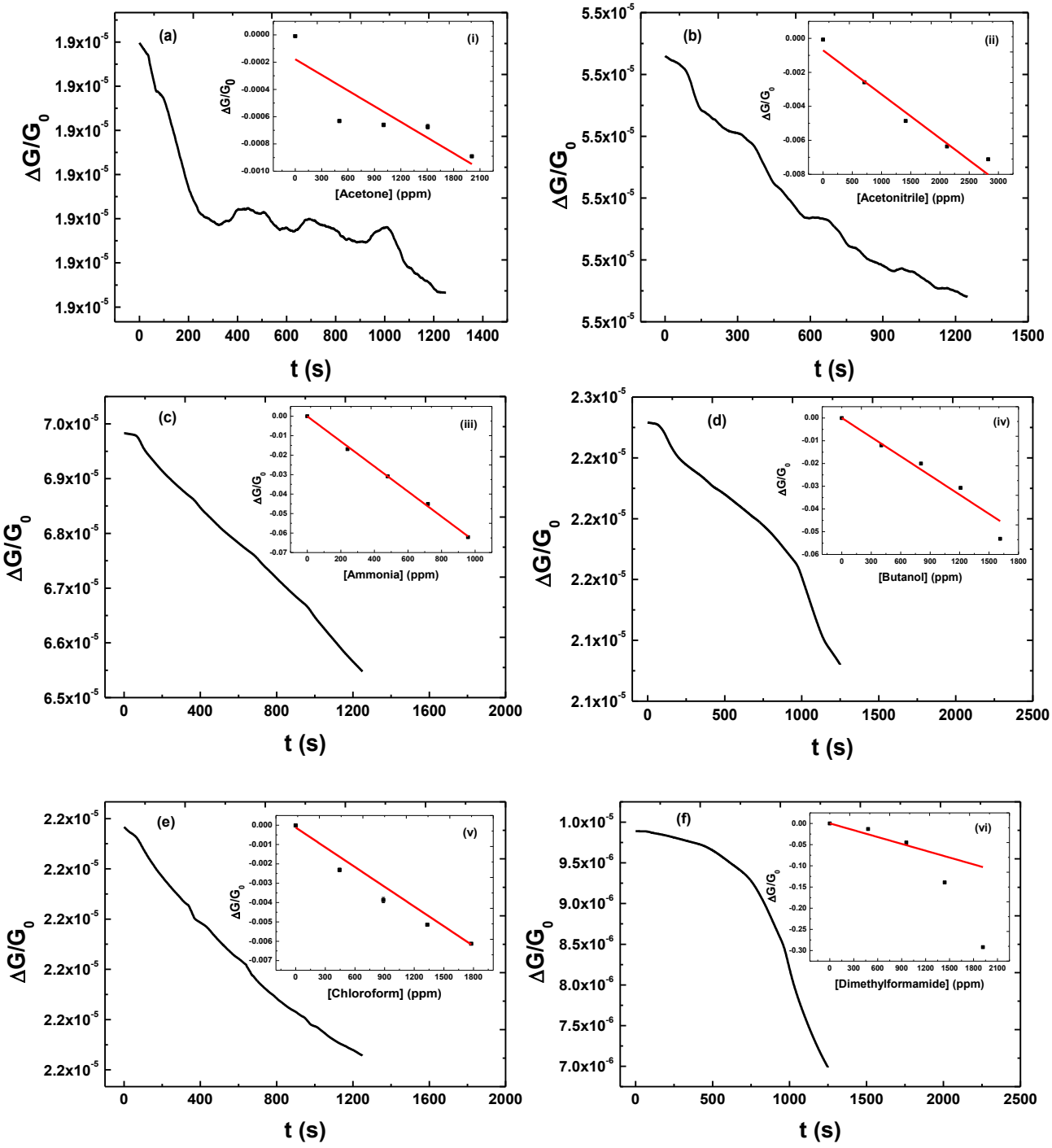


Figure 3.28 (a-k) Relative conductance of OLA/WS_2 sensors (15 min) vs time for NH_3 and several VOCs. Corresponding relative conductance *vs* concentration for each analyte (i-xi) [inset].

It is evident that the sensors are more sensitive to NH_3 and ethanol. Such strong gas response was previously observed for field effect transistors (FETs) based on multilayer WS_2 nanoflakes with NH_3 and ethanol [45, 47].

The short reaction time based sensors displayed a better sensitivity to all analytes than the long reaction times with the exception of NH_3 which gave a positive sensitivity with 180 and 240 min. Of the three short reaction time based sensors (15, 45 and 60 min), the OLA/WS_2 sensor derived from the 45 min nanostructures showed the highest sensitivity for all the analytes. The performance of the sensors is seen to be directly related to the morphology of the nanostructures. This is corroborated by the highest sensitivity towards NH_3 displayed by OLA/WS_2 sensors derived from 45 min nanostructures. At this reaction time, the 'petals' of the microflowers have opened up to expose the well aligned porous 2D nanosheets that make up the microflower. The exposed surface area is larger, ensuring that the gas sensing reaction occurs not only on the surface but also on the inner part of the microflower. This increases gas diffusion leading to high sensitivity [31]. It is known that with a complex and dense arrangement of nanobuilding blocks in a hierarchical structure, the surface area increases at the expense of pore size and total volume [28]. On the other hand, nanoparticles in a hierarchical structure are arranged in a highly periodic and porous manner unlike their agglomerated counterparts [26]. Such high performance towards NH_3 was also observed by other researchers when unusual 3D flower-shaped SnS_2 nanostructures were used as room temperature sensor materials [48]. This was attributed to the atomically thin layers with perfect crystallinity within planar directions, large surface area; and increased concentration of the charge carrier and carrier charge mobility of the nanostructures. The sensitivity of the 15 min nanostructures is not as high compared to the 45 min due to the fact that the 'petals' at this reaction are still tightly closed meaning that the gas reaction takes place only on the surface of the microflowers. As the reaction time is prolonged, a change in morphology is seen accompanied by a decrease in sensor sensitivity. The results depicted in Figures 3.28 are summarized in Table 3.6. The working principle, gas sensing mechanism and response/recovery curves of these sensors were discussed in detail in section 3.1.

(b) Sensitivity and response of 45 min to different analytes



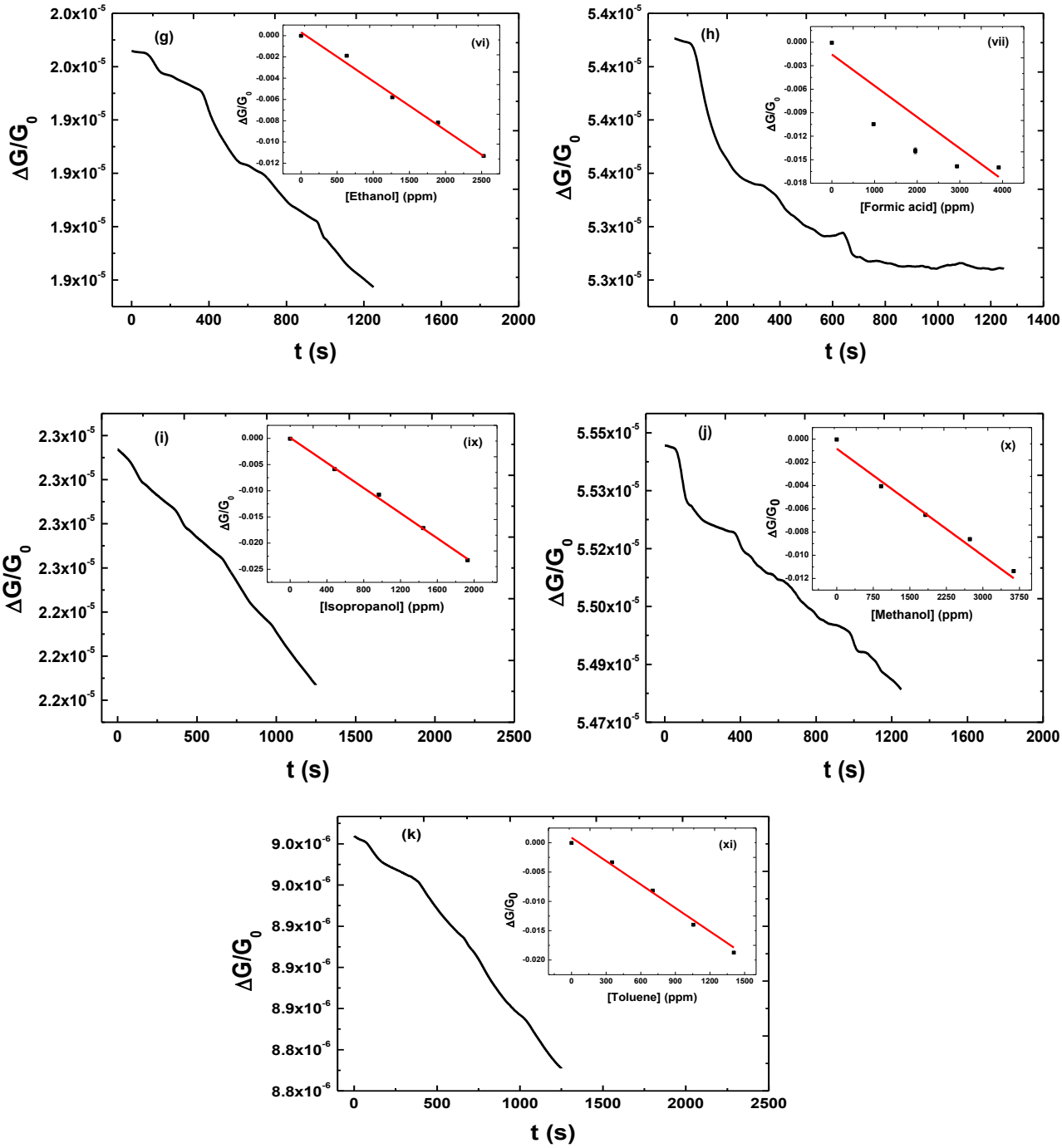
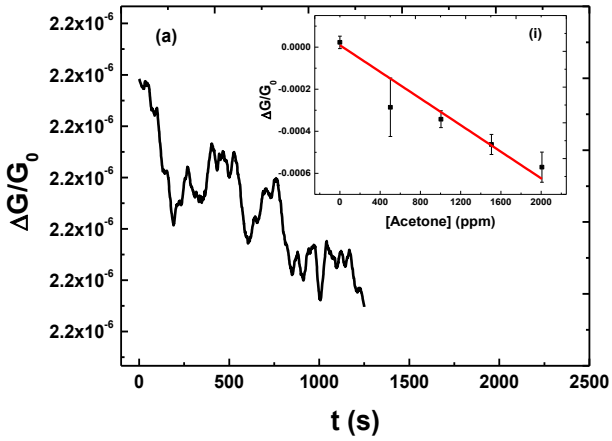
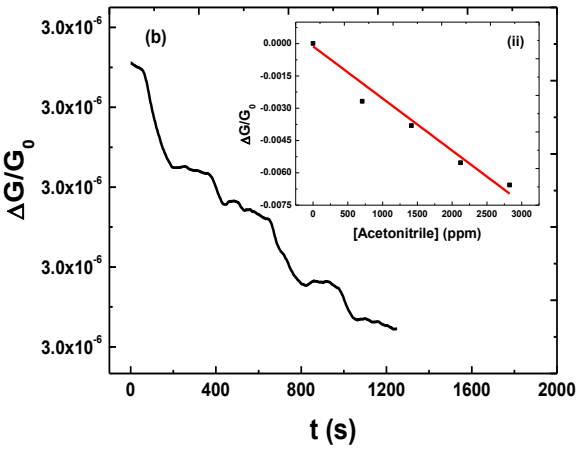
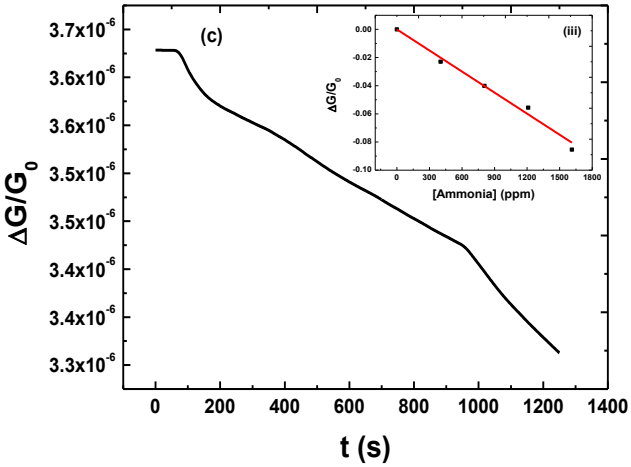


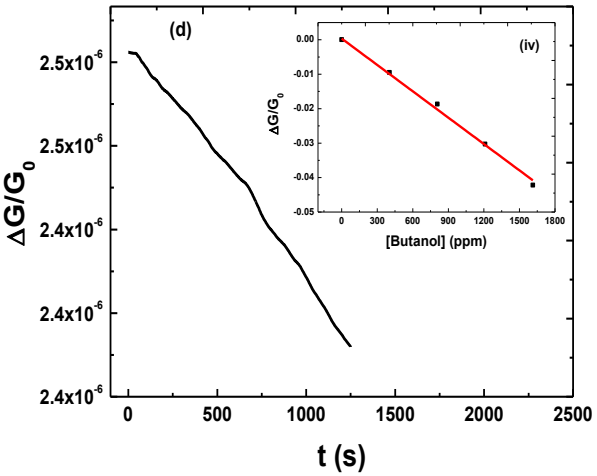
Figure 3.29: (a-k) Relative conductance of OLA/WS_2 sensors (45 min) vs time for NH_3 and several VOCs. Corresponding relative conductance *vs* concentration for each analyte (i-xi) [inset].

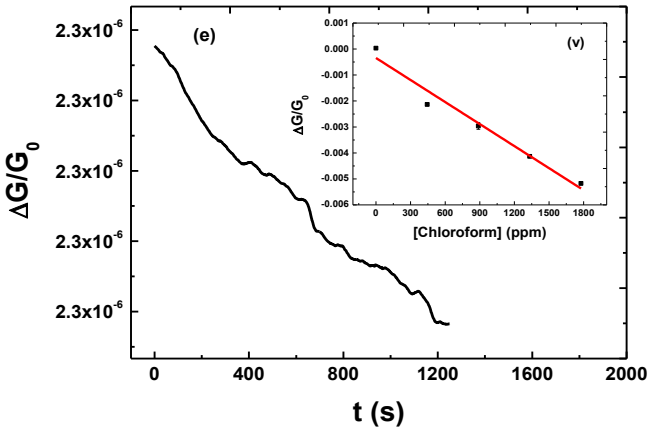
(c) Sensitivity and response of 60 min to different analytes

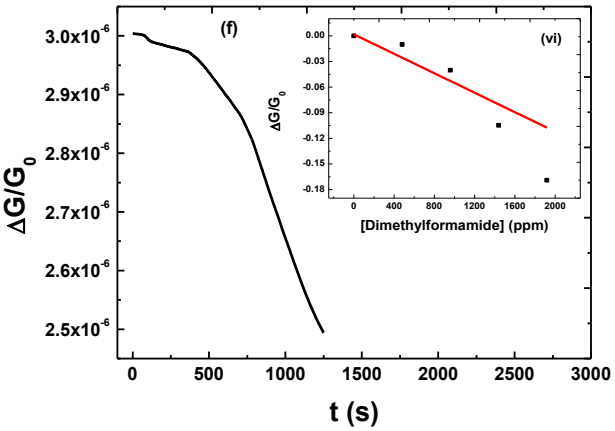












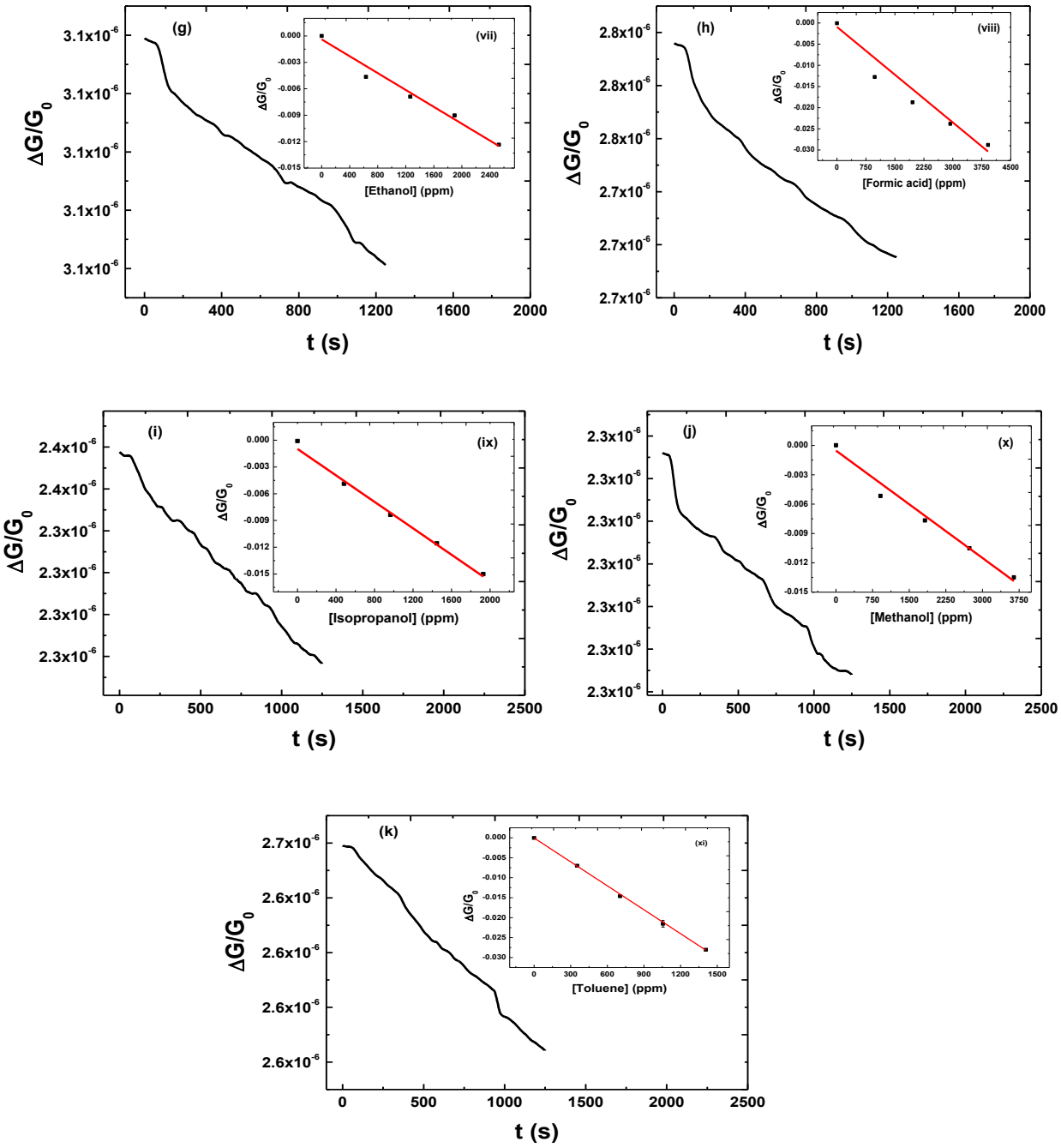
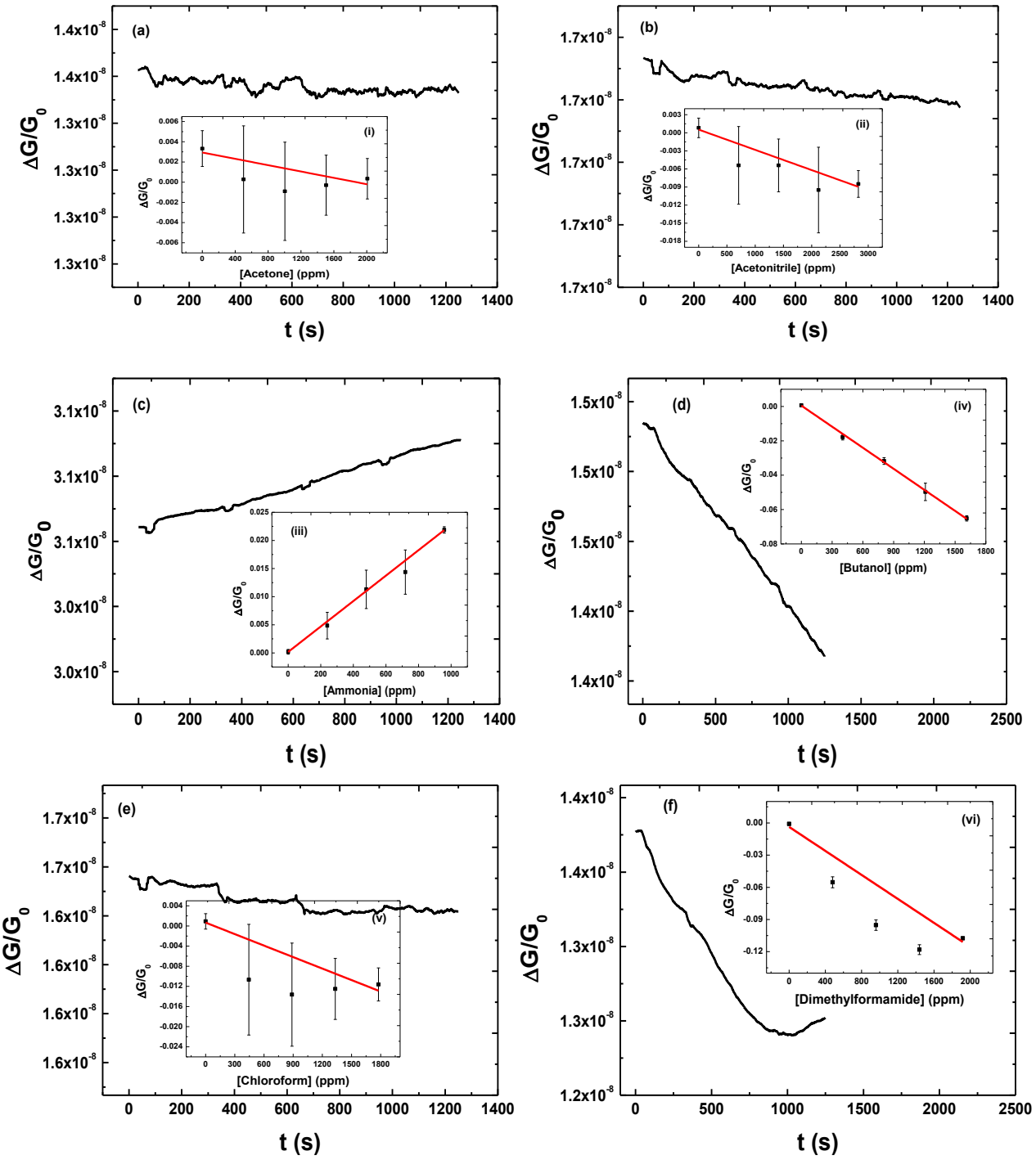


Figure 3.30: (a-k) Relative conductance of OLA/WS_2 sensors (60 min) vs time for NH_3 and several VOCs. Corresponding relative conductance *vs* concentration for each analyte (i-xi) [inset].

(d) Sensitivity and response of 180 min to different analytes



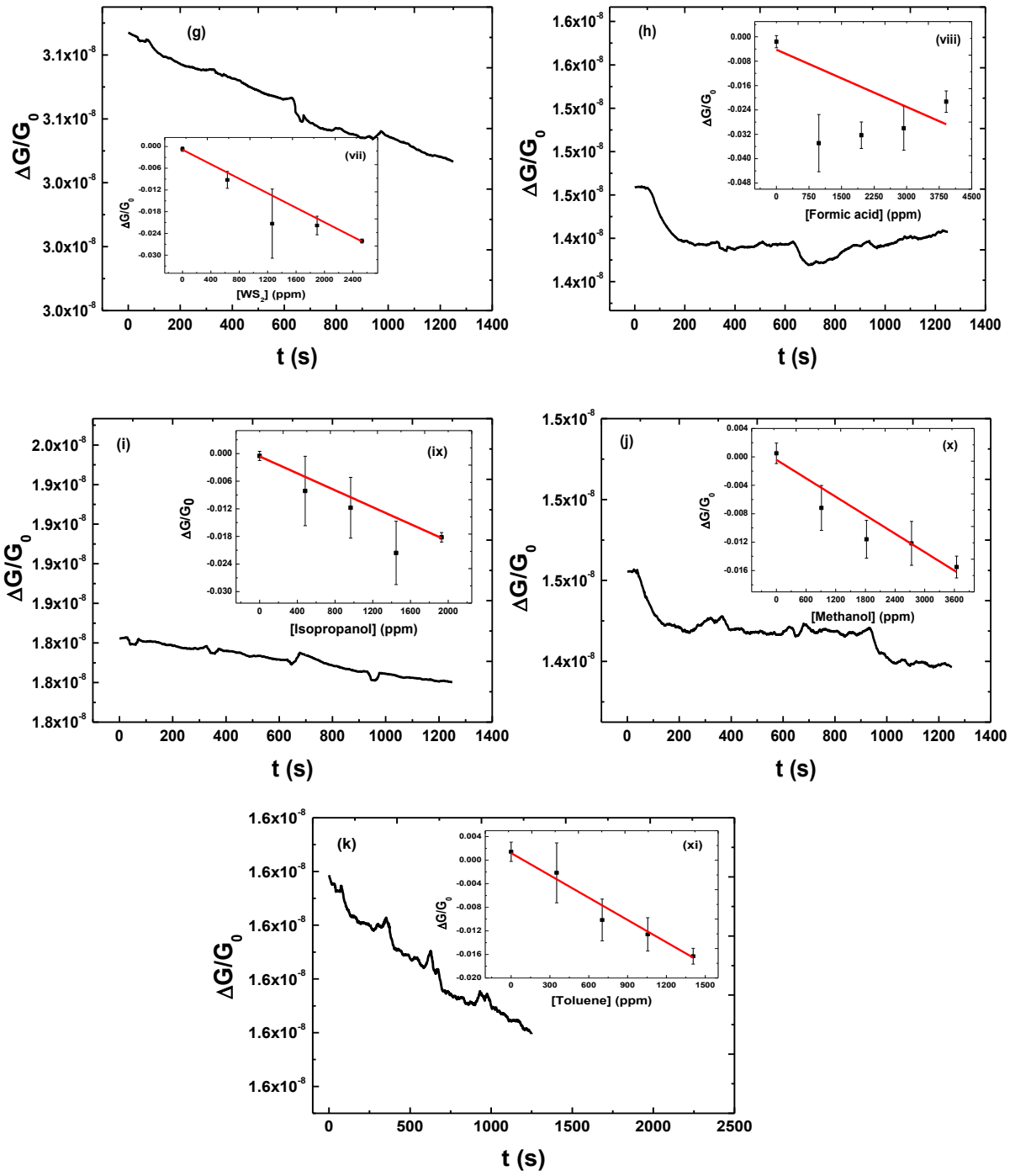
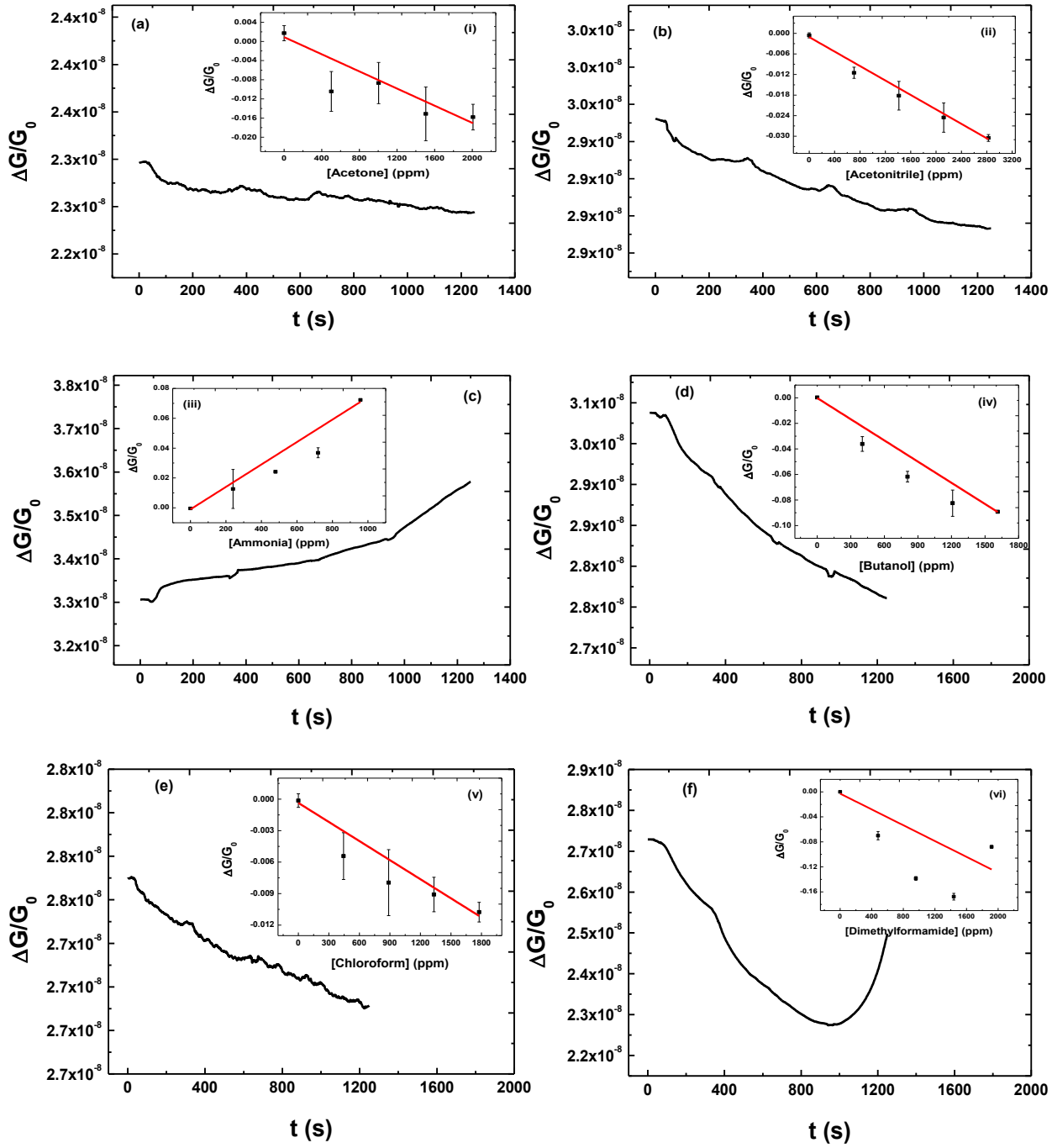


Figure 3.31: (a-k) Relative conductance of OLA/WS_2 sensors (180 min) vs time for NH_3 and several VOCs. Corresponding relative conductance *vs* concentration for each analyte (i-xi) [inset].

(e) Sensitivity and response of 240 min to different analytes



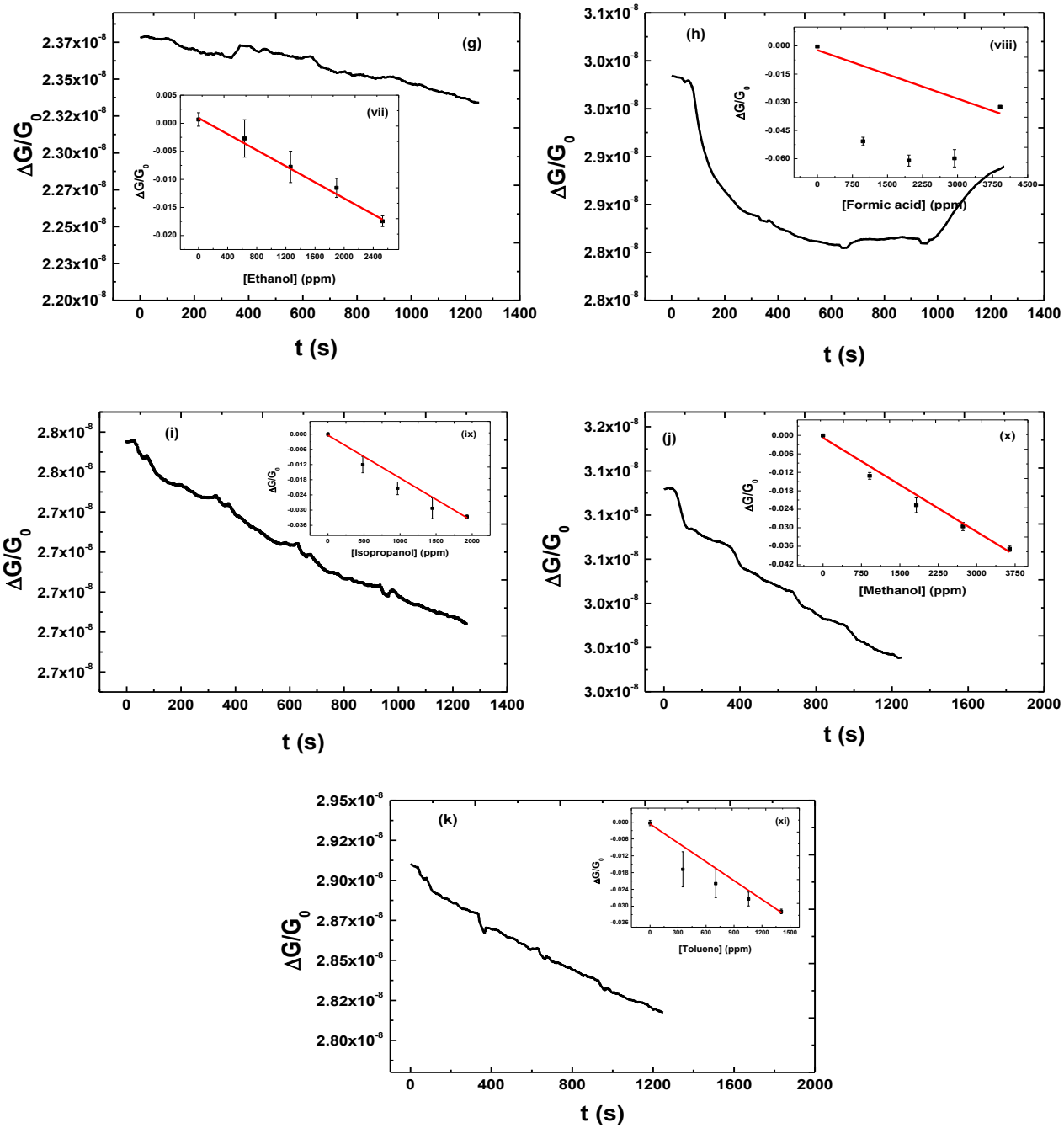


Figure 3.32: (a-k) Relative conductance of OLA/WS_2 sensors (240 min) vs time for NH_3 and several VOCs. Corresponding relative conductance *vs* concentration for each analyte (i-xi) [inset].

Table 3.6: A summary of conductance changes ($\Delta G/G$) and standard deviation for each sensor element exposed to eleven solvents (at 1.5 µL increments).

	Sensor element								
	15 min	SD	45 min	SD	60 min	SD	180 min	SD	240 min
Acetone	-5.63×10^{-7}	-2.4×10^{-7}	-3.8×10^{-7}	1.2×10^{-7}	-3.2×10^{-7}	2.6×10^{-8}	-1.6×10^{-6}	5.5×10^{-7}	-9.0×10^{-6}
Acetonitrile	-5.15×10^{-6}	4.0×10^{-7}	-2.6×10^{-6}	3.0×10^{-7}	-2.4×10^{-6}	1.7×10^{-7}	-3.4×10^{-6}	4.4×10^{-7}	-1.1×10^{-5}
Ammonia	-4.33×10^{-5}	3.4×10^{-6}	-6.4×10^{-5}	1.1×10^{-6}	$-5.\times10^{-5}$	2.1×10^{-6}	2.3×10^{-5}	2.6×10^{-7}	7.5×10^{-5}
Butanol	-2.33×10^{-5}	2.4×10^{-6}	-2.8×10^{-5}	2.3×10^{-6}	-2.6×10^{-5}	7.8×10^{-7}	-4.1×10^{-5}	7.3×10^{-7}	-5.5×10^{-5}
Chloroform	-5.8×10^{-6}	7.6×10^{-7}	-3.4×10^{-6}	1.5×10^{-7}	-2.8×10^{-6}	2.8×10^{-7}	-7.6×10^{-6}	1.4×10^{-6}	-6.1×10^{-6}
Dimethylformamide	-1.1×10^{-4}	2.5×10^{-5}	-5.4×10^{-5}	2.6×10^{-5}	-5.7×10^{-5}	1.8×10^{-5}	-5.6×10^{-5}	6.4×10^{-6}	-6.3×10^{-5}
Ethanol	-4.2×10^{-6}	2.3×10^{-7}	-4.6×10^{-6}	3.4×10^{-7}	-4.8×10^{-6}	3.5×10^{-7}	-1.0×10^{-5}	2.7×10^{-7}	-7.2×10^{-6}
Formic acid	-8.7×10^{-06}	1.4×10^{-6}	-4.0×10^{-6}	8.1×10^{-7}	-7.5×10^{-6}	6.8×10^{-7}	-6.3×10^{-6}	3.0×10^{-6}	-8.6×10^{-6}
Isopropanol	-8.0×10^{-6}	2.5×10^{-7}	-1.2×10^{-5}	2.8×10^{-7}	-7.4×10^{-6}	4.0×10^{-7}	-9.2×10^{-6}	5.4×10^{-7}	-1.7×10^{-5}
Methanol	-2.8×10^{-6}	4.4×10^{-7}	-3.1×10^{-6}	3.4×10^{-7}	-3.7×10^{-6}	2.6×10^{-7}	-4.3×10^{-6}	5.6×10^{-7}	-1.0×10^{-5}
Toluene	-1.6×10^{-5}	6.6×10^{-7}	-1.3×10^{-5}	1.0×10^{-6}	-2.0×10^{-5}	1.6×10^{-7}	-1.3×10^{-5}	6.7×10^{-7}	-2.2×10^{-5}

*The values are averages of four exposures to each solvent.

(ii) Tristimulus analysis

The power of the OLA/WS_2 based sensors array to identify and discriminate different VOCs was investigated using tristimulus analysis. Tristimulus analysis is a mathematical tool used to quantify collective response of the constituent sensors [24]. It allows for the calculation of the coordinates that univocally represent the set of responses in a two-dimensional graph [25]. To demonstrate the utility of the tristimulus analysis, the sensors array was prepared with three OLA/WS_2 nanostructures from different reaction times. For application in sensor arrays, the required moderate chemical selectivity of the OLA/WS_2 based nanostructures can be achieved through variation of their size and morphology. Figure 3.33 shows the collective patterns derived from the output of the sensor arrays through the application of tristimulus

analysis to the sensor responses of 15, 45 and 60 min nanostructures before grouping of analytes into different classes. The tristimulus coordinates 'x' and 'y' are represented by 15 and 45 min; and 60 min respectively. The tristimulus analysis response patterns displayed outstanding separation as well as overlaps between NH_3 and some of the VOCs' patterns. Each cluster of data corresponds to a unique fingerprint that is characteristic of a specific analyte. The star (*) symbol represents the real or ideal value for each target analyte tested in this study.

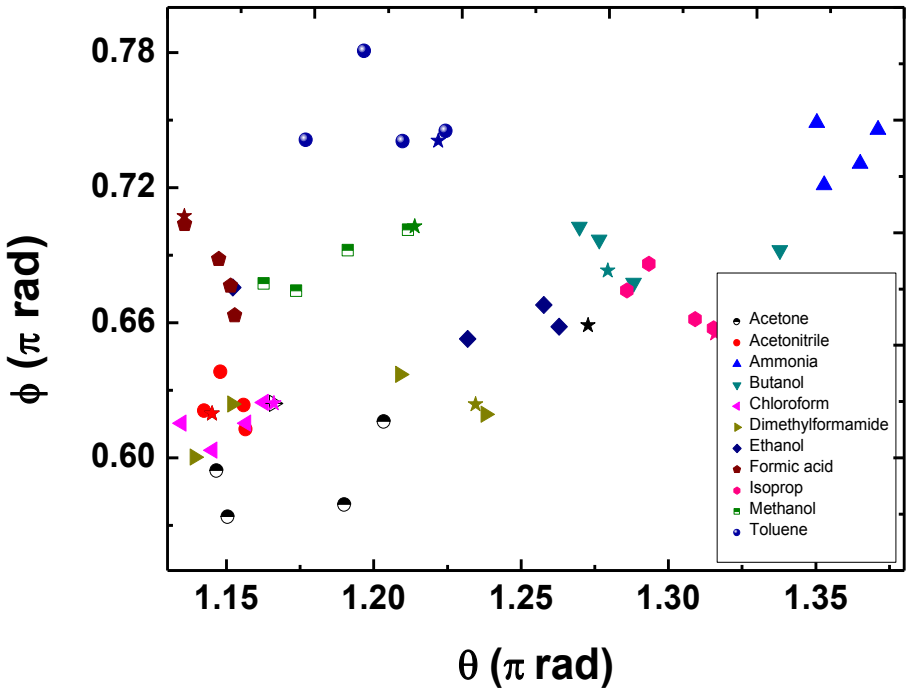


Figure 3.33: Bidimensional plot showing the separation between NH_3 and the various VOCs using an array of three OLA/WS_2 chemiresistive sensors (15, 45 and 60 min) at different concentrations.

The discrimination of NH_3 from different combinations of the VOCs tested in this study is detailed in Figure 3.34 [(a) - (h)]. Once again, it is evident that the sensors have a high selectivity towards NH_3.

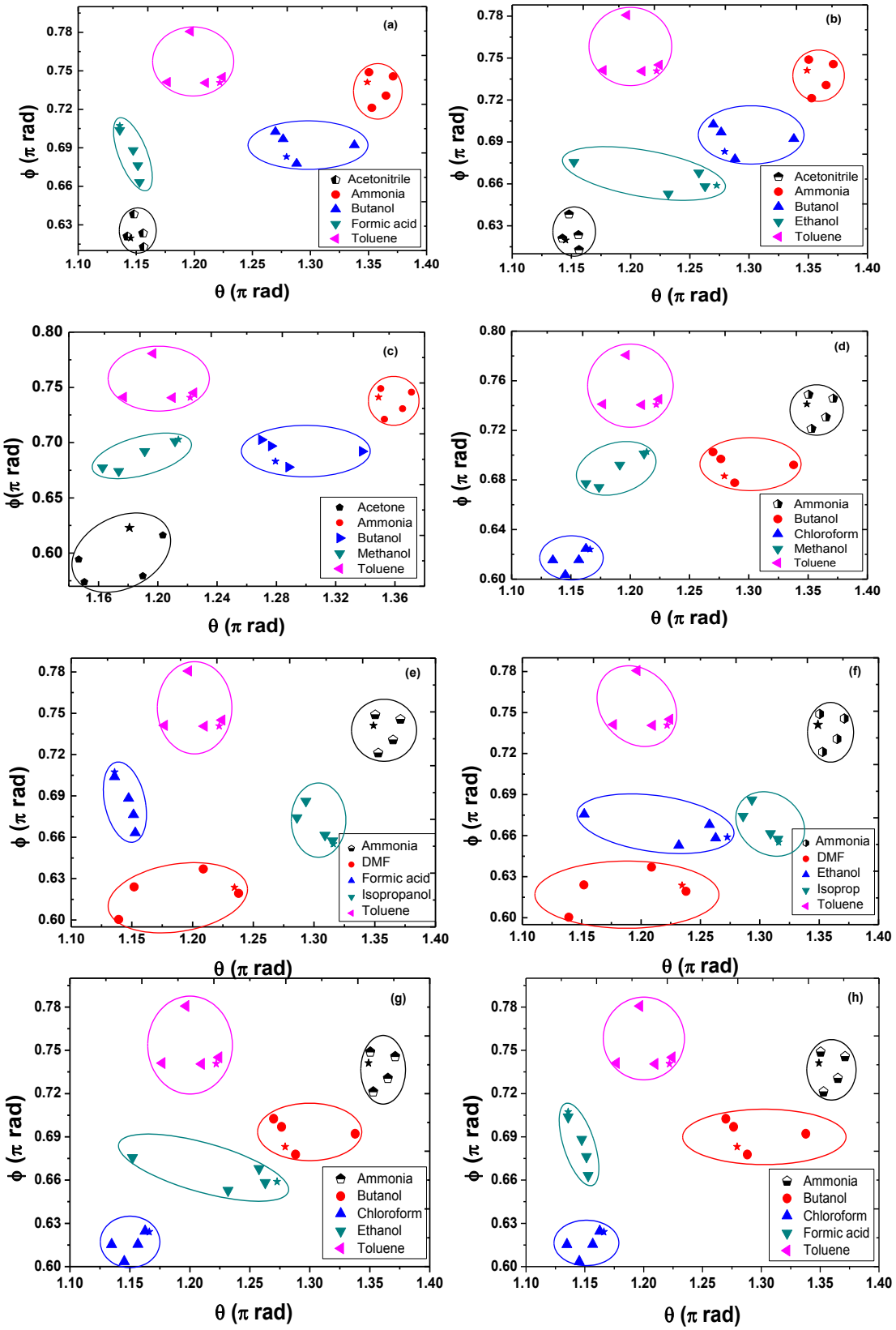


Figure 3.34: TA results differentiating NH_3 from polar and non-polar VOCs at different concentrations.

Figures 3.35 and 3.36 show the discrimination between the solvents according to their specific groups. Non-polar: chloroform and toluene; polar aprotic: (acetone and acetonitrile); polar protic solvents (ammonia, formic acid and alcohols)n respectively.

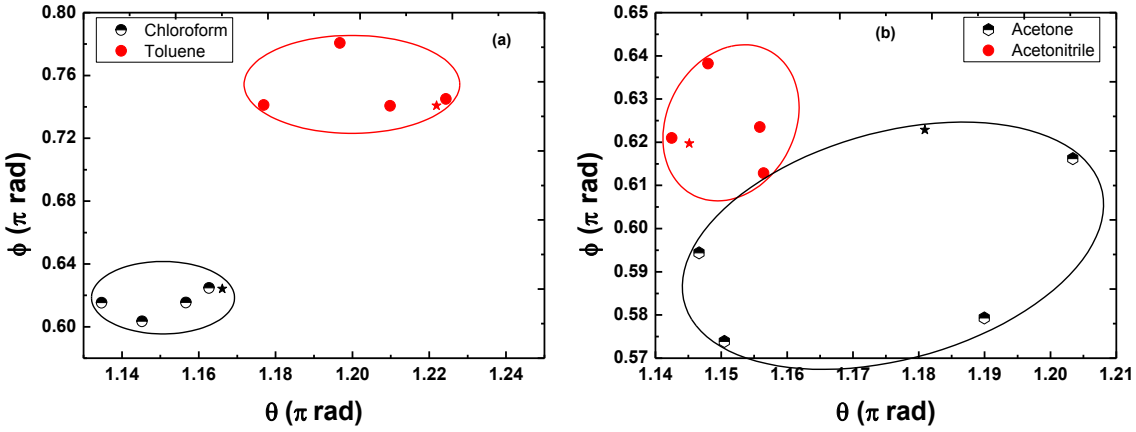


Figure 3.35: Discrimination between (a) non-polar solvents; (b) polar aprotic.

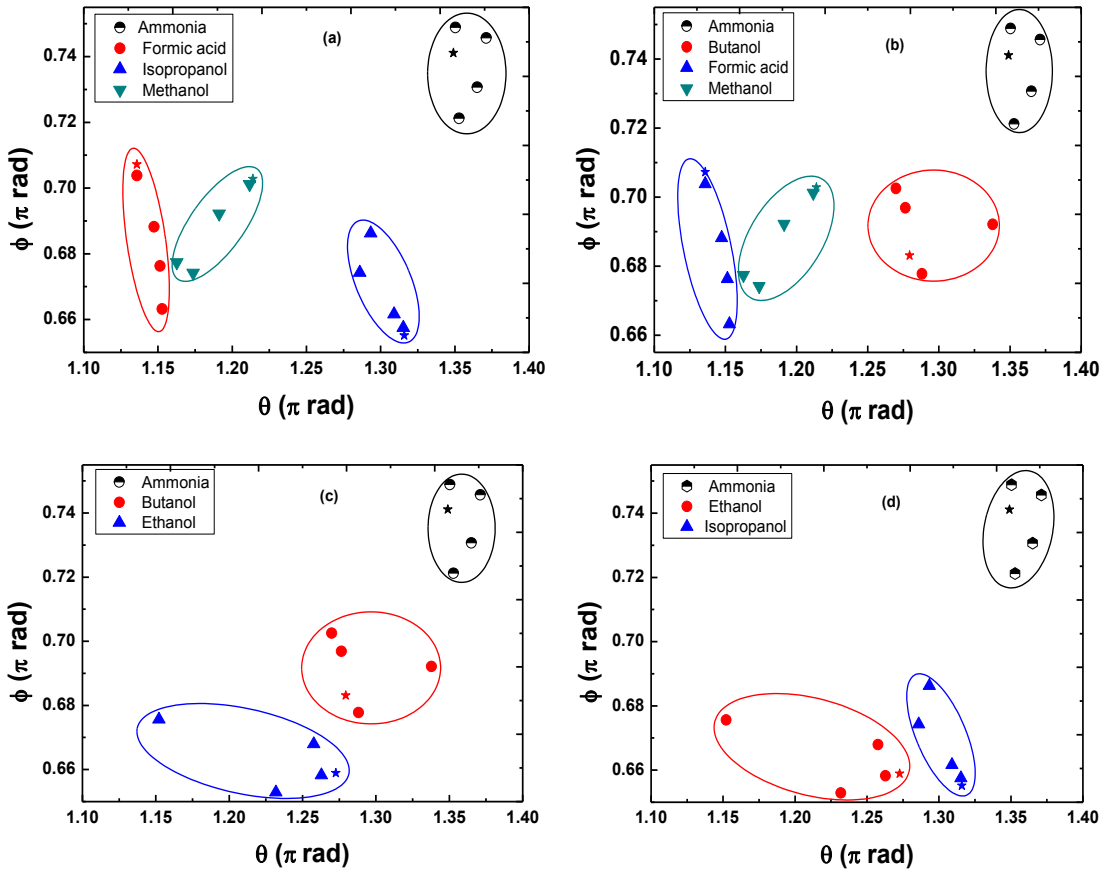


Figure 3.36: Discrimination between ammonia and other polar protic solvents.

Below are patterns of the different combinations of alcohols with very distinct fingerprint patterns. Based on Figure 3.37 (e), it is very evident that there is an overlap between ethanol and methanol.

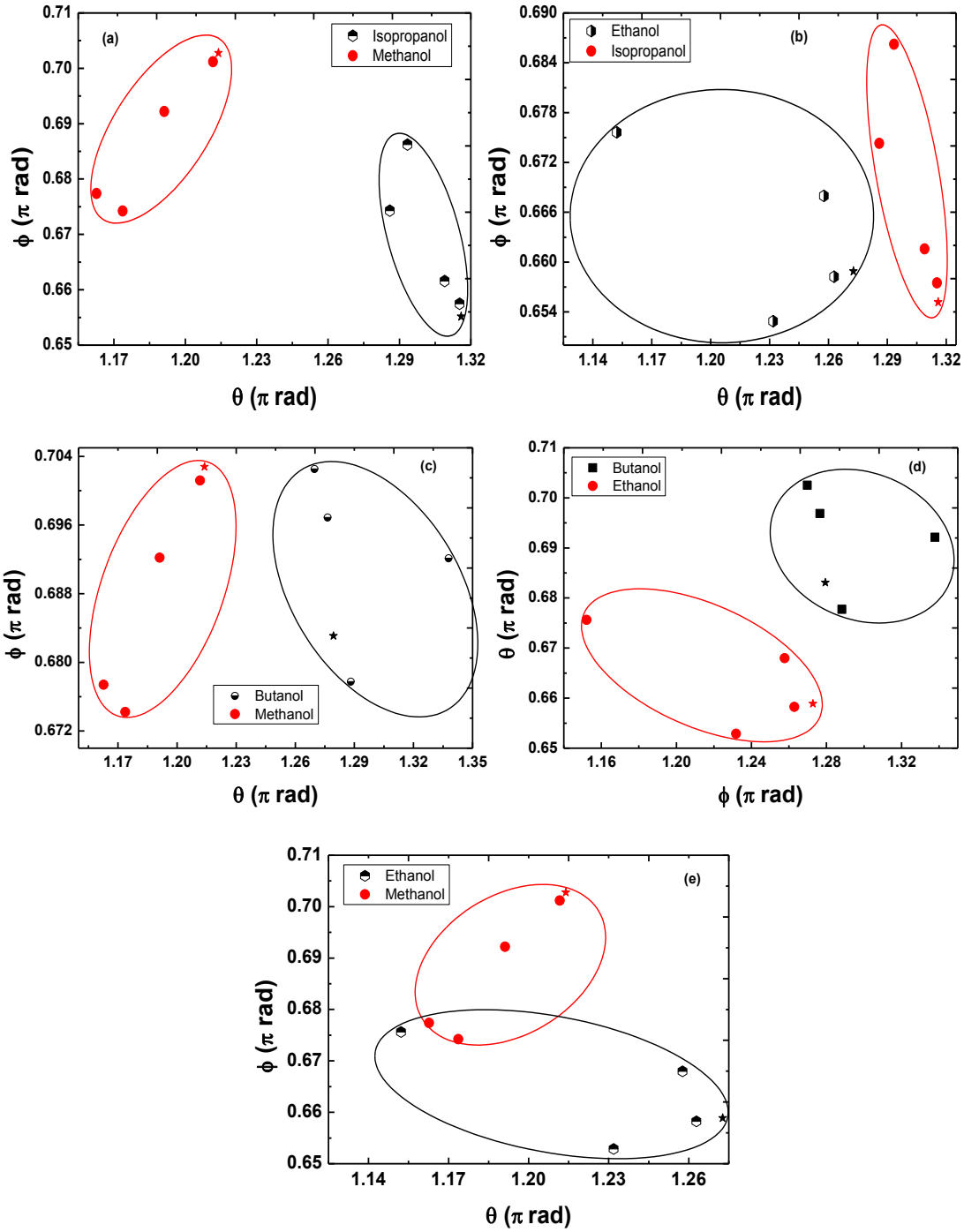


Figure 3.37: Discrimination between polar protic solvents (alcohols).

3.2.4 Conclusion

The results show that our sensor arrays have a substantial potential to identify and discriminate between VOCs of different groups (as well as of the same functional groups). This strategy exploits the size and morphology tunability that afford a reasonable surface area to provide favourable interaction with gaseous molecules. The unique properties of the OLA/WS_2 nanostructures coupled with their diverse morphology make this array approach a promising technique for sensing of VOCs. 3D hierarchical and hollow nanostructures hold exciting new prospects for application in sensor arrays for the identification and quantification of single or multi-component chemical agents. Because of their small size, a few molecules are sufficient to change the electrical properties of the sensing elements in electronic transducers. This allows the detection of very low analyte concentrations. In conclusion, our work suggests that it is possible to develop chemirisistive sensor arrays of the same material provided that they each have different geometric characteristics. Each OLA/WS_2 based sensor has a specific specific response towards each analyte thereby creating a fingerprint by which these analytes can be detected and identified.

3.2.5 References

[1] Khalaf, W., Pace, C. and Gaudioso, M. (2009). Sensors 9, 1678-1691.

[2] Wilson, A. D. and Baietto, M. Sensors 2009, 9, 5099-5148.

[3] Na, N., Zhang, S., Wang, S. and Zhang. X. (2006). J. Am. Chem. Soc. 128, 14420-14421.

[4] Lonergan, M. C., Severin, E. J., Doleman, B. J., Beaber, S. A., Grubbs, R. H. and Lewis, N. S. (1996). Chem. Mater. *8*, 2298-2312.

[5] Doleman, B. J., Lonergan, M. C., Severin, E. J., Vaid, T. P. and Lewis. N. S. (1998). Anal. Chem. 70, 4177-4190.

[6] Ricco, A. J., Crooks, R. M., and Osbourn. G. C. (1998). Acc. Chem. Res. 31, 289-296.

[7] Ködderitzsch, P., Bischoff, R., Veitenhansl, P., Lorenz, W., and Bischoff, G.

[8] Haddi, Z., Mabrouk, S., Bougrini, M., Tahri, K., Sghaier, K., Barhoumi, H., El Bari, N., Maaref, A., Jaffrezic-Renault, N. and Bouchikhi, B. (2014). Food Chemistry 150, 246–253.

[9] Tisch, U. and Haick, H. (2010). MRS Bulletin 35, 797-803.

[10] Pei, P. , Li, J., Lv, M., Wang, J., Gao, J., Lu, J., Li, Y., Huang, Q., Hu, J. and Fan, C. (2012). J. Am. Chem. Soc. 134, 13843−13849.

[11] Berna, A. (2010). Sensors 10, 3882-3910.

[12] Mart, M. P., Boque, R., Busto, O. and Guasch, J. (2005). Trends in Analytical Chemistry 24, (1), 57-66.

[13] You, C-C., Miranda, O. R., Gider, B., Ghosh, P. S., Kim, I-B., Erdogan, B., Krovi, S. A., Bunz, U. H. F. and Rotello, V. M. (2007). Nature Nanotechnology 2, 318-323.

[14] Bachar, N., Liberman, L., Muallem, F., Feng, X., Müllen, K. and Haick, H. (2013). ACS Appl. Mater. Interfaces 5, 11641−11653.

[15] Choi , S-I., Kim, S-H., Yang, Y. and Jeong, G-M. (2010). Sensors 10, 10387-10400.

[16] Huo, N.; Yang, S.; Wei, Z.; Li, S-S.; Xia, J-B.; Li, J. (2014). Sci. Rep. 4 (5209), 1-9.

[17] Xu, W., Ren, C., Teoh, C. L., Peng, J., Gadre, C. H., Rhee, H-W., Lee, C-L., K. and Chang, Y-T. (2014). Anal. Chem. 86, 8763−8769.

[18] Greene, N. T. and Shimizu, K. D. (2005). J. aM. Chem. Soc. 127, 5695-5700.

[19] Romain, A.-C., Nicolas, J., Wiertz, V., Maternova, J. and Andrí, Ph. (2000). Sensors and Actuators B 62, 73–79.

[20] Nicolas, J., Romain, A-C. and Ledent, C. (2006). Sensors and Actuators B 116, 95–99.

[21] Jeong, G-M., Nghia, N. T. and Choi, S-I. (2015). Sensors 15, 656-671.

[22] Greenshields, M. W. C. C., Cunha, B. B., Mamo, M. A., Coville, N. J., Hümmelgen, I. A. (2015). Int. J. Electroactive Mater. 3, 10 – 14.

[23] Greenshields, M. W. C. C., Cunha, B. B., Coville, N. J., Pimentel, I. C., Zawadneak, M. A. C., Dobrovolski, S., Souza, M. T. and Hümmelgen, I. A. (2016). Chemosensors 4 (19), 1-9.

[24] Greenshields, M. W. C. C., Mamo, M. A., Coville, N. J., Pimentel, I. C., Destro, J. G., Porsani, M. V., Bozza, A. and Hümmelgen, I. A. (2013). Sensors and Actuators B 188, 378–384.

[25] Rodrigues, R. and Hümmelgen, I. A. (2016). J Solid State Electrochem 20, 1295–1301.

[26] Cesarino, I. and Hümmelgen, I. A. (2015). J Solid State Electrochem 19, 3045–3050.

[27] Wang, Q., Lian, J., Li, J., Wang, R., Huang, H., Su, B. and Lei, Z. (2015). Sci. Rep. 5, 13593, 1-9.

[28] Wang, C., Yin, L., Zhang, L., Qi, Y., Lun, N. and Liu, N. (2010). Langmuir 15, 12841–12848.

[29] Sun, P., Yang, F., Zhang, H., Sun, Y. and Geyu Lu. (2012). IMCS 2012 – The 14th International Meeting on Chemical Sensors. DOI 10.5162/IMCS2012/4.3.4. 368-371.

[30] Lee, J-H. (2009). Sensors and Actuators B 140, 319–336.

[31] Zhang, H., Wu, R., Chen, Z., Liu, G., Zhang, Z. and Jiao, Z. (2012). CrystEngComm 14, 1775-1782.

[32] Neri, G. (2015). Chemosensors 3, 1-20.

[33] Zhang, Q., Xie, C., Zhang, S., Wang, A., Zhu, B., Wang, L. Yang, Z. (2005). Sensors and Actuators B 110, 370–376.

[34] Lonergan, M. C., Severin, E. J., Doleman, B. J., Beaber, S. A., Grubbs, R. H. and Lewis, N. S. (1996). Chem. Mater. 8, 2298-2312.

[35] Baldini, L., Wilson, A. J., Hong, J. and Hamilton, A. D. (2004). J. Am. Chem. Soc. 126, 5656-5657.

[36] Greene, N. T. and Shimizu, K. D. (2005). J. Am. Chem. Soc. 127, 5695-5700.

[37] Kanana, S. M.; Waghe, A.; Jensen, B. L.; Tripp, C. P. (2007). Talanta 72, 401–407.

[38] Kuang, X., Liu, T., Li, T., Zeng, W., Peng, X. and Zhang, H. (2016). Materials Technology: Advanced Performance Materials 31 (5), 260-265

[39] Capochichi-Gnambodoe, M., Habba, Y. G. and Leprince-Wang, Y. (2016). Phys. Status Solidi C, 1–5.

[40] Feller, J-F., Gatt, N., Kumar, B. and Castro, M. (2014). Chemosensors *2*, 26-40.

[41] Kim, T. H., Kim, Y. H., Park, S. Y., Kim, S. Y. and Jang, H. W. (2017). Chemosensors 5, 15, 1-19.

[42] Altavilla, C.; Sarno, M.; Ciambelli, P. (2011). Chem. Mater. 23, 3879–3885.

[43] Greenshields, M. W., H¨ummelgen, I. A., Mamo, M. A., Shaikjee, A., Mhlanga, S. D., Van Otterlo, W. A. and Coville, N. J. (2011). J. Nanosci. Nanotechnol.11, 10211–10218.

[44] Mutuma, B. K., Rodrigues, R., Ranganathan, K., Matsoso, B., Wamwangi, D., Hümmelgen, I. A. and Coville, N. J. (2017). J. Mater. Chem. A 5, 2539–2549.

[45] Qin, Z., Zeng, D., Zhang, J., Wu, C., Wen, Y., Shan, B., Xie, C. (2017). Applied Surface Science 414, 244–250.

[46] Cho, B., Hahm, M. G., Choi, M., Yoon, J., Kim, A. R., Lee, Y-J., Park, S-G., Kwon, J-D., Kim, C. S., Song, M., Jeong, Y., Nam, K-S., Lee, S., Yoo, T. J., Kang, C. G., Lee, B. H., Ko, H. C., Ajayan, P. M. and Kim, D-H. (2015). Sci. Rep. 5, 8052, 1-6.

[47] Huo, N., Yang, S., Wei, Z., Li, S-S., Xia, J-B. and Li. (2014). J. Sci. Rep. 4, 5209, 1-9.

[48] Neri, G. (2017). Chemosensors 5, 1-20.

[49] Wang, L-C., Tang, K-T., Teng, I-J., Kuo, C-T., Ho, C-L., Kuo, H-W., Su, T-H., Yang, S-R., Shi, G-N. and Chang, C-P. (2011). Sensors 11, 7763-7772.

[50] Marr, I., Groß, A. and Moos, R. (2014). (2014). J. Sens. Sens. Syst. 3, 29–46.

[51] Korotcenkov, G. (2007). Materials Science and Engineering B 139, 1–23.

[52] Fine, G. F., Cavanagh, L. M., Afonja, A. and Binions, R. (2010). Sensors 10, 5469-5502.

[53] Berna, A. (2010). Sensors 10, 3882-3910.

[54] Li, H., Yin, Z., He, Q., Li, H., Huang, X., Lu, G., Fam, D. W. H., Tok, A. I. Y., Zhang, Q. and Zhang, H. (2012). Small 8 (1), 63–67.
[55] McKelvey, M. J. and Glaunsinger, W. S. (1987). Solid State Ionics 25, 287-294.

3.3 Selectivity of OLA/WS_2 sensors towards different VOCs and their sensitivity to NH_3 under relatively humid conditions

3.3.1 Introduction

Ammonia is a naturally occurring colourless gas found in the atmosphere [1]; it is caustic and hazardous with a characteristic pungent odour [2]. It is a source of nitrogen to living organisms with nitrogen being present in vital biological molecules such as amino acids (the building blocks of proteins) [2]. An increase in ammonia in the atmosphere as a result of continued development in industry and agriculture has been a cause for concern as exposure can endanger human health and vegetation in the long term [2-4]. Ammonia detection, measurement and control have become increasingly important due to its extensive use as a raw material for producing fertilizers, as a refrigerant in the food industry [5], its emission by decomposing fish is used as a measure of freshness of fish [6-8], in medical diagnostics as a biomarker in exhaled breath of patients with renal disorders or ulcers, chemical industry, vehicle industry, fire power plants and environmental protection [1, 9, 10].

A wide variety of sensors have been researched, developed and exploited as effective gas sensing elements for NH_3. Such sensors include inorganic semiconductors, conductive polymers, optical fibers, carbon nanotubes, and two-dimensional materials have been exploited as effective gas sensing elements [3, 9]. Semiconductive oxides, especially, SnO_2 and ZnO are the most commonly used materials and have been widely studied due to their range of conductance variability and their response towards NH_3 [7, 8, 11, 12]. Much effort has been put into improving the gas-sensing properties of these materials by modification with noble metals or other oxides. Although they have attractive advantages including facile fabrication process, easy-controllable morphology, and low-cost, their limitations including high-temperature operation, slow response/recovery time, and low sensitivity remain as major challenges.

Achieving selectivity and still maintain high sensitivity under high humidity conditions has been for the longest time one of the hurdles to overcome in the realization of an effective gas sensor [13]. Sensitivity of sensors to humidity (water vapour) is a very important parameter because it is the most significant interfering vapour [9, 13] and it influences their conductivity and selectivity response to a particular gas [14-18]. Humidity is generally regarded as the measure of water vapour present in a gas [16]. Selectivity in metal oxide gas sensors is achieved by operating between 300 ℃ and 600 ℃ with chemisorption becoming

more important than physisorption [19]. It is common knowledge that physisorbed water converts almost every material operating at low temperature into a humidity sensor [19]. This is the reason metal oxide gas sensors have a heating element that provides the desired temperature for adsorption and desorption of oxygen gas and for reaction of the analyte gases with those reactive adsorbed oxygen species [19]. Characteristics of a good sensor include stability, sensitivity, selectivity, fast response, low cost production and high reliability [4, 13, 24]. Selectivity of a gas sensor material generally refers to the preferential chemiresistive sensing for a particular gas in the presence of another gas under similar operating conditions. The sensitivity and mainly selectivity of any sensing layer strongly depend on the overall sensor construction and type of a specific material which is used for their fabrication. Nanostructures possess a high surface-to-volume ratio which increases the adsorption of gases and therefore enhances their sensitivity to adsorbates. They are relatively easy to fabricate and their surfaces provide versatility for modification towards detection of chosen VOC analytes [9, 24].

3.3.2. Experimental set-up

3.3.2.1 Chemicals and materials

As-prepared OLA/WS_2 nanostructures (15, 45, 60, 180 and 240 min) were used as obtained. All the solvents and salts were of analytical grade and were used as received. Interdigitated electrodes consisting of ENIG (Electroless Nickel Immersion Gold) electrodes in 18 pairs of 7.9 mm long with a gap of 0.1 mm between them and patterned onto FR4 substrate were purchased from Micropress SA. A Hikari HK-T240 Thermohygrometer was used to monitor the temperature and humidity inside the gas chamber during sensitivity measurements towards NH_3 under humid conditions.

3.3.2.2 Preparation of salt solutions

Fresh saturated solutions of magnesium chloride, sodium bromide, sodium chloride, potassium chloride and potassium sulphate were prepared following the procedure outlined by agencies of the Department of Defense [26]. The solutions were used as humidifiers representing relative humidity conditions at 41, 59, 75, 87 and 97 % respectively.

3.3.2.3 Characterization techniques

The evolution of the morphology was monitored by a scanning electron microscope (SEM) by FEI Nova NanoLab FIB/SEM. The oxidation states and atomic composition of the nanostructures were confirmed using XPS analysis.

3.3.2.4 Gas sensing performance

All electrical measurements were performed in the dark at room temperature; and under dry N_2 environment. An LCR meter (Agilent 4284A 20 Hz – 1 MHz Precision LCR meter) attached to a computer interfaced with a GPIB was used for data acquisition. An operational voltage and frequency of 1000 mV and 10 kHz were selected respectively due to their higher signal-to-noise ratio. The systems were allowed to stand for 1h before measurements were performed. The change in conductance was monitored for 50 s, providing a stable baseline before the 1.5 µL of the analyte was introduced. The opening was sealed off immediately to prevent moisture from getting into the chamber. The devices were allowed to reach saturation point (around 300 s) before the next increment.

(i) Chemical vapour measurements under limited light and low humidity environment

The devices were placed in an aluminium foil covered and rubber stoppered 1 L glass jar as shown in Figure 3.38. After fitting the contacts of the device in the cover, the chamber was purged with dry nitrogen for 30 min thereby decreasing the humidity inside the chamber to less than 20 % RH at room temperature.

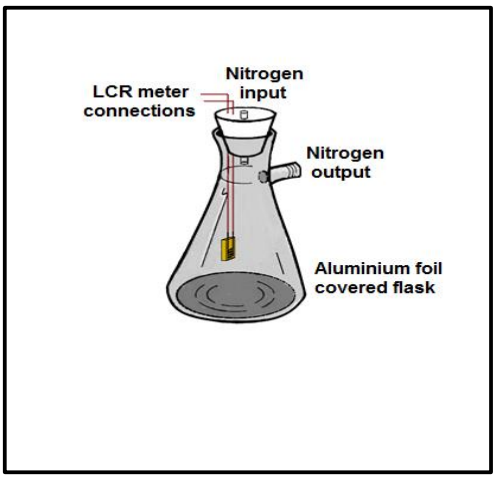


Figure 3.38: Schematic representation of the gas chambers used in sensor measurements.

(ii) Chemical vapour measurements under different relative humidity percentages

The devices were secured in the sweep cover lid of a 3 L glass jar as the dedicated gas chamber as shown in Figure 3.9. The clean, dry gas chamber contained a fan to homogenize the volatiles as well as a hygrometer to monitor the relative humidity and temperature. The beaker containing the salt solution was placed in the gas chamber and the lid which was secured to the chamber. The chamber was flushed with dry N_2 for 30 minutes to bring the humidity down to about 25 %. The lid was then closed tightly and any openings were sealed off with tape. The chamber was allowed to stand for 30 min before measurement.

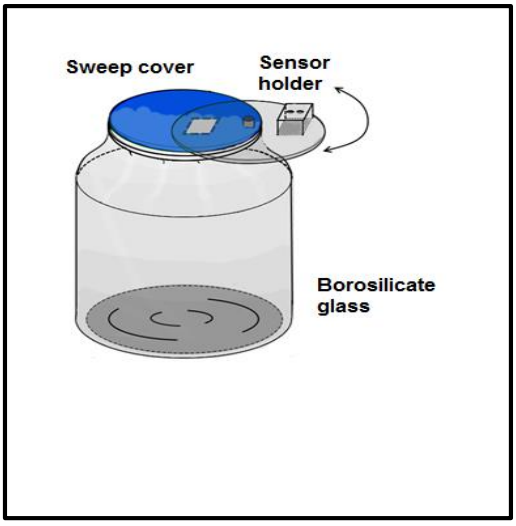


Figure 3.39: Schematic representation of the gas chamber with a sweep cover used under humid conditions.

(iii) Stability test measurements

The same procedure outlined in (i) was followed and 240 ppm of NH_3 was introduced into the chamber through the opening. Conductivity measurements for each OLA/WS_2 sensor (15, 45, 60, 180 and 240 min) was allowed to continue for 5 h.

3.3.3. Results and discussion

3.3.3.1 Characterization of OLA/WS_2 nanostructures

Nanostructure morphology of the powders was studied using a scanning electron microscope (SEM) by FEI Nova NanoLab FIB/SEM. Figure 3.40 shows the OLA/WS_2 nanostructures as presented by the SEM micrographs.

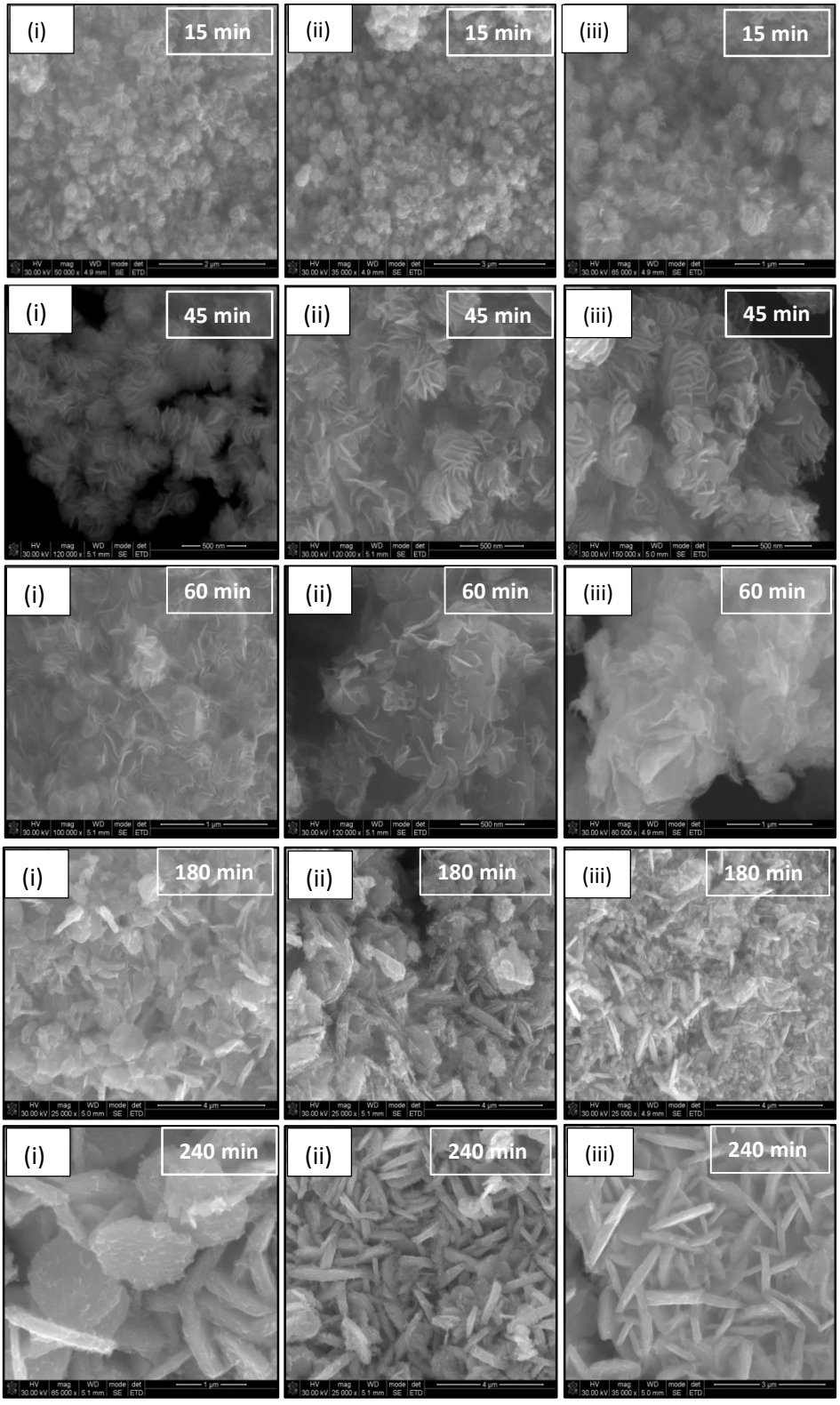


Figure 3.40: SEM micrographs of OLA/WS_2 nanostructures at 15, 45, 60, 180 and 240 min.

The morphological properties of the OLA/WS_2 nanostructures as seen in Figure 3.40 have been discussed at length in section 3.1 and 3.2 of this thesis. XPS analysis of OLA/WS_2 was discussed in detail in section 3.1 in a bid to shed light on the oxidation states and elemental composition of OLA/WS_2 nanostructures. Figure 3.41 shows a survey scan of the OLA/WS_2 from the 45 min reaction time.

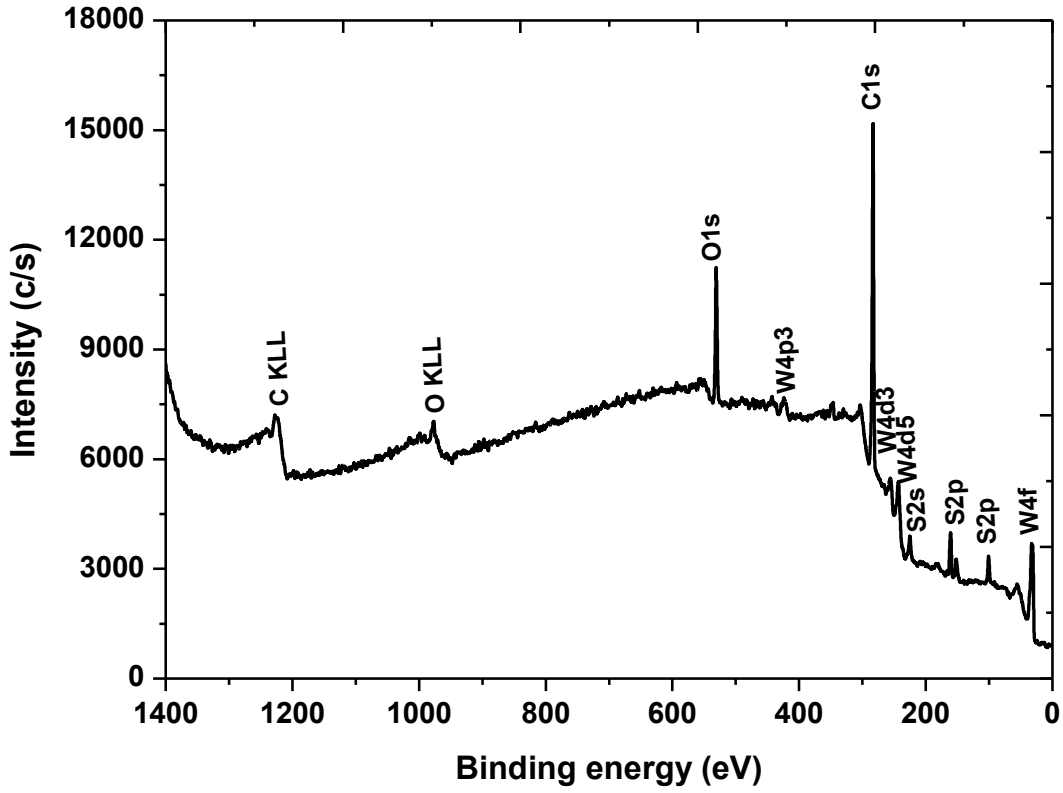


Figure 3.41: XPS survey spectrum of OLA/WS_2 nanostructures (45 min).

The high resolution XPS spectra with the focus on C 1s, O 1s, W 4f and S 2p were generated in order to evaluate the surface in more detail as shown in Figure 3.42.

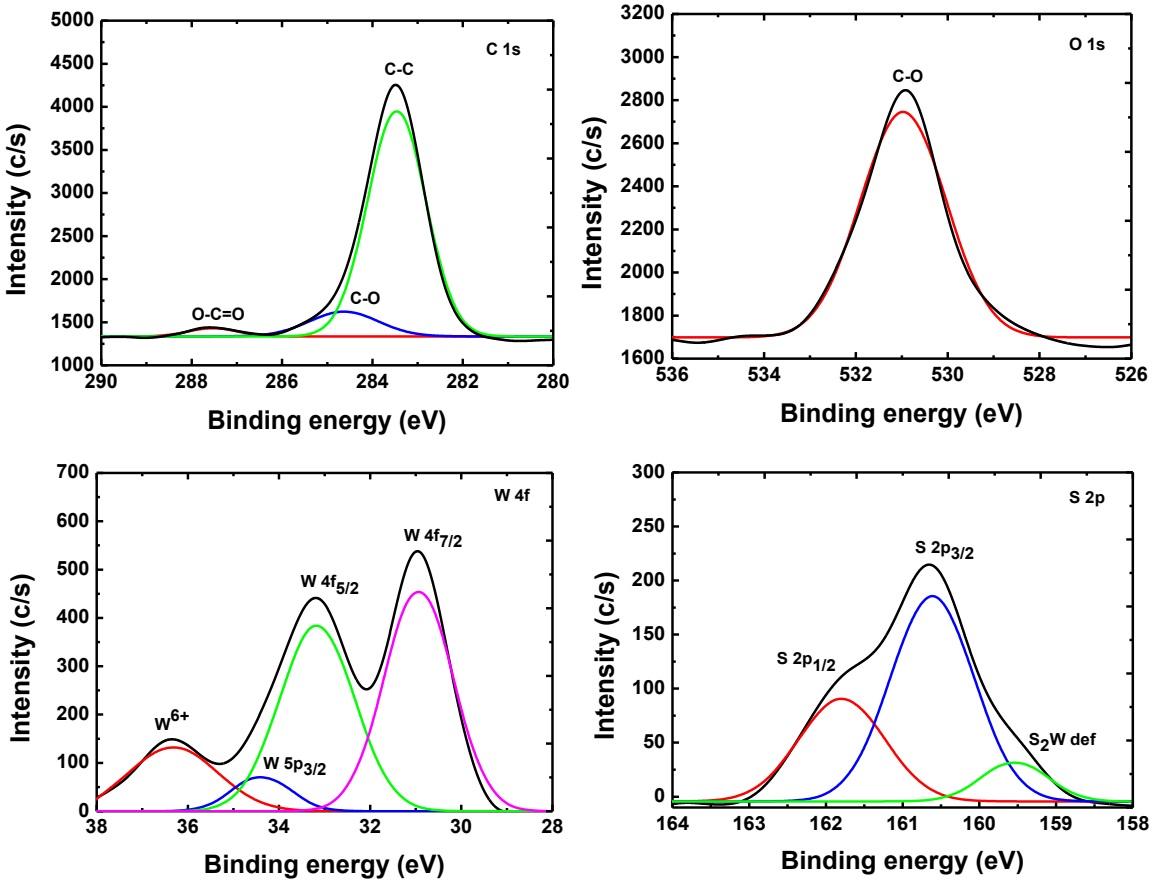


Figure 3.42: High resolution XPS spectrum of OLA/WS_2 nanostructures (45 min).

3.3.3.2 Gas sensing performance

(i) Sensitivity OLA/WS_2 sensors to NH_3 and VOCs

The inherent benefits of 3D hierarchical nanostructures of OLA/WS_2 inspired the investigation into their room temperature gas sensing properties. Five OLA/WS_2 nanostructures derived from 15, 45, 60, 180 and 240 min reaction times were evaluated by measuring their electrical conductance during repeated exposure to different solvent vapours. The results shown in Figures 3.43 - 3.47 are calibration curves of 15, 45, 60, 180 and 240 min response *vs.* concentration of each analyte. OLA/WS_2 sensors are chemiresistive sensors belonging to the electrochemical sensors group whose working principle is based on the measurement of a change in conductance. Sensitivity is defined as:

$$S = (G_g - GN_2)/GN_2 \times 100 \quad (3.3.1)$$

Where G_g is conductance of the device in the target gas, and GN_2 is the conductance of the device in dry N_2. The slope of each of the calibration curves shown in Figures 3.43 – 3.47 represents sensitivity of each device to each target analyte. The sensing response increases rapidly and almost reaches its equilibrium value when it is exposed to a certain concentration of each test analyte. The devices generally displayed significant sensitivity to detect VOCs within a wide analyte gas concentration *e.g* 240, 479, 719 and 958 ppm for NH_3. The conductance of OLA/WS_2 sensors derived from 15, 45, 60, 180 and 240 min nanostructures decreased with the adsorption of the analytes giving a negative sensitivity. The exception to this was 180 and 240 min whose adsorption to NH_3 gave a positive response. It is common knowledge that NH_3 donates electrons to the valence band, decreasing the number of holes; thereby increasing the separation between the Fermi level and valence band [44]. This forms a space charge region at the surface of semiconducting OLA/WS_2 material causing n-type doping. Therefore, NH_3 and other polar solvent vapours increase the conductance of OLA/WS_2 sensors based on a charge transfer mechanism. Apart from polar solvents, a clear response of OLA/WS_2 sensors to non-polar solvent vapours was also observed. A similar negative sensitivity towards NH_3 was observed with MoS_2 [45].

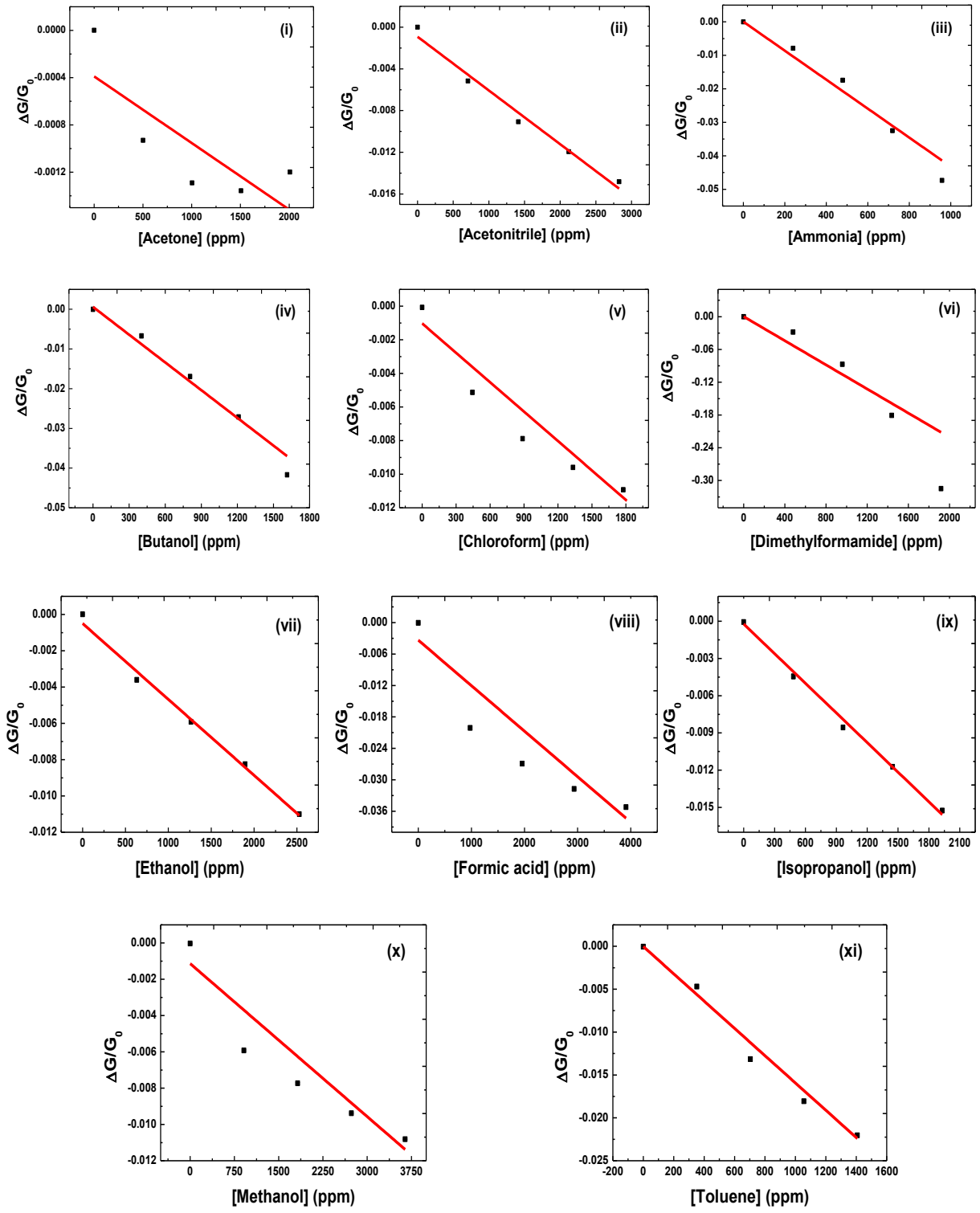


Figure 3.43: Response curves of OLA/WS_2 nanostructures (15 min).

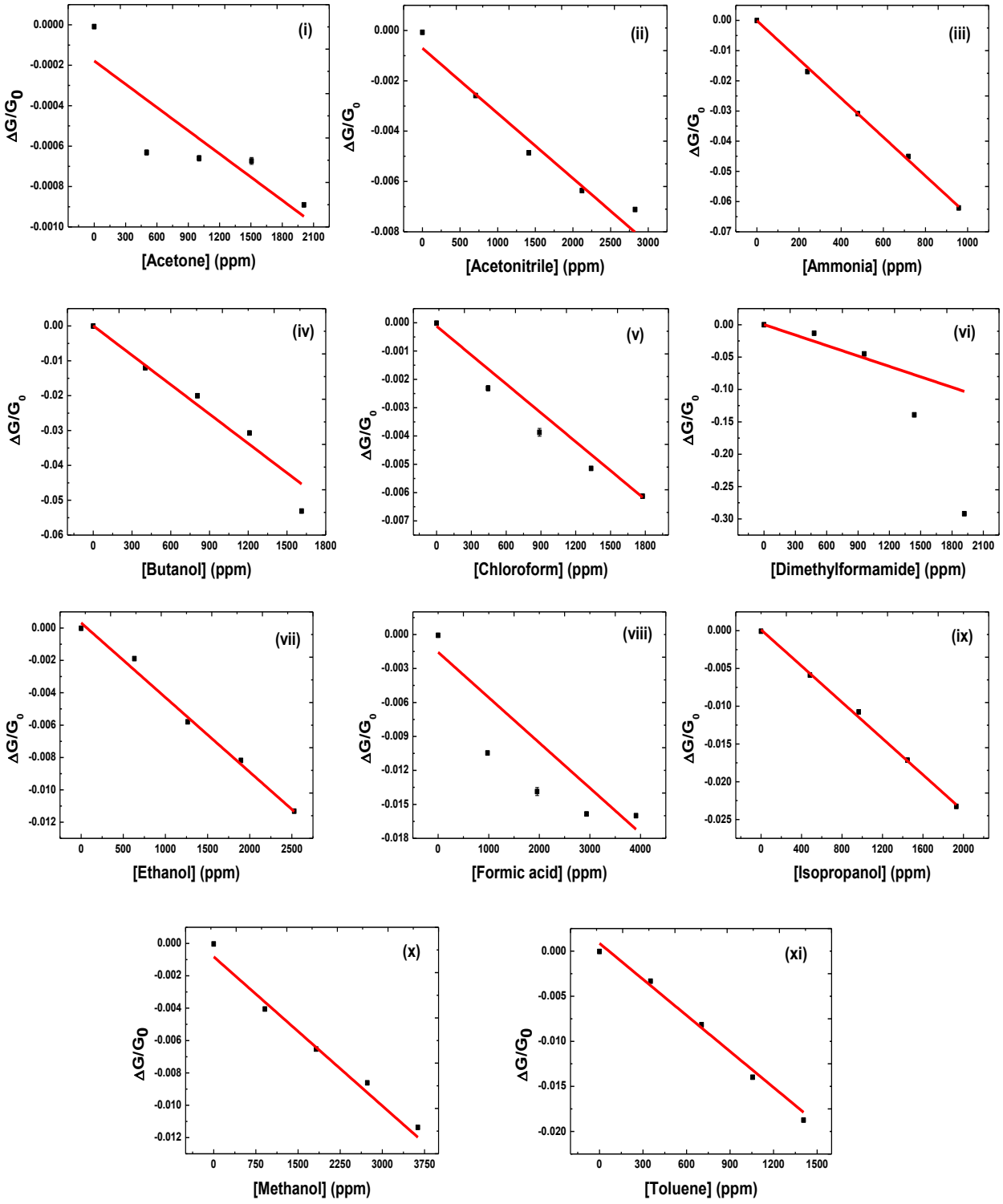


Figure 3.44: Response curves of OLA/WS_2 nanostructures (45 min).

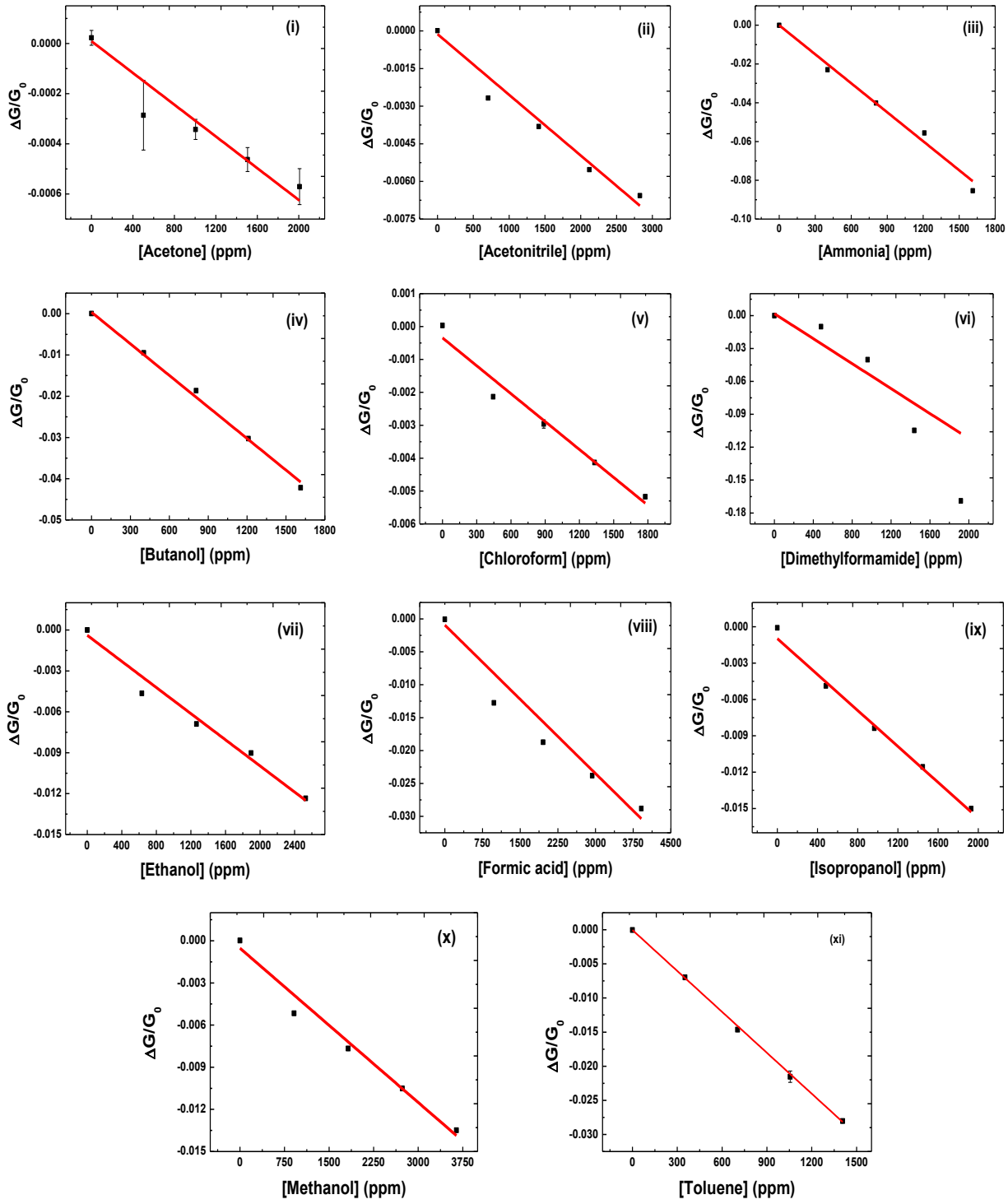


Figure 3.45: Response curves of OLA/WS_2 nanostructures (60 min).

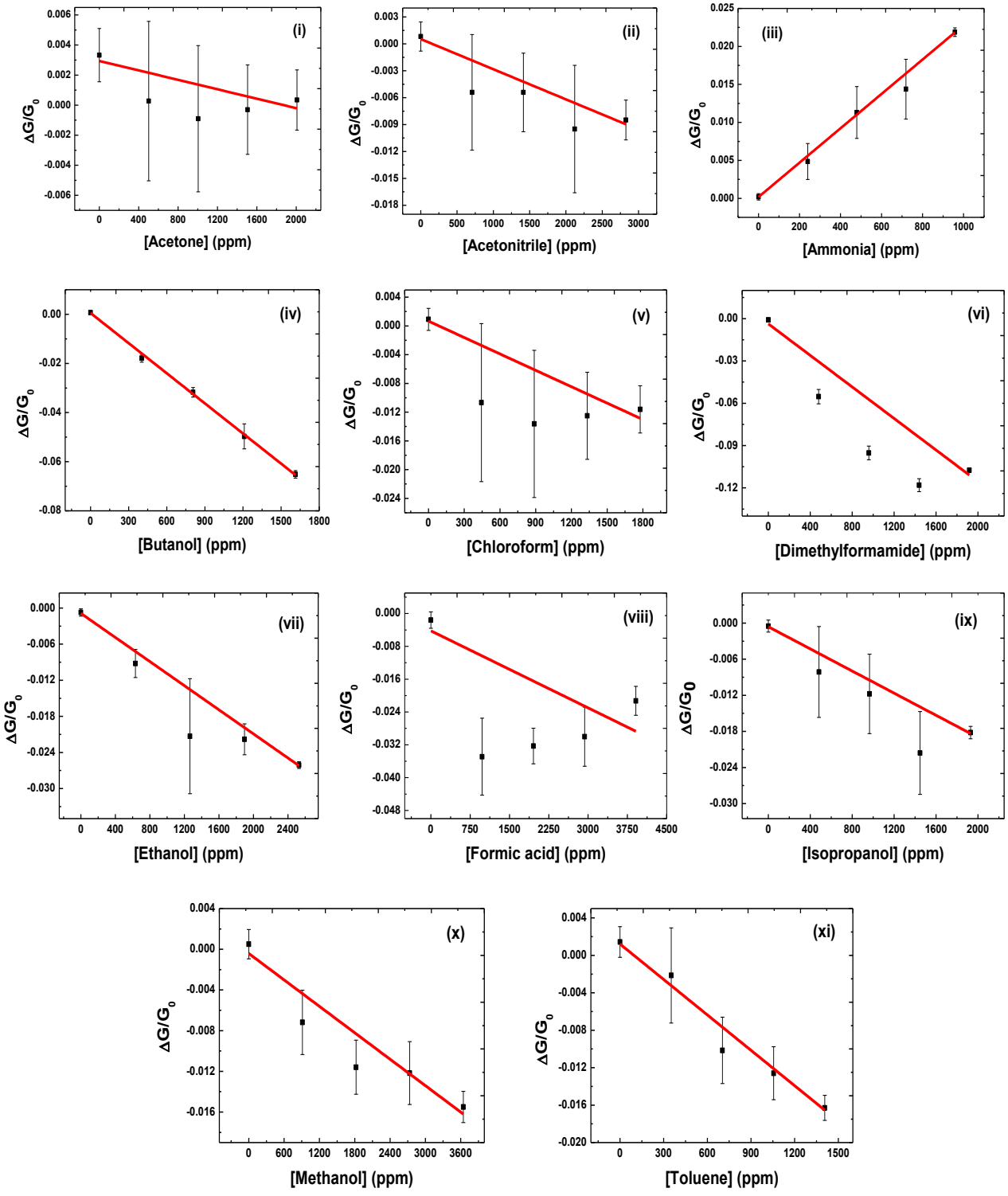


Figure 3.46: Response curves of OLA/WS_2 nanostructures (180 min).

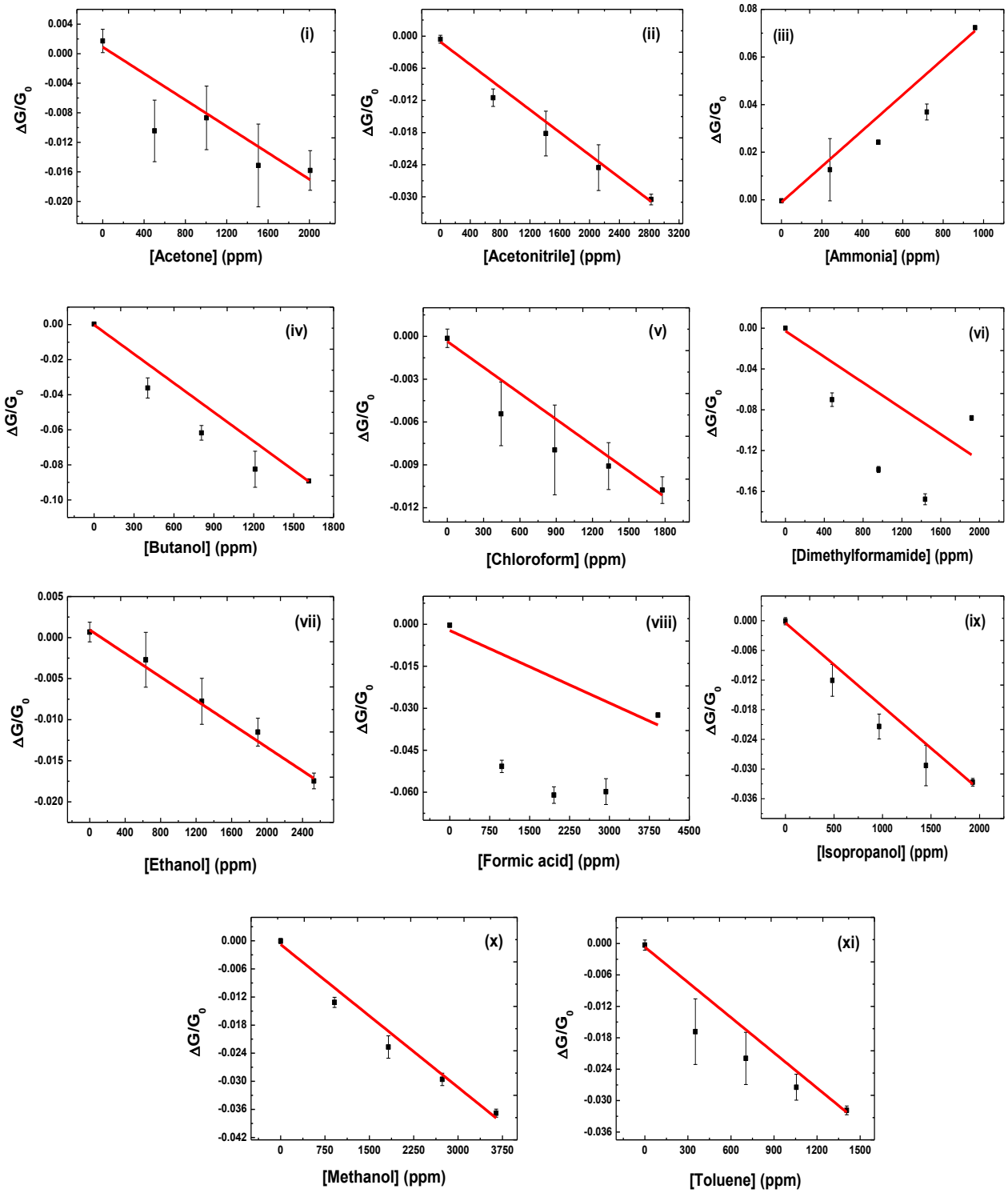


Figure 3.47: Response curves of OLA/WS_2 nanostructures (240 min).

The sensing response is said to be mainly determined by the surface interactions of the target gas with the sensing material. Consequently, the greater the surface area of the material, the stronger the interactions between the adsorbed gases and the sensor surfaces resulting in enhanced gas response and sensitivity [22]. This is evident with the OLA/WS_2 sensor derived from the 45 min sample where the sensitivity towards NH_3 is greater than that of both 15 and 60 min. This can be explained in terms of morphology where the 'petals' of the microflowers at 15 min are mostly closed; meaning most of the gas adsorption takes place on the surface. Meanwhile, at 45 min the 'petals' which are actually 2D nanosheets have opened up exposing the inside of the microflower thereby increasing the surface area for the gas interactions. Therefore, the adsorption not only does it take place on the surface but also inside the microflower. At 60 min, the microflower morphology has but all disintergrated into its building blocks, the 2D nanosheets. Therefore, the gas interaction with the active material takes place only on the surface.

(ii) Selectivity OLA/WS_2 sensors

Selectivity, specificity or cross-sensitivity tests are performed to establish the sensor's ability to discriminate a target analyte in the presence of interfering ones [44]. The selectivity of each sensor was measured by exposing it to different analytes and recording the sensor's response (change in conductance) towards a certain analyte as compared to others. The selectivity of each sensor to the various analytes was calculated using the response from the calibration curves in Figures 3.43 – 3.47. The selectivity of OLA/WS_2-based sensors can be expressed as in Eq. (3.3.2) adapted from Llobet, *et al.* [46].

$$\delta_i = \frac{\left(\Delta G/G_0\right)_i}{\sum_{j=1}^{n}\left(\Delta G/G_0\right)_j} \qquad (3.3.2)$$

Figures 3.47 – 3.51 show the responses of OLA/WS_2-based sensor towards different solvent vapours with 1.5 µL increments of each target analyte at room temperature. As much as each sensor responded to each analyte, the value of the response tells us which analyte each sensor is selective to. It is also interesting to note that the specificity of the sensors was in most cases affected by the concentration of a specific analyte more than the morphology of the OLA/WS_2 nanostructures.

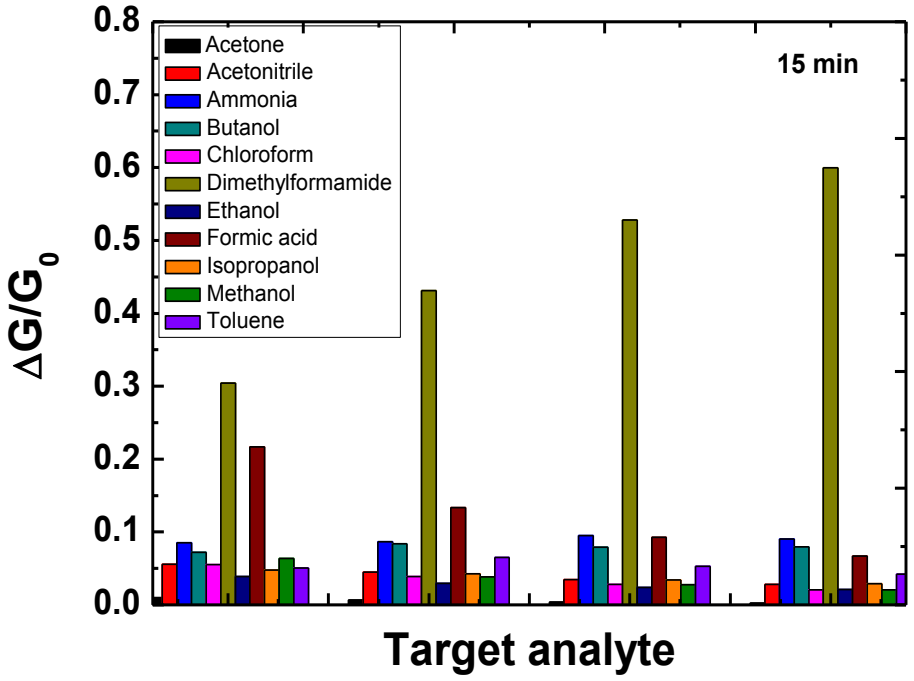


Figure 3.48: Selectivity tests of the OLA/WS_2 sensor (15 min) at 1.5, 3.0, 4.5 and 6.0 µL of NH_3 and various VOCs.

As can be seen from Figure 3.48, the OLA/WS_2 sensor from the 15 min reaction time exhibited higher response to dimethylformamide among the test solvent vapours. The response increased with an increase in concentration (480, 959, 1439 and 1918 ppm represented by 1.5, 3.0, 4.5, and 6.0 µL respectively) of the analyte. This result may be due to dimethylformamide molecules being more easily adsorbed than other analytes; and reacted with defects and mismatches on the surface of the hierarchical nanostructured OLA/WS_2 sensor. This led to a release of more electrons to the conduction band of the microflowers and increased the conductance of the sensing material. The sensor also showed significant selectivity towards formic acid and NH_3 to a lesser extent; the response towards these analytes evidently decreases significantly with an increase in concentration. With increasing concentration of acetone, the response to it becomes negligible, clearly demonstrating the selective nature of this sensor.

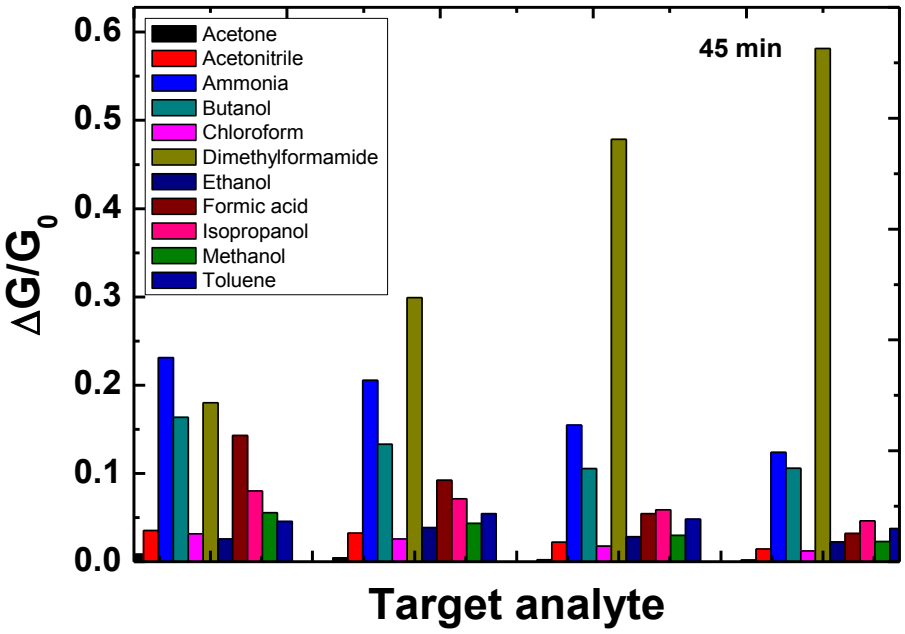


Figure 3.49: Selectivity tests of the OLA/WS_2 sensor (45 min) at 1.5, 3.0, 4.5 and 6.0 µL of NH_3 and various VOCs.

It is worth noting that the 45 and 60 min sensors displayed higher selectivity towards low a concentration (240 ppm, 1.5 µL) of NH_3, (Figures 3.49 and 3.50). This is contrary to what was observed with the OLA/WS_2 sensor from the 15 min reaction time. The sensor also showed notable selectivity towards dimethylformamide, butanol and formic acid. However, at higher concentrations of NH_3 (479, 719 and 958 represented by 3.0, 4.5 and 6.0 µL); the same trend observed with the 15 min sensor and dimethylformamide is also seen. The trend in high selectivity of the sensor to dimethylformamide is maintained for both sensors from the 180 and 240 min reaction times. Interestingly, the selectivity of both sensors towards 1613 ppm (1.5 µL) of butanol increased significantly (Figures 3.51 and 3.52). The selectivity towards acetone is surprisingly significant with the OLA/WS_2 sensor from the 240 min reaction time.

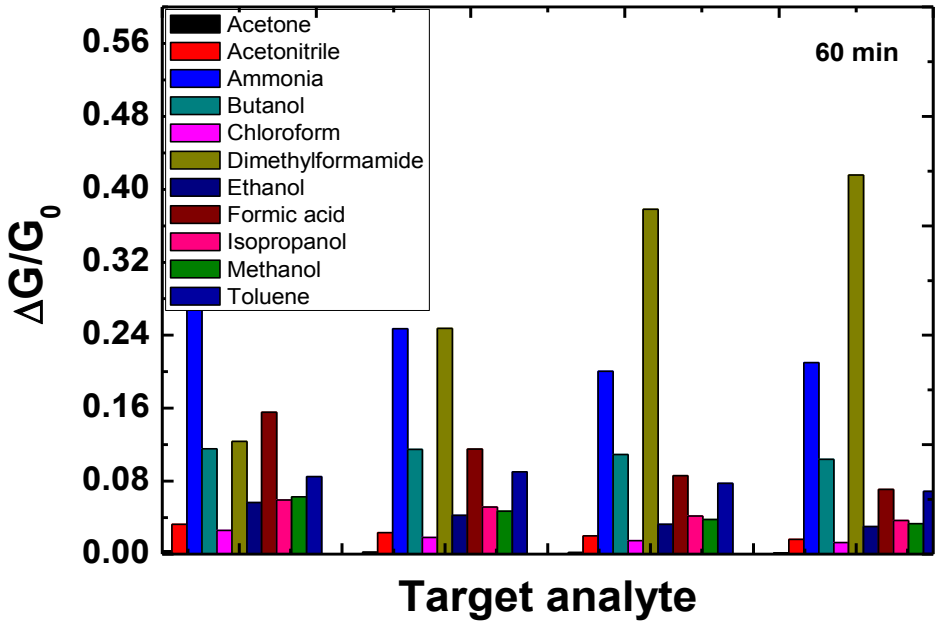


Figure 3.50: Selectivity tests of the OLA/WS_2 sensor (60 min) at 1.5, 3.0, 4.5 and 6.0 µL of NH_3 and various VOCs.

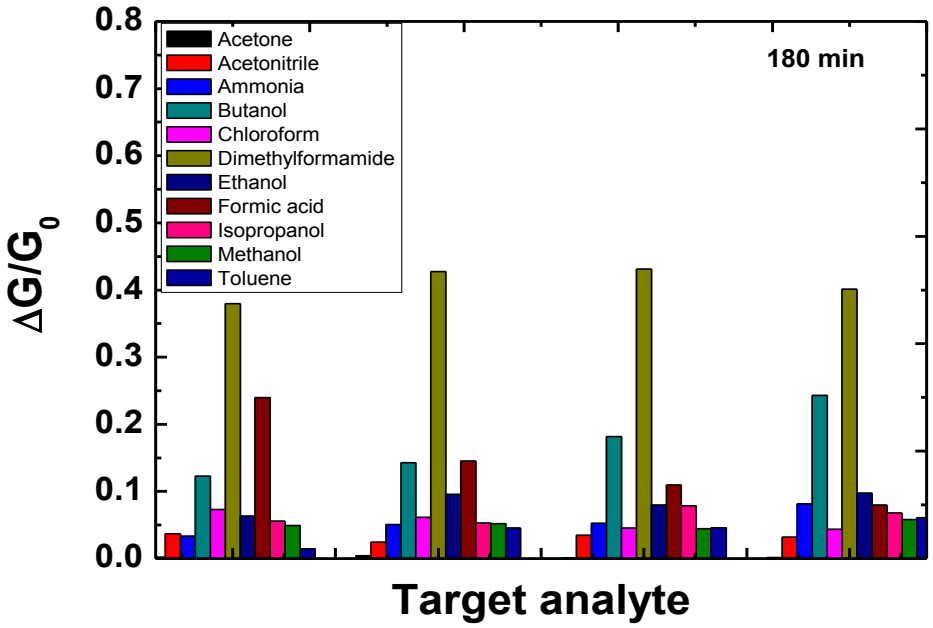


Figure 3.51: Selectivity tests of the OLA/WS_2 sensor (180 min) at 1.5, 3.0, 4.5 and 6.0 µL of NH_3 and various VOCs.

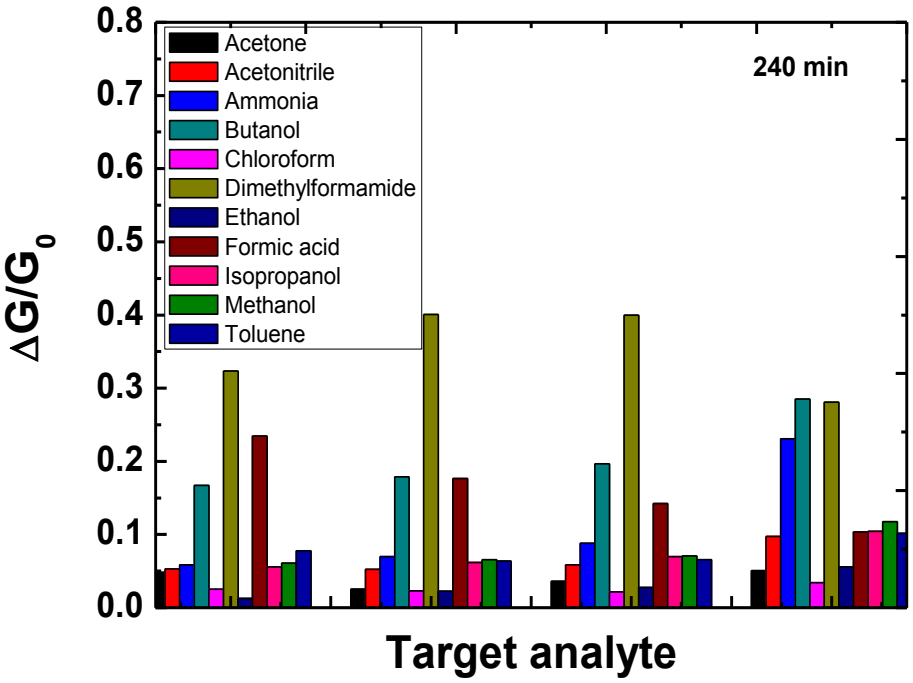


Figure 3.52: Selectivity tests of the OLA/WS_2 sensor (240 min) at 1.5, 3.0, 4.5 and 6.0 µL of NH_3 and various VOCs.

(iii) Detection of NH_3 under various relative humidity percentages

Water molecules also act as a barrier against NH_3 adsorption. The superficial migration of the NH_3 on the OLA/WS_2/WO_3 surface becomes difficult, thus the sensitivity decreases and the response and recovery times increase. Prolonged exposure to humid environments leads to the gradual formation of stable chemisorbed OH^- on the surface causing a progressive deterioration of the sensitivity of gas sensors. As mentioned previously, the sensitivity to humidity is a very important parameter because it is the most significant interfering vapour. The effect of humidity on sensitivity of the 15 and 45 min sensors was studied by exposing the sensor to 240 ppm increments of NH_3 vapour at various humidity conditions (41, 59, 62, 75, 87 and 97 % RH) with the 25 % RH representing dry N_2 conditions. Figure 3.53 represents the sensing characteristics of the OLA/WS_2 sensors from the 15 min reaction time at various humidity conditions when exposed to 240 ppm increments of NH_3 vapour. Fluctuations in response to all concentrations of NH_3 at low % RH made it impossible to establish a trend. Nonetheless, it was discovered that the observed response generally increased as the humidity increased up to 62 % RH. Meanwhile, the response decreased at 75 % RH while it increased at higher humidity levels (87 and 97 % RH).

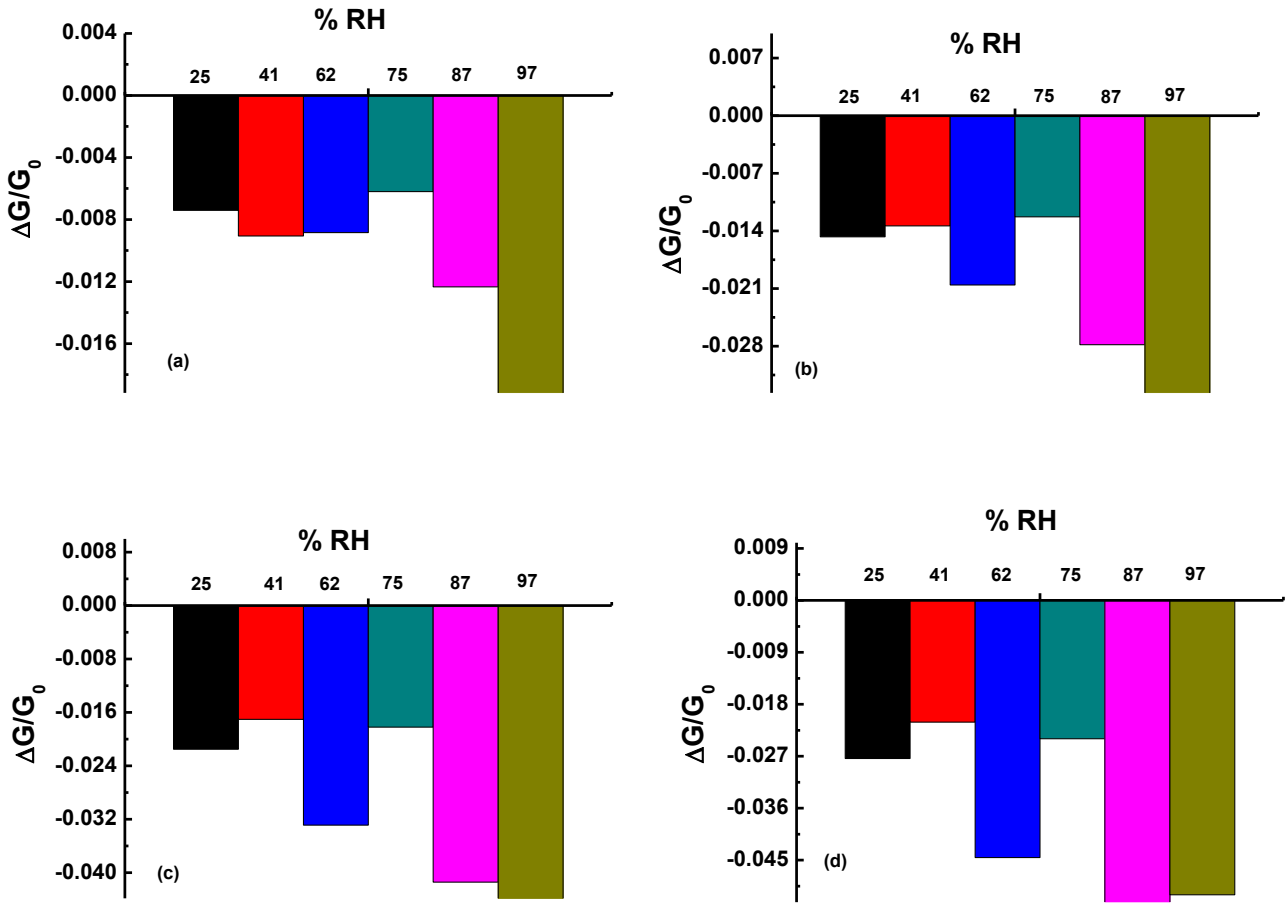


Figure 3.53: Histograms representing the response of OLA/WS_2 sensor (15 min) towards (a) 240 ppm, (b) 479 ppm, (c) 719 ppm and (d) 958 ppm of NH_3 under various humid conditions.

Figure 3.54 represents the sensing characteristics of OLA/WS_2 sensor (45 min) at various humidity conditions when exposed to 240 ppm increments of NH_3 vapour. In contrast to the response observed for the 15 min sensor, the decrease in response to NH_3 under 75 % RH is observed only at the 240 ppm concentration. It is very obvious that humidity affects the detection of NH_3 irrespective of the % RH. This finding is in agreement with observations made by Li, *et al.* about the response of WS_2 based chemiresistive gas sensor to different concentrations of NH_3 at room temperature under different relative humidity [1].

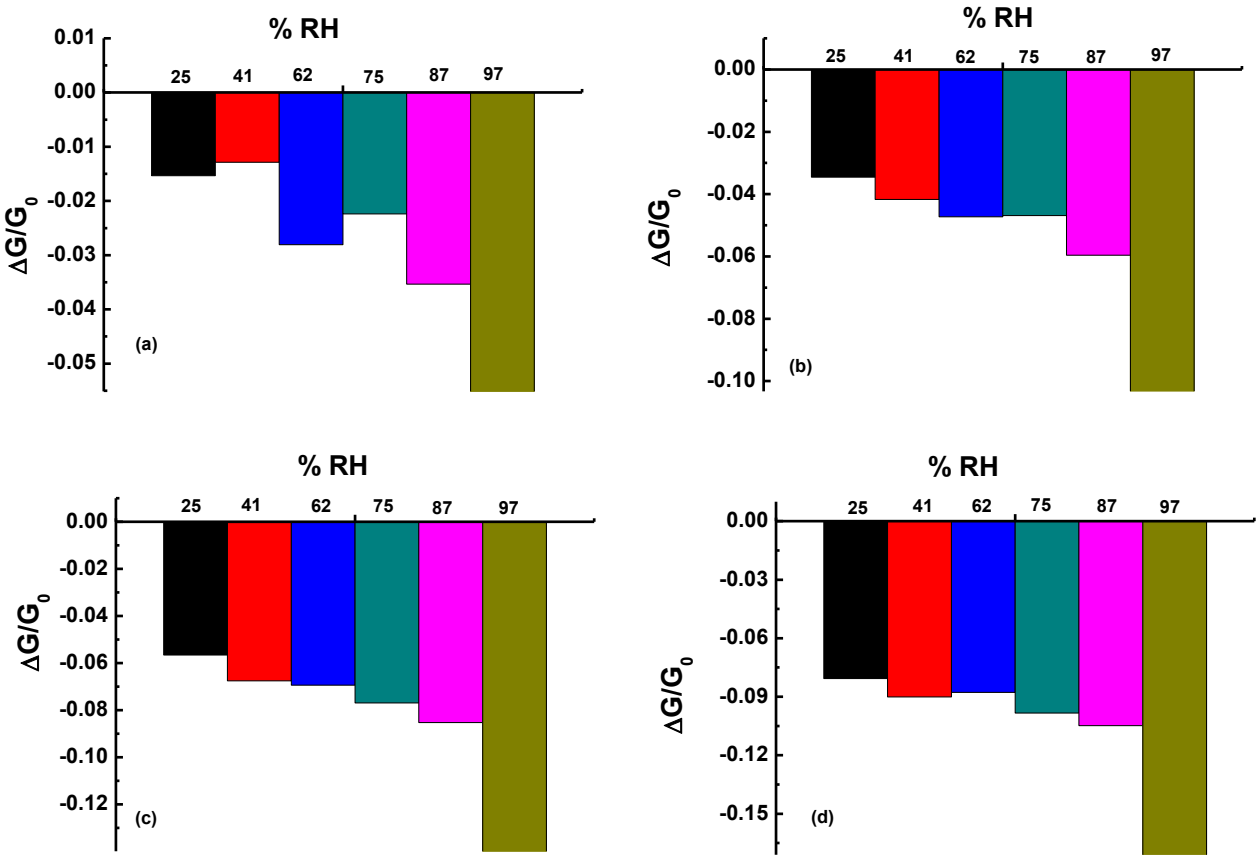


Figure 3.54: Histograms representing the response of OLA/WS_2 sensor (45 min) towards (a) 240 ppm, (b) 479 ppm, (c) 719 ppm and (d) 958 ppm of NH_3 under various humid conditions.

(iv) Working principle and gas sensing mechanism under humidity

It is evident that the conductivity of OLA/WS_2 sensor towards NH_3 increased in the presence of humidity implying that the H_2O molecules present in the saturated salts act as electron donor and results in n-type doping [32]. NH_3 induces n-type doping by donating an electron resulting to an increase in the conductance of the OLA/WS_2 based on a charge transfer mechanism [47]. This leads to a reduction in the density of holes in OLA/WS_2 sensing materials; thereby increasing the separation between the Fermi level and valence band [45]. The molecules present in the saturated salts adsorbed on the surface of OLA/WS_2 also shift the Fermi level closer to the conduction band edge [32]. The OLA/WS_2 sensors showed a high response especially at 97 % RH in the presence of humidity. Adsorbed water increases the surface electrical conductivity of the OLA/WS_2 due to the increased number of charge carriers [22]. A similar finding was made previously with the conductivity of WS_2 nanoflakes not only with NH_3 but with other reducing vapours like ethanol [48]. Humidity sensing is

based on the adsorption of water molecules on the surface of material and proton conduction with the proton acting as an effective carrier for the electrical conductivity [2, 32, 49, 50]. Two stages, chemisorption and physisorption had been identified to explain the mechanism of water adsorption on the surface of the sensing material [19]. Chemisorption is said to occur at relatively low % RH value to form two surface hydroxyls per water molecule [50]. According to Jha and Guha explained the sensing mechanism of NH_3 in the presence of water vapour based on the dangling bonds of OLA/WS_2 nanostructures [49]. The OLA/WS_2 nanostructures have a basal plane which is terminated by sulfur atoms and lacks dangling bonds; while its edges have dangling bonds which act as active sites for water vapour [49]. These edge defects often serve as sites for atmospheric oxygen molecules which replace sulfur. The atmosphere in wet and dry states acts as a donor (reducing gas) and acceptor (oxidizing gas) of electrons respectively from the surface of the sensor because of the presence of water vapour and oxygen. Therefore, the response of a sensor is enhanced or reduced by the atmosphere towards a particular gas and depends on either the target gas or type of material surface [17].

It is well known that water molecules dissociate to form hydroxyl (OH^-) and hydrogen (H^+) ions. During the first stage of water adsorption, a few water molecules chemisorb on the grain surfaces of the sensing material by a dissociative mechanism to form two surface hydroxyls per water molecule [44]. The OH^- ions introduce electrons directly onto the surface sensors leading to an increase in the conductivity of an n-type sensor while having little effect on a p-type sensor [2]. At this stage, water molecules are chemisorbed at the oxygen-activated sites to form an adsorption complex which is transferred to surface hydroxyl group [49]. Further increase in the humidity levels results in the physisorption of the water molecules on top of the chemisorbed layer by condensation in capillary pores through hydrogen bonding on the two neighboring hydroxyl group [22, 50]. As water molecules continue to flow, an extra layer is formed on the first physisorbed layer which is immobilized by the strong hydrogen bonding. This new layer of water molecules is disordered in nature and the degree of disorderliness increases as more and more water molecules accumulate in the gas chamber. This disorderliness leads to protons gaining the freedom to hop inside the condensed water molecule clusters; conductivity increases rapidly with an increase in % RH. Hence, with an increase in the concentration of water molecules, proton conductivity starts, and at higher humidity levels conductivity becomes more identical to conductivity in bulk water [49]. Conduction in this stage occurs mainly by the Grotthuss transport mechanism which suggests

that the conductivity is through the tunneling of proton from one water molecule to the next through hydrogen bonding, which exists between water–OLA/WS_2 interface [2, 22, 49, 50].

The remaining H^+ ions react with the surface oxygen molecules to form negative holes and increasing conductivity [2]. Their free movement along the water layer causes a decrease in film resistance [50]. The electrons are said to hop from the two immobile water layers, *i.e.* the chemisorbed and the first physisorbed layer, to the conduction band of OLA/WS_2 which is an n-type semiconductor in nature. This hopping of electrons from the first two layers of water also contributes significantly in increasing the conductivity, and hence sensor responses even at considerably less humid conditions [14, 49]. Subsequently, an electrolytic conduction in condensed water takes place in addition to the protonic transport in the physisorbed layers. It is this succession of mechanisms that leads to a rapid increase in conduction with increasing humidity content [22]. The presence of pores on the surface of the sensing material also increases the conductivity [22, 50]. The argument about dangling bonds on edge sites was put to a test by using the bulk WS_2 sample and no response was found irrespective of % RH. It was concluded that the irresponsiveness was due to lack of defect sites in bulk WS_2, which is necessary for adsorbing H_2O molecules [49]. WS_2 has an intrinsic hydrophobic nature which could be the contributing factor in the fast response sensing in the presence of humidity [49]. Jha and Guha went further and treated the WS_2 nanosheets with UV to decrease the oxygen content present as an impurity. A noticeable decrease in response in the UV treated sample was reportedly due to a decrease in oxygen content in the sample which helps in the formation of initial water layers on sensing material which in turn helps with proton conductivity in subsequent layers [49].

(v) Stability of OLA/WS_2 sensors

The stability of the sensor was studied by measuring the response of OLA/WS_2 sensors (15, 45, 60, 180 and 240 min) for five hours. The corresponding response versus time curves were plotted and shown in Figure 3.55. It is clear that the sensor has good stability up to the studied period.

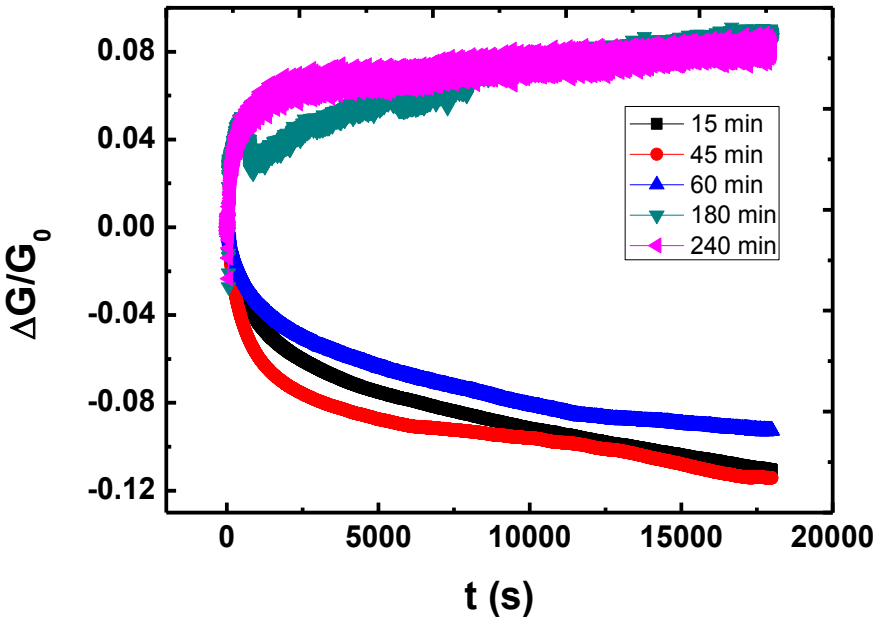


Figure 3.55: Response curves of OLA/WS_2 sensors (15, 45, 60, 180 and 240 min) towards at 240 ppm of NH_3 for five hours.

3.3.4 Conclusion

OLA/WS_2 sensors showed significant sensitivity towards dimethylformamide, ammonia and formic acid. This behaviour was more a function of concentration than morphology. Therefore, any of the five sensors tested can be used for the detection and identification of these three solvent vapours. We have showed the effect of different relative humidities to the adsorption of NH_3 by the sensors. Increased sensitivity towards NH_3 was observed under high relative humidity.

3.3.5 References

[1] Li, X., Li, X., Li, Z., Wang, J., Zhang, J. (2017). Sensors and Actuators B 240, 273–277.

[2] Fine, G. F., Cavanagh, L. M., Afonja, A. and Binions, R. (2010). Sensors 10, 5469-5502.

[3] Wu, J., Tao, K., Miao, J. and Norford, L. K. (2015). ACS Appl. Mater. Interfaces 7, 27502-27510.

[4] Rigoni, F., Drera, G., Pagliara, S., Goldoni, A. and Sangaletti, L. (2014). Carbon 80, 356-363.

[5] Sizun, T., Bouvet, M. and Suisse, J.-M.. IMCS 2012-The 14th International Meeting on Chemical Sensors. DOI 10.5162/IMCS2012/P1.1.20. 869-872

[6] Egashira, M., Shimizu, Y. and Takao, Y. (1990). Sensors and Actuators, El, 108-112.
[7] Kwon, T-H., Park, S-H, Ryu, J-Y. and Choi, H-H. (1998). Sensors and Actuators B 46, 75-79.
[8] Zhang, W-H. and Zhang, W-D. (2008). Sensors and Actuators B 134, 403-408.
[9] Šetka, M., Drbohlavová, J. and Hubálek, J. (2017). Sensors, 17, 562, 1-27.
[10] Qin, Z., Zeng, D., Zhang, J., Wu, C., Wen, Y., Shan, B. and Xie, C. (2017). Applied Surface Science 414, 244-250.
[11] Wagh, M. S., Jain, G. H., Patil, D. R., Patil, S. A. and Patil, L. A. (2006). Sensors and Actuators B 115, 128-133.
[12] Kanan, S. M., El-Kadri, O. M., Abu-Yousef, I. A. and Kanan, M. C. (2009). Sensors, 9, 8158-8196.
[13] Some, S., Xu, Y., Kim, Y., Yoon, Y., Qin, H., Kulkarni, A., Kim, T. and Lee, H. (2013). Sci. Rep. 3, 1868, 1-8.
[14] Wang, C., Yin, L., Zhang, L., Xiang, D. and Gao, R. (2010). Sensors 10, 2088-2106.
[15] Ionescu, R., Llobet, E., Brezmes, J., Vilanova, X. and Correig, X. (2003). Sensors and Actuators B 95, 177-182.
[16] Roy, S., Banerjee, N., Bhattacharyya, P. and Sarkar, C. K. (2013). Journal of Materials Science and Chemical Engineering, 1-5.
[17] Shankar, P. and Rayappan, J. B. B. (2015). ScienceJet 4, 126, 1-18.
[18] Gu, H., Wang, Z. and Hu, Y. (2012). Sensors 12, 5517-5550.
[19] Sharma, S. and Madou, M. (2016). Phil. Trans. R. Soc. A 370, 2448-2473.
[20] Chen, W-P., Zhao, Z-G., Liu, X-W., Zhang, Z-X and Suo, C-G. (2009). Sensors 9, 7431-7444.
[21] Cunha, B. B., Greenshields, M. W. C. C., Mamo, M. A., Coville, N. J. and Hümmelgen, I. A. (2015). J Mater Sci: Mater Electron 26, 198-4201.
[22] Yadav, B. C., Agrahari, K., Singh, S. and Yadav, T. P. (2016). J Mater Sci: Mater Electron 27, 4172–4179.
[23] Greenspan, L. (1977). Journal of Research of the National Bureau of Standards - A. Phys ics and Chemistry 81 A (1), 89-96.
[24] Calvi, A., Ferrari, A., Sbuelz, L., Goldoni, A. and Modesti, S. (2016). Sensors 16, 731, 1-9.
[25] Altavilla, C.; Sarno, M.; Ciambelli, P. (2011). Chem. Mater. 23, 3879-3885.
[26] Designation: E104 – 02 (Reapproved 2012) by agencies of the Department of Defense.

[27] Atewologun, A., Ge, W. and Stiff-Roberts, A. D. (2013). Journal of Electronic Materials 42, 809-814.

[28] Liu, I-S., Lo, H-H., Chien, C-T., Lin, Y-Y, Chen, C-W., Chan, Y-F., Sue, W-F., Liou, S-C. (2008). J. Mater. Chem. 18, 675-682.

[29] Qin, Z., Ouyang, C., Zhang, J., Wan, L., Wang, S., Xie, C. and Zeng, D. (2017). Sensors and Actuators B 253, 1034–1042.

[30] McCreary, K. M., Hanbicki, A. T., Jernigan, G. G., Culbertson, J. C. and Jonker, B. T. (2016). Sci. Rep. 6, 19159, 1-7.

[31] Koçak, Y., Akaltun, Y. and Gür, E. (2016). Journal of Physics: Conference Series 707, 012028, 1-7.

[32] Pawbake, A. S., Waykar, R. G., Late, D. J. and Jadkar, S. R. (2016). ACS Appl. Mater. Interfaces 8, 3359-3365.

[33] Pagona, G., Bittencourt, C., Arenal, R and Tagmatarchis, N. (2015). Chem. Commun. 51, 12950-12953.

[34] Liu, S., Shen, B., Niu, Y. and Xu, M. (2017). Journal of Colloid and Interface Science 488, 20-25.

[35] Ko, K. Y., Song, J-G., Kim, Y., Choi, T., Shin, S., Lee, C. W., Lee, K., Koo, J., Lee, H., Kim, J., Lee, T., Park, J., and Kim, H. (2016). ACS Nano 10, 9287-9296.

[36] Bhandavat, R., David, L. and Singh, G. (2012). J. Phys. Chem. Lett. 3, 1523−1530.

[37] Zhou, L., Yan, S., Pan, L., Wang, X., Wang, Y. and Shi, Y. (2016). Nano Res. 9 (3), 857–865.

[38] Lukowski, M. A., Daniel, A. S., English, C. R., Meng, F., Forticaux, A., Hamers, R. J. and Jin, S. (2014). Energy Environ. Sci. 7, 2608–2613.

[39] Liu, Y., Wang, W., Wang, Y. and Peng, X. (2014). Nano Energy 7, 25–32.

[40] Li, H., Yu, K., Fu, H., Guo, B., Lei, X. and Zhu, Z. (2015). Phys. Chem. Chem. Phys. 17, 29824-29833.

[41] Lin, L., Xu, Y., Zhang, S., Ross, I. M., Ong, A. C. M. and Allwood, D. A. (2013). ACS Nano 7 (9), 8214–8223.

[42] Nethravathi, C., Jeffery, A. A., Rajamathi, M., Kawamoto, N., Tenne, R., Golberg, D., and Bando, Y. (2013). ACS Nano 7 (8). 7311-7317.

[43] Perrozzi, F., Emamjomeh, S. M., Paolucci, V., Taglier, G., Ottaviano, L. and Cantalini, C. (2017). Sensors and Actuators B 201 243, 812-822.

[44] Cantalini, C., Valentini, L., Armentano, I., Lozzi, L., Kenny, J. M. and Santucci, S. (2003). Sensors and Actuators B 95, 195-202.

[45] Cho, B., Hahm, M. G., Choi, M., Yoon, J., Kim, A. R., Lee, Y-J., Park, S-G., Kwon, J-D., Kim, C. S., Song, M., Jeong, Y., Nam, K-S., Lee, S., Yoo, T. J., Kang, C. G., Lee, B. H., Ko, H. C., Ajayan, P. M. and Kim, D-H. (2015). Sci. Rep. 5, 8052, 1-6.

[46] Llobet, E., Molas, G., Molinàs, P., Calderer, J., Vilanova, X., Brezmes, J., Sueiras, J. E. and Correiga, X. (2000). Journal of The Electrochemical Society 147 (2) 776-779.

[47] Late, D. J., Huang, Y-K. Liu, B., Acharya, J., Shirodkar, S. N., Luo, J., Yan, A., Charles, D., Waghmare, U. V., Dravid, V. P. and Rao, C. N. R. (2013). ACS Nano 7 (6), 4879-4891.

[48] Huo, N., Yang, S., Wei, Z., Li, S-S., Xia, J-B. and Li, J. (2014). Rep. 4, 5209, 1-8.

[49] Jha, R. K. and Guha, P. K. (2016). Nanotechnology 27, 475503, 1-11.

[50] Kannana, P. K., Saraswathia, R., Rayappan, J. B. B. (2010). Sensors and Actuators A 164, 8-14.

3.4 Effect of ligand exchange and annealing on the sensitivity of OLA/WS_2 sensors towards NH_3

3.4.1 Introduction

Compared to their bulk counterparts, nanomaterials have a higher surface energy due to their reduced sized which may unfortunately lead to instability [1]. Stabilization of nanomaterials in solution is afforded by ligands, surfactants, capping or stabilizing agents which bind on the surface of the growing crystal to not only inhibit aggregation but passivate undercoordinated surface atoms of the nanomaterials, maintain solubility, protect against oxidation and tune their organic surface characteristics for exploitation in diverse applications [2-15]. Capping agents also play a key role in kinetic balancing of nucleation and growth rate; and by extension control of particle morphology, reaction pathways and particle size distribution [2-10, 14-18]. Bulk crystals or molecular clusters are a result of a nucleation rate that is either too slow or too fast with respect to the growth rate [4]. Commonly used capping agents including long-chain carboxylic and phosphonic acids (e.g., oleic acid and *n*-octadecylphosphonic acid), alkanethiols (e.g., dodecanethiol), alkyl phosphines and alkylphosphine oxides (e.g., trioctylphosphine, TOP, and trioctylphosphine oxide, TOPO), and alkylamines (e.g., hexadecylamine, oleylamine and octadecylamine stabilize nanomaterials electrostatically, sterically, by hydration forces, depletion, and by van de Waals forces [1, 4, 5, 7, 10, 16, 18-22]. However, their length and functionality create an insulating shell thereby blocking the access of molecular species to the surface which affects electron transfer process and carrier transport properties of nanomaterials [7, 9, 13, 17, 19, 20, 22-30].

Several studies have been dedicated to reducing the insulating organic capping agents for efficient charge generation and transport. Incidentally, most capping agents are interchangeable, allowing the exchange of pendant functionalities or the switch from organic to aqueous phases, or vice versa [3]. As-synthesized nanomaterials undergo surface treatment or modification through ligand exchange by replacing native ligands with shorter hydrophylic molecules to improve conductivity of nanomaterials [7, 9, 16, 17, 19, 20, 23, 24, 29, 31, 32]. Ligand exchange may afford solubility of the nanomaterials in special solvents, variation in surface anchoring group, introduction of new properties, new functional groups to the surface, reduction of the ligand shell [6, 11, 16, 17, 33, 34]. Furthermore, it may also change the energy alignment of organic-inorganic semiconductor interfaces, thereby providing a potential route to increasing the open voltage (Voc) [17]. During ligand exchange, an excess

of the ligand that is required to displace the original ligand on the surface of the nanomaterials is added to the nanomaterial solution [36]. Ligand exchange can be explained by the adsorption-desorption dynamics of capping ligands on the surface of nanomaterials. These dynamics depend mainly on the dynamic equilibrium of the adsorption reaction kinetic constant, desorption reaction kinetic constant, and steric repulsion of ligand molecules [17]. The new ligand molecules must have a strong affinity to the inorganic core so as to quickly and effectively replace the original ligand [34]. In addition, the molecular geometry of the ligands in relation to the particle diameter influences how densely the molecules are packed around the particles, which in turn influences ultimately the colloidal stability of the particles [34]. Solution ligand exchange with pyridine, ethanedithiol, mercaptopropionic acid, butylamine, thiophenes, hydrazine, hexanoic acid, nitrilotriacetic acid, dimercaptosuccinic acid, 4-dihydroxyhydrocinnamic acid, dopamine, imidazole or in the solid state with crosslinking agents like dithiols or diamines have been used to replace bulky ligands in fully inorganic and in hybrid organic/inorganic devices based on NCs such as solar cells, photodetectors or transistors [9, 17, 26, 28, 31, 32, 34]. It is worthy to note that the NCs capped with short alkylthiols, alkylamines, and pyridine, are very sensitive to oxidation and thermal degradation attributed to the relatively weak binding strength of small molecules. This leads to the reduced NC size and charge transfer, and increased carrier recombination [17]. On the other hand, post synthetic ligand exchange often goes hand in hand with the generation of surface trap states, which are detrimental for NCs' luminescence and charge transport properties [31]. The annealing of NC films often leads to the sintering of NCs and generation of undesirable carbonaceous species by partial ligand pyrolysis [27].

3.4.2. Experimental set-up

3.4.2.1 Chemicals and materials

All the solvents and salts were all of analytical grade and were used as received. Interdigitated electrodes consisting of ENIG (Electroless Nickel Immersion Gold) electrodes in 18 pairs of 7.9 mm long with a gap of 0.1 mm between them and patterned onto FR4 substrate were purchased from Micropress SA.

3.4.2.2 Ligand exchange

It is worthy to note that the ligand exchange was done post deposition.

(i) 1, 2-Ethanedithiol (EDT)

OLA was exchanged with EDT by dropping 60 µL of 2 % EDT (in acetonitrile) on the OLA/WS_2 sensor placed on a spin coater while spinning at 2000 rpm. EDT was alternated with 60 µL of acetonitrile after every 20 s. The cycle was repeated 15 times.

(ii) Mercaptoethanol (ME)

The procedure in (i) was followed for ME with 5 % of ME (in methanol) being used.

3.4.2.3 Annealing

OLA/WS_2, EDT/WS_2 and ME/WS_2 sensors were annealed at 100, 150 and 300 ℃ for 3 h each. Annealing at 300 ℃ was extended to 6 h.

3.4.2.4 Characterization techniques

The crystallographic structures of the OLA/WS_2 (before and after annealing) and EDT/WS_2 (after annealing) sensors for both 15 and 45 min was by determined by PXRD. The sensors annealed at 200 ℃ for 3 h were selected.

3.4.2.5 Gas sensing measurements

(i) Chemical vapour sensing measurements under limited light and low humidity environment

The devices were placed in an aluminium foil covered and rubber stoppered 1 L glass jar as shown in Figure 3.56. After fitting the contacts of the device in the cover, the chamber was purged with dry nitrogen for 30 min thereby decreasing the humidity inside the chamber to less than 20 % RH at room temperature. The devices were made from OLA/WS_2, EDT/WS_2 and ME/WS_2 and were measured before and after annealing.

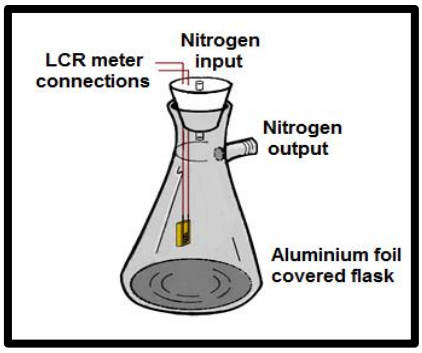


Figure 3.56: Schematic representation of the gas chambers used in sensor measurements.

3.4.3. Results and discussion

(i) Characterization: XRD analysis

The XRD patterns of the OLA/WS_2 and EDT/WS_2 nanostructures synthesized at 15 and 45 min are shown in Figure 3.57. The OLA/WS_2 nanostructures (before and after annealing) from both reaction times showed primary peaks at 16.26 (002), 27.59 (004), 32.35 (101), 38.71 (103), 45.42 (006), 56.44 (106) and 68.95 (008) degrees. However, the peaks had shifted to lower angles for the annealed sensors. All the diffraction patterns are indexed to the 2H-WS_2 polytype according to PDF No: 00-002-0131\JCP2.2CA. The peaks of the annealed EDT/WS_2 sensors could not be matched to WS_2 or WO_3.

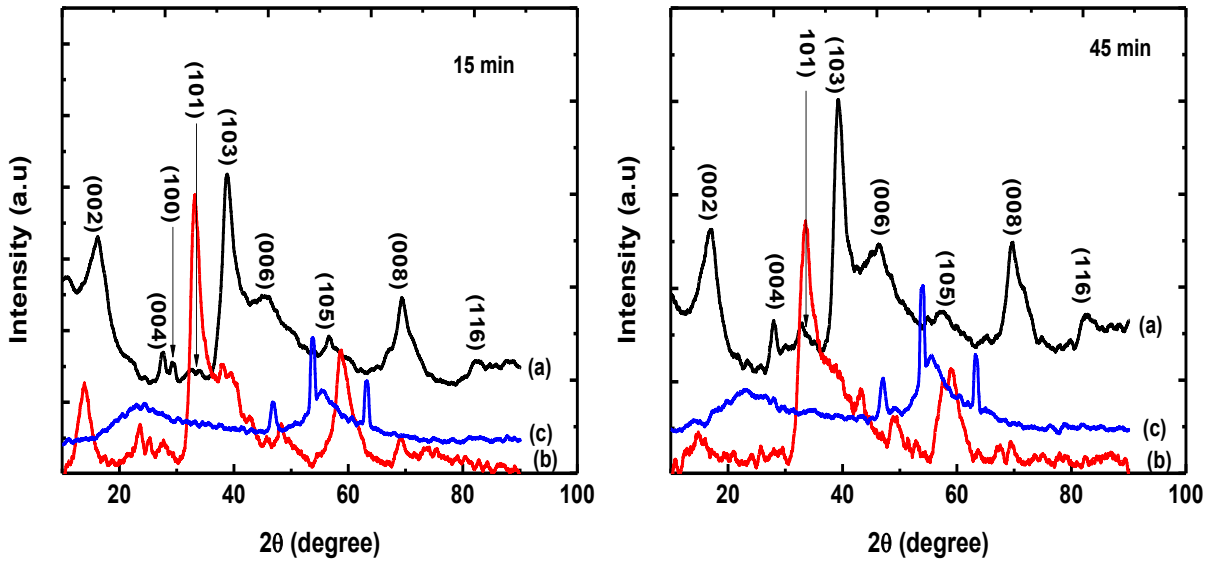


Figure 3.57: XRD patterns of WS_2 nanostructures synthesized at 15 and 45 min: (a) OLA/WS_2 before annealing; (b) OLA/WS_2 after annealing and (c) EDT/WS_2 after annealing. The annealing was performed for 3 h at 200 ℃.

(ii) Gas sensing performance before annealing

Figure 3.58 shows histograms representing the gas sensing response of OLA/WS_2 sensor, the ligand exchange sensors, EDT/WS_2 and ME/WS_2 derived from the 15 and 45 min reaction times. OLA is a long chain alkylamine ligand with seventeen carbons and its bulkiness transforms the semiconductor into an insulator. Meanwhile, EDT and ME are short chain thiol ligands with two carbons. It is well known that OLA can be easily displaced from the metal ion by thiol ligands and ligand exchange is performed. Thus, ligand exchanged sensors are expected to perform better than the OLA capped ones. From the response displayed in

Figure 3.58 (a), this expecation holds true for the EDT/WS_2 and ME/WS_2 derived from the 15 min reaction time. EDT/WS_2 response towards NH_3 was significantly higher than that of both OLA/WS_2 and ME/WS_2; and decreased gradually with increased concentrations of NH_3 due to saturation. Even though the response of EDT/WS_2 towards NH_3 at 240 and 479 ppm was higher than that of OLA/WS_2, a drastic decrease in response with higher concentrations of NH_3 was evident. The response of EDT/WS_2 was almost the same as that of OLA/WS_2 at 719 ppm and eventually became lower at 958 ppm. The response by the OLA/WS_2 sensor derived from 45 min was unexpectedly higher than that of EDT/WS_2 and ME/WS_2, Figure 3.58 (b). This response showed a drastic decrease with increased concentrations of NH_3. This decrease was seen with the ligand exchanged sensors as well. The EDT/WS_2 sensor still performed better than the ME/WS_2 sensor, an observation seen previously with the 15 min reaction time. The better performance of EDT when compared to ME could be linked to the functional groups. EDT has two thiol groups while ME has a thiol and an OH group.

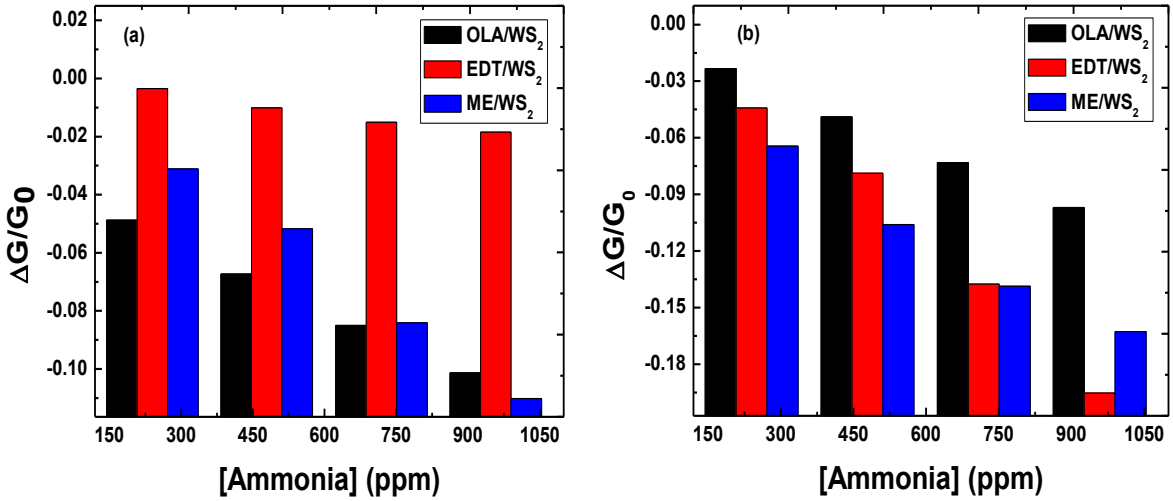


Figure 3.58: Histograms representing the response of OLA/WS_2, EDT/WS_2 and ME/WS_2 sensors from the (a) 15 min and (b) 45 min towards 240, 479, 719 and 958 ppm of NH_3 under limited light and low humidity.

(ii) Gas sensing performance after annealing

(a) 15 min

Figure 3.59 shows the responses of the sensors derived from the 15 min reaction time upon exposure to various concentrations of NH_3 after annealing at different temperatures. The responses for all the sensors towards exposure to 249 ppm of NH_3 before and after annealing are summarized in Table 3.7. As expected, a significant improvement in the response of the OLA/WS_2 sensor was observed after annealing at 100 ℃ for 3h. This response remained unchanged after three hours of annealing at 150 ℃; and started decreasing with heating at 200 ℃. A drastic reduction in performance was recorded after prolonged annealing at 200 ℃. It is known that WS_2 easily oxidizes easily to WO_3. The EDT/WS_2 and ME/WS_2 sensors also displayed an improved response after annealing at 100 ℃ for 3h which decreased gradually after annealing at higher temperatures. As is known, short chain ligands do not offer complete protection of the surface layer leaving the particles vulnerable to oxidation. A large amount of WO_3 on the surface of WS_2 leads to reduced response because the operating working temperature of the oxide counterpart is higher than the room temperature. WO_3 was not detected by PXRD as previously observed with the unannealed OLA/WS_2 nanostructures (Figure 3.57) but was detected XPS analysis. Upon comparing the three sensors with each other at 249 ppm of NH_3, it was discovered that ME/WS_2 sensor displayed the best response towards NH_3 than OLA/WS_2 and EDT/WS_2 after annealing at 100 ℃ for 3h. At the same time, the response decreases with an increased concentration of NH_3 as seen previously before annealing. Once again, annealing at higher temperatures and/or for longer periods reduced the sensors' performance.

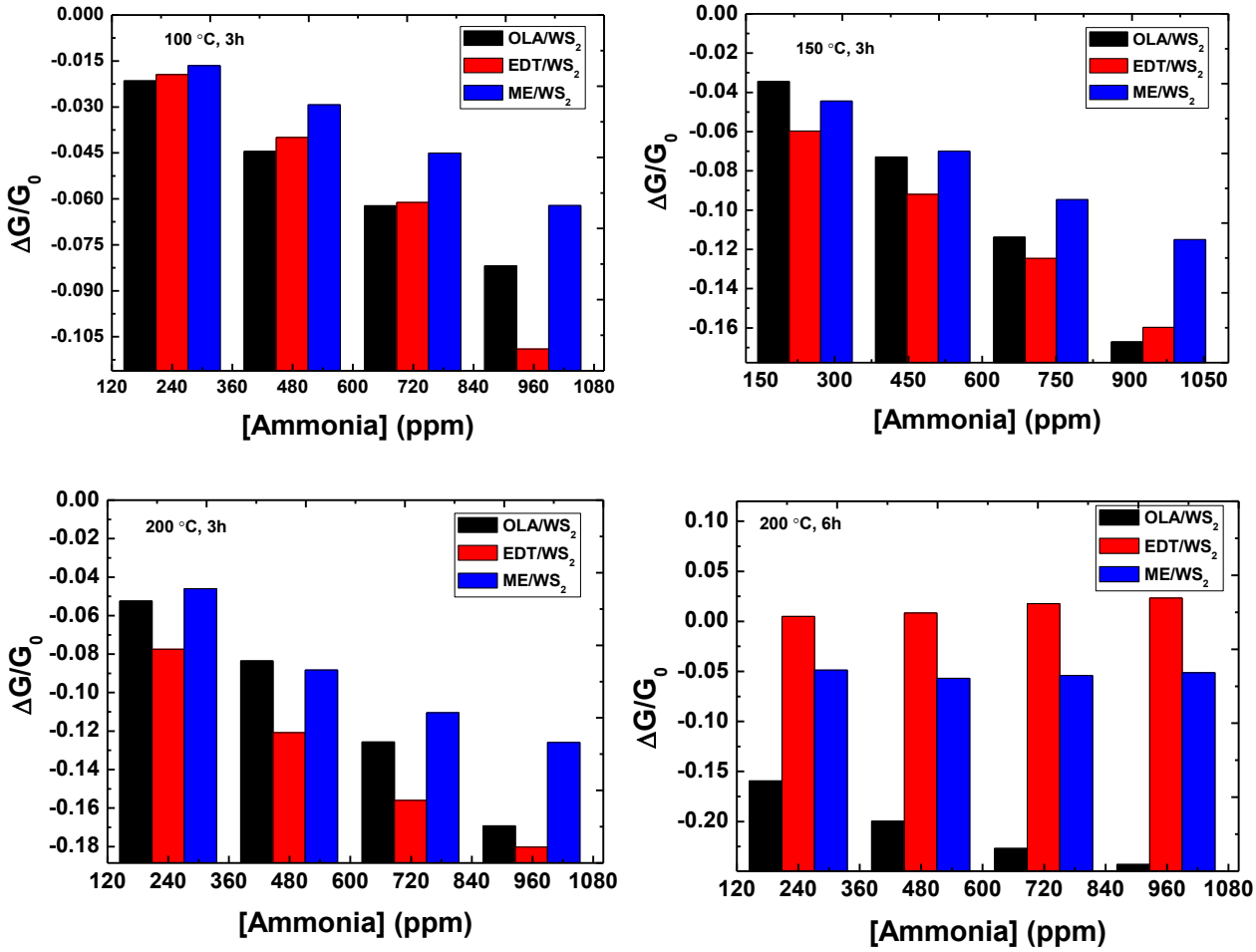


Figure 3.59: Histograms representing the response of OLA/WS_2, EDT/WS_2 and ME/WS_2 sensors from the 15 min reaction time towards 240, 479, 719 and 958 ppm of NH_3 under limited light and low humidity.

Table 3.7 A summary of the responses of the 15 min sensors towards 249 ppm NH_3.

Sensor (15 min)	Annealing temperature (degrees)	Sensor response (variation)
OLA/WS_2	0	4.81
	100	8.11
	150	8.12
	200, 3h	7.25
	200, 6h	2.42
EDT/WS_2	0	7.95
	100	8.33
	150	6.65
	200, 3h	5.85
	200, 6h	6.86
ME/WS_2	0	6.09
	100	8.58
	150	7.49
	200, 3h	7.56
	200, 6h	5.43

(b) 45 min

The responses for the sensors from the 45 min reaction time are represented by histograms in Figure 3.60. The variations in response to NH_3 are summarized in Table 3.8. Interestingly, the OLA/WS_2 sensor presented a reduced response to 240 ppm of NH_3 after 3h of annealing at 100 ℃. Meanwhile, EDT/WS_2 and ME/WS_2 sensors exhibited higher responses after annealing at the same temperature. Of all the three sensors, ME/WS_2 showed the best performance. Annealing at higher tempertaures reduced the response of all the sensors.

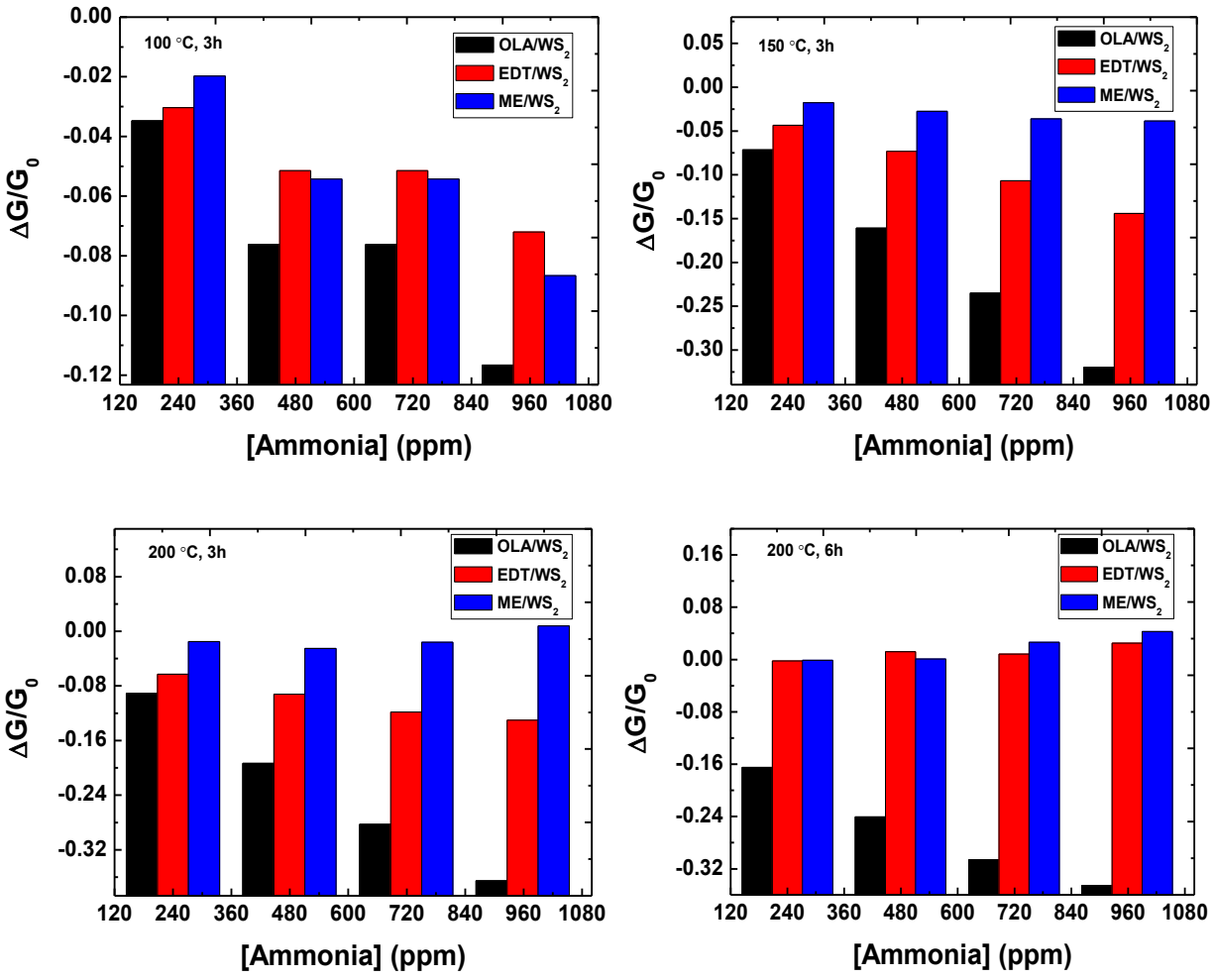


Figure 3.60: Histograms representing the response of OLA/WS_2, EDT/WS_2 and ME/WS_2 sensors from the 45 min reaction time towards 240, 479, 719 and 958 ppm of NH_3 under limited light and low humidity.

Table 3.8: A summary of the responses of the 45 min sensors towards 249 ppm NH_3.

Sensor (45 min)	Annealing temperature (degrees)	Sensor response (variation)
OLA/WS_2	0	8.47
	100	7.18
	150	6.41
	200, 3h	5.53
	200, 6h	3.47
EDT/WS_2	0	7.49
	100	7.56
	150	7.07
	200, 3h	6.09
	200, 6h	6.44
ME/WS_2	0	6.58
	100	8.37
	150	7.71
	200, 3h	6.97
	200, 6h	6.44

3.4.5 Conclusion

Preliminary investigations into the effect of replacement of OLA with EDT and ME showed an improvement in the response of the sensors towards NH_3 vapours. Annealing of the sesnsors at low temperature also improved their performance towards NH_3. Further analysis of the sensors by XPS is warranted to confirm the success of the ligand exchange and elucidate any changes to the morphology, structure and chemical composition of the nanostructures after annealing. This will assist in the determination of the reason behind the decrease in response after annealing at high temperatures.

3.4.6 References

[1] Toh, H. S., Jurkschat, K. and Compton, R. G. (2015). Chem. Eur. J. 21, 2998-3004.

[2] Niu, Z. and Li, Y. (2014). Chem. Mater.26, 72-83.

[3] Green, M. (2010). J. Mater. Chem. 20, 5797-5809.

[4] Talapin, D. V., Lee, J-S., Kovalenko, M. V. and Shevchenko, E. V. (2010). Chem. Rev. 110, 389-458.

[5] Cara, C., Musinu, A., Mameli, V., Ardu, A., Niznansky, D., Bursik, J., Scorciapino, M. A., Manzo, G. and Cannas, C. (2015). Cryst. Growth Des. 15, 2364-2372.

[6] Wang, X-S., Dykstra, T. E., Salvador, M. R., Manners, I., Scholes, G. D. and Winnik, M. A. (2004). J. Am. Chem. Soc.126, 7784-7785.

[7] Colbert, A. E., Wu, W., Janke, E. M., Ma, F. and Ginger, D. S. (2015). J. Phys. Chem. C 119, 24733-24739.

[8] You, H., Yang, S., Ding, B. and Yang, H. (2013). Chem. Soc. Rev. 42, 2880-2904.

[9] Zhang, Z-X., Zhou, Z-J., Bai, B., Liu, M-H., Zhou, W-H., Kou, D-X., Wu, S-X. (2015). J Nanopart Res 17 (463), 1-8.

[10] Duan, H., Wang, D. and Li, Y. (2015). Chem. Soc. Rev. 44, 5778-5792.

[11] Knauf, R. R., Lennox, J. C. and Dempsey, J. L. (2016). Chem. Mater. 28, 4762-4770.

[12] Kim, S. B., Cai, C., Kim, J., Sun, S. and Sweigart, D. A. (2009). Organometallics 28, 5341-5348.

[13] Nag, A., Zhang, H., Janke, E. and Talapin, D. V. (2015). Phys. Chem. 229 (1–2), 85-107.

[14] Dai, M. Q. and Yung, L-Y., L. (2013). Chem. Mater. 25, 2193-2201.

[15] de Mello Donegá, C. (2011). Chem. Soc. Rev. 40, 1512-1546.

[16] Lokteva, I., Radychev, N., Witt, F., Borchert, H., Parisi, J. and Kolny-Olesiak, J. (2010). J. Phys. Chem. C 114, 12784-12791.

[17] He, M., Qiu, F. and Lin, Z. (2013). J. Phys. Chem. Lett. 4, 1788-1796.

[18] Boles, M. A., Ling, D., Hyeon, T. and Talapin, D. V. (2016). Nature Materials 15, 141-153.

[19] Dong, A., Ye, X., Chen, J., Kang, Y., Gordon, T., Kikkawa, J. M. and Murray, C. B. (2011). J. Am. Chem. Soc. 133, 998-1006.

[20] Liu, W., Lee, J-S., Talapin, D. V. (2013). (2013). J. Am. Chem. Soc. 135, 1349-1357.

[21] Wei, J., Schaeffer, N. and Pileni, M-P. (2014). J. Phys. Chem. B 118, 14070-14075.

[22] Klokkenburg, M., Hilhorst, J. and Erné, B. H. (2007). Vibrational Spectroscopy 43, 243-248.

[23] Lee, D., Lim, J., Park, M., Kim, J. Y., Song, J., Kwak, J., Lee, S., Char, K and Lee, C. (2015). Nanotechnology 26, 465401, 1-9.

[24] Kim, B-S., Hong, J., Hou, B., Cho, Y., Sohn, J. I., Cha, S. N. and Kim, J. M. (2016). Applied Physics Letters 109, 063901, 1-4.

[25] Kumar, B. G. and Muralidharan, K. (2011). J. Mater. Chem. 21, 11271-11275.

[26] He, J., Chen, J., Yu, Y., Zhang, L., Zhang, G., Jiang, S., Liu, W., Song, H., Tang, J. (2014). J Mater Sci: Mater Electron 25, 1499-1504.

[27] Kovalenko, M. V., Bodnarchuk, M. I., Zaumseil, J., Lee, J-S. and Talapin, D. V. (2010). J. Am. Chem. Soc. 2010, 132, 10085-10092.

[28] Fu, W., Shi, Y., Qiu, W., Wang, L., Nan, Y., Shi, M., Li, H. and Chen, H.(2012). Phys. Chem. Chem. Phys. 14, 12094-12098.

[29] Law, M., Luther, J. M., Song, Q., Hughes, B. K., Perkins, C. L. and Nozik, A. J. (2008). J. Am. Chem. Soc.130, 5974-5985.

[30] Tang, J., Kemp, K. W., Hoogland, S., Jeong, K. S., Liu, H., Levina, L., Furukawa, M., Wang, X., Debnath, R., Cha, D., Chou, K. W., Fischer, A., Amassian, A., Asbury, J. B. and Sargent, E. H. (2011). Nature Materials 10, 765-771.

[31] Lefrançois, A., Pouget, S., Vaure, L., Lopez-Haro, M. and Reiss, P. ChemPhysChem, 2016, 654-659.

[32] Wang, X., Tilley, R. D. and Watkins, J. J. (2014). Langmuir 30, 1514-1521.

[33] Woehrle, G. H., Brown, L. O. and Hutchison, J. E. (2005). J. Am. Chem. Soc. 127, 2172-2183.

[34] Sperling, R. A. and Parak, W. J. (2010). Phil. Trans. R. Soc. A 368, 1333-1383.

[35] Bagaria, H. G., Ada, E. T., Shamsuzzoha, M., Nikles, D. E., and Johnson, D. T. (2006). Langmuir 22, 7732-7737.

Chapter 4 : Synthesis, characterization and application of indium sulphide nanostructures in gas sensing

4.1 Investigation of the influence of reaction time and concentration of sulphur on the morphology of β-In_2S_3 nanostructures.

4.1.1 Introduction

Indium sulphide, a group III-VI chalcogenide [1-17] has two compositions InS and In_2S_3 [6, 18-22] with band gaps of 2.44 eV [1, 18, 20-22] and 1.9-2.9 eV [1, 3, 5, 8, 9, 12-14, 17-37] respectively. In_2S_3 has three polymorphs defect spinel β-In_2S_3, defect cubic α-In_2S_3 and layered γ- In_2S_3 [1, 2, 4-6, 8, 10-13, 15-19, 23, 24, 26, 33, 37-39] which come into existence as a function of temperature and pressure [11, 12, 19, 20]. β-In_2S_3 is stable up to 1027 K [2, 20, 24, 30, 31, 35], cubic α-In_2S_3 is stable up to 693 K while layered γ- In_2S_3 is stable above 1027 K [1, 4-6, 8, 10, 11, 13, 16-19, 26, 31, 33, 37-39]. Of interest to us is β-In_2S_3 which has been proven to be the most stable polymorph at room temperature [12, 16, 39, 40]. β-In_2S_3 is an n-type semiconductor [1, 3, 8, 9, 12-14, 17, 19, 24, 26, 28-31, 37, 32, 34, 40, 41] with inherent optical, electronic, optoelectronic [1,3, 6, 7, 13, 17, 21, 23, 26-29, 37], catalytic [1, 27, 29, 26, 36], acoustic [3, 17, 18, 21, 26, 28], gas sensing [27, 36] and biological image sensing [6] properties associated with its defect structure. Its high photoconductive, photoelectric conversion, photoluminescent and photosensitive properties [3, 11, 13, 23-26, 39, 42-46] have inspired applications in the preparation of green and red phosphors in the manufacture of picture tubes for color televisions, cells, and heterojunction for use in photocurrent generation, photocatalyst for dye degradation, photochemical evolution of hydrogen and selective oxidation [3, 17, 28, 42]. A large volume of research is dedicated to its potential as a buffer layer to replace highly toxic CdS [7, 9, 10, 13, 16, 23, 29, 30, 41, 46]. However, its potential as a gas sensing material remains largely untapped.

The structure of β-In_2S_3 presents a large number of intrinsic vacancies [40, 47-51] with a third of the tetrahedral sites remaining empty due to incompletely coordinated sulfur atoms [25, 30, 38, 47]. These vacancies have rendered it a suitable host to various cations and anions [21, 23, 29, 30, 39, 47, 51] to produce materials with superior semiconductive and/or magnetic properties [30, 47]. Furthermore, the vacancies impart efficient carrier separation such that In_2S_3 nanostructures demonstrate good NIR photocatalytic performance as well as very high efficient UV and visible light photocatalytic activities [51]. Crystalline β-In_2S_3 (Figure 4.1) exists in either tetragonal [33, 52] or cubic form [17, 21] with either a direct [8,

24, 25, 33, 44, 48] or indirect conduction to valence band transitions [48, 53]. β-In_2S_3 has a large exciton Bohr radius (34 nm) [1, 8, 30] which makes it a suitable material for the study of quantum confinement effects in various morphologies and sizes [1].

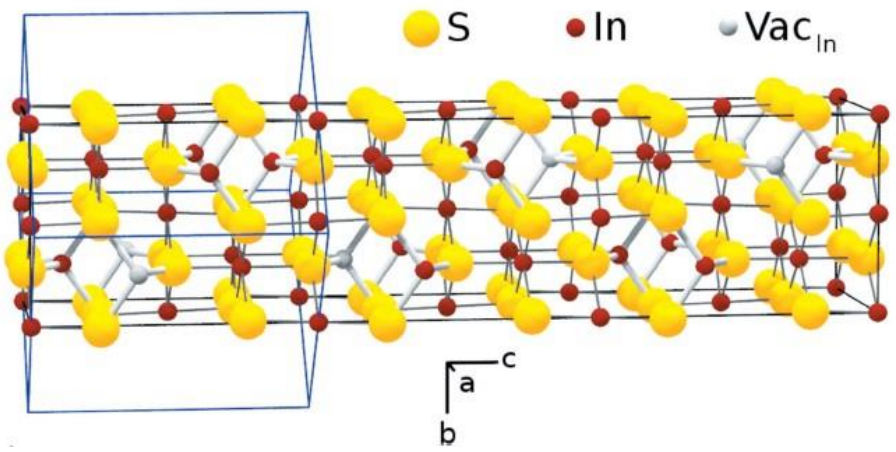


Figure 4.1: Structure model of β-In_2S_3 unit cell. The indium vacancies are marked as grey spheres. In the tetragonal β-In_2S_3 configuration, the vacancies are ordered on a 41 screw axis parallel to the c-axis of the crystal. In the α-In_2S_3 configuration, the vacancies are randomly distributed over all tetrahedral indium sites. The edges of the unit cell of the tetragonal β-In_2S_3 structure (cubic α-In_2S_3) structure are indicated by black (blue) lines [43].

The chemical composition, structure and phase of a semiconductor are not the only factors that determine its application; its shape, size, size distribution and dimensionality also play a crucial role. It is for this reason that in the past few years many researchers focused on the fabrication of nanometer materials with various morphologies, urchin-like [36, 57], nanobelts [1, 18], nanofibers [26], nanoplates [24], nanoflakes [1, 21, 45], nanosheets [29, 32], nanorods [9]. Several wet chemical synthetic routes have been developed to fabricate different morphologies of both the tetragonal [58, 55] and cubic [59, 60] forms of β-In_2S_3 with and without capping agents. The choice of capping agents in colloidal synthesis is very crucial as they not only stabilize the particles prevent aggregation and overgrowth; they influence size, shape and interactions with surrounding solvent, [61-68]. Capping agents control the morphology of nanostructure because of their soft template effect, ability to regulate reaction kinetics and ease of manipulation [61]. Capping agents selectively adsorb on particular crystallographic planes to induce anisotropic growth, thus particles shape to non-spherical forms, such as disk or rod [61, 62]. In this study, the heating up method was

employed to synthesize well-shaped β-In_2S_3 nanostructures with low polydispersity in the presence of oleylamine. The reaction parameters, time and concentration were investigated for their effect on the structure, size, morphology and optical properties of the nanostructures. The resulting nanostructures were used as the active component of gas sensing devices for the detection of solvent vapours like ethanol and formaldehyde.

4.1.2 Experimental procedure

4.1.2.1 Chemicals and materials

Indium (III) chloride, sulphur powder, oleylamine (OLA), chloroform, toluene, dichloromethane, acetone, isopropyl alcohol, formaldehyde and ethanol were purchased from Sigma Aldrich. Interdigitated electrodes consisting of ENIG (Electroless Nickel Immersion Gold) electrodes in 18 pairs of 7.9 mm long with a gap of 0.1 mm between them and patterned onto FR4 substrate were purchased from Micropress SA.

4.1.2.2 Synthesis of β-In_2S_3 nanostructures

(i) 1:1 (In:S)

In a 100 mL three-neck round bottom flask attached to a Schlenk line via a condenser, 17 mL of OLA was heated to 100 ℃ with continuous stirring under the flow of nitrogen gas. It was held at this temperature for 20 min to get rid of any water molecules and air. Ultimately, a clear light yellow liquid was obtained into which 5 mmol of indium (III) chloride and 5 mmol of sulphur powder were added. The mixture was then heated rapidly to 220 ℃ and held at this temperature for 330 min with aliquots of the yellow colloidal solution taken at 60, 90, 120, 150, 210, 300 and 330 min. The aliquots were allowed to cool to 80 ℃ and ethanol was added to flocculate the nanostructures. The nanostructures were then collected by centrifugation for 10 min at 3000 rpm and washed several times with ethanol and dichloromethane in order to remove unreacted precursors and excess OLA. The resultant products were left to dry at room temperature for 12 h to obtain yellow powders. The effect of reaction time and ratio of sulphur powder to indium (III) chloride was investigated.

(ii) 1:1.5 (In:S)

The same procedure as in (i) above was followed but 7.5 mmol of S was used.

(iii) 1:2 (In:S)

The same procedure as in (i) above was followed but 10 mmol of S was used.

4.1.2.3. Preparation of nanostructure dispersions

A 10 mg/mL dispersion of finely ground β-In_2S_3 in toluene was prepared using nanostructures from the 330 min reaction time (1:1 reaction system). The dispersion was sonicated at room temperature for 30 min.

4.1.2.4 Fabrication of β-In_2S_3 gas sensors

(i) Preparation of devices

Metal contacts were soldered onto IDEs and cleaned by sonicating in acetone, water and isopropanol sequentially in a 135 W ultrasonic bath for 20 min each. The IDEs were air dried and finally placed in a UV ozone cleaner (Novascan; intense 185 nm and 254 nm ultraviolet light) for 30 min to remove organic residues.

(ii) Preparation of thick films

A film of β-In_2S_3 was prepared by drop casting 20 μL of the 330 min nanostructure dispersion onto the IDEs. The IDEs were later dried in the oven at 100 ℃ under vacuum for 30 min.

(iii) Preparation of the gas chamber

A clean and dry 2.4 L glass bottle with a rotating lid was used as a gas chamber (Figure 4.2). The chamber was covered with aluminium foil and black tape to create a dark environment. The aluminium foil was earthed to reduce its noise contribution.

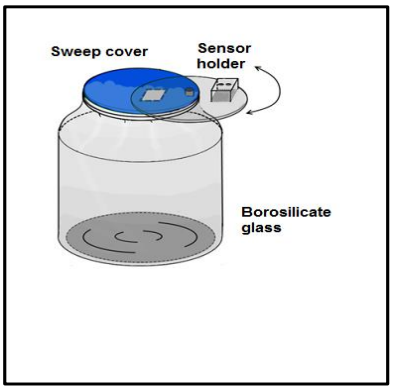


Figure 4.2: Schematic representation of the gas chamber (with a sweep cover).

4.1.2.5 Gas sensing measurements

Preliminary electrical measurements were performed at room temperature and in the dark. An LCR meter (Agilent 4284A 20 Hz – 1 MHz Precision LCR meter) attached to a computer interfaced with a GPIB was used for data acquisition. An operational voltage and frequency of 1000 mV and 10 kHz were selected respectively due to their higher signal-to-noise ratio. The system was allowed to stand for 1h before measurements were performed. The baseline was measured for 30 s, with the device exposed to the outer environment (dry nitrogen filled glove box; RH < 20%). The cap was swept and the sensor was exposed to the formaldehyde saturated (1000 ppm) atmosphere inside the chamber until the baseline stabilized (around 100 s). The cap was then swept back and the sensor was again exposed to the outer environment. This cycle was repeated a number of times; the signal was allowed to return to the baseline value before exposing the sensor to another 1000 ppm of formaldehyde.

4.1.3 Characterization techniques

4.1.3.1 Structural properties of the nanostructures

The stoichiometry and phase of the finely ground powder of β-In_2S_3 were determined by a Bruker MeasSrv (D2-205530)/D2-205530 diffractometer using secondary graphite monochromated CuKα radiation (λ 1.54060 Å) at 30 kV/30 mA. The evolution of the morphology was monitored by transmission electron microscopy (TEM) using a Technai G2 TEM Spirit operated at 200 kV and a high resolution electron microscope (HRTEM) by JEOL JEM-2100, operated at 200 kv. The TEM samples were prepared by drop-casting the chloroform dispersion onto the carbon-coated copper grids and allowed to dry at room temperature.

4.1.3.2 Optical properties of the nanostructures

A chloroform dispersion of β-In_2S_3 nanostructures was placed in a quartz cuvette with 1 cm path length for the determination of its optical properties. A Specord 50 AnalytikJena UV-Vis spectrophotometer was used to carry out the absorption measurements while an Agilent Cary Eclipse fluorescence spectrometer was used to measure the photoluminescence of the nanostructures. The presence of the capping agent on the surface of the nanostructures was confirmed by using a Bruker Tensor 27 FT-IR.

4.1.4 Results and discussion

4.1.4.1 Synthesis of OLA/β-In_2S_3 nanostructures

(i) 1:1 (In:S)

$InCl_3$ is thermally decomposed by while elemental sulphur is reduced by OLA. The proposed chemical reaction is:

$$2In^{3+} + 2S^{2-} \xrightarrow[N_2,\ OLA]{220\ ℃} In_2S_3\ (s) \qquad (4.1.1)$$

The TEM images of OLA/β-In_2S_3 nanostructures are shown below in Figure 4.3. As can be seen from Figure 4.3 (a)-(g), the reaction time affected the morphology and size of the nanostructures.

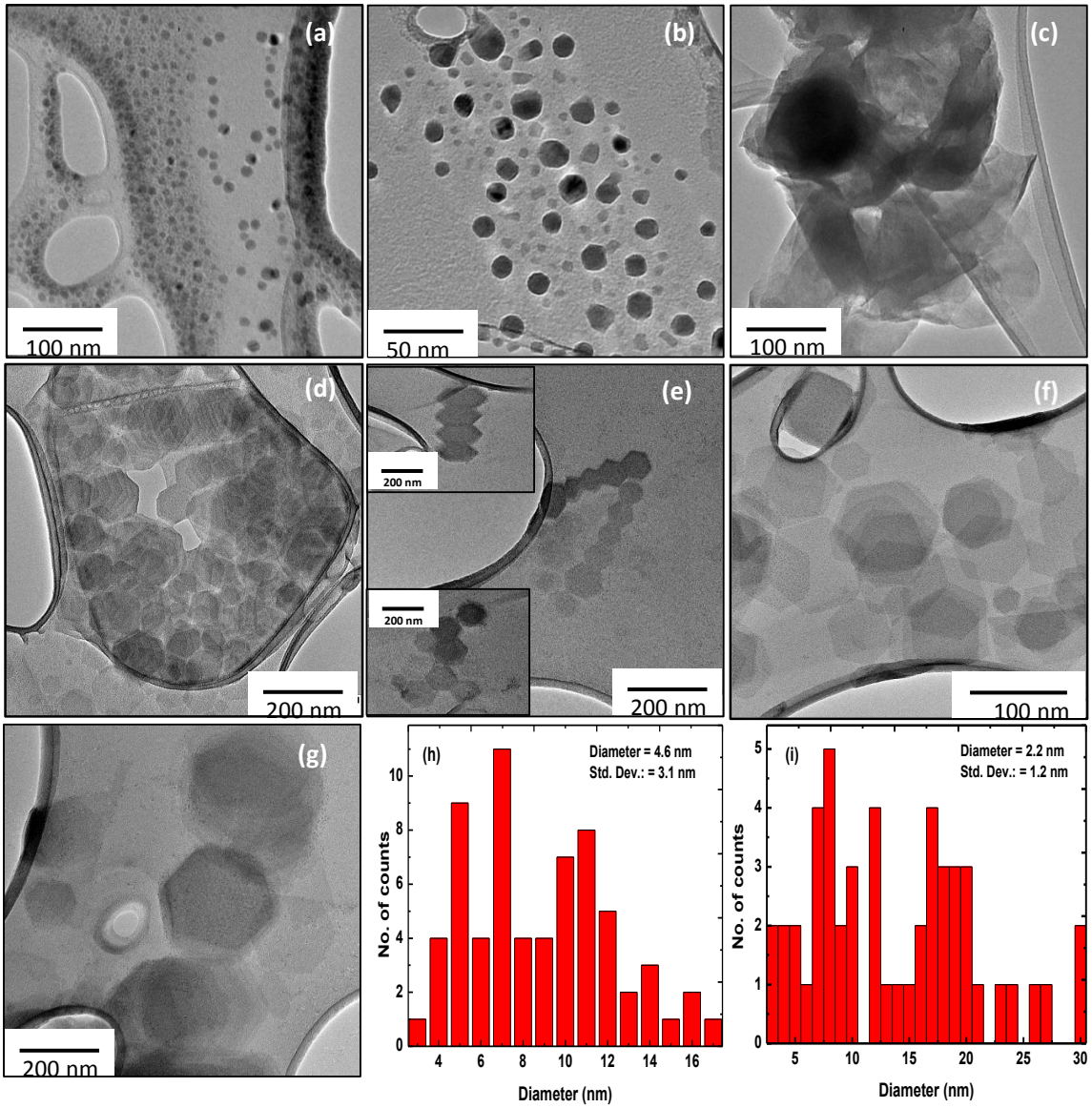


Figure 4.3: The TEM images of OLA/β-In_2S_3 nanostructures in the 1:1 (In:S) reaction system at: (a) 60 min, (b) 90 min, (c) 120 min, (d) 150 min, (e) 210 min, (f) 300 min, (g) 330 min; (h) and (i) represent size distribution for 60 and 90 min nanostructures respectively.

Figure 4.3 (a) shows the growth of nanoparticles with an average diameter of 4.6 $\pm$ 3.1 nm in 60 min which develop facets with further heating for 90 min (average diameter 2.2 $\pm$ 1.2 nm) as shown in (b). The polydispersed nature of the nanoparticles is clearly evident from the size distribution presented in the insets (h) and (i). It was discovered that prolonging the reaction time to 120 min resulted in nanosheets as shown Figure 4.3 (c). Further heating saw the emergence of the hexagonal nanoplate morphology with different assembly arrangements at 150, 210, 300 and 330 min with widths between 74 and 198 nm as represented by Figure 4.3 (d)-(g).

Representative XRD patterns of the as-prepared nanostructures of OLA/β-In_2S_3 at different reaction times are shown in Figure 4.4.

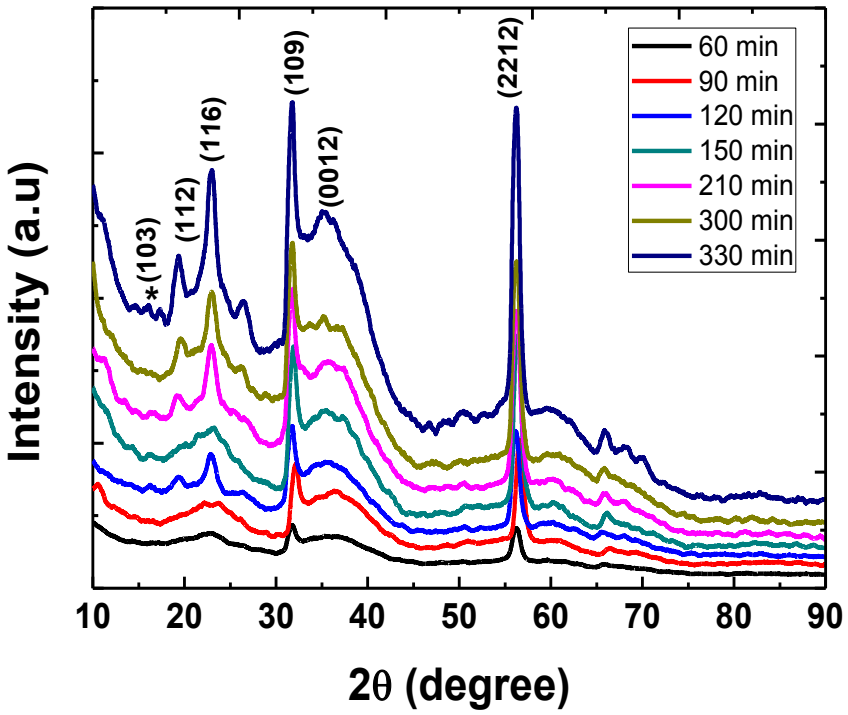


Figure 4.4: XRD patterns of OLA/β-In_2S_3 nanostructures at different reaction times in the 1:1 (In:S) reaction system.

All the diffraction peaks can be indexed to the tetragonal phase of β-In_2S_3 crystal structure (PDF card no.: 00-025-0390) with a preferred plane orientation of (109) and (2212). Generally, the reflections became sharper and stronger with prolonged reaction time indicating improved crystallinity of the nanostructures.

Typical UV-vis spectra of the as-synthesized OLA/β-In_2S_3 nanostructures with the characteristic step-like shape (inset) [20, 23] are presented in Figure 4.5. The band gap values were obtained by extrapolating the absorption edge by a linear fit method. It is clear that reaction time also affected the band gap as evident with the values summarized in Table 4.1. Interestingly, the nanostructures at shorter reaction times (60, 90 and 120 min) showed a blue shift and maintained a band gap of 2.5 eV despite the change in morphology. This is associated with their smaller size (diameters less than the Bohr radius, 34 nm), an indication of quantum confinement. On the contrary, the nanostructures obtained at longer reaction

times (150, 210, 300 and 330 min) showed a slight shift towards longer wavelengths accompanied by reduced band gaps (2.1-2.3 eV). It is known that extended reaction times result in larger particle sizes as seen from the TEM images in Figure 4.3 (d)-(g).

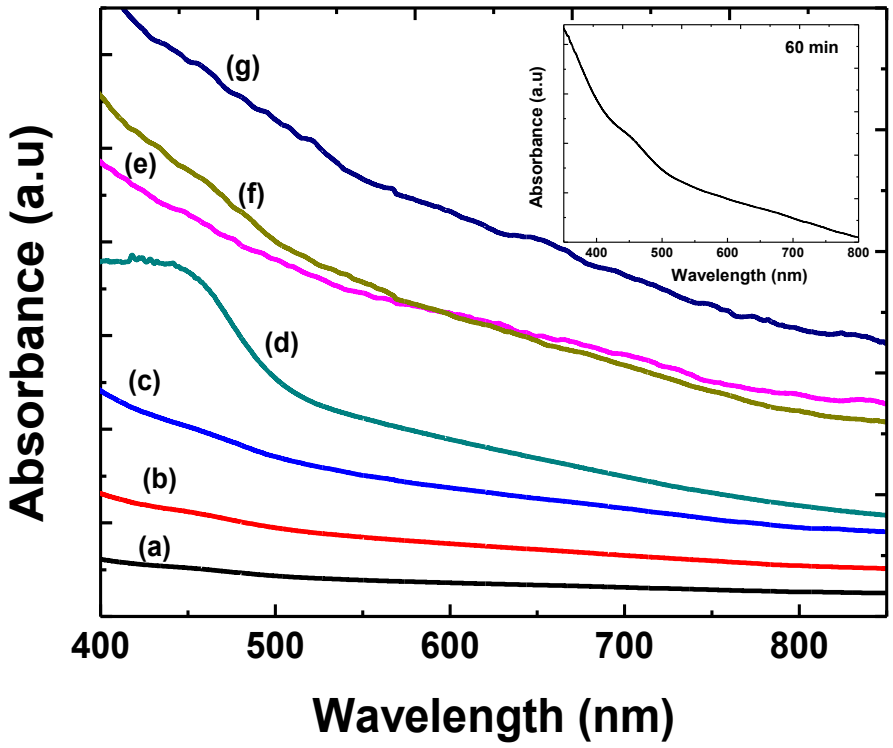


Figure 4.5: UV-vis spectra of OLA/β-In_2S_3 nanostructures at (a) 60 min, (b) 90 min, (c) 120 min, (d) 150 min, (e) 210 min, (f) 300 min, and (g) 330 min in the 1:1 (In:S) reaction system.

Band gap is not only affected by morphology but also by the size of the nanostructures. It is therefore not surprising to see different band gap values of the synthesized nanostructures given their different sizes as corroborated by the TEM images. The larger widths of the nanoplates accompanied by the stacking and overlapping arrangement constituted bigger nanostructures. Nonetheless, a blue shift from the bulk absorption of 620 nm (2.0 eV) [10, 15, 24, 38] is evident. The blue shift is an indication of smaller sized nanoparticles and valence to conduction band transition in OLA/β-In_2S_3 [22]. The band-to-band transition is corroborated by the steep shape of the visible region absorption band of β-In_2S_3 [30].

Room temperature PL of the as-prepared nanostructures is presented in Figure 4.6. All the nanostructures presented a broad emission extending from 390 to 610 nm under PL excitation of 300 nm with tailing towards longer wavelengths. The emissions were characterized by

shoulders, the λ are summarized in Table 4.1. The 330 min nanostructures presented an interesting emission with four shoulders. Three strong blue light emissions located at 454, 479 and 504 nm were observed and these are attributed to the presence of several deep trap states or inherent defects in the structure. This is in agreement with reported results where indium interstitial sites [18, 23, 24] and sulphur vacancies were cited as the source of new energy levels in the band gap [33].

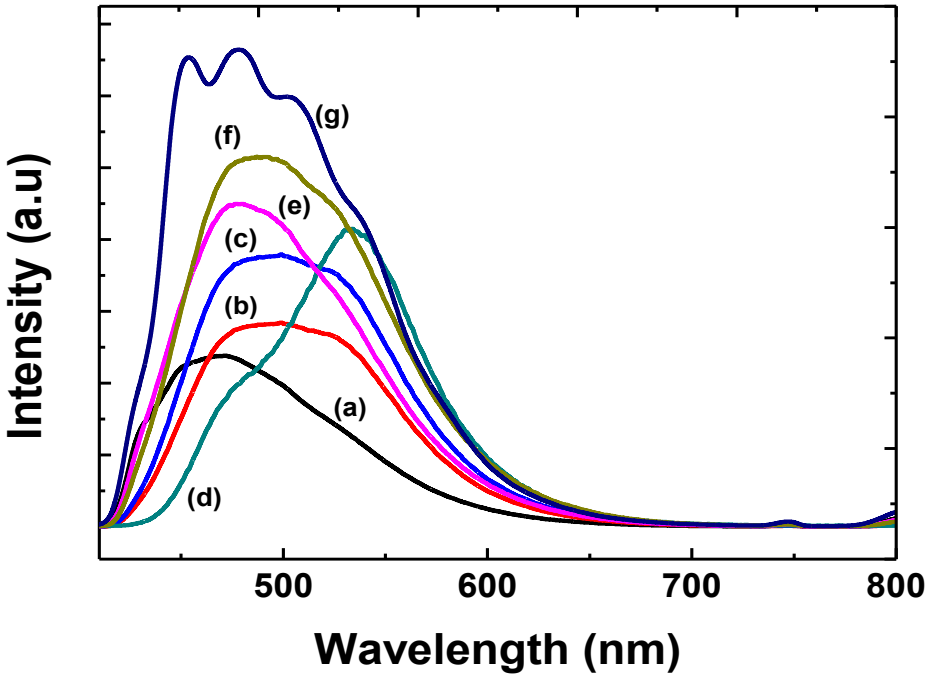


Figure 4.6: PL spectra of OLA/β-In_2S_3 nanostructures at (a) 60 min, (b) 90 min, (c) 120 min, (d) 150 min, (e) 210 min, (f) 300 min, and (g) 330 min in the 1:1 (In:S) reaction system.

Indium interstitial defects are well known common defect emitters in indium-rich binary and ternary chalcogenides [23, 60]. It is said that the green emission is due to transitions between donors created by vacancies of sulfur (V_s) and acceptors due to vacancies of indium (V_{In}). Meanwhile, the red emission arises as a transition from indium interstitial (In_i) donors to oxygen in vacancy of sulfur (O_{Vs}) acceptors [18]. Their intensity is related to their stronger absorption in this region as observed from the absorption spectra. A weak green emission at 539 nm is due to band-band transitions in OLA/β-In_2S_3. The luminescent character of as-prepared nanostructures points to the existence of electronic transitions at certain wavelengths in contrast to non-luminescent bulk β-In_2S_3 [22, 23, 24, 31, 65]. This is in

agreement with the blue shifted band gaps from the bulk observed in UV-vis as an indication of transition from conduction to valence band.

Table 4.1: Optical parameters at different reaction times for 1:1 (In:S) mole ratio in OLA.

Reaction time (min)	Band gap eV	UV-vis wavelength (nm)	PL wavelength (nm)
60	2.5	490	432, 598
90	2.5	504	501, 528
120	2.5	496	500, 527
150	2.2	552	475, 534
210	2.1	594	480, 427
300	2.3	538	488, 528
330	2.2	569	454, 479, 504 & 539

(ii) 1:1.5 (In:S)

The development of the morphology was monitored by TEM. The images of OLA/β-In_2S_3 nanostructures are shown below in Figure 4.7. Nanostructures obtained in 60 min were of irregular shape, Figure 4.7 (a). Further heating to 120 min resulted into somewhat incomplete hexagonal nanoplates, Figure 4.7 (b). The regular hexagonal nanoplate morphology emerged in 150 min with widths between 13 and 40 nm, Figure 4.7 (c). It is worthy to note that the nanoplate morphology is still maintained even with increased sulphur concentration to indium (1:1.5) and that its evolution is a function of time as seen previously with 1:1 (In:S) in Figure 4.3 (d)-(f). The nanoplates are free standing unlike the stacking and overlapping seen previously with the 1:1 system. However, the colloidal solution became increasingly difficult to handle after 90 min and it was decided to terminate the reaction at 150 min.

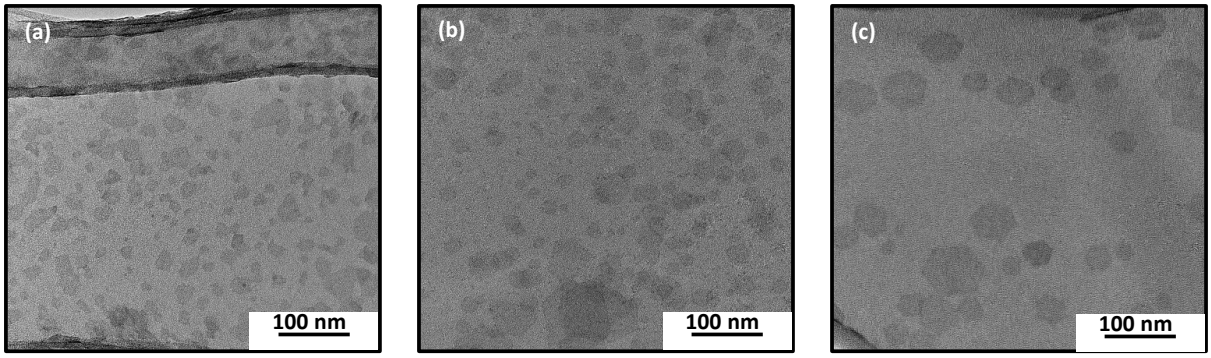


Figure 4.7: The TEM images of OLA/β-In_2S_3 nanostructures for (a) 60 min, (b) 120 min, and (c) 150 min in 1:1.5 (In:S) reaction system.

Typical XRD patterns of the as-prepared nanostructures of OLA/β-In_2S_3 at 60, 120 and 150 min are shown in Figure 4.8. All the reflections can be indexed to the tetragonal phase of β-In_2S_3 crystal structure (PDF card no.: 00-025- 0390) with a preferred plane orientation of (2212). Generally, the reflections became sharper and stronger with prolonged reaction time indicating improved crystallinity of the nanostructures as seen previously with the 1:1 reaction system.

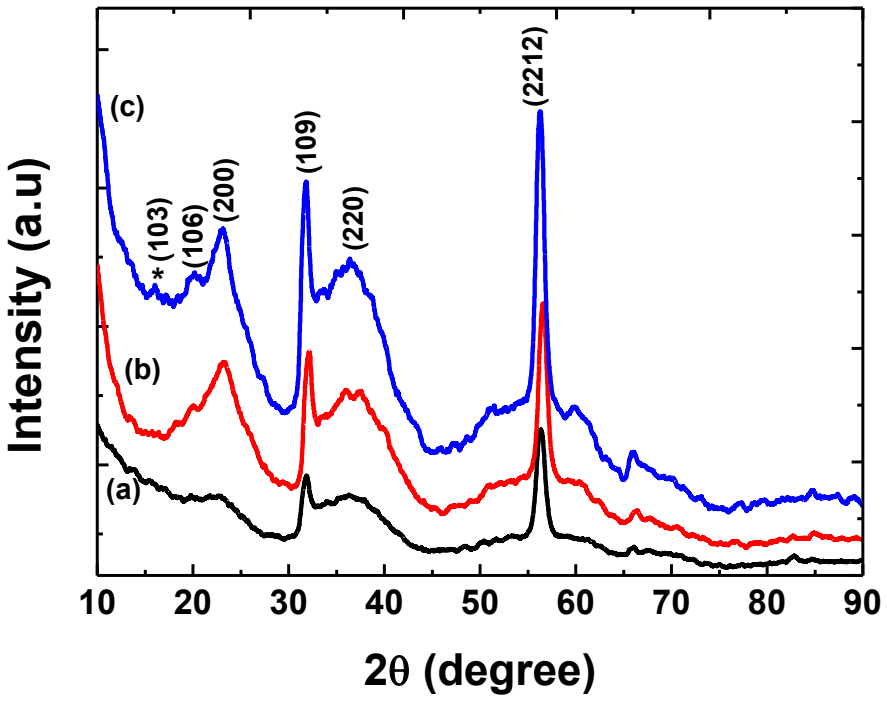


Figure 4.8: XRD patterns of OLA/ β-In_2S_3 nanostructures synthesized for (a) 60 min, (b) 120 min, and (c) 150 min in the 1:1.5 (In:S) reaction system.

Representative UV-vis spectra of the as-synthesized OLA/β-In_2S_3 nanostructures obtained at different reaction times are presented in Figure 4.9. The characteristic step-like shape of the curve is observed.

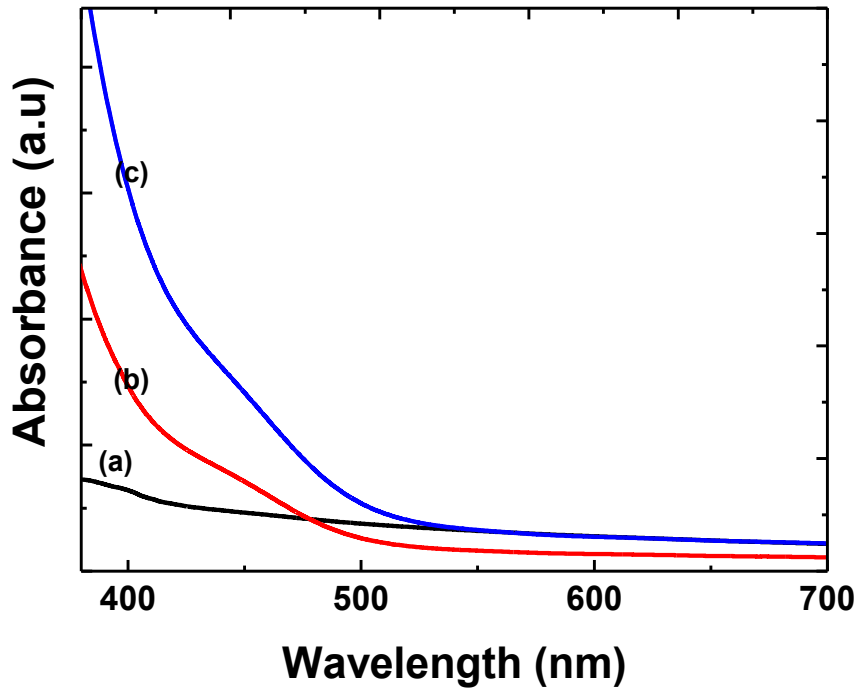


Figure 4.9: UV-vis spectra of OLA/β-In_2S_3 nanostructures synthesized for (a) 60 min, (b) 120 min, and (c) 150 min in the 1:1.5 (In:S) reaction system.

The band gap values are summarized in Table 4.2. An increase in the band gap values was seen from 60 min to 120 and 150 min. This increase is associated with the reaction time and size of nanostructures.

The PL spectra of the as-synthesized nanostructures are presented in Figure 4.10. Broad emissions characterized by shoulders are also observed with this system. The emissions are in the blue light region.

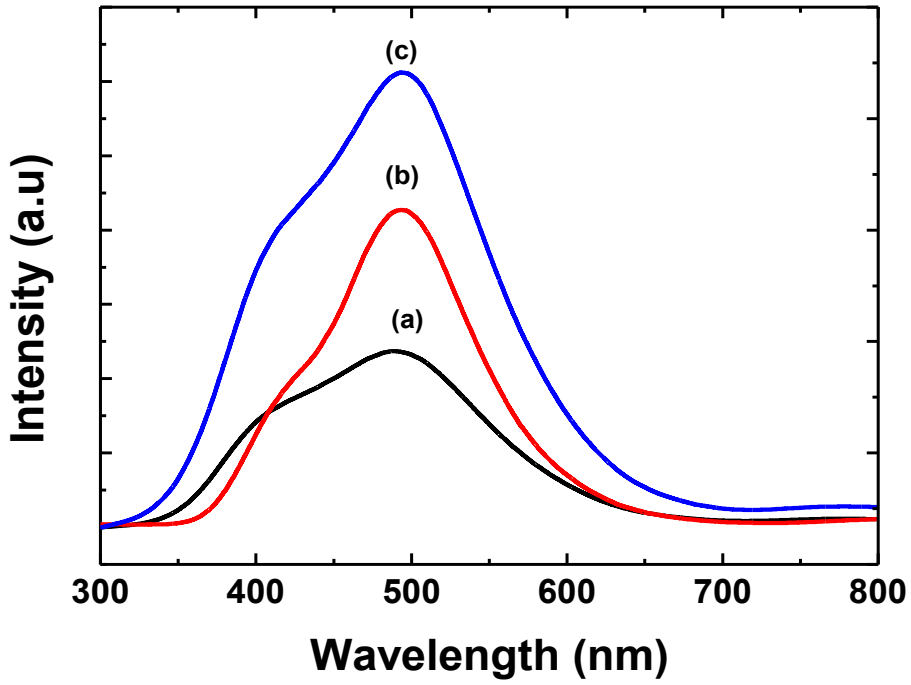


Figure 4.10: PL spectra of OLA/ β-In_2S_3 nanostructures synthesized for (a) 60 min, (b) 120 min, and (c) 150 min in the 1:1.5 (In:S) reaction system.

Table 4.2: Optical parameters at different reaction times for 1:1.5 (In:S) mole ratio in OLA.

Reaction time (min)	Band gap eV	UV-vis wavelength (nm)	PL wavelength (nm)
60	2.6	469	412, 494
120	2.9	433	411, 492
300	2.9	425	410, 491

(iii) 1:2 (In:S)

The TEM images of OLA/β-In_2S_3 nanostructures are presented in Figure 4.11. Nanoflakes were obtained in 60 min which transformed into sheet-like nanostructures in 120 min as shown in Figure 4.11 (a) and (b) respectively. Prolonging the reaction time to 150 min resulted in the overlapping of the sheet-like nanostructures. It can be clearly seen that doubling the amount of sulphur did not favour the hexagonal nanoplate morphology.

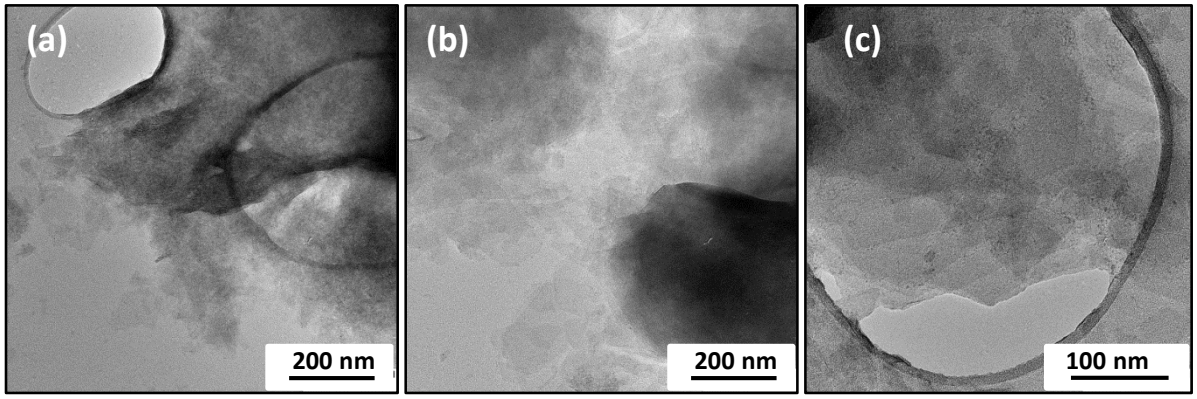


Figure 4.11: TEM images of OLA/ β-In_2S_3 nanostructures synthesized for (a) 60 min, (b) 120 min, and (c) 150 min in the 1:2 (In:S) reaction system.

XRD patterns of the as-prepared nanostructures of OLA/β-In_2S_3 at 60, 120 and 150 min are shown in Figure 4.12. All the diffraction peaks can be indexed to the tetragonal phase of β-In_2S_3 crystal structure (PDF card no.: 00-025- 0390) with a preferred plane orientation of (2212). As seen previously with the 1:1 and 1:1.5 reaction systems, the reflections became sharper and stronger with prolonged reaction time indicating improved crystallinity of the nanostructures.

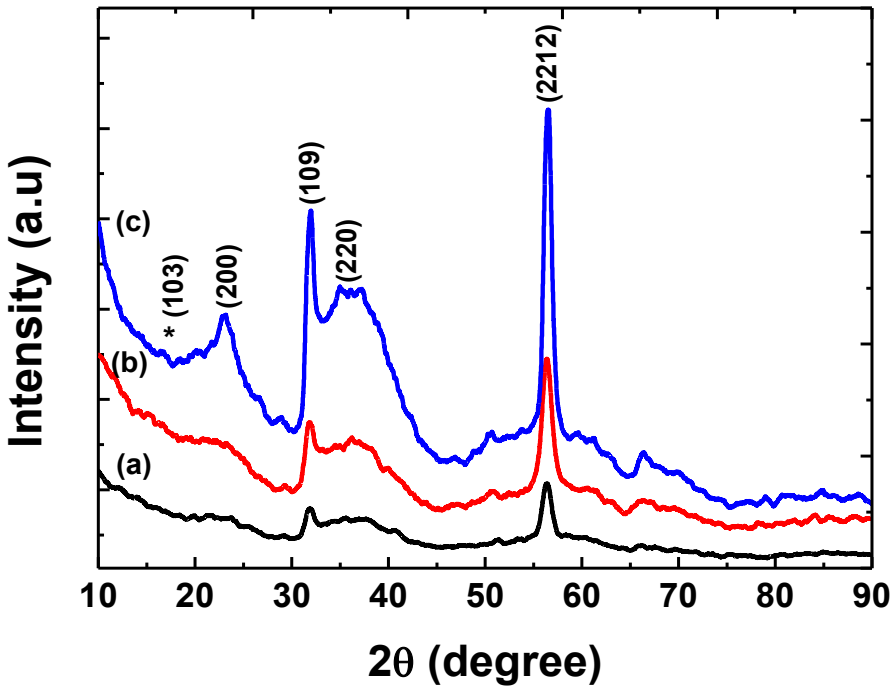


Figure 4.12: XRD patterns of OLA/β-In_2S_3 nanostructures synthesized for (a) 60 min, (b) 120 min, and (c) 150 min in the 1:2 (In:S) reaction system.

The optical properties of the OLA/β-In_2S_3 nanostructures obtained at different reaction times are presented in Figure 4.13. The characteristic step-like shape of the curve is observed indicating band-to-band transitions. The band gap values of the nanostructures are summarized in Table 4.3. The band gap value at 60 min is 2.7 eV and a decrease is observed with a change in morphology is a result of reaction time.

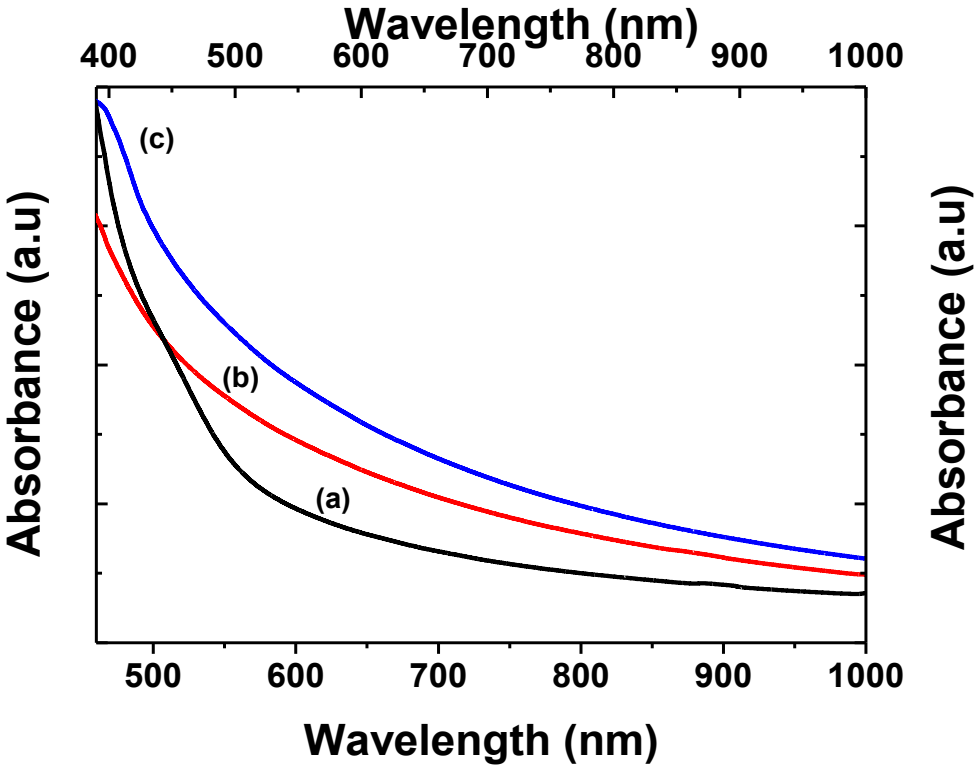


Figure 4.13: UV-vis spectra of OLA/β-In_2S_3 nanostructures synthesized for (a) 60 min, (b) 120 min, and (c) 150 min in the 1:2 (In:S) reaction system.

The PL spectra of the as-synthesized nanostructures are presented in Figure 4.14. Broad emissions characterized by shoulders are observed as with 1:1 and 1:1.5 systems. The emissions are in the blue light region.

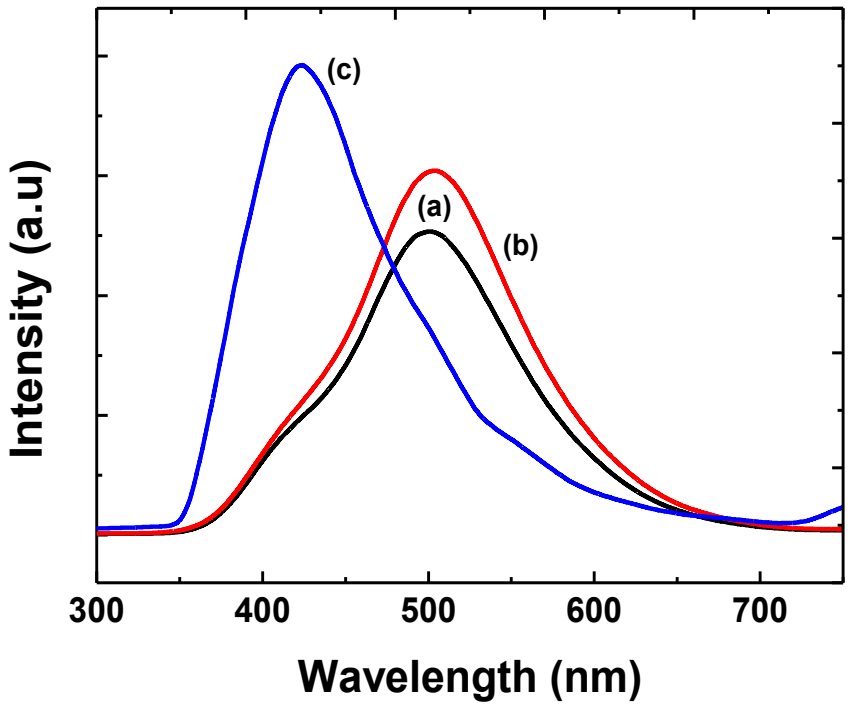


Figure 4.14: PL spectra of OLA/β-In_2S_3 nanostructures synthesized for (a) 60 min, (b) 120 min, and (c) 150 min in the 1:2 (In:S) reaction system.

Table 4.3: Optical parameters at different reaction times for 1:2 (In:S) mole ratio in OLA.

Reaction time (min)	Band gap eV	UV-vis wavelength (nm)	PL wavelength (nm)
60	2.7	452	412, 501
120	2.2	565	413, 503
150	2.1	562	423, 497

Excess sulphur in the reaction medium affected the morphology and band gaps, as seen with the 1:2 (In:S) reaction system. In a study by Revathi, *et al.*, different ratios of In:S affected the crystal structure of the nanostructures [69]. A tetragonal phase was obtained for 1:1, while both cubic and tetragonal phases were obtained for 1:1.3. (In:S). Reflections of the 1:1.5 sample suggested the tetragonal phase as the predominant phase. In a separate study, Kim, *et*

al. reported the effect of concentration of sulphur on the diameter of nanotubes [70]. A mole ratio of 1:1.5 (In:S) produced nanotubes with a diameter of 5.0 nm. An increase in the amount of sulphur (1:2 and 1:3) resulted in a decrease in diameter of the nanotubes to 2.3 and 1.8 nm respectively.

4.1.4.2 Gas sensing performance of OLA/β-In_2S_3 nanostructures

Preliminary results of the gas sensing potential of the OLA/β-In_2S_3 based sensor (330 min reaction time) towards formaldehyde are presented in Figure 4.15. The sensor displayed fairly good recovery upon exposure to the outer environment. This result is in agreement with the gas sensing performance of InSe nanoparticles on formaldehyde [71]. Both In_2S_3 and InSe belong to the III-VI group of compounds. Recovery by a sensor is a desirable characteristic for practical use. The results showed linear dependence of the sensor's response to the concentration of formaldehyde. Further work on the In_2S_3 sensors using the reported samples has been reported on a thesis by Rodrigues et al. [72].

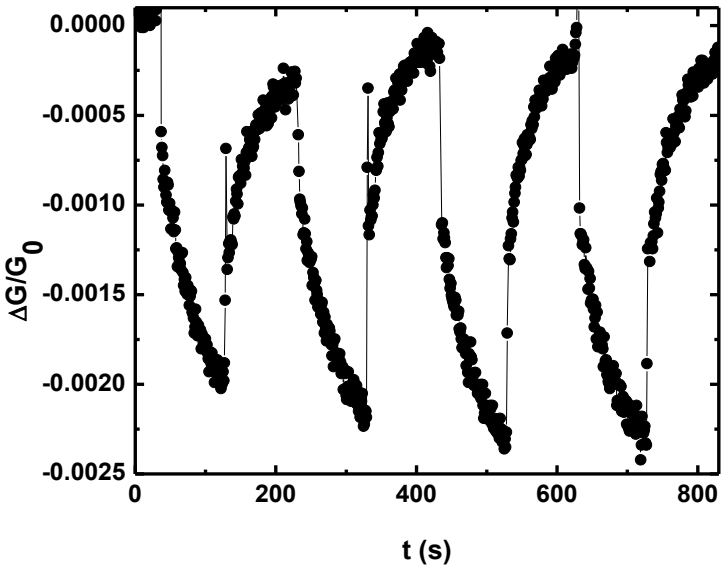


Figure 4.15: Response of β-In_2S_3 sensor to successive introductions of formaldehyde vapour over time.

4.1.5 Conclusions

Crystalline tetragonal OLA/β-In_2S_3 nanostructures were successfully synthesized by a relatively simple colloidal synthetic route where OLA played the double role of capping and reducing agent. The variation of reaction time and molar ratios of sulphur to indium resulted in a change in morphology which in turn had an effect on the band gap values. For both the 1:1 and 1:1.5 (In:S) reaction systems, hexagonal nanoplates were formed as a function of time. Doubling the amount of sulphur; did not favour the formation of nanoplates regardless of time. As reaction time affected the morphology of the nanostructures, so was the band gap. The nanostructures showed very strong absorption in the visible region and can be used as blue light emitters. It can be concluded that the amount of sulphur and/or reaction time can be manipulated to obtain desired band gaps through morphology and size of the nanostructures. The OLA/β-In_2S_3 sensor (330 nm) showed good response/recovery behaviour towards formaldehyde vapour. The nanostructures' sensing performance towards formaldehyde and other VOCs will be studied in detail.

4.1.6 References

[1] Tian, Y., Wang, L., Tang, H. and Zhou, W. (2015). J. Mater. Chem. A 3, 11294-11301.

[2] Ranjith, R., John, T. T., Kartha, C. S., Vijayakumar, K. P., Abeb, T. and Kashiwaba, Y. (2007). Materials Science in Semiconductor Processing 10, 49-55.

[3] Xiong, Y., Xie, Y., Du, G., Tian, X. and Qian, Y. (2002). Journal of Solid State Chemistry 166, 336-340.

[4] Acharya, S., Dutta, M., Sarkar, S., Basak, D., Chakraborty, S. and Pradhan, N. (2012). Chem. Mater. 24, 1779-1785.

[5] Chen, L-Y., Zhang, Z-D. and Wang, W-Z. (2008). J. Phys. Chem. C 112, 4117-4123.

[6] Cingarapu, S., Ikenberry, M. A., Hamal, D. B., Sorensen, C. M., Hohn, K. and Klabunde, K. J. (2012). Langmuir 28, 3569-3575.

[7] Rajeshmon, V. G., Poornima, N., Kartha, C. S. and Vijayakumar, K. P. (2013). Journal of Alloys and Compounds 553, 239-244.

[8] Zhang, Y., Zhu, J., Liu, F., Wu, G., Wei, J., Hu, L., Huang, Y., Zhang, C., Tang, J. and Dai, S. (2014). Journal of Photochemistry and Photobiology A: Chemistry 281, 53-58.

[9] Franzman, M. A. and Brutchey, R. L. (2009). Chem. Mater. 21, 1790-1792.

[10] Sharma, Y. and Srivastava, P. (2012). Materials Chemistry and Physics 135, 385-394.

[11] El-Nahass, M. M., Khalifa, B. A., Soliman, H. S. and Seyam, M. A. M. (2006). Thin Solid Films 515, 1796-1801.

[12] Gorai, S., Guha, P., Ganguli, D. and Chaudhuri, S. (2003). Materials Chemistry and Physics 82, 974-979.

[13] Rengaraj, S., Venkataraj, S., Tai, C-w., Kim, Y., Repo, E. and Sillanpää, M. (2011). Langmuir 27, 5534-5541.

[14] Cao, G., Zhao, Y. and Wu, Z. (2009). Journal of Alloys and Compounds 472, 325-327.

[15] Yang, M-Q., Weng, B., and Xu, Y-J. (2013). Langmuir 29, 10549-10558.

[16] Siol, S., Dhakal, T. P., Gudavalli, G. S., Rajbhandari, P. P., DeHart, C., Baranowski, L. L. and Zakutayev, A. (2016). ACS Appl. Mater. Interfaces 8, 14004-14011.

[17] Li, T., Zhang, S., Meng, S., Ye, X., Fu, X. and Chen, S. (2017). RSC Adv. 7, 6457-6466.

[18] Du, W., Zhu, J., Li, S. and Qian, X. (2008). Crystal Growth & Design 8 (7), 2131-2136.

[19] Zhu, H., Wang, X., Yang, W., Yang, F. and Yang, X. (2009). Materials Research Bulletin 44, 2033-2039.

[20] Liu, Y., Zhang, M., Gao, Y., Zhang, R. and Qian, Y. (2007). Materials Chemistry and Physics 101, 362-366.

[21] Fu, X., Wang, X., Chen, Z., Zhang, X., Li, Z., Leung, D. Y. C.,
Wu, L. and Fu, X. (2010). Applied Catalysis B: Environmental 95, 393-399.

[22] Afzaal, M., Malik, M. A. and O'Brien, P. (2004). Chem. Commun., 334-335.

[23] Chai, B., Zeng, P., Zhang, X., Mao, J., Zan, L. and Peng, T. (2012). Nanoscale 4, 2372-2377.

[24] Park, K. H., Jang, K. and Son, S. U. (2006). Angew. Chem. Int. Ed. 45, 4608-4612.

[25] Wang, Y-P., Ho, C-H. and Huang, Y-S. (2010). J. Phys. D: Appl. Phys. 43, 415301, 1-5pp.

[26] Zhu, X., Ma, J., Wang, Y., Tao, J., Zhou, J., Zhao, Z., Xie, L. and Tian, H. (2006). Materials Research Bulletin 41, 1584-1588.

[27] Zhang, L. X., Zhang, Y. C. and Zhang, M. (2009). Materials Chemistry and Physics 118, 223-228.

[28] Chen, X., Zhang, Z., Zhang, X., Liu, J. and Qian, Y. (2005). Chemical Physics Letters 407, 482-486.

[29] Acharya, S., Dutta, M., Sarkar, S., Basak, D., Chakraborty, S. and Pradhan, N. (2012). Chem. Mater. 24, 1779-1785.

[30] Cao, X., Gu, L., Zhuge, L., Qian, W., Zhao, C., Lan, X., Sheng, W. and Yao, D. (2007). Colloids and Surfaces A: Physicochem. Eng. Aspects 297, 183-190.

[31] Avivi (Levi), S., Palchik, O., Palchik, V., Slifkin, M. A., Weiss, A. M. and Gedanken, A. (2001). Chem. Mater. 13, 2195-2200.

[32] Acharya, S., Sarkar, S. and Pradhan, N. (2012). J. Phys. Chem. Lett. 3, 3812-3817.
[33] Ning, J., Men, K., Xiao, G., Zhao, L., Wang, L., Liu, B. and Zou, B. (2010). Journal of Colloid and Interface Science 347, 172-176.
[34] Gorai, S. and Chaudhuri, S. (2005). Materials Chemistry and Physics 89, 332-335.
[35] Mathew, M., Jayakrishnan, R., Kumar, P. M. R., Kartha, C. S. and Vijayakumar, K. P. (2006). Journal of Applied Physics 100, 033504, 2006, 1-8.
[36] Yang, Z., Huang, X., Li, J., Zhang, Y., Yu, S., Xu, Q. and Hu, X. (2012). Microchim Acta 177, 381-387.
[37] Batabyal, S. K., Lu, S. E. and Vittal, J. J. (2016). Cryst. Growth Des. 16, 2231-2238.
[38] Barreau, N. (2009). Solar Energy 83, 363-371.
[39] Gao, W., Liu, W., Leng, Y., Wang, X., Wang, X., Hu, B., Yu, D., Sang, Y. and Liu, H. (2015). Applied Catalysis B: Environmental 176, 83-90.
[40] Maha, M. H. Z., Bagheri-Mohagheghi, M-M.and Azimi-Juybari, H. (2013). Thin Solid Films 536, 57-62.
[41] McCarthy, R. F., Schaller, R. D., Gosztola, D. J., Wiederrecht, G. P. and Martinson, A. B. F. (2015). J. Phys. Chem. Lett. 6, 2554-2561.
[42] Xing, C., Wu, Z., Jiang, D. and Chen, M. (2014). Journal of Colloid and Interface Science 433, 9-15.
[43] Pistor, P., Merino, J. M., Álvarez, León, M., di Michiel, M., Schorr, S., Klenk, R. and Lehmann, S. (2016). Acta Cryst. B 72, 410-415.
[44] Ho, C-H. (2012). Physica B 407, 3052-3055.
[45] Hsiao, Y-J., Lu, C-H., Ji, L-W., Meen, T-H., Chen, Y-L. and Chi, H-P. (2014). Nanoscale Research Letters 9 (32), 1-7.
[46] Wang, F., Jin, Z., Jiang, Y., Backus, E. H. G., Bonn, M., Lou, S. N., Turchinovich, D. and Amal, R. (2016). Applied Catalysis B: Environmental 198, 25-31.
[47] Nagesha, D. K., Liang, X., Mamedov, A. A., Gainer, G., Eastman, M. A., Giersig, M., Song, J-J., Ni, T. and Kotov, N. A. (2001). J. Phys. Chem. B 105, 7490-7498.
[48] Liu, L., Liu, H., Kou, H-Z., Wang, Y., Zhou, Z., Ren, M., Ge, M. and He, X. (2009). Crystal Growth & Design 9, (1), 113-117.
[49] Cherian, A. S., Mathew, M., Kartha, C. S. and Vijayakumar, K. P. (2010). Thin Solid Films 518, 1779-1783.
[50] Kraini, M., Bouguila, N., Koaib, J., Vázques-Vázquez, C., López-Quintela, M. A. and Alaya, S. (2016). Journal of Electronic Materials 45 (11), 5936-5947.
[51] Chen, J., Liu, W. and Gao, W. (2016). Applied Surface Science 368, 288-297.

[52] Liu, Y., Xu, H. and Qian, Y. (2006). Crystal Growth & Design 6 (6), 1304-1307.

[53] Allsop, N. A., Schönmann, A., Belaidi, A., Muffler, H-J., Mertesacker, B., Bohne, W., Strub, E., Röhrich, J., Lux-Steiner, M. C. and Fischer, Ch-H. (2006). Thin Solid Films 513, 52-56.

[54] Yamaguchi, K., Yoshida, T. and Minoura, H. (2003). Thin Solid Films 431-432, 354-358.

[55] Ge, S., Cai, L., Li, D., Fa, W., Zhang, Y. and Zheng, Z. (2015). J Nanopart Res 17 (488), 1-11.

[56] Liu, L., Xiang, W., Zhong, J., Yang, X., Liang, X., Liu, H. and Cai, W. (2010). Journal of Alloys and Compounds 493, 309-313.

[57] Bai, H. X., Zhang, L. X. and Zhang, Y. C. (2009). Materials Letters 63, 823-825.

[58] Kumar, B. G. and Muralidharan, K. (2011). J. Mater. Chem. 21, 11271-11275.

[59] Pejova, B. and Bineva, I. (2013). J. Phys. Chem. C 117, 7303-7314.

[60] Bera, P. and Seok, S. I. (2011). J Nanopart Res 13, 1889-1896.

[61] Phan, C. M., and Nguyen, H. M. (2017). J. Phys. Chem. A 121, 3213-3219.

[62] Niu, Z. and Li, Y. (2014). Chem. Mater. 26, 72-83.

[63] Hosseinzadeh, G., Maghari, A., Farniya, S. M. F., Keihan, A. H. and Moosavi-Movahedi, A. A. (2017). Materials Science and Engineering C 77, 836-845.

[64] Ajitha, B., Reddy, Y. A. K., Reddy, P. S., Jeon, H-J. and Ahn, C. W. (2016). RSC Adv. 6, 36171-36179.

[65] Quek, X-Y., Pestman, R., van Santen, R. A. and Hensen, E. J. M. (2013). ChemCatChem 5, 3148 – 3155.

[66] Sahu, N., Brahme, N. and Sharma, R. (2016). Luminescence 31, 1400-1406.

[67] Park, J. Y., Aliaga, C., Renzas, J. R., Lee, H. and Somorjai, G. A. (2009). Catal Lett 129, 1-6.

[68] Mohamed, M. B., Wang, Z. L. and El-Sayed, M. A. (1999). J. Phys. Chem. A 103, 10255-10259.

[69] Revathi, N., Prathap, P. and Reddy, H. T. R. (2010). Energy Procedia 2, 195-198.

[70] Kim, Y. H., Lee, J. H., Shin,D-W., Park, S. M., Moon, J. S., Namc, J. G. and Yoo, J-B. (2010). Chem. Commun., 46, 2292–2294.

[71] Airo, M. A., Rodrigues, R., Gqoba, S., Ntholeng, N., Otieno, F., Moloto, M. J., Greenshields, M. W. C. C., Hümmelgen, I. A. and Moloto, N. (2016). Sensors and Actuators B 236, 116-125.

[72] Rodrigues, R., Sensores químicos para a detecção de compostos voláteis orgânicos e misturas binárias, https://acervodigital.ufpr.br/bitstream/handle/1884/55920/R%20-%20T%20-%20RAFAEL%20RODRIGUES.pdf?sequence=1&isAllowed=y

4.2 Amine and thiol ligand tag team for β-In_2S_3 hexagonal nanoplates

4.2.1 Introduction

The need to obtain well-defined shapes of semiconducting nanomaterials has been spurred on by the new functionalities they impart on optoelectronic devices. In addition, the unique size and shape (or degree of anisotropy) dependent properties of semiconducting nanomaterials emerge at nanoscale range [1-7]. Perhaps even more exciting is the possibility to modify the properties during synthesis [8, 9] without altering their chemical composition [1]. It is therefore not surprising to find a sizable volume of research into the synthesis of nanomaterials being dedicated to the control of their shape, size, composition, structure and crystallinity to tailor them for intended applications [10-17]. Effective monitoring and therefore proper balance of nucleation and growth processes that modulate nanocrystal synthesis is the key to tailored size, morphology, composition and mono- or narrowly polydispersed nanoparticles [13, 18-21]. This can be achieved via thermodynamic and kinetic parameters which are in turn determined by the synthetic route and reaction conditions such as capping agents (surface ligands), temperature, time, precursors, reactivity of the two cations in the case of ternary NCs, solvent, concentration and reducing agents [3, 8, 9, 11, 13, 18, 19, 22-30]. Surface ligands have the pivotal role of determining the ultimate properties of nanostructures [8, 9, 31] by imparting the desired surface chemistry and functionality [29]. While controlling nucleation and growth during the synthesis, ligands stabilize colloidal nanostructures against aggregation, make them soluble in different in solvents, protect surface atoms against oxidation, provide a trap states-free surface, promote decomposition of precursors at low temperature and can act as both solvents and reducing agents, thereby eliminating the need for additional reagents [9, 30-41] which could complicate the purification stages. The ligand could also serve as a source of sulphur during colloidal synthesis of sulphur based nanomaterials in the case of 1-DDT [7, 42, 43]. Amines, thiols, acids, phosphines are some of the commonly used types of surface ligands [41].

Mixed ligands can be used to display and explain the different roles played by each ligand in a reaction system. Yang and Klabunde reported the influence of both TOP and OLA ligands on the synthesis of Pd nanoparticles [44]. Only aggregated Pd particles were generated when OLA was used as the only ligand. Nearly monodisperse Pd nanoparticles were obtained when an appropriate amount of TOP was added. The researchers went on and increased the molar ratio of TOP/Pd(II) to 2 resulting in the formation of Pd(II)-TOP coordination complexes [44]. Peng, *et al.* detailed how the regulation of growth kinetics of CdSe nanocrystals and

ultimately their shapes was made possible by the simple addition of hexyl-phosphonic acid (HPA), a strong cadmium ligand to trioctylphosphine oxide (TOPO) thereby changing the composition of the reaction medium [45]. Growth of either form of the pure stoichiometric phases of tin selenide ($SnSe_2$ and SnSe) nanocrystals in OLA depended on the presence (specific amount) or absence of 1-dodecanethiol (1-DDT) respectively [28]. The study also highlighted the importance of the ratio of OLA/1-DDT where an amount different from the optimal one resulted in mixed phase nanocrystals. This is further substantiated by Sebastian, et al, where a controlled ratio of oleic acid (OA) and OLA resulted in faceted platinum (Pt) nanocrystals [13]. In the same study, the roles of other parameters like the reducing agent and temperature are clearly defined. The inhibition of the reduction of Fe^{3+} to Fe^{2+} in the absence of OLA during the synthesis of magnetite and titania, while it was promoted in its presence corroborates the reduction role of surface ligands [37]. The synthesis of monodispersed gold nanoparticles with OLA clearly displayed its dual role as a reducing and capping agent [46]. Several other works by different research groups illustrate the undisputable diverse roles of surface ligands in shape control of nanostructures [29, 43, 47-52].

Two-dimensional (2D) including single layer and multi-layered nanosheets, nanodiscs, nanoplates, nanoflakes and nanobelts have attracted attention because of their interesting electronic and physical properties [53-56] due to their large surface area [53, 57-60]. Monodispersed 2D nanoparticles can self-organize into closed-packed arrays which together with the large surface area would improve the carrier transport capabilities in solar cells and reduce loss of photogenerated current [59, 60]. It would also be relatively easier to assemble 2D nanoparticles than 1D, and are more compatible with current thin technologies [61, 62]. Indium sulphide (In_2S_3) is a 2D layered material with very interesting optical properties and most importantly, a tunable bandgap which makes it desirable as a semiconducting material. The III-VI semiconductors of which β-In_2S_3 is a member [63-69], are compound materials comprising of a group III (13) metal and a group 16 (VI) chalcogen [57]. This group has band gaps that match well with the solar spectrum and can be further tuned by adjusting a variety of reaction parameters [57]. It is a lucrative material for catalysis, photovoltaics, and solar cells along with other optoelectronic device applications [56].

In this chapter, a faster method to grow β-In_2S_3 nanoplates in a combination of structure directing solvents is reported. A mixed ligand of OLA and 1-DDT resulted in the early appearance of hexagonal nanoplates. A controlled amount of 1-DDT was very crucial in this

reaction system in order to obtain the desired hexagonal nanoplates. The source of sulphur and choice of sole solvent were also influential in determining the morphology and the subsequent optical properties.

4.2.2 Experimental procedure

4.2.2.1 Chemicals and materials

Indium (III) chloride, sulphur powder, oleylamine (OLA), 1-dodecanethiol (1-DDT), chloroform, dichloromethane and ethanol were purchased from Sigma Aldrich.

4.2.2.2 Synthesis of β-In_2S_3 nanostructures

(i) OLA and 1-DDT

In a 100 mL three-neck round bottom flask attached to a Schlenk line via a condenser, 17 mL of OLA and 0.2 mL of 1-DDT were heated to 100 ℃ with continuous stirring under the flow of nitrogen gas. It was held at this temperature for 20 min to get rid of any water molecules and air. Ultimately, a clear light yellow liquid was obtained into which 5 mmol of indium (III) chloride and 5 mmol of elemental sulphur powder were added. The mixture was then heated rapidly to 220 ℃ and held at this temperature for 330 min with aliquots of the yellow colloidal solution taken at different time intervals. The aliquots were allowed to cool to 80 ℃ and ethanol was added to flocculate the nanostructures. The nanostructures were then collected by centrifugation for 10 min at 3000 rpm and washed several times with ethanol and dichloromethane in order to remove unreacted precursors and excess OLA. The resultant products were left to dry at room temperature for 12 h to obtain yellow powders. The effect of reaction time was investigated. The effect of concentration of 1-DDT was investigated by doubling its amount (0.4 mL) and keeping the rest of the quantities unchanged.

(ii) 1-DDT as sole solvent

OLA was replaced with 1-DDT and the rest of procedure in (i) was followed. The effect of reaction time was investigated.

(iii)1-DDT as sulphur source

The procedure in (i) was followed with OLA as the sole solvent and 1-DDT (5 mmol) was used as the source of sulphur. The effect of reaction time was studied.

4.2.3 Characterization techniques

4.2.3.1 Optical properties of the nanostructures

A Specord 50 AnalytikJena UV-Vis spectrophotometer was used to carry out the absorption measurements. An Agilent Cary Eclipse fluorescence spectrometer was used to measure the photoluminescence of the particles. The presence of the capping agent on the surface of the nanomaterials was confirmed by using a Bruker Tensor 27 FT-IR. The nanoparticles were used as dry powders for FT-IR analysis, while they were dissolved in chloroform and placed in quartz cuvettes (1cm path length) for UV-Vis and PL spectral analyses.

4.2.3.2 Structural properties of the nanostructures

Nanomaterial sizes and morphology were studied using FEI Spirit 120 kV transmission electron microscope operated at an acceleration voltage of 200 kV with a beam spot size of 20 - 100 nm in TEM mode. Powders of nanomaterials were dispersed in chloroform and drop cast onto carbon lacey copper grids. The solvent was then evaporated at room temperature. The phases of the structures were determined by powder XRD with. ^{1}HNMR was also used to confirm the presence of the capping agent. The nanostructures were dissolved in deuterated chloroform. The spectra were recorded at room temperature on Bruker Avance III 500 MHz spectrometer.

4.2.4 Results and discussion

4.2.4.1 Structural properties

$InCl_3$ is thermally decomposed into In^{3+} and Cl^- while elemental sulphur is reduced by 1-DDT. The proposed chemical reaction is:

$$2In^{3+} + 2S^{2-} \xrightarrow[N_2,\ OLA,\ 1\text{-}DDT]{220\ ℃} In_2S_3\ (s) \qquad (4.2.1)$$

TEM was used to monitor the growth of the nanostructures at different reaction time intervals. In order to put the current results into perspective, it is worthy to mention the growth of the hexagonal nanoplates in OLA as the sole solvent from the previous chapter. OLA/β-In_2S_3 hexagonal nanoplates evolved as a function of time as shown in Figure 4.16:

(a) the formation of spherical particles through the solvothermal reactions between $InCl_3$ and elemental S in a mono-ligand system (OLA) in 60 min;

(b) development of facets on the spherical nanoparticles in 90 min;

(c) formation of nanosheets in 120 min and;

(d) evolution of nanoplates in 150 min.

The growth and stabilization of these nanostructures was controlled by the presence of OLA acting as a capping agent. OLA also played the role of reductant, thereby controlling the nucleation and growth rates of the nanostructures. OLA also facilitated the thermal decomposition of $InCl_3$ to In^{3+} and Cl^- at a relatively lower temperature [30, 39].

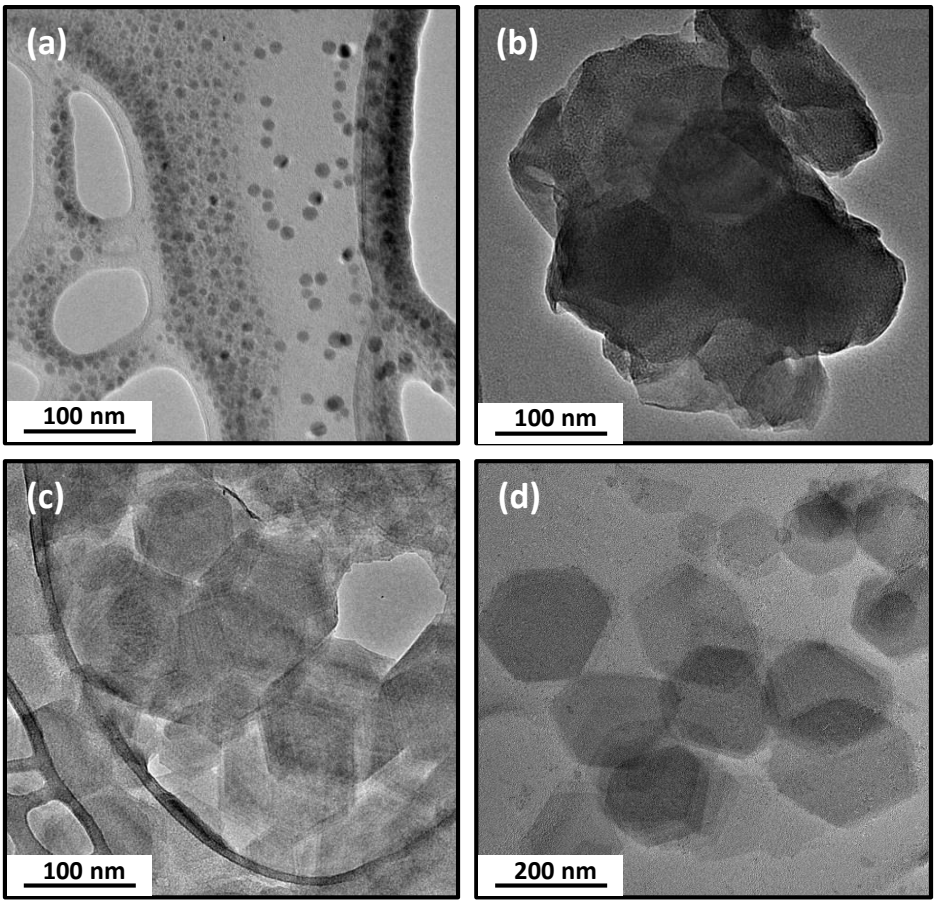


Figure 4.16: The TEM images of OLA/β-In_2S_3 nanostructures in the 1:1 (In:S) reaction system: (a) 60 min, (b) 90 min, (c) 120 min and (d) 150 min.

In this chapter, β-In_2S_3 nanostructures were grown in an OLA and 1-DDT reaction medium. The TEM images of the nanostructures from different time intervals are presented in Figure 4.17. The well-defined hexagonal nanoplate morphology is retained and was formed in 60 min as shown in Figure 4.17 (a). At this reaction time, the nanoplates were mostly free standing and displayed low stacking character with widths between 30 and 74 cm. Further

heating of the reaction mixture promoted both stacking and overlapping arrangements of the nanoplates in 90 min (84-136 nm) and 150 min (74-151 nm) as shown in Figure 4.17 (b) and (c) respectively. The early emergence of nanoplates is a great improvement from the previous results as time has profound implications on costs especially where heat is involved. The ability of the nanoplates to self-organize (stacking and overlapping) when drop cast on a copper grid is observed in the bi-ligand system (Figure 4.17) as was in the mono-ligand system [Figure 4.16(c) and (d)]. This is a very desirable character and it is hoped that it will be displayed when the nanoplates are deposited on substrates as thin films.

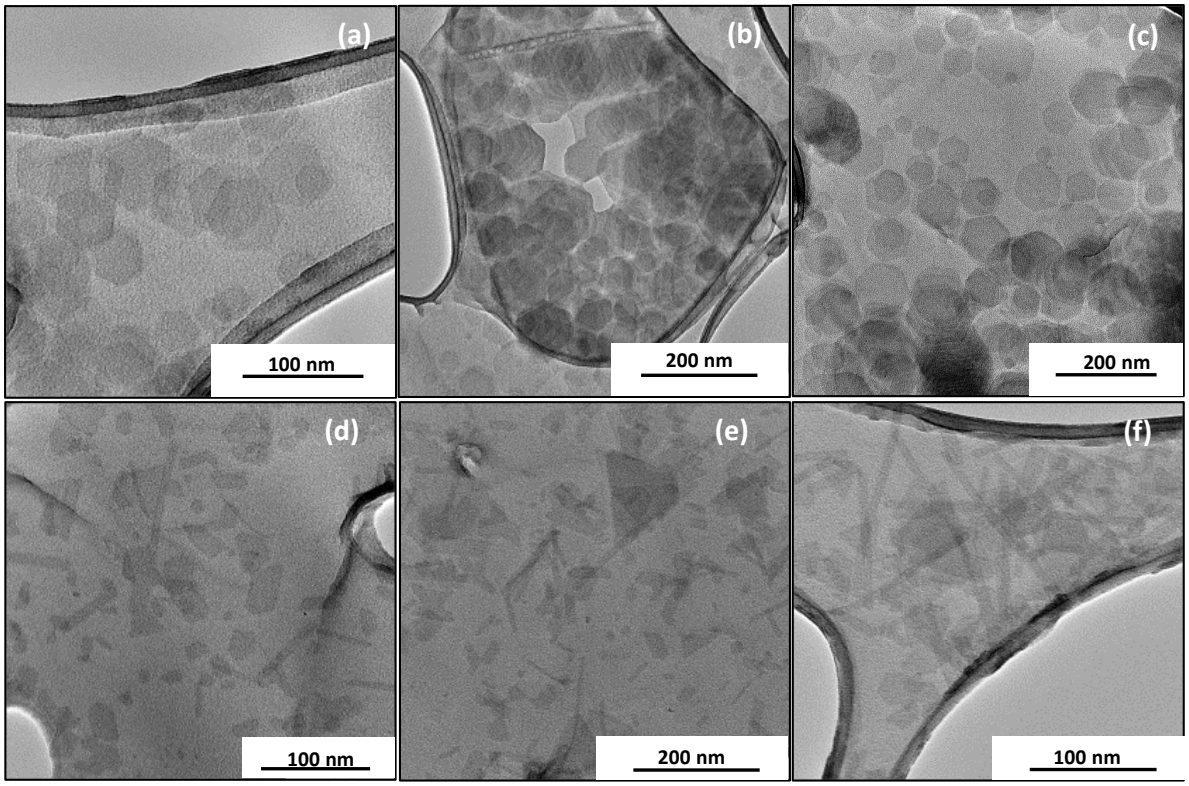


Figure 4.17: The TEM images of β-In_2S_3 nanostructures in: OLA_0.2 mL of 1-DDT at (a) 60 min, (b) 90 min, and (c) 150 min; OLA_0.4 mL of 1-DDT at (d) 60 min, (e) 90 min, and (f) 150 min in the 1:1 (In:S) reaction system.

Figure 4.18 is a schematic diagram for the arrangement of the nanoplates at different reaction times.

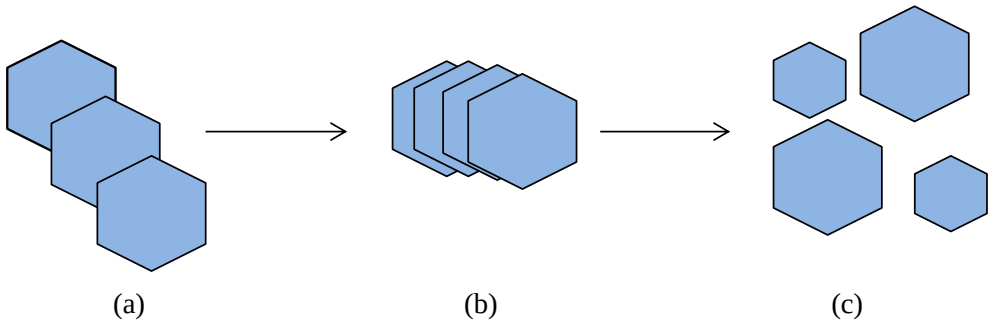


Figure 4.18: A schematic illustration of the growth mechanism of β-In_2S_3 nanostructures in: OLA_0.2 mL of 1-DDT at (a) 60 min, (b) 90 min, and (c) 150 min in the 1:1 (In:S) reaction system.

It is clear that the presence of 1-DDT influenced the early emergence of the hexagonal nanoplates. It is therefore important to define its role in the bi-ligand system. Like OLA, 1-DDT can assume the roles of solvent, reductant and capping agent [7]. OLA is known to assume the role of solvent and capping agent in the presence of a stronger reductant [6]. The monomers, In^{3+} and S^{2-} are important for the nucleation phase. It is assumed that 1-DDT reduced elemental S to S^{2-}, leading to fast nucleation [69]. Therefore, 1-DDT regulated the nucleation and growth rates of the nanostructures [49]. Doubling the amount of 1-DDT resulted in nanostructures of mixed morphologies (short and long nanobelts, nanotriangles, hexagonal, sphere-like and irregular) as presented in Figure 4.17 (d)-(f). This change in morphology proves that 1-DDT is also structure-directing. It also proved the importance of controlling the OLA/1-DDT ratio in order to obtain the desired hexagonal shape. This is in agreement with an assertion made by a number of researchers on the importance of OLA/1-DDT ratio in the synthesis of $CuInS_2$ nanocrystals [35, 70, 71, 43]. Singh, *et al.* and Ghosh, *et al.* also reported a change in morphology with excess 1-DDT resulting in rod-shaped wurtzite Cu_2ZnSnS_4 nanocrystals instead of bullet-shaped ones [72] and an agglomerated amorphous product respectively [7]. Prolonged reaction time to 150 min resulted into longer belt-like structures as seen in Figure 4.17 (f).

Micrographs of the nanostructures of 1-DDT/β-In_2S_3 are presented in Figure 4.19. 1-DDT was used as the sole solvent and not only did it play the role of reductant to elemental S but also a capping agent.

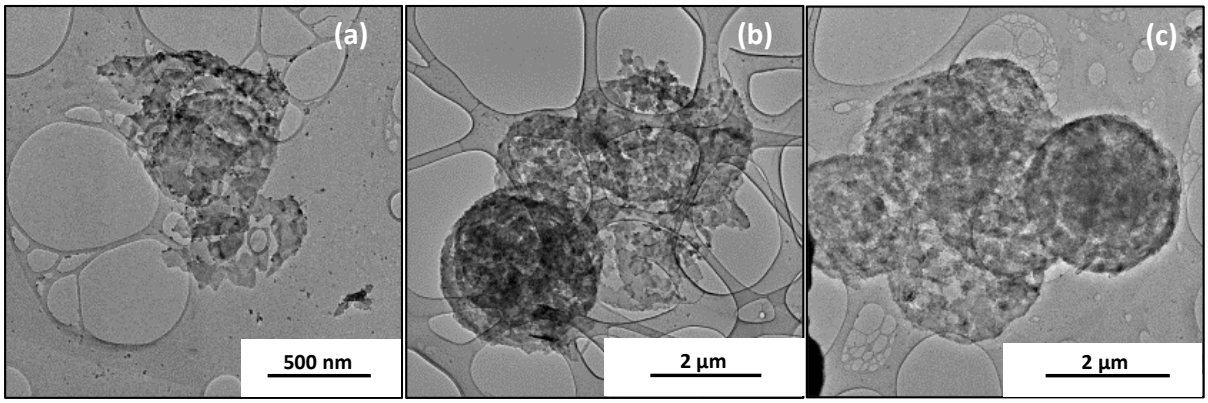


Figure 4.19: TEM images of 1-DDT/β-In_2S_3 nanostructures synthesized for (a) 60 min, (b) 90 min, and (c) 150 min in the 1:1 (In:S) reaction system.

Nanosheets and nanoparticles of 1-DDT/β-In_2S_3 were the resultant morphologies in 60 min as shown in Figure 4.19 (a). Figure 4.19 (b) demonstrated the emergence of sphere-like structures suggesting the transformation of nanosheets after heating to 90 min. Further heating to 150 min resulted into well-defined microspheres as presented in Figure 4.19 (c). It should be noted that the nanosheets and sphere-like materials appeared to have a rough surfaces and gaps in between. The gaps could serve as electron traps thereby compromising the use of these nanostructures as potential materials in optoelectronic devices. These resultant morphologies are an indication that the 1-DDT medium is not favourable for the hexagonal shape of β-In_2S_3. This further confirms that OLA was responsible for the hexagonal morphology. A similar result was obtained by Xu's research group where irregular nanoparticles were obtained with 1-DDT alone (as a capping agent) instead of nanowires when used in a mixed solvent with ethylenediamine [71]. The choice of ligand is therefore, crucial in obtaining a desired morphology.

Typical TEM images obtained when 1-DDT was used as the source of S are shown in Figure 4.20. The nanostructures developed after 120 min as presented in Figure. 4.20 (a). TEM micrographs from this reaction time showed fewer and poorly defined hexagonal nanoplates of OLA/β-In_2S_3. Nucleation and growth process as indicated by visual observation of the

formation of the thick yellow colloidal solution was considered slow in this instance compared to when elemental S was used. This slowness is attributed to the low concentration of monomers associated with the gradual release of S by 1-DDT, a phenomenon reported by Soosaimanickan, *et al*. [73].

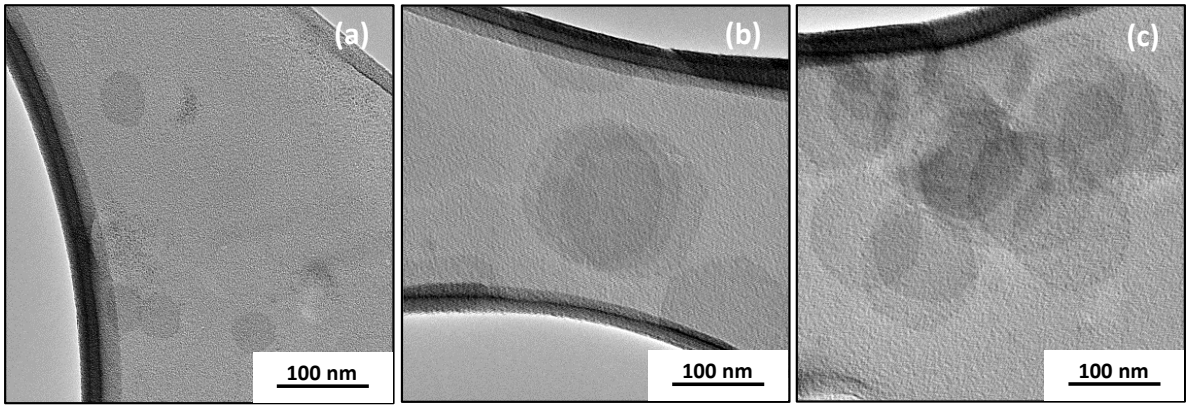


Figure 4.20: TEM images of OLA/β-In_2S_3 nanostructures synthesized for (a) 120 min, (b) 150 min, and (c) 180 min in OLA with 1-DDT as source of sulphur.

Another example of slow release of S from a precursor was observed with the formation of β-In_2S_3 nanocrystals after 420 min when di-*tert*-butyl disulfide was reacted with $In(acac)_3$ in OLA [35]. Low monomer activity at shorter reaction times is known to lead to nanospheres, a thermodynamically controlled growth [14]. The number of nanoplates increased dramatically and the shape improved with evident sharper facets at longer reaction times, Figure 4.20 (b) and (c). The sphere-like nanostructures at intermediate reaction times, Figure 4.20 (a) are an indication of increased growth, a result of higher monomer activity [14]. Meanwhile, the hexagonal nanoplates formed at longer reaction times (150 and 180 min) as a result of kinetically controlled growth [14]. This is in agreement with Peng and co-workers where slow growth rate was reported for the sphere-like nanoparticles while a rod-like faceted shape was achieved at increased growth rates [45]. The emergence of the hexagonal nanoplates once again confirms that OLA is responsible for this morphology.

Nanostructure growth was also monitored by XRD. Diffraction patterns of the nanostructures are shown in Figure 4.21 for the OLA/1-DDT systems.

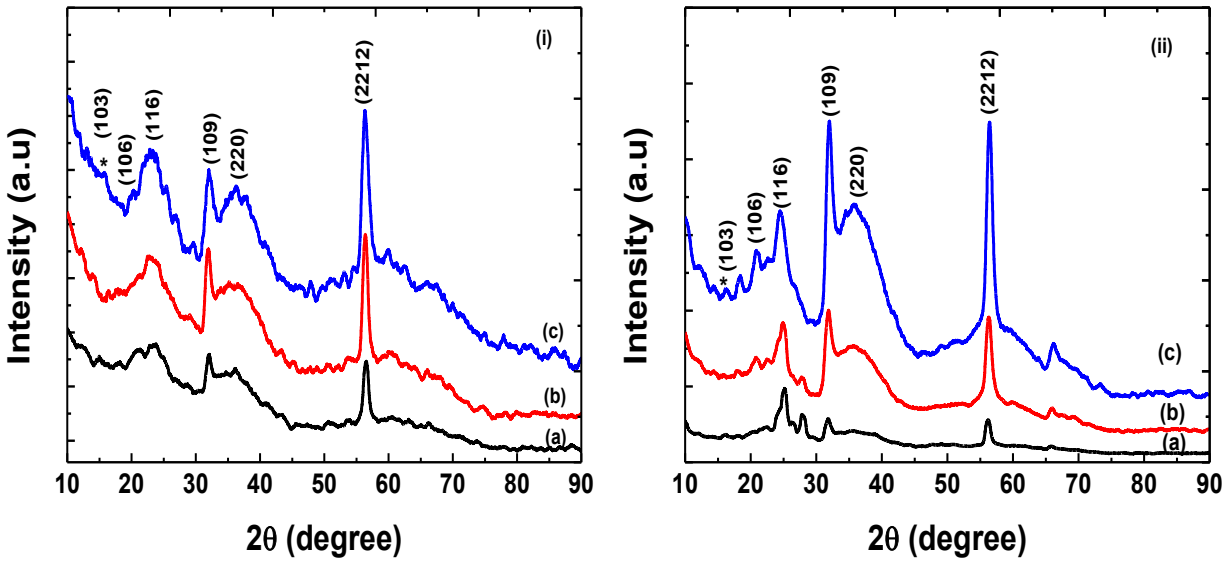


Figure 4.21: XRD patterns of OLA/β-In_2S_3 nanostructures at (a) 60 min, (b) 90 min, and (c) 150 min; (i) OLA /0.2 mL of 1-DDT and (ii) OLA /0.4 mL 1-DDT.

All the reflections were indexed to the defect tetragonal phase of the β-In_2S_3 crystalline structure. The identified peaks common to both systems correspond to the (103), (116), (109), (220) and (2212) lattice planes (PDF card no.: 00-025-0390). The growth of the nanostructures is oriented towards the (2212) peak for the system (i), while it is towards the (109) and (2212) peaks for system (ii). However, well resolved peaks were observed when 1-DDT was used as the sole solvent, Figure 4.22 (i) more than the OLA/1-DDT systems above (Figure 4.21), indicating good crystallinity of the nanostructures. All the reflections were indexed to the defect tetragonal phase of the β-In_2S_3 crystalline structure. The identified peaks correspond to the (103), (116), (109), (220), (1015) and (2212) lattice planes (PDF card no.: 00-025-0390). The growth of the nanostructures is oriented towards the (109) peak with noticeable additional peaks between 60 and 90 degrees. However, the peaks did not correspond to any of the lattice planes of the other crystalline phase (cubic) of β-In_2S_3 thereby ruling out the existence of a mixed phase.

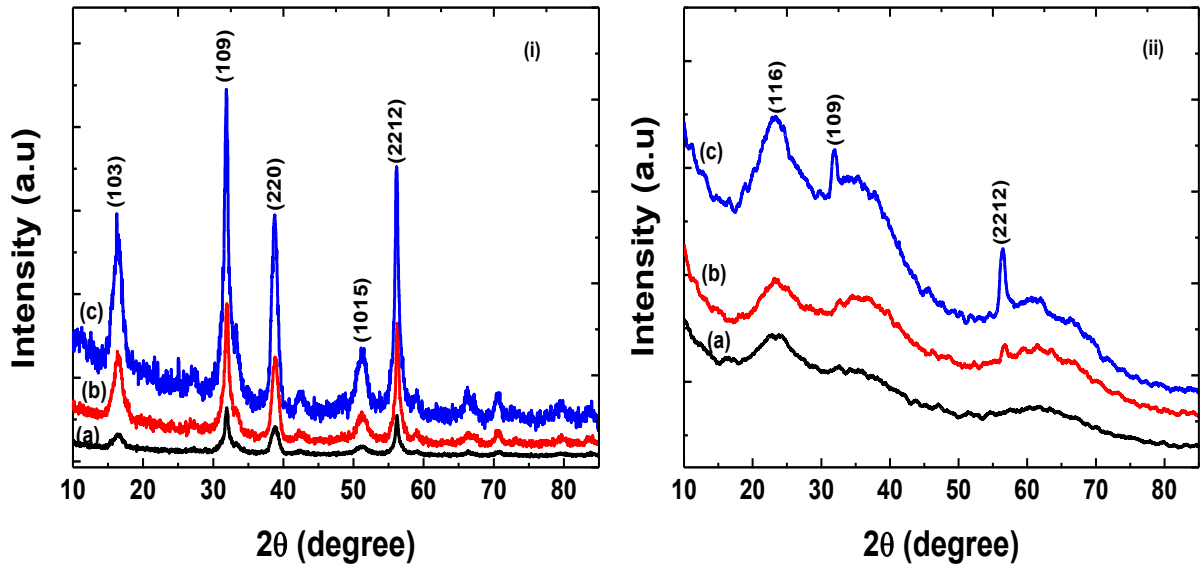


Figure 4.22: XRD patterns of (i) 1-DDT/β-In_2S_3 nanostructures at (a) 60 min, (b) 90 min, and (c) 150 min; (ii) OLA/β-In_2S_3 nanostructures at (a) 120 min, (b) 150 min, and (c) 180 min.

Use of 1-DDT as a sulphur source resulted in fewer reflections an indication of nanostructures with poor crystallinity, Figure 4.22 (ii). However, the crystallinity improved somewhat after heating to 180 min. All the reflections were indexed to the defect tetragonal phase of the β-In_2S_3 crystalline structure. The identified peaks correspond to the (116), (109) and (2212) lattice planes (PDF card no.: 00-025-0390). The growth of the nanostructures is oriented towards the broad but more intense (109) peak.

More light on whether OLA or 1-DDT or both capped the β-In_2S_3 nanostructures was shed by ^{1}HNMR spectroscopy. The spectra of free OLA and 1-DDT are presented in Figures 4.23 and 4.24 respectively.

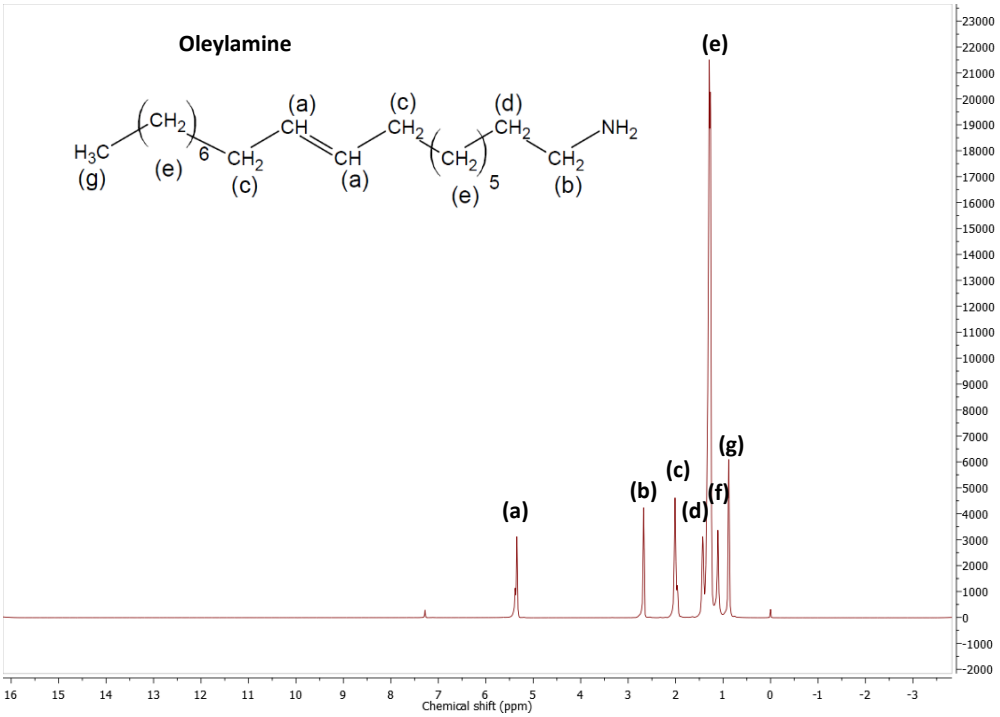


Figure 4.23: Solution ^{1}HNMR spectra obtained on $CDCl_3$ dispersions of pure OLA.

The OLA spectrum displays the vinyl protons peak between 5.0 and 5.5 ppm which will be used to distinguish between OLA and 1-DDT capped nanostructures (Figure 4.23).

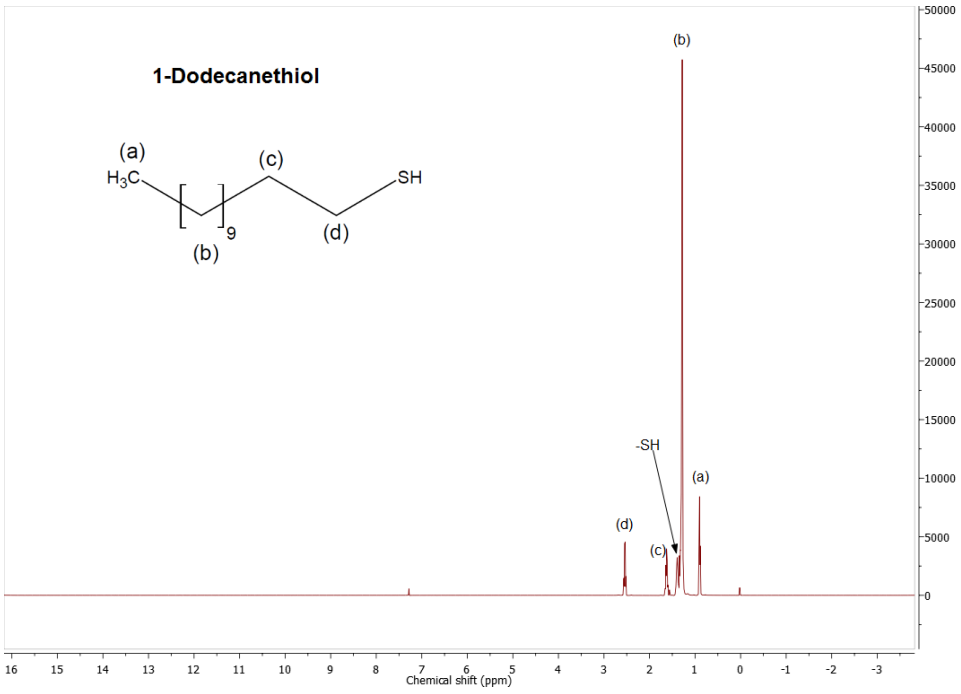


Figure 4.24: Solution ^{1}HNMR spectra obtained on $CDCl_3$ dispersions of pure 1-DDT.

The spectrum of 1-DDT displays the characteristic resonance for α-methylene protons assigned peak at about 2.5 ppm (Figure 4.23). The β-methylene group is found at about 1.6 ppm while thiol group protons are at about 1.2 ppm. The vinyl protons peak is expectedly present in the spectra for OLA/β-In_2S_3 (Figure 4.25). However, it was surprisingly present in OLA/0.2 mL_1-DDT/β-In_2S_3 spectrum as well; 1-DDT easily displaces OLA [6, 14, 74] and co-ordinates strongly to metal ions than OLA [44, 69, 74]. It is therefore highly possible that 1-DDT capped a few of the surface molecules due to the small amount used. A similar scenario was portrayed during partial ligand exchange of OLA by 1-DDT on Ge NCs [44].

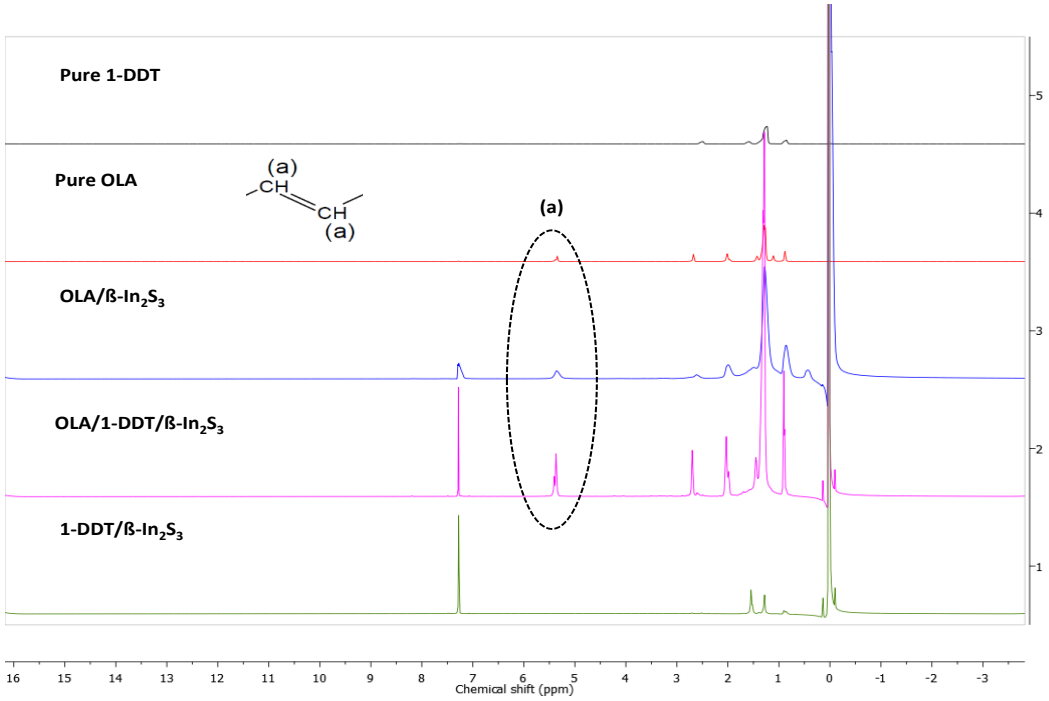


Figure 4.25: Solution ^{1}HNMR spectra obtained on $CDCl_3$ dispersions of the free capping agents and capped β-In_2S_3 nanostructures.

4.2.4.2 Optical properties

The UV-vis spectra displayed the characteristic step-like absorption band due to the valence-to-conduction-band transition as presented in Figure 4.26.

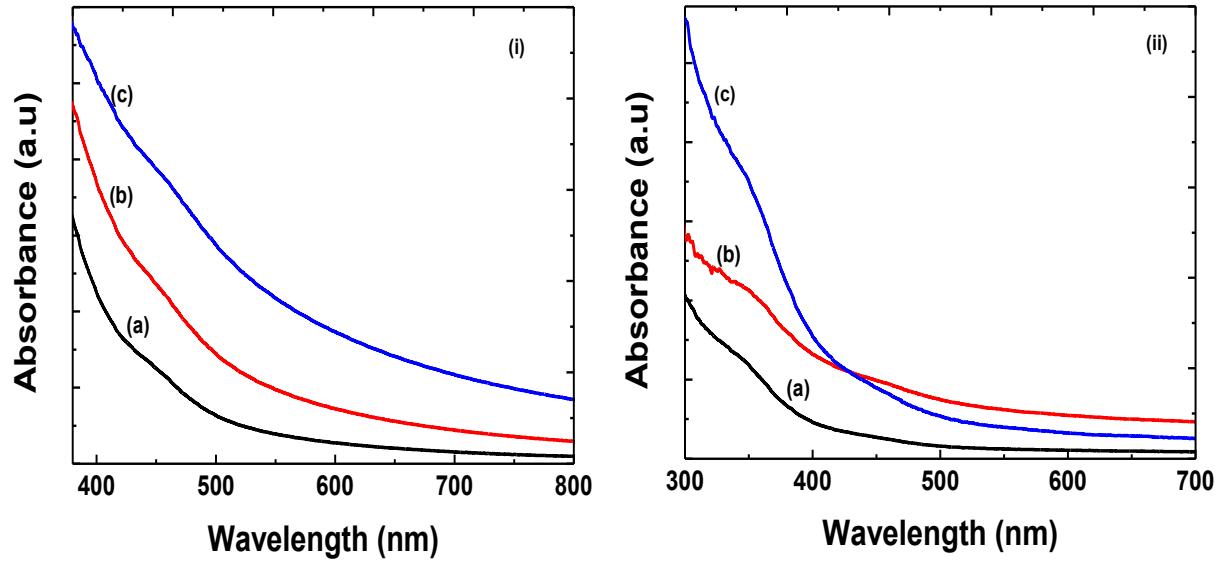


Figure 4.26: UV-vis spectra of (i) OLA/0.2 mL_1-DDT/β-In_2S_3 nanostructures and (ii) OLA/0.4 mL_1-DDT/β-In_2S_3 nanostructures at (a) 60 min, (b) 90 min, and (c) 150 min.

The band gap values of the OLA/0.2 mL_1-DDT/β-In_2S_3 were all blue shifted from the bulk (2.0 eV) [75], indicating reduced size of nanostructures (Table 4.4). This happens when the size of a particle approaches its exciton Bohr diameter, 34 nm in the case of β-In_2S_3 [75].

Typical PL spectra of the nanostructures are displayed in Figure 4.27. The nanostructures exhibited blue light emission (441-444 nm) at room temperature with 250 nm excitation wavelength as shown in Figure 4.2.7 and Table 4.4.

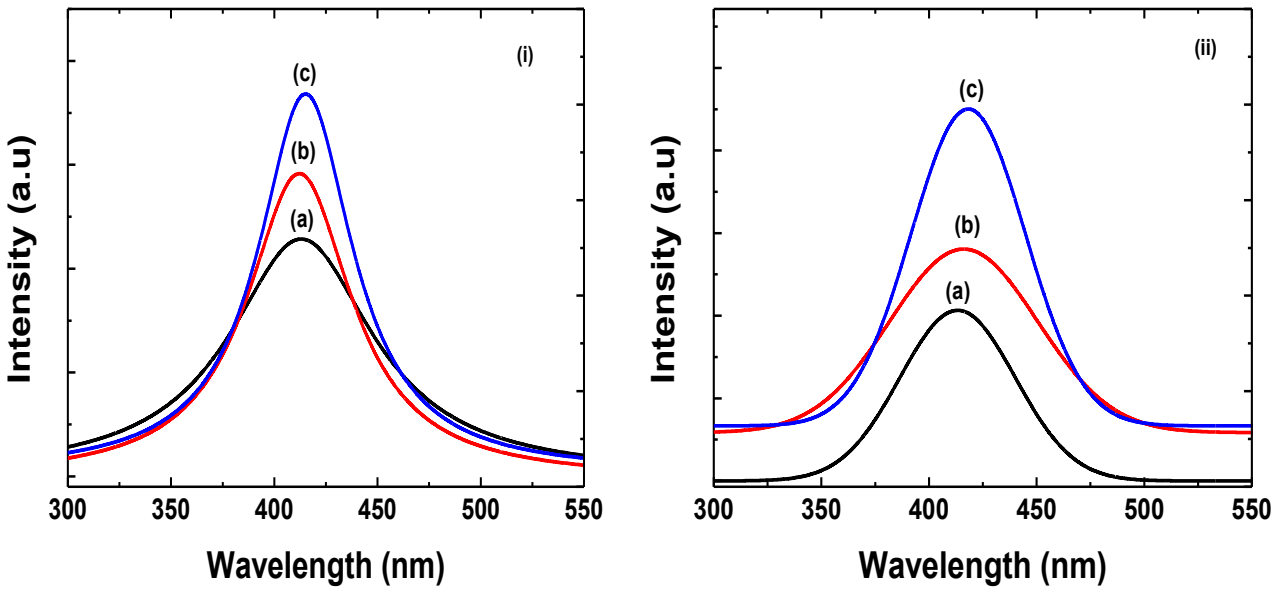


Figure 4.27: PL spectra of (i) OLA/0.2 mL_1-DDT/β-In_2S_3 nanostructures and (ii) OLA/0.4 mL_1-DDT/β-In_2S_3 nanostructures at (a) 60 min, (b) 90 min, and (c) 150 min.

Band gap values of the nanostructures obtained when the amount of 1-DDT was doubled were significantly higher (Table 4.4). The larger blue shift implies the existence of strong quantum confinement of the excitonic transition [75]. This proves that the amount of 1-DDT could be used to adjust the band gap. These nanostructures could be used as photocatalysts.

Table 4.4: Optical parameters at different reaction times.

Reaction time (min)	Band gap (eV)	UV-vis wavelength (nm)	PL wavelength (nm)
OLA/0.2 mL_1-DDT			
60	3.1	397	444
90	2.9	428	441
150	2.7	468	444
OLA/0.4 mL_1-DDT			
60	3.7	334	447
90	3.1	407	422
150	3.8	331	417

Absorption spectra for the nanostructures synthesized in OLA with 1-DDT as sulphur source are presented in Figure 4.28.

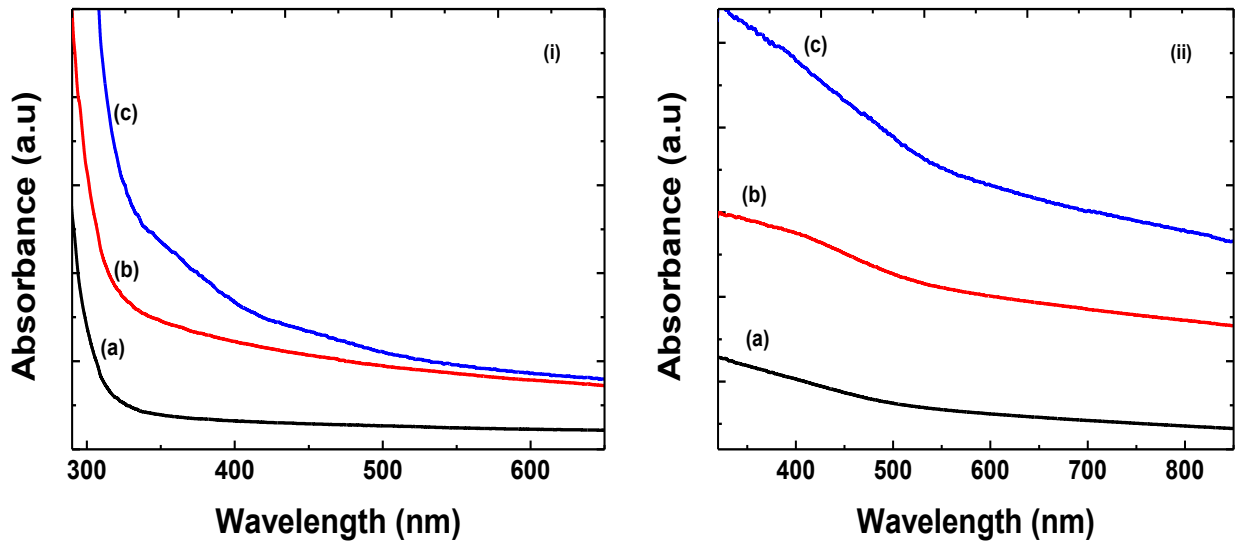


Figure 4.28: (i) UV-vis spectra of OLA/β-In_2S_3 at (a) 120 min, (b) 150 min, and (c) 180 min with 1-DDT as sulphur source; (ii) 1-DDT/β-In_2S_3 at (a) 60 min, (b) 90 min, and (c) 150 min.

The characteristic step-like absorption is observed once again and the calculated band gaps are wide (Table 4.5). Therefore, the source of sulphur can also be used to adjust band gaps to absorb in the desired region of the solar spectrum. Meanwhile, 1-DDT capped β-In_2S_3 nanostructures presented bulk band gaps. The red shifted absorption is not surprising given the size of the microspheres. Blue light emission was observed in both cases (Figure 4.29).

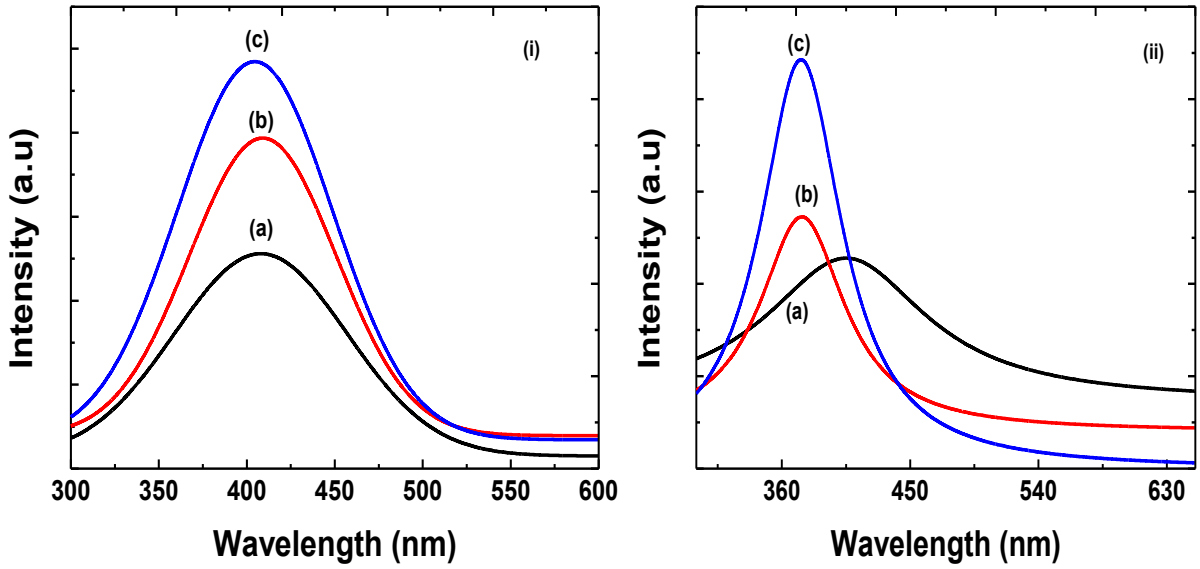


Figure 4.29: (i) PL spectra of OLA/β-In_2S_3 at (a) 120 min, (b) 150 min, and (c) 180 min with 1-DDT as sulphur source; (ii) 1-DDT/β-In_2S_3 at (a) 60 min, (b) 90 min, and (c) 150 min.

Table 4.5: Optical parameters for the OLA/β-In_2S_3 (1-DDT as S source) and 1-DDT/β-In_2S_3 nanostructures.

Reaction time (min)	Band gap (eV)	UV-vis wavelength (nm)	PL wavelength (nm)
OLA/β-In_2S_3			
120	4.2	295	400
150	4	308	400
180	4.1	299	388
1-DDT/β-In_2S_3			
60	2	620	388
90	2.2	566	384
150	2.2	566	387

4.2.5 Conclusions

The study displayed the advantage of using a bi-ligand system to grow the desired hexagonal nanoplates of β-In_2S_3. The two ligands have different binding strengths to In^{3+}; however, a balance was struck by carefully selecting the ratio of 1-DDT to OLA leading to the desired morphology. This ratio limited 1-DDT to the leading role of reductant and controlled the nucleation rate. It is possible that 1-DDT also played a minor role of capping agent due to the small amount used. Meanwhile, OLA was responsible for the hexagonal shape because this morphology was obtained without 1-DDT in the previous study (Section 4.1) as a function of time. The experimental results indicated that the presence of OLA is crucial for the formation of the hexagonal shape. This was corroborated by the formation of microspheres as a function of time when 1-DDT was used as the sole solvent. The study also exhibited that the amount of capping agent and S source can be used to manipulate the band gaps as seen when the amount of 1-DDT to OLA was doubled and 1-DDT was used instead of elemental S respectively.

4.2.6 References

[1] Talapin, D.V., Lee, J-S., Kovalenko, M. V. and Shevchenko, E. V. (2010). Chem. Rev. 110, 389-458.

[2] Singh, S., Bharti, A. and Meena, V. K. (2015). J Mater Sci: Mater Electron 26, 3638-3648.

[3] Sajanlal, P. R., Sreeprasad, T. S., Samal, A. K. and Pradeep, T. (2011). Nano Reviews 2, 5883- DOI: 10.3402/nano.v2i0.5883.

[4] Cabrera-Trujillo, J. M., Montejano-Carrizales, J. M., Rodríguez-López, J. L., Zhang, W., Velázquez-Salazar, J. J. and José-Yacamán, M. (2010). J. Phys. Chem. C 114, 21051-21060.

[5] Burda, C., Chen, X.; Narayanan, R. and El-Sayed, M. A. (2005). Chem. Rev. 105, 1025-1102.

[6] Mourdikoudis, S. and Liz-Marzan, L. M. (2013). Chem. Mater. 25, 1465-1476.

[7] Ghosh, A. B., Saha, N., Sarkar, A., Srivastava, D. N., Paul, P. and Adhikary, B. (2015). RSC Adv. 5, 102818-102827.

[8] Xia, Y., Xia, X. and Peng, H-C. (2015). J. Am. Chem. Soc. 137, 7947-7966.

[9] Chang, J. and Waclawik, E. R. (2014). RSC Adv. 4, 23505-23527.

[10] Burrows, D., Vartanian, M., Abadeer, N. S., Grzincic, E. M., Jacob, L. M., Lin, W., Li, J., Dennison, J. M., Hinman, J. G. and Murphy, C. J. (2016). J. Phys. Chem. Lett. 7, 632-641.

[11] Marzán, L. M. L. (2006). J. Mater. Chem. 16, 3891-3892.

[12] Zhang, B., Guo, F., Yang, L. and Wang, J. (2014). Journal of Crystal Growth 405, 142-149.

[13] Sebastian, V., Smith, C. D. and Jensen, K. F. Shape-controlled continuous synthesis of metal nanostructures (2016). Nanoscale 8, 7534-7543.

[14] van der Stam, W., Gradmann, S., Altantzis, T., Ke, X.; Baldus, M., Bals, S. and de Mello Donega, C. (2016). Chem. Mater. 28, 6705-6715.

[15] Fang, J., You, H., Kong, P., Yi, Y., Song, X. and Ding, B. (2007). Crystal Growth & Design 7 (5), 864-867.

[16] Wang, Q., Lian, J., Li, J., Wang, R., Huang, H., Su, B. and Lei, Z. (2015). Scientific Reports 5 (13593), 1-9.

[17] Li, L., Pandey, A., Werder, D. J., Khanal, B. P., Pietryga, J. M. and Klimov, V. I. (2011). J. Am. Chem. Soc. 133, 1176-1179.

[18] Duan, H., Wang, D. and Li, Y. (2015). Chem. Soc. Rev. 44, 5778-5792.

[19] Wang, Y., Peng, H-C., Liu, J., Huang, C. Z. and Xia, Y. (2015). Nano Lett. 15, 1445-1450.

[20] Peng, Z. A. and Peng, X. (2002). J. Am. Chem. Soc. 124, 3343-3353.

[21] Talapin, D. V., Nelson, J. H., Shevchenko, E. V., Aloni, S.; Sadtler, B. and Alivisatos, A. P. (2007). Nano Lett. 7 (10), 2951-2959.

[22] Sau, T. K. and Murphy, C. J. (2004). J. Am. Chem. Soc. 126, 8648-8649.

[23] Zhu, C., Zeng, J., Tao, J., Johnson, M. C., Schmidt-Krey, I., Blubaugh, L., Zhu, Y., Gu, Z. and Xia, Y. (2012). J. Am. Chem. Soc. 134, 15822-15831.

[24] Jun, Y-W., Lee, S. M., Kang, N. J. and Cheon, J. (2011). J. Am. Chem. Soc. 123, 5150-5151.

[25] Kolny-Olesiak, J. (2014). CrystEngComm 16, 9381-9390.

[26] Saunders, A. E., Ghezelbash, A., Sood, P. and Korgel, B. A. (2008). Langmuir 24, 9043-9049.

[27] Leach, A. D. P and Macdonald, J. E. (2016). J. Phys. Chem. Lett. 7, 572-583.

[28] Ramasamy, K., Malik, M. A., Revaprasadu, N. and O'Brien, P. (2013). Chem. Mater. 25, 3551-3569.

[29] Georgiadou, V., Kokotidou, C., Le Droumaguet, B., Carbonnier, B., Choli-Papadopouloub, T. and Dendrinou-Samara, C. (2014). Dalton Trans. 43, 6377-6388.

[30] Pan, D., An, L., Sun, Z., Hou, W., Yang, Y., Yang, Z and Lu, Y. (2008). J. Am. Chem. Soc. 130, 5620-5621.

[31] Klokkenburg, M., Hilhorst, J. and Erne, B. H. (2007). Vibrational Spectroscopy 43, 243-248.

[32] Castro, E. G., Salvatierra, R. V., Schreiner, W. H., Oliveira, M. M. and Zarbin, A. J. G. (2010). Chem. Mater. 22, 360-370.

[33] Chen, H. M. and Liu, R.-S. (2011). J. Phys. Chem. C 115, 3513-3527.

[34] Pein, A., Baghbanzadeh, M., Rath,T., Haas, W., Maier, E., Amenitsch, H., Hofer, F., Kappe, C. O. and Trimmel, G. (2011). Inorganic Chemistry 50 (1), 193-200.

[35] Norako, M. E., Franzman, M. A. and Brutchey, R. L. (2009). Chem. Mater. 21, 4299-4304.

[36] Turo, M. J. and Macdonald, J. E. (2014). ACS Nano 8 (10), 10205-10213.

[37] Cara, C., Musinu, A., Mameli, V., Ardu, A., Niznansky, D., Bursik, J., Scorciapino, M. A., Manzo, G. and Cannas, C. (2015). Cryst. Growth Des. 15, 2364-2372.

[38] Rodríguez-Ortiz, G., Téllez-Vázquez, O., Gutiérrez-Wing, C., Esparza, R. and Pérez, R. (2013). Materials Science Forum 755, 83-89.

[39] Xu, Z., Shen, C., Hou, Y., Gao, H. and Sun, S. (2009). Chem. Mater. 21, 1778-1780.
[40] Pradhan, N. and Katz, B. (2003). J. Phys. Chem. 107, 13843-13854.
[41] Nagesha, D. K., Liang, X., Mamedov, A. A., Gainer, G., Eastman, M. A., Giersig, M., Song, J-J., Ni, T. and Kotov, N. A. (2001). J. Phys. Chem. B 105, 7490-7498.
[42] Niu, J., Xu, W., Shen, H., Li, S., Wang, H. and Li, L. S. (2012). Bull. Korean Chem. Soc. 33 (2), 393-397.
[43] Aldakov, D., Lefrancois, A. and Reiss, P. (2013). J. Mater. Chem. C 1, 3756-3776.
[44] Muthuswamy, E., Zhao, J., Tabatabaei, K., Amador, M. M., Holmes, M. A., Osterloh, F. E. and Kauzlarich, S. M. (2014). Chem. Mater. 26, 2138-2146.
[45] Peng, X., Manna, L., Yang, W., Wickham, J., Scher, E., Kadavanich, A. and Alivisatos, A. P. (2000). Nature 404 (2), 59-61.
[46] Polavarapu, L. and Xu, Q-H. (2009). Nanotechnology 20 (185606) 1-7.
[47] Batabyal, S. K., Lu, S. E. and Vittal, J. J. (2016). Cryst. Growth Des. 16, 2231-2238.
[48] Chang, H., Xie, J., Zhao, B., Liu, B., Xu, S., Ren, N., Xie, X., Huang, L. and Huang, W. (2015). Nanomaterials *5*, 1-25.
[49] Carenco, S., Boissiere, C., Nicole, L., Sanchez, C., Le Floch, P. and Mezailles, N. (2010). Chem. Mater. 22, 1340-1349.
[50] Senapati, D., Singh, A. K. and Ray, P. C. (2010). Chemical Physics Letters 487, 88-91.
[51] Norako, M. E. and Brutchey, R. L. (2010). Chem. Mater. 22, 1613-1615.
[52] Kruszynska, M., Borchert, H., Parisi, J. and Kolny-Olesiak, J. (2011). J Nanopart Res 13, 5815-5824.
[53] Xiang, G., Li, T., Zhuang, J. and Wang, X. (2010). Chem. Commun. 46, 6801-6803.
[54] Yang, S., Li, Y., Wang, X., Huo, N., Xia, J.-B., Li, S.-S. and Li, J. (2014). Nanoscale 6, 2582-2587.
[55] Samnakay, R., Jiang, C., Rumyantsev, S. L., Shur, M. S. and Balandin, A. A. (2015). Appl. Phys. Lett. 106 (023115), 1 -5.
[56] Tian, Y., Wang, L., Tang H. and Zhou, W. (2015)J. Mater. Chem. A 3, 11294-11301.
[57] Perkins, F. K., Friedman, A. L., Cobas, E., Campbell, P. M., Jernigan, G. G. and Jonker, B. T. Nano Lett. 13, 668-673.
[58] Feng, J., Wu, C., Peng, L., Lin, C., Hu, S., Yang, J. and Xie, Y. (2011). J. Am. Chem. Soc. 133, 17832-17838.
[59] Acharya, S., Dutta, M., Sarkar, S., Basak, D., Chakraborty, S. and Pradhan, N. (2012). Chemistry of Materials 24, 1779-1785.

[60] Wang, H., Yu, L., Lee, Y.-H., Shi, Y., Hsu, A, Chin, M. L., Li, L.-J., Dubey, M., Kong, J. and Palacios, T. (2012). Nano Lett. 12, 4674-4680.

[61] Hu, P A., Wang, L., Yoon, M., Zhang, J., Feng, W., Wang, X., Wen, Z., Idrobo, J.C., Miyamoto, Y., Geohegan, D.B. and Xiao, K. (2013). Nano Lett. 13, 1649-1654.

[62] Radisavljevic, B., Radenovic, A., Brivio, J., Giacometti, V. and Kis, A. (2011). Nature Nanotechnology 6, 147-150.

[63] Chen, L-Y., Zhang, Z-D. and Wang, W-Z. (2008). Journal of Physical Chemistry C 112, 4117-4123.

[64] Afzaal, M. and O'Brien, P. (2006). J. Mat. Chem. 16, 1597-1602.

[65] Cingarapu, S., Ikenberry, M. A., Hamal, D. B.,Sorensen, C. M., Hohn, K. and Klabunde, K. J. (2012). Langmuir 28, 3569-3575.

[66] Xing, Y., Zhang, H., Song, S., Feng, J., Lei, Y., Zhao, L. and Li, M. (2008). Chem. Commun., 1476-1478.

[67] Rengaraj, S., Selvaraj, Venkataraj, S., Tai, C., Kim, Y., Repo, E. and Sillanpää, M. Langmuir 27, 5534-5541.

[68] El-Nahass, M. M., Khalifa, B. A., Soliman, H. S. and Seyam, M. A. M. (2006). Thin Solid Films 151, 1796-1801.

[69] Belosˇ, M. V., Abazović, N. D., Jakovljević, J. K., Janković, I., Ahrenkiel, S. P., Mitrić, M. and Comor, M. I. (2013). J. Nanopart. Res. 15 (2148), 1-11.

[70] Zhao, X., Luo, B., Long, R., Wang C. and Xiong, Y. (2015). J. Mater. Chem. A 3, 4134-4138.

[71] Xu, D., Liu, Z., Liang, J. and Qian, Y. (2005). J. Phys. Chem. B 109, 14344-14349.

[72] Singh, A., Geaney, H., Laffir, F. and Ryan, K.M. (2012). J. Am. Chem. Soc. 134, 2910-2913.

[73] Soosaimanickam, A., Jeyagopal, R., Hayakawa, Y. and Sridharan, M. B. (2015). Japanese Journal of Applied Physics 54, 08KA10, 1-4.

[74] Shen, S., Zhuang, J., Xu, X., Nisar, A., Hu, S. and Wang, X. (2009). Inorg. Chem. 48, 5117-5128.

[75] Du, W., Zhu, J., Li, S. and Qian, X. (2008). Crystal Growth & Design 8, (7), 2008, 2130-2136.

4.3 Tuning the optical properties of β-In_2S_3 nanostructures with alkylamine ligands and the influence of 1-dodecanethiol on their shape

4.3.1 Introduction

Semiconductor nanocrystals are one of the key role players in the search for novel materials with superior properties. These materials have been used important components for electronic devices such as solar cell absorber layers, photodetectors, light emitting diodes, photocatalysts, chemical sensors and superconductors [1-3]. One such material is indium sulphide (In_2S_3) [4, 5], a member of the III-IV group of semiconductors [6-11]. It has three polymorphs, namely α (defect cubic), γ (layered) and β [6, 8, 10, 12-19]. The β polymorph is the most stable at room temperature [17, 18] with a large number of vacancies which influence photoelectric conversion [19]. It in turn crystallizes into either cubic or tetragonal phases and has a band gap of 2.0 – 2.2 eV [20-22].

The size and shape dependent optical properties [23-25] can be tuned across the visible and infrared ranges of the solar spectrum [2, 26]. In return, the size and shape can be tuned by varying reaction parameters [27] such as the nature of the reagents and solvent, reaction time, temperature, pressure, pH and concentration. Solvothermal synthesis in an organic solvent provides a platform to manipulate these key reaction parameters. The organic solvent is usually a ligand or capping agent to provide electronic stabilization, restrict particle growth, control nucleation, control morphology and prevent agglomeration of nanoparticles [28-32]. Extensive research has been done on the role of capping agents such as oleylamine (OLA) [27, 33-38], oleic acid (OA) [29, 31], tri-octylphosphine oxide (TOPO) [2], trioctylphosphine (TOP) [39], 1-dodecanethiol (1-DDT) [2, 3, 26, 27, 30, 33, 34, 30] and tert-dodecanethiol (tert-DDT) [2] and their mixtures [1, 26, 29, 36, 40-56] in the synthesis of semiconductor nanocrystals and magnetic nanoparticles. 1-DDT can act as a source of sulphur, solvent, capping agent or reductant [30, 57, 58]. However, there has not been much research done on the combination of 1-DDT with HDA or ODA. In this study different shapes of β-In_2S_3 using HDA, ODA as sole solvents as well as combinations with 1-DDT. The effect of 1-DDT and reaction time on the morphology was investigated.

4.3.2 Experimental procedure

4.3.2.1 Chemicals and materials

Indium (III) chloride, sulphur powder, hexadecylamine (HDA), octadecylamine (ODA), 1-dodecanethiol (1-DDT), chloroform, dichloromethane, ethanol and methanol were purchased from Sigma Aldrich.

4.3.2.2 Synthesis of β-In_2S_3 nanostructures

(i) HDA

In a 100 mL three-neck round bottom flask attached to a Schlenk line via a condenser, 7g of HDA was heated to 50 ℃ to allow it to melt. The melt was degassed for 20 minutes under the flow of nitrogen and strong magnetic stirring. Elemental sulphur powder (0.1603 g, 5 mmol) was added to the flask and the mixture was heated to 100 ^{o}C. The colour of the mixture changed from yellow to brown indicating the reduction of sulphur by HDA. Indium chloride (1.106 g, 5 mmol) was added to the flask and the mixture was heated to 220 ^{o}C for 150 min. The colour of the reaction changed from brown to yellow and thickened, indicating the formation of colloids. Aliquots were taken at 60, 90 and 150 min. Excess methanol was added to the nanoparticles once they had cooled down and centrifuged at 3000 rpm. The separated particles were then washed with ethanol several times. The effect of reaction time was studied. The effect of 1-DDT was investigated by following the same procedure same with 0.2 mL of 1-DDT added to the melt. The effect of 1-DDT and reaction time were studied.

(ii) ODA

HDA was replaced with ODA (5g) and heated to 57 ℃ to allow it to melt. The rest of the experiment was carried out as in (i) above.

4.3.2.3 Characterization techniques

(i) Structural properties of the nanostructures

Nanomaterial sizes and morphology were studied using FEI Spirit 120 kV transmission electron microscope operated at an acceleration voltage of 200 kV with a beam spot size of 20 - 100 nm in TEM mode. Powders of nanomaterials were dispersed in chloroform and drop cast onto carbon lacey copper grids. The solvent was then evaporated at room temperature.

(ii) Optical properties of the nanostructures

A Specord 50 AnalytikJena UV-Vis spectrophotometer was used to carry out the absorption measurements. An Agilent Cary Eclipse fluorescence spectrometer was used to measure the photoluminescence of the particles. The nanoparticles were dissolved in chloroform and placed in quartz cuvettes (1cm path length) for UV-Vis and PL spectral analyses.

4.3.3 Results and discussion

4.3.3.1 Synthesis of β-In_2S_3 nanostructures

$InCl_3$ is thermally decomposed into In^{3+} and Cl^- while elemental sulphur is reduced by HDA and ODA in the mono-ligand system and by 1-DDT in the bi-ligand system. The proposed chemical reactions are:

$$2In^{3+} + 2S^{2-} \xrightarrow[N_2,\ \text{HDA or HDA/ 1-DDT}]{220\ ^\circ C} In_2S_3\ (s) \qquad (4.3.1)$$

$$2In^{3+} + 2S^{2-} \xrightarrow[N_2,\ \text{ODA or ODA/ 1-DDT}]{220\ ^\circ C} In_2S_3\ (s) \qquad (4.3.2)$$

(i) Structural properties

(a) HDA/β-In_2S_3 nanostructures

TEM was used to monitor the growth of the nanostructures at different reaction time intervals. Figure 4.30 (a)-(c) shows a variation in morphology as a function of time when HDA was used as sole solvent. A mass of nanostructures was formed in 60 min which transformed into nanoparticles with further heating to 90 min. Prolonged heating to 150 min resulted in nanosheet-like structures. A combination of HDA and 0.2 mL of 1-DDT also resulted in different morphologies which evolved with time as shown in Figure 4.30 (d)-(f). Nanosheets were formed in 60 min and transformed into irregular nanostructures in 90 min. Further heating to 150 min saw the emergence of nanobelts and the irregular nanostructures could still be seen.

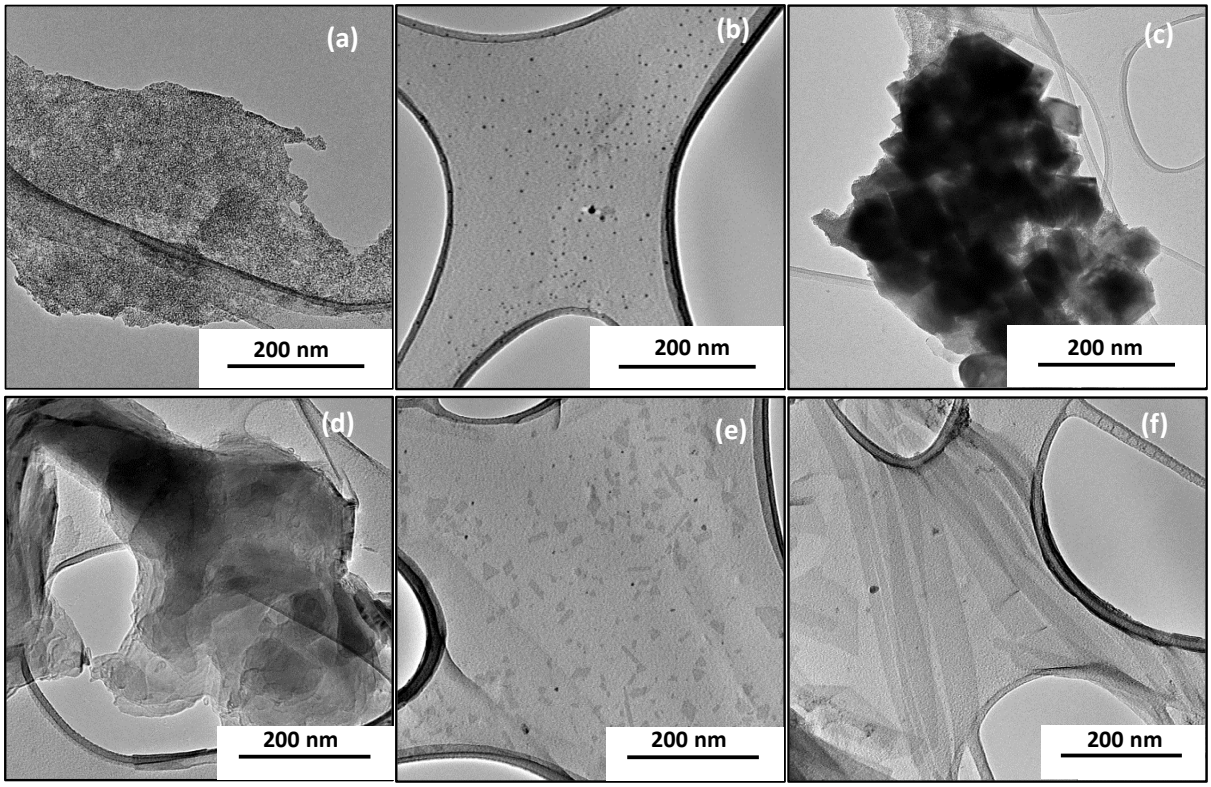


Figure 4.30: TEM images of HDA/β-In_2S_3 at (a) 60 min, (b) 90 min, and (c) 150 min; HDA/1-DDT_β-In_2S_3 at (d) 60 min, 90 min and (f) 150 min.

(b) ODA/β-In_2S_3 nanostructures

Variation of time once again resulted in transformation of morphology. ODA as sole solvent resulted in the formation of nanoparticles in 60 min which transformed into cubes with further heating to 90 min, Figure 4.31 (a) and (b). Prolonged heating to 150 min shows incomplete formation of hexagonal nanoplates, Figure 4.31 (c). Well-defined hexagonal nanoplates were formed in 60 min when a combination of ODA and 0.2 mL of 1-DDT was used as the reaction medium as shown in Figure 4.31 (d). However, heating to 90 min displayed what looks like the disintegration of the nanoplates into rod-like nanostructures, Figure 4.31 (e). Further heating to 150 min resulted in the complete transformation of the nanoplates into nanorods, [Figure 4.31 (f)].

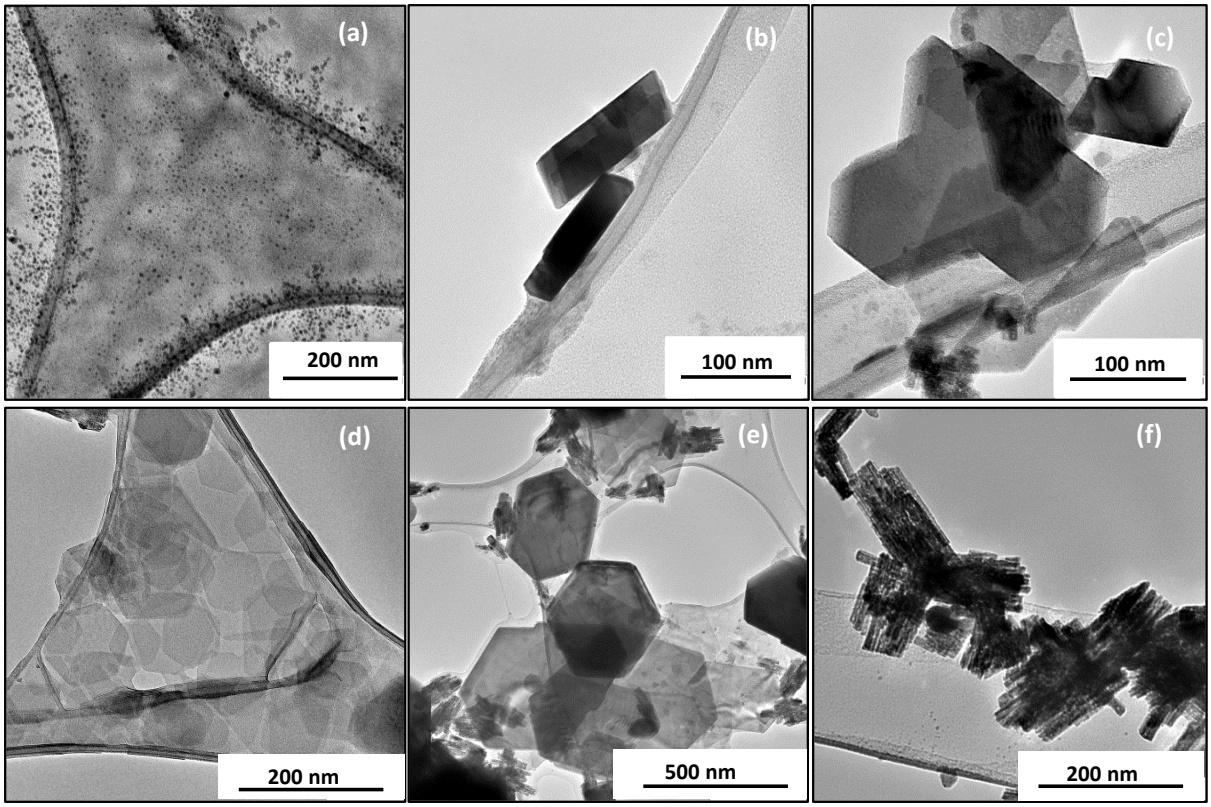


Figure 4.31: TEM images of ODA/β-In_2S_3 at (a) 60 min, (b) 90 min, and (c) 150 min; ODA/1-DDT_β-In_2S_3 (d) 60 min, (b) 90 min and (f) 150 min.

The XRD patterns of the synthesized β-In_2S_3 nanosheets are shown in Figure 4.32 below.

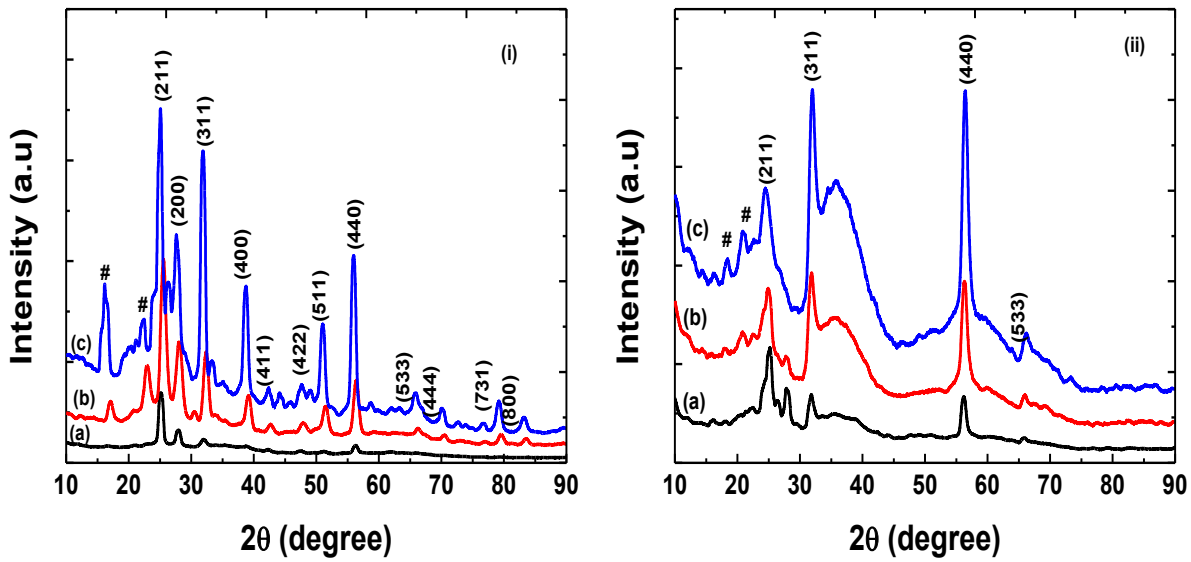


Figure 4.32: XRD patterns of (i) HDA/β-In_2S_3 at (a) 60 min, (b) 90 min, and (c) 150 min; (ii) HDA/1-DDT_β-In_2S_3 at (a) 60 min, (b) 90 min and (c) 150 min. The reflections marked with # represent InS.

The peaks from all the patterns confirm the cubic crystallographic phase which suggest that 1-DDT did not affect the crystallographic phase (JCPDS No. 00-032-0456 for HDA only and 03-065-0459 for HDA/0.2 mL_1-DDT combination). More peaks were observed for HDA suggesting improved crystallinity. However, peaks belonging to the InS composite were also identified at all reaction times, Figure 4.32 (i). Figure 4.32 (ii) shows that fewer peaks were formed for HDA/0.2 mL_1-DDT mixture were seen pointing to poor crystallinity; InS impurity was still present.

Figure 4.33 shows the patterns for both ODA (i) and ODA/0.2 mL_1-DDT (ii) grown nanostructures. All the peaks were indexed to the cubic crystallographic phase of β-In_2S_3 (JCPDS No. 03-065-0459). The presence of 1-DDT had no effect on the crystallographic phase. Both systems show a number of peaks suggesting improved crystallinity. However, peaks (20-30°) belonging to ODA were identified as impurities for both systems. ODA, like HDA is a solid at room temperature making it difficult to get rid of an excess during the purification step.

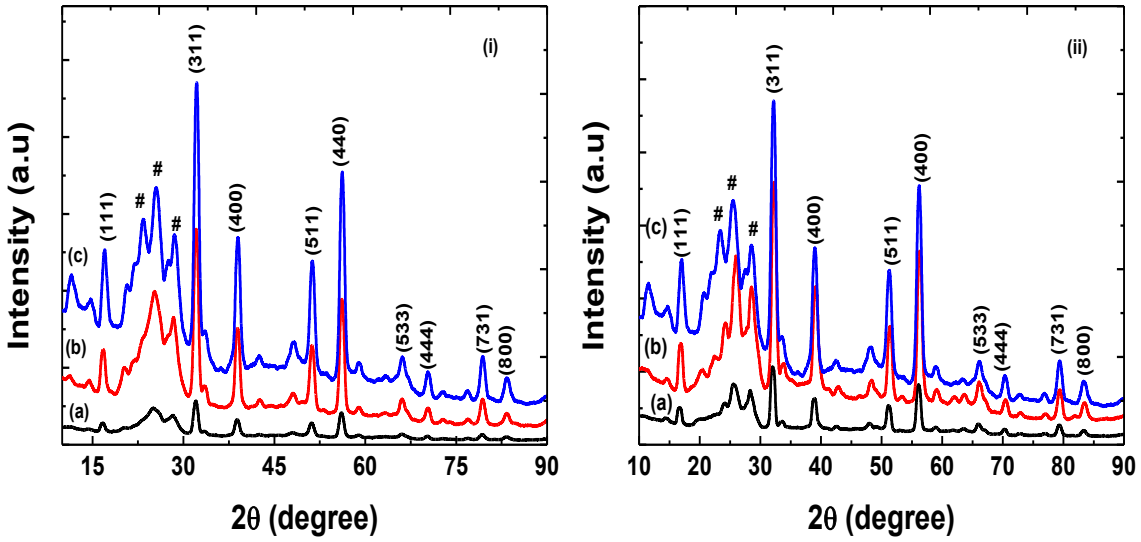


Figure 4.33: XRD patterns of (i) ODA/β-In_2S_3 at (a) 60 min, (b) 90 min, and (c) 150 min; (ii) ODA/1-DDT_β-In_2S_3 at (a) 60 min, (b) 90 min and (c) 150 min. The reflections marked with # represent ODA.

(ii) Optical properties

(a) HDA/β-In_2S_3 nanostructures

The optical properties of the synthesized nanoparticles were studied using the UV-vis and PL characterization techniques. Figure 4.34 shows spectra of the nanostructures from both HDA and HDA/0.2 mL_1-DDT. The unmistakable step-like absorption (200 - 700 nm) was observed and is attributed to the valence-to-conduction-band transition in β-In_2S_3 [38]. The significant blue shift (Table 4.6) from the bulk (2.0 – 2.2 eV) suggests a considerable reduction of nanoparticle size [6, 21, 59]. The band gap values indicate that the use of 1-DDT did not affect the optical properties of the nanostructures. The large band gap values could be due to the impurities present as detected by XRD [1].

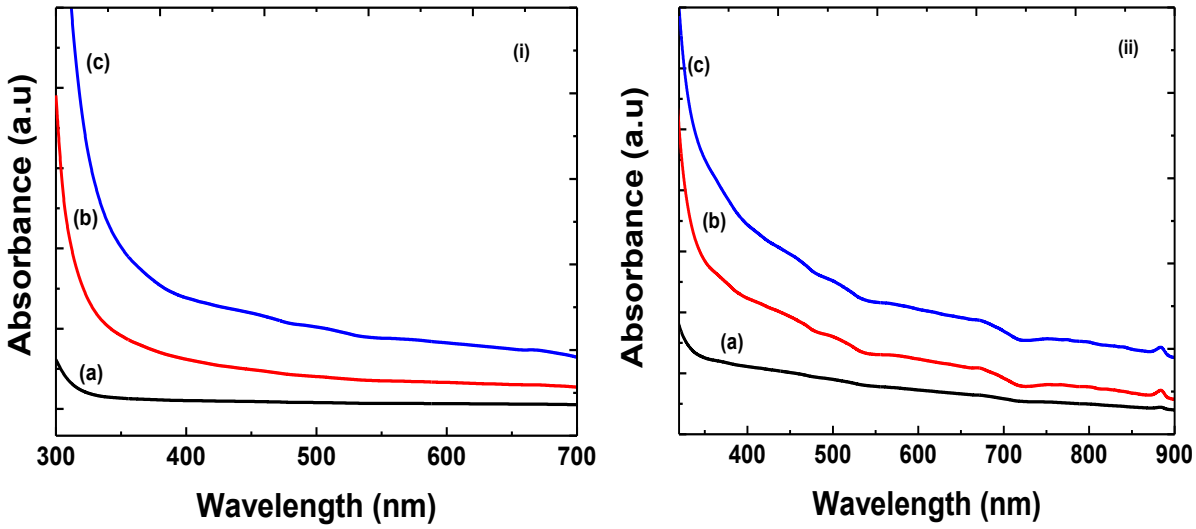


Figure 4.34: UV-vis spectra of (i) HDA/β-In_2S_3 at (a) 60 min, (b) 90 min, and (c) 150 min; (ii) HDA/1-DDT_β-In_2S_3 at (a) 60 min, (b) 90 min and (c) 150 min.

Both systems presented blue shifted emission characterized by broad maxima indicating a broad size distribution under room temperature excitation at 250 nm, Figure 4.35. The luminescence suggests the existence of an electronic transition which is stronger than in its virtually non-luminescent bulk counterpart.

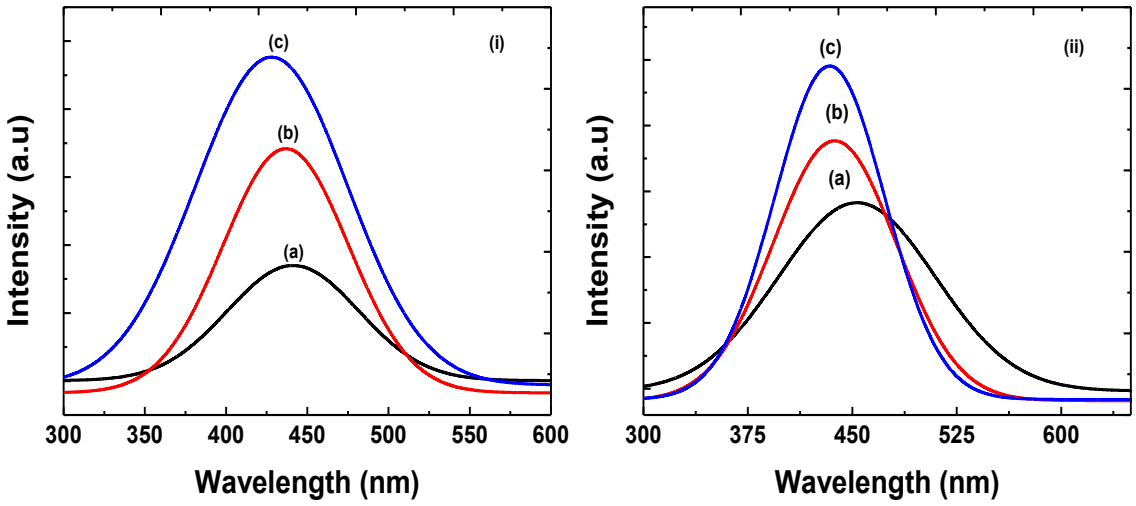


Figure 4.35: PL spectra of (i) HDA/β-In_2S_3 at (a) 60 min, (b) 90 min, and (c) 150 min; (ii) HDA/1-DDT_β-In_2S_3 at (a) 60 min, (b) 90 min, and (c) 150 min.

Table 4.6: Optical parameters at different reaction times.

Reaction time (min)	Band gap (eV)	UV-vis wavelength (nm)	PL wavelength (nm)
HDA/ß-In_2S_3			
60	4.2	295	441
90	4.1	302	437
150	4.1	302	428
HDA/1-DDT_ß-In_2S_3			
60	4	310	453
90	4.1	310	437
150	4.1	302	433

(b) ODA/β-In_2S_3 nanostructures

The UV-vis and PL spectra of the nanostructures from both ODA and ODA/0.2 mL_1-DDT are presented in Figures 4.36 and 4.37 respectively.

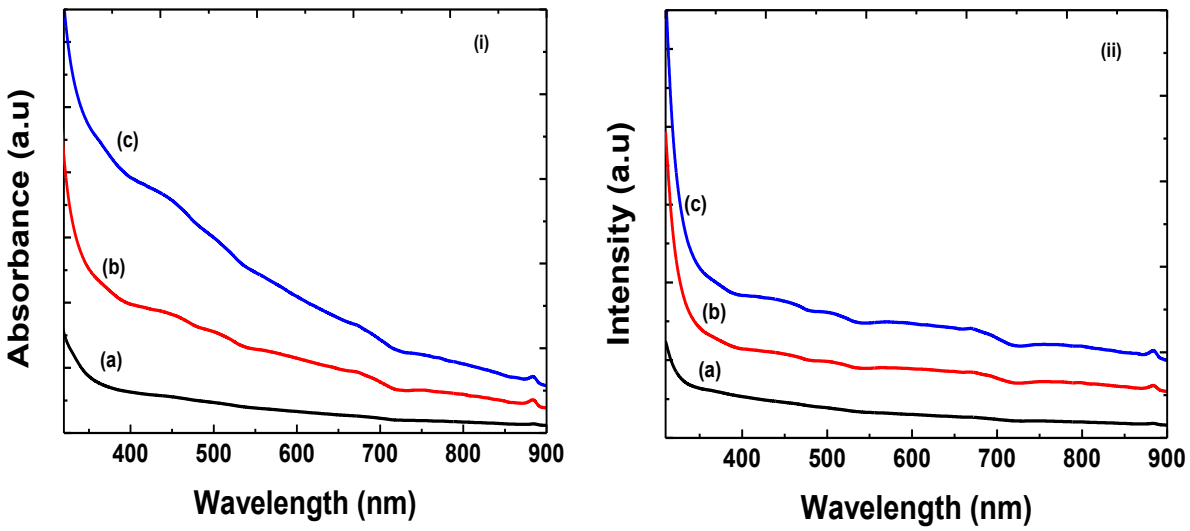


Figure 4.36: UV-vis spectra of (i) ODA/β-In_2S_3 at (a) 60 min, (b) 90 min, and (c) 150 min; (ii) ODA/1-DDT_β-In_2S_3 at (a) 60 min, (b) 90 min, and (c) 150 min.

The β-In_2S_3 valence-to-conduction-band transition as represented by the step-like absorption (200 – 700 nm) was observed in β-In_2S_3 (Figure 4. 36). The band gaps are significantly blue shifted (Table 4.7) from the bulk (2.0 – 2.2 eV), a clear indication of considerable reduction of nanoparticle size [6, 21, 59]. As seen with HDA and HDA/0.2 mL_1-DDT, the band gap values indicate that the use of 1-DDT did not affect the optical properties of the nanostructures. The blue shifted emission spectra were characterized by broad maxima indicating a broad size distribution, Figure 4.37.

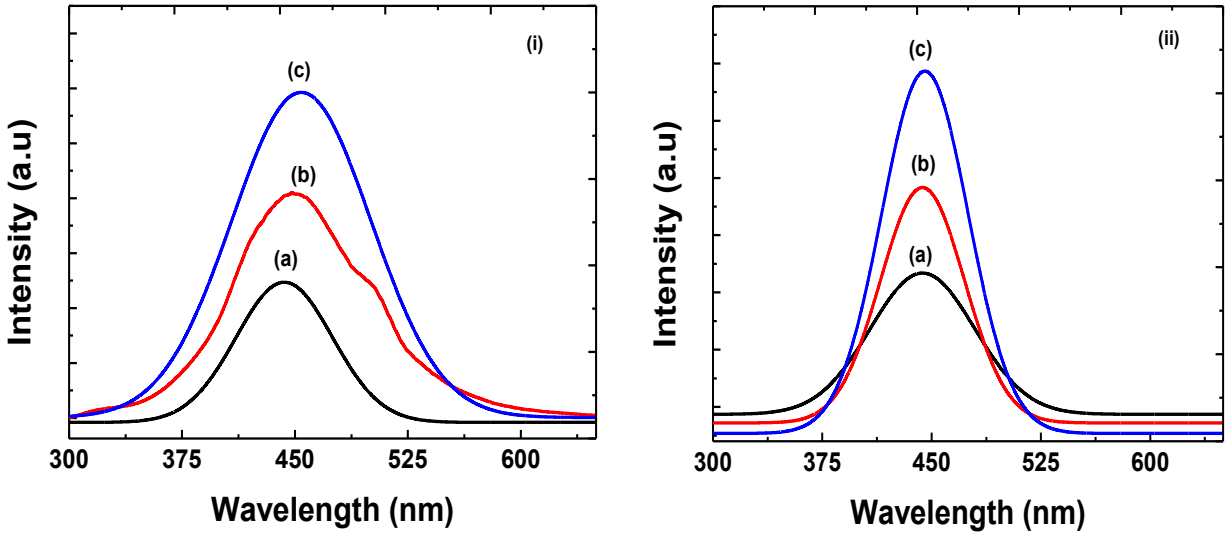


Figure 4.37: PL spectra of (i) ODA/β-In_2S_3 at (a) 60 min, (b) 90 min, and (c) 150 min; (ii) ODA/1-DDT_β-In_2S_3 at (a) 60 min, (b) 90 min, and (c) 150 min.

Table 4.7: Optical parameters at different reaction times.

Reaction time (min)	Band gap (eV)	UV-vis wavelength (nm)	PL wavelength (nm)
ODA/ß-In_2S_3			
60	4.1	302	443
90	4.2	295	449
150	4.1	302	456
ODA/1-DDT_ß-In_2S_3			
60	4.1	302	444
90	4.1	302	444
150	4.1	302	445

4.3.4 Conclusions

Cubic crystallographic phase of β-In_2S_3 nanostructures were successfully synthesized as confirmed by XRD patterns. The nanostructures were capped with HDA and ODA leading to different morphologies at each reaction time. The inclusion of 1-DDT into the reaction medium also led to a change in morphologies. Therefore, variation of reaction time and choice of capping agents are useful parameters to obtain different morphologies. The nanostructures boasted wide band gap values with potential application as UV photocatalysts.

4.3.5 References

[1] Aldakov, D., Lefrançois, A. and Reiss, P. (2013). J. Mater. Chem. C, 1, 3756–3776.

[2] Kruszynska, M., Borchert, H., Parisi, J. and Kolny-Olesiak, J. (2010). Journal of the American Chemical Society 132 (45), 15976-15986.

[3] Niu, J., Xu, W., Shen, H., Li, S., Wang, H. and Li, L. S. (2012). Bulletin of the Korean Chemical Society 33 (2), 393-397.

[4] Shi, Y., Yang, Y-L., Fan, R-Q., Li, L., Yu, J. and Li, S. (2014). RSC Adv. 4 17245-17248.

[5] Marsillac, S., Mangale, N. S., Gade, V. and Khare, S. V. (2011). Thin Film Solids 519, 5679-5683.

[6] Chen L-Y., Zhang, Z-D. and Wang, W-Z. (2008). Journal of Physical Chemistry C 112, 4117-4123.

[7] Afzaal, M. and O'Brien, P. (2006). J. Mat. Chem. 16, 1597-1602.

[8] Cingarapu, S., Ikenberry, M. A., Hamal, D. B., Sorensen, C. M., Hohn, K. and Klabunde, K. J. (2012). Langmuir 28, 3569-3575.

[9] Xing, Y., Zhang, H., Song, S., Feng, J., Lei, Y., Zhao, L. and Li, M. (2008). Chem. Commun., 1476-1478.

[10] Rengaraj, S., Venkataraj, S., Tai, C., Kim, Y., Repo, E. and Sillanpaa, M. (2011). Langmuir 27, 5534-5541.

[11] El-Nahass, M. M., Khalifa, B. A., Soliman, H. S. and Seyam, M. A. M. (2006). Thin Solid Films 151, 1796-1801.

[12] Zhu, H., Wang, X., Yang, W., Yang, F. and Yang, X. (2009). Materials Research Bulletin 44, 2033-2039.

[13] Zhu, X., Ma, J., Wang, Y., Tao, J., Zhou, J., Zhao, Z., Xie, L. and Tian, H. (2006). Materials Research Bulletin 41, 1584-1588.

[14] Barreau, N. (2009). Solar Energy 83, 363-371.

[15] Sharma, Y. and Srivastava, P. (2012). Materials Chemistry and Physics 135, 385-394.

[16] Chai, B., Zeng, P., Zhang, X., Mao, J., Zan, L. and Peng, T. (2012). Nanoscale 4, 2372-2377.

[17] Maha, M. H. Z., Bagheri-Mohagheghi, M-M. and Azimi-Juybari, H. (2013). Thin Solid Films 536, 57-62.

[18] Rao, P. and Kumar, S. (2012). This Solid Films 524, 93-99.

[19] Wang, Y-P., Ho, C-H. and Huang, Y-S. (2010). J. Phys. D: Appl. Phys. 43, 1-5.

[20] Cao, C., Zhao, Y. and Wu, Z. (2009). Journal of Alloys and Compounds 472, 325-327.

[21] Xiong, Y., Xie, Y., Du, G., Tian, X. and Qian, Y. (2002). Journal of Solid State Chemistry 166, 336-340.

[22] Franzman, M. A. and Brutchey, R. L. (2009). Chem. Mater. 21, 1790-1792.

[23] Liu, L., Lui, H., Kou, H-Z., Wang, Y., Zhou, Z., Ren, M., Ge, M. and He, X. (2009). Crystal Growth & Design 9 (1), 113-117.

[24] Chen L-Y., Zhang, Z-D.; Wang, W-Z. (2008). Journal of Physical Chemistry C, 112, 4117-4123.

[25] Kim, Y. H., Lee, J.H., Shin, D-W., Park, S. M., Moon, J. S., Nam, J. G. and Yoo, J-B. (2010). Chem. Commun. 46, 2292-2294.

[26] Norako, M. E., Franzman, M. A. and Brutchey, R. L., (2009). Chemistry of Materials 21 (18), 4299-4304.

[27] Gqoba, S., Airo, M., Ntholeng, N., Machogo, L., Sithole, R., Moloto, M.J., van Wyk, J. and Moloto, N. (2015). Materials Today: Proceedings 2, 3901-3908.

[28] Duan, H., Wang, D. and Li, Y. (2015). Chemical Society Reviews 44 (16), 5778-5792.

[29] Cara, C., Musinu, A., Mameli, V., Ardu, A., Niznansky, D., Bursik, J., Scorciapino, M. A., Manzo, G. and Cannas, C. (2015). Cryst. Growth Des. 15, 2364-2372.

[30] Castro, E. G., Salvatierra, R. V., Schreiner, W. H., Oliveira, M. M. and Zarbin, A. J. G. (2010). Chem. Mater. 22, 360-370.

[31] Muthuswamy, E., Zhao, J., Tabatabaei, K., Amador, M. M., Holmes, M. A., Osterloh, F. E. and Kauzlarich, S. M. (2014). Chem. Mater. 26, 2138-2146.

[32] Ziegler, K. J., Doty, R. C., Johnston, K. P. and Korgel, B. A. (2001). J. Am. Chem. Soc. 123, 7797-7803.

[33] Cui, Y., Wang, G. and Pan, D. (2013). *CrystEngComm* 15 (48), 10459-10463.

[34] Zhao, X., Luo, B., Long, R., Wang, C. and Xiong, Y. (2015). Journal of Materials Chemistry A, 3 (8), 4134-4138.

[35] Georgiadou, V., Kokotidou, C., Le Droumaguet, B., Carbonnier, B., Choli-Papadopoulou T. and Dendrinou-Samara, C. (2014). Dalton Trans. 43, 6377-6388.

[36] Nose, K., Soma, Y., Omata, T. and Otsuka-Yao-Matsuo, S. (2009). Chem. Mater. 21, 2607-2613.

[37] Cholula-Díaz, J. L., Wagner, G., Friedrich, D., Oeckler, O and Krautscheid, H. (2015). Dalton Trans. 44, 14227-14234.

[38] Park, K. H., Jang, K. and Son, S. U. (2006). Angew. Chem. Int. Ed. 45, 4608-4612.

[39] Chen, S., Zhang, X., Zhang, Q. and Tan, W. (2009). Nanoscale Res Lett 4, 1159-1165.

[40] Tang, A., Qu, S., Li, K., Hou, Y., Teng, F., Cao, J., Wang, Y. and Wang, Z. (2010). Nanotechnology 21, 285602, 1-9.

[41] Shen, S., Zhuang, J., Xu, X., Nisar, A., Hu, S.and Wang, X. (2009). Inorg. Chem. 48, 5117-5128.

[42] Carenco, S., Boissière, C., Nicole, L., Sanchez, C., Le Floch, P. and Mézailles, N. (2010). Chem. Mater. 22, 1340-1349.

[43] Green, L. A. W. and Thanh, N. T. K. (2014). RSC Adv. 4, 1168-1173.

[44] Wang, Y-H. A., Zhang, X., Bao, N., Lin, B. and Gupta, A. (2011). J. Am. Chem. Soc. 133, 11072-11075.

[45] Pan, D., An, L., Sun, Z., Hou, W., Yang, Y., Yang, Z. and Lu, Y. J. Am. Chem. Soc. 130, 5620-5621.

[46] Liu, Y., Yao, D., Shen, L., Zhang, H., Zhang, X. and Yang, B. (2012). J. Am. Chem. Soc. 134, 7207-7210.

[47] Yang, Z. and Klabunde, K. J. (2009). Journal of Organometallic Chemistry 694, 1016-1021.

[48] Vahidshad, Y., Tahir, M. N., Mirkazemi, S. M., Zad, A. I., Ghasemzadeh, R. and Treme, W. (2015). J Mater Sci: Mater Electron 26, 8960-8972.

[49] Panthani, M. G., Akhavan, V., Goodfellow, B., Schmidtke, J. P., Dunn, L., Dodabalapur, A., Barbara, P. F. and Korgel, B. A. (2008). J. Am. Chem. Soc. 130, 16770-16777.

[50] Vaughn II, D. D., In, S-I. and Schaak, R. E. (2011). ACS Nano 5 (11) 8852-8860.

[51] Ramasamy, P., Manivasakan, P. and Kim, J. (2015). CrystEngComm 015 (17), 807-813.

[52] Singh, A., Geaney, H., Laffir, F. and Ryan, K. M. (2012). J. Am. Chem. Soc. 134, 2910-2913.

[53] Ghosh, A. B., Saha, N., Sarkar, A., Srivastava, D. N., Paul, P. and Adhikary, B. (2015). RSC Adv. 5, 102818-102827-

[54] Zhao, X., Luo, B., Long, R., Wang, C. and Xiong, Y. (2015). J. Mater. Chem. A, 3, 4134-4138.

[55] Choi, S-H., Kim, E-G. and Hyeon, T. (2006). J. Am. Chem. Soc. 128, 2520-2521.

[56] Beloš, M. V., Abazović, N. D., Jakovljević, J. K., Janković, I., Ahrenkiel, S. P., Mitrić, M. and Ćomor, M. I. (2013). J Nanopart Res 15 (2148), 1-11.

[57] Soosaimanickam, A., Jeyagopal, R., Hayakawa, Y. and Sridharan, M. B. (2015). Jpn. J. Appl. Phys. 54, 08KA10, 1-4.

[58] Turo, M. J. and Macdonald, J. E. (2014). ACS Nano 8 (10), 10205-10213.

[59] Nagesha, D. K., Liang, X., Mamedov, A. A., Gainer, G., Eastman, M. A., Giersig, M., Song, J-J., Ni, T. and Kotov, N. A. (2001). J. Phys. Chem. B, 105, 7490-7498.

Chapter 5: General conclusions and recommendations

5.1 Conclusions

5.1.1 Synthesis and characterization of capped WS_2 and ß-In_2S_3 nanostructures

The nanostructures were successfully synthesized via a relatively low temperature colloidal route. The synthesis of the nanostructures was optimized at 320 ℃. Oleylamine capped tungsten sulphide nanostructures ranging from 3D nanoflowers, 2d flake-like and 1D rod-like nanostructures by manipulating the reaction time. The effect of morphology on optical properties was investigated. The number of layers of the nanostructures at each reaction time was estimated as it is directly linked to the resulting optical properties.

ß-In_2S_3 nanostructures capped with different alkylamines (OLA, HDA and ODA), alkythiol (1-DDT) and combinations of the alkylamines with a controlled amount of 1-DDT (OLA/1-DDT, HDA/1-DDT and ODA/1-DDT) were synthesized. All the reaction systems were optimized at 1:1 (In:S) ratio, 220 ℃. The effect of the ligands on the morphology of the nanostructures was investigated. It was discovered that the OLA only reaction system coupled with variation of reaction time favoured the development of well-defined hexagonal nanoplates. A combination of OLA and a controlled amount of 1-DDT was conducive to the faster emergence of well-defined hexagonal nanoplates. The hexagonal shape was retained even with extended reaction time. In the case of ODA only system, hexagonal nanoplates evolved as a function of time. The hexagonal nanoplates were however not as well-defined. An ODA/1-DDT combination yielded well-defined hexagonal nanoplates which later transformed into nanorods with prolonged reaction time. Use of 1-DDT as a source of sulphur also yielded the hexagonal naoplates but at a very slow rate due to the slow release of S. A ratio of 1:1.5 (In:S) in the OLA only reaction system also produced hexagonal nanoplates as a function of time.

A ratio of 1:2 (In:S) in the OLA only system, an increased amount of 1-DDT in the OLA/1-DDT combination, 1-DDT only, HDA only and HDA/1-DDT systems were not favourable for the hexagonal morphology. All the resulting morphologies gave different band gaps with respect to their sizes.

5.1.2 Application of OLA/WS_2 and OLA/ ß-In_2S_3 nanostructures in gas detection

Potential gas detection of the nanostructures was demonstrated using thick films deposited on prefabricated IDEs. All the OLA/WS_2 nanostructures responded to vapours of NH_3 and the selected VOCs tested. However, it was clear that the sensitivity of the nanostructures to the gas analyte was related to the morphology. The sensors based on the nanostructures from the shorter reaction times (15 and 45 min) exhibited higher sensitivity. At 15 and 45 min, the nanoflower morpghology with its large surface-to-volume ratio was still present while flake-like and rod-like shapes were obtained at 60, 180 and 240 min respectively. The sensors showed increased sensitivity towards NH_3 at different relative humidities. Different combinations of the sensors were used in the tristimulus analysis and yielded distinct patterns in response to each of the analytes they were exposed to. Not only that, the sensors detected and distinguished between polar and non-polar groups; as well as between similar compounds like alcohols. These fingerprints can thus be used to detect and differentiate between different analytes present in a given environment. Therefore, OLA/WS_2 sensors hold promise for use as components in chemical sensor arrays by virtue of their different morphologies. It is worthy to note that one of the requirements for use in chemical sensor arrays is that the components must have different chemical compositions. Post deposition ligand exchange from OLA to EDT and ME displayed improvement of sensitivity towards NH_3 vapours. Annealed samples of OLA, EDT and ME sensors also showed improved sensitivity but only at low temperatures. This is attributed to the onset of oxidation. Preliminary gas sensing measurements of OLA/ ß-In_2S_3 nanostructures from the 330 min reaction time also showed potential towards methanol, formic acid and formaldehyde.

5.2 Recommendations

It is suggested that further measurements be taken in a more automated gas chamber system. The OLA/WS_2 should be doped with either metals or carbon nanostructures in order to shorten the response/recovery times. Preliminary gas measurements after doping with carbon spheres (CS), hollow carbon spheres (HCS) and nitrogen-doped carbon spheres (N-CS) had showed vast improvement in sensitivity towards NH_3. The doped nanostructures also showed improved distinction between methanol and ethanol in a solution of vodka spiked with methanol. XPS analysis should be performed after ligand exchange to confirm the displacement of the OLA by EDT and ME. The presence and amount of WO_3 on the annealed sensors should be determined by XPS to substantiate the reasons behind the reduction in gas response. An increased amount of WO_3 on OLA/WS_2 surface means only a

small amount of OLA/WS_2 is available for gas detection at room temperature. This would lead to decreased gas response as the WO_3 requires thermal activation.